Title

Surface Processes and Tectonics in the Outer Solar System: Insights from the Saturnian Moons Titan and Enceladus

Author

Schoenfeld, Ashley Marie

Publication Date

2023

Peer reviewed|Thesis/dissertation

UNIVERSITY OF CALIFORNIA

Los Angeles

Surface Processes and Tectonics in the Outer Solar System: Insights from the Saturnian Moons Titan and Enceladus

A dissertation submitted in partial satisfaction of the

requirements for the degree of Doctor of Philosophy

in Geophysics & Space Physics

by

Ashley Marie Schoenfeld

2023

ABSTRACT OF THE DISSERTATION

Surface Processes and Tectonics in the Outer Solar System: Insights from the Saturnian Moons Titan and Enceladus

by

Ashley Marie Schoenfeld

Doctor of Philosophy in Geophysics & Space Physics

University of California, Los Angeles, 2023

Professor An Yin, Chair

Icy satellites of the outer solar system have become the primary target for planetary exploration because of their relevance to understanding of solar-system evolution and to the origin of life. Despite this importance, it remains unclear how different combinations of tectonic deformation, climate conditions, and surficial and interior processes have shaped geologically diverse paths of satellite evolution, as evident from their widely different surface morphologies. Here I address this fundamental question by conducting geological mapping of Enceladus and Titan, the two end-member icy satellites of Saturn; Enceladus has tectonic activity expressed by erupting plumes along active faults while Titan has a thick atmosphere that exerts strong control on its surface processes and hence surface morphologies.

My studies on Enceladus focus on two subjects: (1) the transport time scale for nanoparticles of silica from the ocean floor to the erupting plumes and (2) the role of the non-tidal stress in controlling the phase lag of time-varying plume fluxes that share the same periodicity with the diurnal tide. I assess the transport time scale of silica particles based on experimentally determined scaling relationships for convection systems under rotation and entrainment of particles in thermally-driven convecting fluids. The physics-based analytical relationships obtained from this approach allow the establishment of the size of the silica particles to the thermal regime of the core, which in turn provides the basis for estimating the transport time scale of the particle through the ocean, which I find to be on the order of months. To assess the role of the non-tidal stress in controlling the phase lag of plume eruption on Enceladus, I conducted detailed structural mapping along geyser-hosting faults zones (i.e., the informally named tiger stripes in the literature). My mapping shows that the geysers are preferentially located at local extensional structures along overall strike-slip faults. In order to have simultaneous strike-slip fault motion and local development of extensional structures along the strike-slip faults, coeval shear and tensile failure is required. Imposing this condition and assuming that the peak-eruption time is the result of the superposed tidal and non-tidal stresses reaching the maximum tensile-stress value, I am able to use a stress-decomposition model to determine the static non-tidal stress field along geyser-hosting faults. The required non-title stress field is best explained by lateral viscous flow induced by the gradient of gravitational potential stored in an unevenly thick ice shell.

My research on Titan focuses on the geomorphological response in space and time to climate change and tectonic deformation. In this end, I established the spatial distribution and temporal relationships among morphologically distinctive terrains through mapping in the South

Belet and Soi Crater regions. The major finding of the work is that dunes and lakes are the youngest geomorphologic units resulting from the youngest climate condition that are superposed on top of hummocky, labyrinth, pitted, and mountainous terrains. The presence of dune fields requires aeolian transport, the lake and labyrinth terrains surface and subsurface fluid-flow activities, and the pitted terrain removal of volatile materials. The oldest mountainous terrain is best explained by early tectonic deformation. The spatial distribution of dunes and lakes is consistent with the global mapping results that climate-sensitive terrains are distributed symmetrically with respect to the equator, reflecting the symmetry of the atmosphere circulation.

The dissertation of Ashley Marie Schoenfeld is approved.

Rosaly Lopes

David C. Jewitt

David A. Paige

Hilke E. Schlichting

An Yin, Committee Chair

University of California, Los Angeles

2023

For Dad, Grandma, and my little Chifa

TABLE OF CONTENTS

LIST OF FIGURES

LIST OF TABLES

ACKNOWLEDGMENTS

I would first like to thank my advisor, An Yin, who made me into the geologist I am today. When I started, I knew very little about structural geology but now I feel I have so much to contribute to planetary science as a structural geologist. I would also like to thank An for always reminding me of my strengths, for encouraging me, and for boosting my confidence when I most needed it. I am also very grateful to my committee members, Dave Jewitt, Dave Paige, and Hilke Schlichting, for their patience and support, and for sharing their knowledge and professional insights that made me a better scientist. Lastly, I am thankful for the additional support and mentorship from Mackenzie Day and Carolina Lithgow-Bertelloni; despite not being on my committee, they nonetheless always had their door open for me.

I also want to thank all the wonderful people at JPL who have been so supportive of me and of my career. I especially want to thank my JPL co-mentor Rosaly Lopes for taking a chance on an undergrad with no mapping experience, giving me my first real opportunity to do research. She made my dream to work for NASA come true and put me on the path to getting a PhD. I am thankful for her continued support, bringing me back to work on the Titan project, for all the career advice and help, and just in general her kindness. I would not be here today if not for her. I also want to especially thank Mike Malaska, my second JPL co-mentor, who also has supported me and encouraged me so much, giving me invaluable advice on grad school and job applications, all the while building up my confidence as a scientist and as a person. I enjoy our science conversations, our conversations about culture, and all the colorful stories shared over coffee. Other JPL colleagues I would like to thank are Karl Mitchell, Julie Castillo-Rogez, Steve Vance, Mohit Melwani Daswani, Jennifer Scully, Sona Hosseini, Steve Wall, Diane Evans, Tom Farr, Larry James, Tiffany Verlander, and Meghan Florence.

I would like to thank my fellow Yin lab members, past and current, my office mates and friends: Valeria Jaramillo, Abijah Simon, Julia Miller, Hanzhang Chen, Erin Leonard, Margaret Deng, Kobe Wang, and Peter Haproff. Thank you for listening to me complain, brag, joke, and share my excitement and enthusiasm for whatever was the object of my obsession that week. And thank you most of all for the support and collaboration, for answering my questions and providing advice when I needed it.

I want to thank the graduate students in the EPSS department. They are some of the most wonderful people I have ever met, making all the trials and challenges of graduate school bearable. I have made incredible connections these past years, friendships that I will treasure for life. Thank you to Sebastian Krause, Heather Kirkpatrick, Kynan Hughson, Colin Wilkins, Akash Gupta, Sarah Marcum, Max Parks, Hannah Tandy, Krista Sawchuk, Jason Utas, Emily Hawkins, Ashna Aggarwal, Yufan Xu, Sanjana Prabhu Desai, Jordan Bretz, Kevin Shao, Justin Higa, Emmanuel Masongsong, Elisha Jhoti, Taylor Dorn, Tyler Horvath, Tyler Powell, Ariel Graykowski, and Will Misener. And thank you to my friends who have stuck around with me for the long hall, since before UCLA and even before UC Berkeley: Jasmin Donoso, Natalie Manno, Aaron Rosenfield, and Collin Hightower.

Thank you to my family: to my father Gerard Schoenfeld, who told me I could do anything and everything if I put my mind to it. He cultivated my curiosity and love of science at a young age, yet encouraged me to pursue all my passions, to never forget my love for art and film and books and the world. I miss you every day, I know you are proud of me. To my mother, Virginia Schoenfeld, whose strength inspires me when I am at my lowest, who kept our family together and did what she needed to do to ensure I could take flight, providing me with what I needed for a happy and full life. Who also told me I could do anything and shared her pride and

love freely. To my brother, Johann Schoenfeld, my best friend and confidant. Thank you for being there when I needed a shoulder and an ear, for always being my personal cheerleader. For your sage advice and encouragement. To my grandma, Rosario Gutierrez, for your love and generosity. I will also miss you. And to my dogs: Ozzy, Ebony, Chifa, and Chucky. Thank you for bringing so much joy to my life.

Special thank you to Dr. Karen Payne and Dr. Gily Chechel for keeping me sane, and to Dr. Alan Sull and Pamela Van Laningham for fixing my left arm so I was able to finish writing this thing.

Lastly, I would like to thank the National Science Foundation for funding my research through the Graduate Student Research Fellowship Program (grant number DGE-1650604).

Chapter 2 is an adapted version of the following publication, of which the author of this dissertation was the lead author:

Schoenfeld, A.M., Hawkins, E.K., Soderlund, K.M., Vance, S.D., Leonard, E. and Yin, A., 2023. Particle entrainment and rotating convection in Enceladus' ocean. *Communications Earth & Environment*, *4*(1), p.28. https://doi.org/10.1038/s43247-023-00674-z

Chapter 3 is an adapted version of a manuscript that was prepared for submission to *Icarus*, of which the author of this dissertation was the lead author:

Schoenfeld, A.M. and Yin, A., in prep. Quantifying Tidal versus Non-tidal stresses in driving time-varying fluxes of Enceladus' Plume Eruptions.

Chapter 4 is an adapted version of the following publication, of which the author of this dissertation was the lead author:

Schoenfeld, A.M., Lopes, R.M., Malaska, M.J., Solomonidou, A., Williams, D.A., Birch, S.P., Hayes, A.G., Corlies, P., Le Gall, A., Janssen, M.A. and Le Mouélic, S., 2021. Geomorphological map of the South Belet Region of Titan. *Icarus*, *366*, p.114516. https://doi.org/10.1016/j.icarus.2021.114516

Chapter 5 is an adapted version of the following publication, of which the author of this dissertation was the lead author:

Schoenfeld, A.M., Solomonidou, A., Malaska, M.J., Lopes, R.M.C., Birch, S.P.D., Le Mouélic, S., Florence, M., Verlander, T., Wall, S.D. and Elachi, C., 2023. Geomorphological map of the Soi crater region on Titan. *Journal of Geophysical Research: Planets*, p.e2022JE007499. https://doi.org/10.1029/2022JE007499

Chapter 6 is based upon work that the author of this dissertation undertook as a co-author, including carrying out the global mapping and subsequence analysis, which is published as:

Lopes, R.M., Malaska, M.J., Schoenfeld, A.M., Solomonidou, A., Birch, S.P.D., Florence, M., Hayes, A.G., Williams, D.A., Radebaugh, J., Verlander, T. and Turtle, E.P., 2020. A global geomorphologic map of Saturn's moon Titan. *Nature astronomy*, *4*(3), pp.228-233. https://doi.org/10.1038/s41550-019-0917-6

VITA

EDUCATION

PhD	University of California Los Angeles (UCLA) Dept. of Earth, Planetary, and Space Sciences Geophysics, GPA: 3.9/4	Sept 2016 - Present
MS	University of California Los Angeles Dept. of Earth, Planetary, and Space Sciences Geophysics, GPA: 3.9/4	Sept 2016 - Mar 2020
BA	University of California Berkeley Dept. of Earth and Planetary Science Geophysics, GPA: 3.6/4	Aug 2011 - May 2015

HONORS AND AWARDS

AGU Student Travel Grant	Oct 2022
Division of Physical Sciences Excellence in Outreach Award, UCLA	Sept 2021
EPSS Department Research Award, UCLA	Sept 2020
Titan Through Time Travel Grant, CU Boulder	Mar 2020
EPSS Department Outreach Award, UCLA	Sept 2019
EPSS Department Teaching Award, UCLA	Sept 2018
EPSS Department Extramural Funding Award, UCLA	Sept 2018
NASA Earth and Space Sciences Fellowship (NESSF) Awardee	April 2018
NSF Graduate Research Fellowship (GRFP) Awardee	April 2018
Titan Surface Meeting Travel Grant, Cornell University	May 2018
EPSS Department Teaching Award, UCLA	Sept 2017
EPSS Department Scholarship, UCLA	Sept 2016
Dean's List, University of California, Berkeley	2011-2015
Honors Standing, University of California, Berkeley	2011-2015

PEER REVIEWED PUBLICATIONS

First Author **Schoenfeld, A.M.,** et al., 2021. Geomorphological Map of the South Belet Region of Titan. *Icarus*, 366, p. 114516.

Schoenfeld, A.M., et al., 2023. Particle Entrainment and Rotating Convection in Enceladus's Ocean. *Communications Earth and Environment*, 4(1), p. 28.

Schoenfeld, A.M., et al., 2023. Geomorphological map of the Soi crater region of Titan. *Journal of Geophysical Research: Planets*, p. e2022JE007499

Schoenfeld, A.M. and Yin, A. Quantifying tidal versus tectonic stresses in driving time-varying flux of Enceladus' plume eruptions. Submitted.

Co-Author

Solomonidou, A., **Schoenfeld, A.M.**, et al., in review. Detailed morphology and chemical composition of Titan's surface: unveiling the Soi crater region. *Journal of Geophysical Research: Planets*.

Malaska, M.J., **Schoenfeld, A.M.**, et al., 2022. Potential caves: inventory of subsurface access points on the surface of Titan. *Journal of Geophysical Research: Planets, 127(11).*

Miller, J.W. et al. (including **Schoenfeld, A.M.**), 2021. Fluvial Features on Titan and Earth: Lessons from Planform Images in Low-Resolution SAR. *The Planetary Science Journal*, 2, 142.

Moore, K. et al. (including **Schoenfeld, A.M.**), 2021. Bridge to the stars: A mission concept to an interstellar object. *Planetary and Space Science.*

Malaska, et al. (including **Schoenfeld, A.M.**), 2020. Labyrinth Terrain on Titan. *Icarus*. p.113764.

Solomonidou, A. et al., (including **Schoenfeld, A.M.**), 2020. The chemical composition of impact craters on Titan: Implications for exogenic processing. *Astronomy and Astrophysics*, 641, A16.

Lopes, R.M., Malaska, M.J., **Schoenfeld, A.M.,** et al., 2020. A global geomorphologic map of Saturn's moon Titan. *Nature Astronomy*, pp.1-6.

Solomonidou, A., et al. (including **Schoenfeld, A.M.),** 2019. Spectral and emissivity analysis of the raised ramparts around Titan's northern lakes. *Icarus*.

Griffith, C.A., Penteado, P.F., Turner, J.D., Neish, C.D., Mitri, G., Montiel, N.J., **Schoenfeld, A.M.,** and Lopes, R.M., 2019. A corridor of exposed ice-rich bedrock across Titan's tropical region. *Nature Astronomy*, *3*(7), pp. 642-648.

Lopes, R.M.C., et al. (including **Schoenfeld, A.M.**), 2019. Titan as revealed by the Cassini radar. *Space Science Reviews*, *215*(4), pp. 33.

Solomonidou, A., et al. (including **Schoenfeld, A.M.**), 2018. The spectral nature of Titan's major geomorphological units: constraints on surface composition. *Journal of Geophysical Research: Planets*, *123*(2), pp. 489-507.

Lopes, R.M.C., et al. (including **Schoenfeld, A.M.**), 2016. Nature, Distribution, and Origin of Titan's Undifferentiated Plains. *Icarus*, v. 270, pp. 162-182.

Malaska, M.J., Lopes, R.M.C., Williams, D.A., Neish, C.D., Solomonidou, A., Soderblom, J.M., **Schoenfeld, A.M.,** et al., 2016. Geomorphological map of the Afekan Crater Region, Titan: Terrain relationships in the equatorial and mid-latitude regions. *Icarus*, 270, pp.130-161.

- Chapter 1 -

1.1.Introduction

From the cross-cutting normal faults of Tethys and Rhea to the equatorial ridges of Iapetus, the Cassini-Huygens Mission revealed the icy moons of the Saturnian system to be geologically diverse and dynamic worlds (e.g., Porco et al., 2006; Collins et al., 2010; Schenk et al., 2018). Many of these moons are interpreted to harbor either regional seas or global subsurface oceans (e.g., Nimmo and Pappalardo, 2016), making them compelling astrobiological targets (e.g., McKay et al., 2014; Hendrix et al., 2019; Cable et al., 2021). Two moons of the Saturnian system in particular, Titan and Enceladus, exemplify the breadth of geologic complexities. Titan has a thick atmosphere that contributes to a sedimentary, organic landscape (Lorenz et al., 2006; Radebaugh et al., 2008), a hydrological cycle of methane rainfall and precipitation (Stofan et al., 2007; Mitri et al., 2007; Brown et al., 2008; Hayes et al., 2008), as well as potential cryovolcanism (Lopes et al., 2007, 2013; Le Corre et al., 2009; Wood and Radebaugh, 2020) and tectonic deformation (Radebaugh et al., 2007; Cook-Hallet et al., 2015; Liu et al., 2016a, 2016b; Burkhard et al., 2022). Enceladus is comparatively much smaller than Titan, yet has a highly deformed surface (Bland et al., 2012; Helfenstein et al., 2015; Crow-Willard et al., 2015; Yin and Pappalardo, 2015), active cryovolcanism at the south pole (Porco et al., 2006, 2014; Spencer et al., 2009), and a thermal output that cannot be explained fully by tidal dissipation alone (Spencer et al., 2006; Nimmo et al., 2014). Both moons are confirmed ocean worlds, with several lines of evidence pointing to global subsurface oceans beneath icy outer shells (e.g., Thomas et al., 2016; Hemingway et al., 2018). As such, both moons present compelling astrobiological targets and remain priority targets for the coming decade of planetary exploration (Hendrix et al., 2019; National Academies of Sciences, Engineering, and Medicine, 2022).

Through careful observation and analysis of both Titan and Enceladus' surface geology, constraints can be put on the moon's interior environment, and on possible habitable niches, despite not being directly accessible by remote sensing means. However, the influence of other forces, particularly exogenic influences such as from tides or atmospheres, need to be extracted out to accurately assess interior environments. The motivation questions of the research presented in this thesis are thus:

1) What controls the surface evolution of icy satellites?
2) What is the relative importance between exogenic and endogenic processes in governing icy satellite evolution?

In the following chapters, I explore the relative importance of endogenic and exogenic processes in shaping the surfaces of two end member moons: Titan and Enceladus. Titan represents one extreme in that it is the only moon with a substantial atmosphere, while Enceladus represents another extreme, possessing little to no atmosphere but demonstrating very active geology in the form of cryovolcanism. Chapter 2 presents a particle entrainment model that allows us to infer heat flux at the core/ocean interface below the southern polar region of Enceladus, and to constrain transport times in a convecting ocean. Chapter 3 presents detailed structural mapping along segments of Enceladus tiger stripe fractures and uses kinematic constraints to quantify tectonic stresses in the ice shell. Chapters 4, 5, and 6 focus on detailed regional and global geomorphological mapping of Titan's surface. Chapter 7 is the summary of the key conclusions reached from my PhD research.

1.2 Enceladus

Enceladus is one of five mid-sized satellites orbiting Saturn, approximately 500 km in diameter. Ground-based observations in the early 1980's connected Enceladus' orbital path with the diffuse "E" ring, while the *Voyager* Saturn flybys subsequently made observations of its complex surface geology and measured a remarkably high albedo (~ 90% of incident light; Smith et al. 1982), making it one of the most reflective objects in the Solar System.

The first indication of activity came when Cassini's magnetometer detected a deflection of Saturn's magnetic field around Enceladus (Dougherty et al., 2006). Cassini's thermal infrared spectrometer (CIRS) discovered a hot spot centered at the southern pole during a 2005 flyby (Spencer et al., 2006). Cassini's Imaging Science Subsystem (ISS) made visual observations confirming the warmest regions to be associated with four nearly parallel, linear structures colloquial known as the "tiger stripe fractures" (TSF), and visually observed the active plume jets (Porco et al., 2006). The tiger stripes were measured to be more than 100 K warmer than the surrounding terrain (Spencer et al., 2013) and were confirmed to be the source of substantial plume materials being ejected into space (Spitale and Porco, 2007; Porco et al., 2014). The geologically distinct South Polar Terrain, or SPT, in which the stripes reside, is characterized by extensive tectonic deformation and a conspicuous lack of craters similarly suggestive of a dynamic and youthful surface (Porco et al., 2006), perhaps <1 Ma. By the end of the mission, Cassini had flown through Enceladus' plume seven times, making in situ measurements of its gas content (Waite et al., 2006) and icy particulate (Postberg et al., 2011). While most of the ejected plume material eventually falls back to Enceladus' surface, the smallest grains that escape ultimately source Saturn's E ring (Mitchell et al., 2015; Kempf et al., 2010). The plume material is thought to be sourced (perhaps directly) from a global subsurface liquid water ocean beneath Enceladus' outer icy shell (Thomas et al., 2016).

Observations from Cassini have identified nanometer-sized silica grains in Saturn's E-ring (Hsu et al., 2015), yet their origin is unclear. Tidal deformation within Enceladus' silicate core has been predicted to generate hot hydrothermal fluids that rise from the core-ocean boundary and traverse the subsurface ocean (Choblet et al., 2017). This raises the possibility that the particles observed by Cassini could have been produced by hydrothermal alteration and ejected via the south polar plumes. In Chapter 2, I use an analytical model to quantify potential for particle entrainment in Enceladus' ocean. I use scaling relations to characterize ocean convection and define a parameter space that enables particle entrainment. I find that both the core-ocean heat fluxes and the transport timescale necessary to drive oceanic convection and entrain particles of the observed sizes are consistent with observations and predictions from existing thermal models. I conclude that hydrothermal alteration at Enceladus' seafloor could indeed be the source of silica particles in Saturn's E-ring. This work has been completed and is published in *Communications Earth and Environment* (Schoenfeld et al., 2023).

In Chapter 3, I present detailed structural mapping along two segments of the tiger stripe fractures. Through that mapping, I identify observational evidence suggestive of left-slip deformation along the tiger stripe fractures. Based on the observed left-slip kinematics, we assume a tensile-shear failure criterion that allows us to decompose the total stress field at Enceladus' southern pole into a tidal and tectonic component. In doing so, I find that the tectonic stress field is comparable in magnitude to the diurnal tide suggesting that both components are relevant in determining timing and style of plume eruption. The magnitude of stress generated by topography surrounding the South Polar Terrain (SPT; Fig. 1.1) and ice shell variations is on

order of the tectonic stresses I infer with my model. This work has been completed and will be submitted to *Icarus*.

1.3 Titan

Titan is Saturn's largest moon, slightly larger in size than the planet Mercury. It is the only moon in the Solar System with a substantial atmosphere, first characterized in detail by Voyager 1 (Tyler et al., 1981; Lindal et al., 1983). Titan is also the only other solar system body besides Earth with stable surface liquids. However, with surface temperatures at a breezy 93 K, it is liquid hydrocarbons, not water, that sculpts Titan's landscape. Instead, solid water-ice constitutes the moon's eroding bedrock. Titan's rain is that of methane, its lakes and seas filled with liquid methane, liquid ethane, and a small amount of liquid propane (Cordier et al., 2009; 2013). Despite the differences in materials, temperatures, and gravity fields between Earth and Titan, many of their surface features are similar and can be interpreted as products of the same fundamental geologic processes. However, Titan's thick and hazy atmosphere has challenged the identification of its geologic features at visible wavelengths and the study of its surface composition.

The earliest measurements of Titan came in 2005 with the in-situ delivery of ESA's Huygens probe to Titan, becoming the first successful descent and landing on an outer solar system body. The surface pressure was determined to be ~1.5 times that of Earth (Fulchignoni et al., 2005) and compositional analysis of the atmosphere identified that Titan's atmosphere is predominantly nitrogen (~95%) and methane (5%), with trace amounts of argon, krypton, and xenon (Niemann et al., 2005). Huygens landed in the Adiri region, an equatorial area characterized by linear mountain chains, sand seas, and transitional plains between the two.

During descent, the probe collected images at an altitude of ~10 km, revealing dendritic channel patterns on a steep-sloped hillside. Rounded, smoothed ice pebbles at the landing site suggests transport and deposition by fluvial means (Pérez-Ayúcar et al., 2006).

Planetary geologic mapping is a tool that helps us inventory and interpret the regional or global geologic history of planets and moons and to establish sequence of geologic events. For Saturn's moon Titan, we inventory the landscape using geomorphological terrain units defined by common radar backscatter and morphological characteristics (e.g., Lopes et al., 2016; Malaska et al., 2016a; Lopes et al., 2020; Schoenfeld et al., 2021), which may or may not correspond to true geological units (which are defined by rock composition, age, and history). We therefore refer to the map presented in this study as a geomorphologic map, which nonetheless allows us to infer geologic and temporal relationships.

In Chapter 4, I present detailed mapping of Titan's South Belet region (Fig. 1.2). We used Cassini RADAR in its Synthetic Aperture Radar (SAR) mode data as our basemap, supplemented with data from the RADAR's radiometry mode, the Imagining Science Subsystem (ISS), the Visual and Infrared Mapping Spectrometer (VIMS), and topographic data. We followed the mapping procedure described in Malaska et al. (2016a) and identified four major terrain classes in South Belet: craters, hummocky/mountainous, plains, and dunes. There are two terrain units that were not included in previous studies but were identified in our mapping of South Belet: "bright alluvial plains" and "pitted hummocky". The introduction of these new units is necessary to capture the full range of morphologies seen in South Belet and expands our understanding of processes typical of Titan's equatorial and mid-latitude regions. However, analysis of our geomorphological mapping results suggests the geology of South Belet is

consistent with the narrative of organics dominating the equatorial and mid-latitudes. This work has been completed and is published in *Icarus* (Schoenfeld et al., 2021).

In Chapter 5, I present Titan's Soi crater region (Fig. 1.2) mapped at 1:800,000 scale using methodology by Malaska et al. (2016a) and Schoenfeld et al. (2021). I use Cassini Synthetic Aperture Radar (SAR) as the primary mapping dataset. For areas where SAR was not available, I used lower resolution data from the Imaging Science Subsystem (ISS), the Visible and Infrared Mapping Spectrometer (VIMS), radiometry, and high-altitude SAR (HiSAR) for complete mapping coverage of the region. I identify 22 geomorphological units, 3 of which have been discussed in existing literature but have not yet been incorporated into the detailed mapping investigations (e.g., Schoenfeld et al., 2021; Malaska et al., 2016). These units are the sharp-edged depressions (*bse*), ramparts (*brh*), and bright gradational plains (*pgh*). All six major terrain classes are represented in this region: Craters, Labyrinth, Hummocky/mountainous, Plains, Dunes, and Basin and Lakes. I also observe empty lakes as far south as 40°N. The Soi crater region largely has the same collection and proportion of geomorphological units to other mapped regions on Titan. These results further support the hypothesis that surface processes are, broadly speaking, the same across Titan's middle and equatorial latitudes. This work has been completed and is published in *Journal of Geophysical Research: Planets* (Schoenfeld et al., 2023).

In Chapter 6, I present a global map of Titan's surface, with major geological units identified and described. This project was carried out at the Jet Propulsion Laboratory in collaboration with the Titan Radar Team. Correlations between datasets enabled us to produce a global map even where SAR is incomplete. Because of the lower resolution of the non-SAR datasets, this map was conducted at the 1:20,000,000 scale and units were broadly classified as either Plains, Dunes, Hummocky, Basin and Lakes, Labyrinth, or Craters. Based on their spatial

superposition, we infer that dunes and lakes are relatively young, whereas the hummocky or mountainous terrains are the oldest on Titan. These results also show that Titan's surface is dominated by sedimentary or depositional processes with a clear latitudinal variation, with dunes at the equator, plains at mid-latitudes and labyrinth terrains and lakes at the poles. This work has been completed as in published in *Nature Astronomy* (Lopes et al., 2020). This project was conceived of and completed by the first author; as a co-author, I developed the non-SAR mapping methodology, carried out the global mapping, and conducted subsequence statistics and analysis.

1.4 Figures

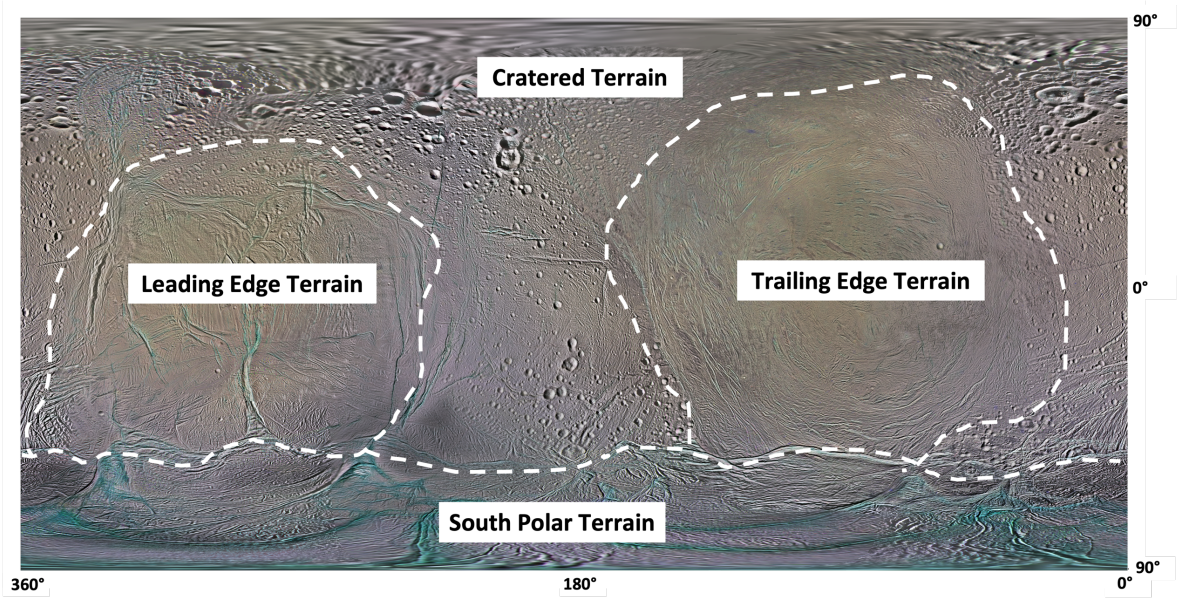

Fig. 1.1 Global ISS mosaic of Enceladus from the USGS. The four main provinces are labeled: Cratered Terrain, Trailing Edge Terrain, Leading Edge Terrain, and South Polar Terrain (SPT).

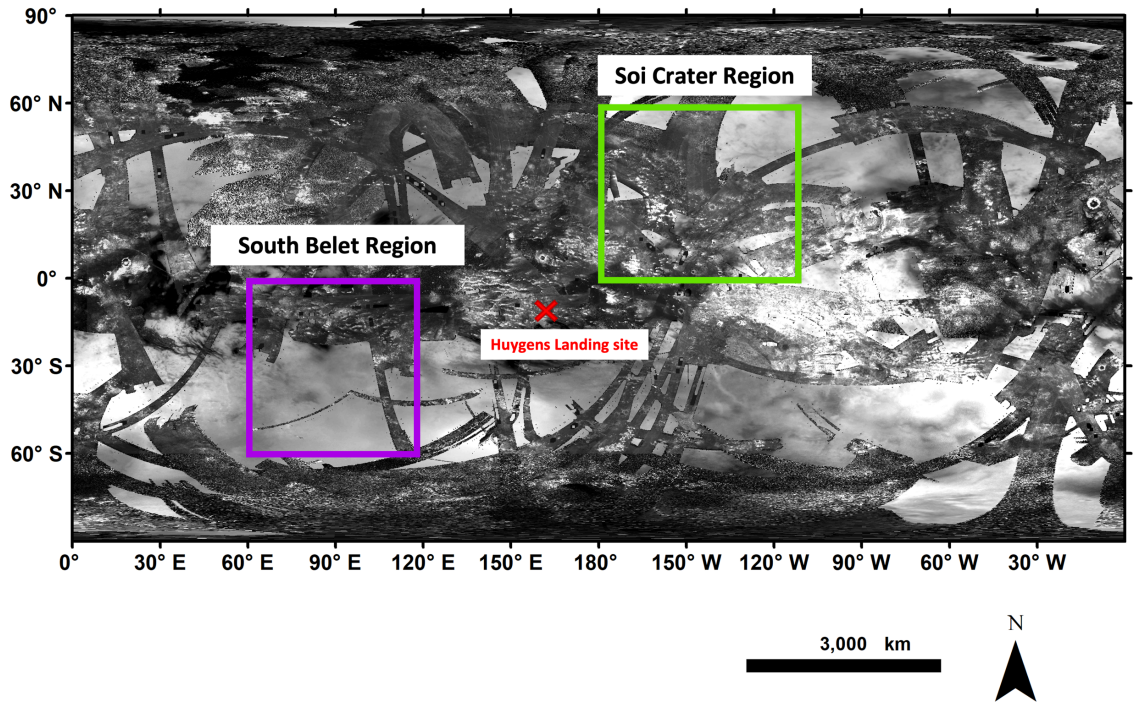

Fig. 1.2 Global context of the Soi crater region (green outline) and the South Belet region (purple outline). Red "x" marks the location of the Huygen's landing site. SAR swaths covering the region are superposed on a global mosaic of Titan created from Imaging Science Subsystem (ISS) data (USGS Astrogeology Science Center). Scale bar applies to equatorial latitudes. North is at the top.

1.5 References

Bland, M.T., Singer, K.N., McKinnon, W.B. and Schenk, P.M., 2012. Enceladus' extreme heat flux as revealed by its relaxed craters. Geophysical Research Letters 39.

Brown, R.H., Soderblom, L.A., Soderblom, J.M., Clark, R.N., Jaumann, R., Barnes, J.W., Sotin, C., Buratti, B., Baines, K.H. and Nicholson, P.D., 2008. The identification of liquid ethane in Titan's Ontario Lacus. Nature 454, 607-610.

Burkhard, L. M., Smith-Konter, B. R., Fagents, S. A., Cameron, M. E., Collins, G. C., &

Pappalardo, R. T. (2022). Strike-slip faulting on Titan: Modeling tidal stresses and shear failure conditions due to pore fluid interactions. *Icarus*, *371*, 114700.

Cable, M.L., Porco, C., Glein, C.R., German, C.R., MacKenzie, S.M., Neveu, M., Hoehler, T.M., Hofmann, A.E., Hendrix, A.R., Eigenbrode, J. and Postberg, F., 2021. The science case for a return to Enceladus. The planetary science journal 2, 132.

Collins, G.C., McKinnon, W.B., Moore, J.M., Nimmo, F., Pappalardo, R.T., Prockter, L.M. and Schenk, P.M., 2009. Tectonics of the outer planet satellites. Planetary tectonics 11, 229.

Choblet, G., Tobie, G., Sotin, C., Běhounková, M., Čadek, O., Postberg, F. and Souček, O., 2017. Powering prolonged hydrothermal activity inside Enceladus. Nature Astronomy 1, 841-847

Cook-Hallett, C., Barnes, J.W., Kattenhorn, S.A., Hurford, T., Radebaugh,J., Stiles, B.,Beuthe, M., 2015. Global contraction/expansion and polar lithospheric thinning on Titan from patterns of tectonism, Journal of Geophysical Research: Planets 120, 1220–1236. doi:10.1002/2014JE004645.

Cordier, D., Mousis, O., Lunine, J.I., Lavvas, P. and Vuitton, V., 2009. An estimate of the chemical composition of Titan's lakes. The Astrophysical Journal 707, L128.

Cordier, D., Barnes, J.W. and Ferreira, A.G., 2013. On the chemical composition of Titan’s dry lakebed evaporites. Icarus 226, 1431-1437.

Crow-Willard, E.N. and Pappalardo, R.T., 2015. Structural mapping of Enceladus and implications for formation of tectonized regions. Journal of Geophysical Research: Planets 120, 928-950.

Dougherty, M.K., Khurana, K.K., Neubauer, F.M., Russell, C.T., Saur, J., Leisner, J.S. and

Burton, M.E., 2006. Identification of a dynamic atmosphere at Enceladus with the Cassini magnetometer. Science 311, 1406-1409.

Fulchignoni, M., Ferri, F., Angrilli, F., Ball, A.J., Bar-Nun, A., Barucci, M.A., Bettanini, C., Bianchini, G., Borucki, W., Colombatti, G. and Coradini, M., 2005. In situ measurements of the physical characteristics of Titan's environment. Nature, 438(7069), pp.785-791.

Hayes, A., Aharonson, O., Callahan, P., Elachi, C., Gim, Y., Kirk, R., Lewis, K., Lopes, R., Lorenz, R., Lunine, J., Mitchell, K., Mitri, G., Stofan, E., Wall, S., 2008. Hydrocarbon lakes on Titan: Distribution and interaction with a porous regolith. Geophysical Research Letters 35, L09204. doi: 10.1029/2008GL033409.

Helfenstein, P. and Porco, C.C., 2015. ENCELADUS'GEYSERS: RELATION TO GEOLOGICAL FEATURES. The Astronomical Journal 150, 96.

Hendrix, A.R., Hurford, T.A., Barge, L.M., Bland, M.T., Bowman, J.S., Brinckerhoff, W., Buratti, B.J., Cable, M.L., Castillo-Rogez, J., Collins, G.C. and Diniega, S., 2019. The NASA roadmap to ocean worlds. Astrobiology 19, 1-27.

Hsu, H.W., Postberg, F., Sekine, Y., Shibuya, T., Kempf, S., Horányi, M., Juhász, A., Altobelli, N., Suzuki, K., Masaki, Y. and Kuwatani, T., 2015. Ongoing hydrothermal activities within Enceladus. Nature 519, 207-210.

Iess, L., Jacobson, R.A., Ducci, M., Stevenson, D.J., Lunine, J.I., Armstrong, J.W., Asmar, S.W., Racioppa, P., Rappaport, N.J. and Tortora, P., 2012. The tides of Titan. Science 337, 457-459.

Iess, L., Stevenson, D.J., Parisi, M., Hemingway, D., Jacobson, R.A., Lunine, J.I., Nimmo, F., Armstrong, J.W., Asmar, S.W., Ducci, M. and Tortora, P., 2014. The gravity field and interior structure of Enceladus. Science 344, 78-80.

Kempf, S., Beckmann, U. and Schmidt, J., 2010. How the Enceladus dust plume feeds Saturn's E ring. Icarus 206, 446-457.

Le Corre, L., Le Mouélic, S., Sotin, C., Combe, J.P., Rodriguez, S., Barnes, J.W., Brown, R.H., Buratti, B.J., Jaumann, R., Soderblom, J. and Soderblom, L.A., 2009. Analysis of a cryolava flow-like feature on Titan. Planetary and Space Science 57, 870-879.

Lindal, G.F., Wood, G.E., Hotz, H.B., Sweetnam, D.N., Eshleman, V.R. and Tyler, G.L., 1983. The atmosphere of Titan: An analysis of the Voyager 1 radio occultation measurements. Icarus 53, 348-363.

Liu, Z.Y.C., Radebaugh, J., Harris, R.A., Christiansen, E.H., Neish, C.D., Kirk, R.L., Lorenz, R.D. and Cassini RADAR Team, 2016. The tectonics of Titan: Global structural mapping from Cassini RADAR. Icarus 270, 14-29.

Lopes, R.M., Mitchell, K.L., Stofan, E.R., Lunine, J.I., Lorenz, R., Paganelli, F., Kirk, R.L., Wood, C.A., Wall, S.D., Robshaw, L.E. and Fortes, A.D., 2007. Cryovolcanic features on Titan's surface as revealed by the Cassini Titan Radar Mapper. Icarus 186, 395-412.

Lopes, R.M.C., Kirk, R.L.; Mitchell, K.L., Le Gall, A., Barnes, J.W., hayes, A., Kargel, J., Wye, L., Radebaugh, J., Stofan, E.R., Janssen, M., Neish, C., Wall, S., Wood, C.A., Lunine, J.I., Malaska, M.J., 2013. Cryovolcanism on Titan: New results from Cassini RADAR and VIMS. Journal of Geophysical Research: Planets 118, 1-20. doi: 10.1002/jgre.20062.

Lopes, R.M.C., Malaska, M.J., Solomonidou, A., LeGall, A., Janssen, M.A., Neish, C., Turtle, E.P., Birch, S.P.D., Hayes, A.G., Radebaugh, J., Coustenis, A., Schoenfeld, A., Stiles, B.W., Kirk, R.L., Mitchell, K.L., Stofan, E.R., Lawrence, K.J., and the Cassini RADAR Team, 2016. Nature, Distribution, and Origin of Titan's Undifferentiated Plains ("Blandlands"). Icarus 270, 162-182.

Lopes, R.M., Malaska, M.J., Schoenfeld, A.M., Solomonidou, A., Birch, S.P.D., Florence, M., Hayes, A.G., Williams, D.A., Radebaugh, J., Verlander, T. and Turtle, E.P., 2020. A global geomorphologic map of Saturn's moon Titan. Nature astronomy 4, 228-233.

Lorenz, R.D., Wall, S., Radebaugh, J., Boubin, G., Reffet, E., … & West, R., 2006. The Sand Seas of Titan: Cassini RADAR Observations of Longitudinal Dunes. Science 312, 724-727. doi: 10.1126/science.1123257.

Malaska, M. J., Lopes, R. M. C., Williams, D. A., Neish, C. D., Solomonidou, A., Soderblom, J. M., et al., 2016a. Geomorphological map of the Afekan Crater region, Titan: Terrain relationships in the equatorial and midlatitude regions. Icarus 270, 130–161.

McKay, C.P., Anbar, A.D., Porco, C. and Tsou, P., 2014. Follow the plume: the habitability of Enceladus. Astrobiology 14, 352-355.

Mitchell, K.L., Barmatz, M.B., Jamieson, C.S., Lorenz, R.D. and Lunine, J.I., 2015. Laboratory measurements of cryogenic liquid alkane microwave absorptivity and implications for the composition of Ligeia Mare, Titan. Geophysical Research Letters 42, 1340-1345.

Mitri, G., Showman, A.P., Lunine, J.I. and Lorenz, R.D., 2007. Hydrocarbon lakes on Titan. Icarus 186, 385-394.

National Academies of Sciences, Engineering, and Medicine. 2022. Origins, Worlds, and Life: A Decadal Strategy for Planetary Science and Astrobiology 2023-2032. Washington, DC: The National Academies Press. https://doi.org/10.17226/26522.

Niemann, H.B., Atreya, S.K., Bauer, S.J., Carignan, G.R., Demick, J.E., Frost, R.L., Gautier, D., Haberman, J.A., Harpold, D.N., Hunten, D.M. and Israel, G., 2005. The abundances of constituents of Titan's atmosphere from the GCMS instrument on the Huygens probe. Nature 438, 779-784.

Nimmo, F., Porco, C. and Mitchell, C., 2014. Tidally modulated eruptions on Enceladus: Cassini ISS observations and models. The Astronomical Journal 148, 46.

Nimmo, F. and Pappalardo, R.T., 2016. Ocean worlds in the outer solar system. Journal of Geophysical Research: Planets 121, 1378-1399.

Pérez-Ayúcar, M., Lorenz, R.D., Floury, N., Prieto-Cerdeira, R. and Lebreton, J.P., 2006. Bistatic observations of Titan's surface with the Huygens probe radio signal. Journal of Geophysical Research: Planets 111.

Porco, C.C., Helfenstein, P., Thomas, P.C., Ingersoll, A.P., Wisdom, J., West, R., Neukum, G., Denk, T., Wagner, R., Roatsch, T. and Kieffer, S., 2006. Cassini observes the active south pole of Enceladus. Science 311, 1393-1401.

Porco, C., DiNino, D. and Nimmo, F., 2014. How the geysers, tidal stresses, and thermal emission across the south polar terrain of Enceladus are related. The Astronomical Journal 148, 45.

Postberg, F., Schmidt, J., Hillier, J., Kempf, S. and Srama, R., 2011. A salt-water reservoir as the source of a compositionally stratified plume on Enceladus. Nature 474, 620-622.

Radebaugh, J., Lorenz, R.D., Kirk, R.L., Lunine, J.I., Stofan, E.R., Lopes, R.M., Wall, S.D. and Cassini Radar Team, 2007. Mountains on Titan observed by Cassini RADAR. Icarus 192, 77-91.

Radebaugh, J., Lorenz, R.D., Lunine, J.I., Wall, S.D., Boubin, G., Reffet, E., Kirk, R.L., Lopes, R.M., Stofan, E.R., Soderblom, L. and Allison, M., 2008. Dunes on Titan observed by Cassini RADAR. Icarus 194, 690-703.

Schenk, P. M., Clark, R. N., Howett, C. J., Verbiscer, A. J., & Waite, J. H. (Eds.). (2018). *Enceladus and the icy moons of Saturn*. University of Arizona Press.

Schoenfeld, A., Lopes, R., Malaska, M., Solomonidou, A., Williams, D., Birch, S., Hayes, A., Corlies, P., Le Gall, A., Janssen, M., Le Mouelic, S., Turtle, E., Florence, M., Verlander, T., 2021. Geomorphological map of the South Belet Region of Titan. Icarus 366, 114516.

Schoenfeld, A.M., Solomonidou, A., Malaska, M.J., Lopes, R.M.C., Birch, S.P.D., Le Mouélic, S., Florence, M., Verlander, T., Wall, S.D. and Elachi, C., 2023a. Geomorphological map of the Soi crater region on Titan. Journal of Geophysical Research: Planets, p.e2022JE007499.

Schoenfeld, A.M., Hawkins, E.K., Soderlund, K.M., Vance, S.D., Leonard, E. and Yin, A., 2023b. Particle entrainment and rotating convection in Enceladus' ocean. Communications Earth & Environment 4, 28.

Smith, B.A., Soderblom, L., Batson, R., Bridges, P., Inge, J.A.Y., Masursky, H., Shoemaker, E., Beebe, R., Boyce, J., Briggs, G. and Bunker, A., 1982. A new look at the Saturn system: The Voyager 2 images. Science 215, 504-537.

Spencer, J.R., Pearl, J.C., Segura, M., Flasar, F.M., Mamoutkine, A., Romani, P., Buratti, B.J., Hendrix, A.R., Spilker, L.J. and Lopes, R.M.C., 2006. Cassini encounters Enceladus: Background and the discovery of a south polar hot spot. Science 311, 1401-1405.

Spencer, J.R., Barr, A.C., Esposito, L.W., Helfenstein, P., Ingersoll, A.P., Jaumann, R., McKay, C.P., Nimmo, F. and Waite, J.H., 2009. Enceladus: An active cryovolcanic satellite. Saturn from Cassini-Huygens, 683-724.

Spencer, J.R. and Nimmo, F., 2013. Enceladus: An active ice world in the Saturn system. Annual Review of Earth and Planetary Sciences 41, 693-717.

Spitale, J.N. and Porco, C.C., 2007. Association of the jets of Enceladus with the warmest regions on its south-polar fractures. Nature 449, 695-697.

Stofan, E.R., Elachi, C., Lunine, J.I., Lorenz, R.D., Stiles, B., Mitchell, K.L., Ostro, S., Soderblom, L., Wood, C., Zebker, H., Wall, S., Janssen, M., Kirk, R., Lopes, R., Paganelli, F., Radebaugh, J., Wye, L., Anderson, Y., Allison, M., Boehmer, R., Callahan, P., Encrenaz, P., Flamini, E., Francescetti, G., Gim, Y., Hamilton, G., Hensley, S., Johnson, W.T.K., Kelleher, K., Muhlman, D., Paillou, P., Picardi, G., Posa, F., Roth, Seu, R., Shaffer, S., Vetrella, S., West, R., 2007. The lakes of Titan. Nature 445, 61-64. doi: 10.1038/nature05438.

Thomas, P.C., Tajeddine, R., Tiscareno, M.S., Burns, J.A., Joseph, J., Loredo, T.J., Helfenstein, P. and Porco, C., 2016. Enceladus's measured physical libration requires a global subsurface ocean. Icarus 264, 37-47.

Tyler, G.L., Eshleman, V.R., Anderson, J.D., Levy, G.S., Lindal, G.F., Wood, G.E. and Croft, T.A., 1981. Radio science investigations of the Saturn system with Voyager 1: Preliminary results. Science 212, 201-206.

Waite Jr, J.H., Combi, M.R., Ip, W.H., Cravens, T.E., McNutt Jr, R.L., Kasprzak, W., Yelle, R., Luhmann, J., Niemann, H., Gell, D. and Magee, B., 2006. Cassini ion and neutral mass spectrometer: Enceladus plume composition and structure. Science 311, 1419-1422.

Wood, C.A. and Radebaugh, J., 2020. Morphologic evidence for volcanic craters near Titan's north polar region. Journal of Geophysical Research: Planets 125, p.e2019JE006036.

Yin, A. and Pappalardo, R.T., 2015. Gravitational spreading, bookshelf faulting, and tectonic evolution of the South Polar Terrain of Saturn's moon Enceladus. Icarus 260, 409-439.

- Chapter 2 -

2 Particle Entrainment and Rotating Convection in Enceladus' Ocean

2.1 Introduction

Enceladus, a ~500-km-diameter moon of Saturn, is characterized by a highly tectonized surface[1-3] and ongoing venting of material from the south pole[4] sourced from a series of parallel ‘‘tiger-stripe" fractures in the ice shell. The tiger-stripe fractures act as conduits that cut through the ice shell, tapping into a sodium- and potassium-bearing subsurface liquid reservoir[5-8]. The detection of significant physical libration[9] further demonstrates that Enceladus' outer ice shell is mechanically decoupled from its rocky core and suggests that the subsurface reservoir is a global ocean.

Subsequent chemical analyses of the south polar plumes with Cassini's Cosmic Dust Analyzer (CDA) have revealed the presence of nanometer-scale silica particles, indicating that the water identified within the plumes was once in contact with silicate rock and subjected to high temperatures[10,11]. Consequently, the chemistry of Enceladus' plumes has been interpreted as evidence for hydrothermal activity at the ocean/core interface. The identification of substantial amounts of H_2 in the plume likewise serves as a marker of hydrothermal processes, as the observed amount exceeds what would be expected from primordial storage or radiolysis[12]. The detection of silica grains in the plumes suggests that there are flows within the ocean capable of transporting materials from the core-ocean interface, through the ocean, and across the ice shell. The means by which oceanic flow within Enceladus could have realized the inferred transport, however, has not been fully addressed.

Fluid motions within Enceladus' ocean may be driven by mechanical and/or thermal forcing. Mechanical forcing is most likely induced by the obliquity, libration, and/or eccentricity of Enceladus[13]. It is debated whether the small obliquity of Enceladus rules out its effectiveness

as a flow-generating mechanism[14-18]. While physical libration could produce oceanic turbulent flows[19,20] and dominates tidally induced dissipation, the overall power dissipated in the ocean is nonetheless small[21]. However, tidal dissipation within the ice shell via eccentricity is often inferred to be a main source of tidal heating capable of maintaining a lasting global ocean inside Enceladus[22]. Furthermore, tidally induced deformation and friction within a porous silicate core may generate hot and narrow upwelling zones at the seafloor[23], sourcing hot water into the cooler ocean layer[24]. The heat flux at the subsurface seafloor thus likely drives convection and mixing in the ocean[25-29].

The suspension of particles in a fluid depends strongly on the mechanism of turbulence generation, namely buoyancy stresses driven by convection (viscous stress associated with buoyancy flux from the seafloor) or Reynolds stresses associated with unsteady turbulent motions (driven by convection or mechanical forcing)[30,31]. For rapidly rotating convection, such as expected for Enceladus' ocean, thermally driven buoyancy forces are typically much larger than non-linear, inertial forces[32]. Moreover, experiments have shown that turbulent shear flows associated with downwelling cold plumes (surface cooling alone) were insufficient to cause entrainment, whereas entrainment occurred when heated from below[30]. These results are consistent with the ratio of Reynolds stresses to the weight per unit area of the particle, $\Delta\rho g D$ (where $\Delta\rho$ represents particle-fluid density difference, g is gravity, and D is particle diameter), being too small for incipient motion of a particle bed[30]. Convective entrainment is, therefore, argued to be the primary cause of upward transport of hydrothermal products, such as silica particles, from the ocean floor to the surface to be ejected at the south polar plumes. Thus, we consider only the role of thermal buoyancy stresses under the presence of rotation in transporting

silica particles across the ocean of Enceladus. The geometry of such a fluid system is conceptualized in Fig. 2.1.

We apply a particle entrainment model based on laboratory experiments[30,31] (see Methods) and use scaling relations[33-37] (see Methods) to characterize length and velocity scales of convection in the ocean using a parameter space constrained from the particle entrainment model results. Physical parameters for Enceladus' ocean are summarized in Table 2.1.

2.2 Results

Eq. (1) (Methods) presents the ratio of buoyancy stress to weight per unit area of the particle; the condition for entrainment of solid particles with a density ρ_P in a thermally convecting fluid with a density ρ_f occurs when this ratio exceeds some critical value[30,31]. For the purposes of this study, we assume equilibrium in ocean composition and that thermal buoyancy dominates entrainment behavior. We algebraically solve for particle diameter with spherical geometry, determining its dependence on heat flux from the silicate core. Fig. 2.2 illustrates the stability of predicted properties with depth and justify our decision to hold heat capacity and ocean density constant in our model. Contours are shown of density, thermal expansivity, and heat capacity vs. ocean salinity and temperature at pressures of 1 and 10 MPa; ~1 MPa is approximately the pressure under 5 km of ice at the south pole, while 10 MPa is potentially 10's of km into the seafloor[38]. When calculating particle size, we assume that the thermal expansion coefficient is always positive so that convection may proceed throughout the ocean. As shown in Fig. 2.2b, buoyancy requires a minimum ocean salinity of ~ 20 g kg^{-1}, or an increase in temperature by roughly half a degree to the point where the thermal expansivity again becomes positive. An ocean salinity of ~ 20 g kg^{-1} is the higher end-member estimate for inferred plume

salinity[6] but fits generally well within other estimates for ocean salinity[10,39-44]. As in previous studies, we assume a base temperature around 274 K[44] and assume $\Delta T = 5$ mK in the normally adiabatic ocean[38]. Contour calculations were made specifying 12 g kg^{-1} seawater to approximate the Cl rich ocean composition inferred from Cassini Dust Analyzer sampling of the plumes[5].

We find that the entrained particle size increases with increasing core heat flux when assuming a constant thermal expansivity of $\alpha = 1x10^{-5}$ K^{-1} (Fig. 2.3a). For a fixed heat flux, the entrained particle size increases with decreasing density contrast, $\Delta\rho$, between the particle and the fluid. Similarly, the relationship between the entrained particle size and heat flux varies with different thermal expansivity coefficients when assuming a constant density contrast of $\Delta\rho =$ 1200 kg m^{-3} (Fig. 2.3b); an order of magnitude change in thermal expansivity results in an order of magnitude change in estimated heat flux. For particles with silica density of 2200 kg m^{-3} [10], we find that a heat flux of $\geq$ 0.3 W m^{-2} is necessary to explain entrainment of the largest detected particles.

We can compare the results of our particle entrainment model to the results from ref.[24]. Their model shows that the distribution of heat flux along the seafloor is dominated by radially advecting water that varies laterally in temperature. These narrow upwellings are characterized as powerful hotspots, from 1 to 5 GW, with temperatures in excess of 363 K. For a core radius of ~190 km [45] and assuming that heat flux at the surface is confined to an area comparable in size to the modelled hot spots in ref.[24] —approximately ~10% of the polar area—we estimate a heat flux of ~ 3 GW, which fits well into this 1-5 GW range. Ref.[24] also predicts localized heat fluxes on the order of 1 to 8 W m^{-2}, averaged over a period of 10 Myr.

We calculate flow speeds (Eq. (5), Methods) in terms of the dimensionless free-fall Rossby number (i.e. the ratio of inertial to Coriolis forces) to be on the order of 10^{-4} to 10^{-3},

demonstrating the importance of rotation on convective transport. Fig. 2.3c shows the turbulent length scale (Methods) versus heat flux. The range of heat fluxes reported above, based on observed plume particle sizes[10], are highlighted by the yellow shaded area in Fig. 2.3c. Varying the ocean thicknesses H at 20 km, 40 km, and 60 km to accommodate the distribution of ice shell thickness variations[9,16,45,46] leads to turbulent length scales on the order of 100's of meters to a few kilometers. Fig. 2.3d shows free-fall velocity versus heat flux.

Vertical flow speeds are on the order of a few mm s^{-1}, representing an upper bound. The corresponding transport time of entrained silica particles from the core-ocean boundary to the base of the ice shell can be estimated by $T_{ff} = H/u_{ff}$, which is on the order of several months and conversely represents a lower bound. Note that the length scale begins to plateau with increasing heat flux, suggesting that there is an upper bound on characteristic fluid length scale despite increasing heat flux. Conversely, there is also a minimum velocity, and by extension minimum length scale, that exists as heat is injected into the system.

Due to water's anomalous thermal expansion coefficient, there exists a stably stratified layer in the upper ocean, extending from where the thermal expansion coefficient is negative at the freezing front to where the thermal expansion coefficient becomes positive such that convection proceeds. This layer provides a thermally conductive barrier between the convecting ocean and the ice and is similar to the stratified layer that has been hypothesized to exist in the ocean of Europa[47]. The fluid beneath the ocean would be close to the temperature of water's zero thermal expansivity, or about 0.5 K above freezing for 20 g kg^{-1} seawater at 1 MPa. For k = 0.5 W m^{-1} K^{-1}, ΔT_s = ~0.5 K (across the stagnant layer), and q = 0.3 W m^{-2}, we use Eq. (6) (Methods) and calculate the equilibrium thickness of such a stagnant layer to be h_s ~ 1 m. With no convection in the stratified layer, the vertical transport of tracers would be primarily achieved by

diffusion with a timescale, τ_{diff}, given by Eq. (7). For h_s = 1 m, and κ = 1.3x10^{-7} m^2 s^{-1}, τ_{diff} ~ 3 months. However, ref.[48] estimates that vertical mixing through the stratified layer will take hundreds of years, provided mixing is dominated by molecular diffusivity. The difference in timescales comes from the difference in assumed heat flux; ref.[48] use an average global heat flux when calculating the stagnant layer thickness, whereas we use the heat flux under the south pole as inferred from our model. The two heat fluxes differ by an order of magnitude, resulting in a stagnant layer smaller by an order of magnitude, and resulting in a diffusive timescale smaller by three orders of magnitude. The thickness of a conducting stratified layer will likely vary with latitude; we argue that since heat flux is expected to be highest under the south pole, as supported by both observation and modeling, the thinnest possible section of such a layer would be found under the south pole. Ref.[48] similarly explore the possibility that vertical mixing in the ocean may be enhanced by turbulence, induced either from libration or tidal dissipation. In such a scenario, molecular diffusivity would be replaced by turbulent diffusivity, increasing both the depth of the stratified layer and the upward transport timescales, potentially increasing the diffusive timescale by three orders of magnitude. For the purposes of our study, we only invoke molecular diffusivity in our calculations, as the magnitude of turbulent diffusivity relevant to Enceladus is highly unconstrained.

We consider some alternate estimates for the ability of a rising particle to breach the stagnant layer. First, we suggest that the ability of an ascending plume to penetrate a stagnant layer can be estimated using the Brunt–Väisälä frequency (Eq. 8; Methods). Given sufficient upwelling momentum, a rising fluid parcel may overcome loss of buoyancy at the layer interface. For g = 0.113 m s^{-2}, ρ = 1000 kg m^{-3}, and $\frac{\partial \rho}{\partial z}$ ~ -5x10^{-4} kg m^{-3} m^{-1}, N ~ 0.24 mHz, or a period of ~ 70 minutes. Thus, a fluid parcel encountering the stagnant region needs a velocity of greater than

0.24 mm s^{-1} to traverse the boundary. In regions away from the south pole, the heat flux at the ice interface is likely about 100x lower, and the stagnant region would be proportionally thicker. As such, away from the south pole the necessary speed is likely closer to 24 mm s^{-1}. The characteristic vertical velocities we calculate (on the order of several mm s^{-1}) thus imply that rising materials could reach the ice at the south pole where heat fluxes are high. Second, we consider Stokes dynamics for a vertically upwelling nanoparticle. Plugging in appropriate values into Eq. (9), we calculate rise times that are on the order of nanoseconds and rise heights that are subatomic. Stokes dynamics are thus not expected to apply to nanometer sized particles, such that Brownian motion is more appropriate. Consequently, further investigation is required to determine how such a stratified layer may affect material transport in Enceladus' upper ocean, as well as more consideration for boundary layer physics that may determine a particle's final transition from ocean to vacuum.

2.3 Discussion

The new results we present for transport times through Enceladus' ocean have important differences from predictions made by other models. Ref.[10] use the precipitation chemistry of silica to estimate transport times through and out of the ocean; the detected nano-silica particles with radii <10 nm imply fast and continuous upward transport of hydrothermal products, likely within months to years. In contrast, ref.[24] use tidal dissipation models to predict that particles are carried from the seafloor to the bottom of the ice crust within a few weeks to months. Despite the differences in methodology, our calculations for transport times of several months are similar to lower end model predictions by ref.[10] and higher end predictions by ref.[24]. Ocean circulation models similarly predict vertical flow speeds of a few mm s^{-1} when driven by thermal

convection, strongly constrained by rotation across the entire ocean domain[28], again similar to our estimates. Our results imply that relatively fresh (i.e. more recently expelled) materials from hydrothermal vents (and possible biosignatures) are capable of being transported directly from the core to the south polar plumes and can be sampled and analyzed with a suitable instrument suite.

We note that while our assumed salinity is within previously estimated values, it is possible that salinity measurements inferred from direct plume sampling represent an underestimate of the ocean's bulk salinity. Heterogeneity in the thickness of Enceladus's ice shell suggests regions of localized freezing and melting exist at the ocean–ice interface, resulting in the modification of the density (and salinity) of the upper ocean via freshwater fluxes and brine rejection[44]. The ensuing low salinity layer could penetrate up to ~1 km below the ocean–ice interface and would vary from the pole to the lower latitudes[48,49]. If such a layer were to have salinity below a critical point of about 20 g kg^{-1}, vertical transport of particles to the ice-ocean interface may be suppressed. If the upper part of Enceladus' ocean is stably stratified, for example, transit timescales may be on the order of hundreds of years[50].

We now briefly address observational biases and potential consequences for our results. Salts, organics, and silica components have been identified within Saturn's E-ring and Enceladus' plumes via direct sampling and have been interpreted to originate as submicron particles floating below the icy crust, eventually serving as submicron condensation cores for the ice grains freezing out of plume ejecta[51]. The observed nanometer-sized silica particles from ref.[10] were initially embedded in icy grains and released as stream particles via sputter erosion in the E-ring; size estimates come from both integration of the Si+ signal and from dynamical analysis[52]. Stream-particle measurements offer the highest quality CDA spectra with the lowest

possible signal contamination from refractory constituents, such as salt, that are otherwise prevalent in the E-ring and Enceladus' plume[53]. Stream particles are defined as nanometer-sized grains twice removed from the plume: they are particles that were able to escape from Enceladus plumes into the E-ring, were stripped down by plasma interactions, and subsequently ejected into interplanetary space at speeds of >100 km s^{-1} [52,53]. Ultimately, however, the source of the Saturnian stream particles is Enceladus, and thus stream particles can be used to probe the moon's interior.

If we consider the hotspot heat fluxes of 1-5 W m^{-2} from ref.[24], our model suggests that silica grains of ~100 nanometers are capable of being entrained and transported to the ocean-core interface (see Fig. 2.3a and b). However, aside from the observed range of 2-9 nm radii particles, Cassini did not report larger silica grains. As discussed in ref.[10], the size of a silica grain is controlled by its residency time within the ocean, as prescribed by thermo-chemical properties of a silica-water system. The argument for a hydrothermal origin for the silica nanoparticles is two-fold[10]: 1) the metal-poor (or metal-free) stream particle spectra[54] are not in agreement with those of typical rock-forming silicate minerals (that is, olivine or pyroxene), and 2) the improbability of homogeneous fragmentation of pure bulk silica into particles with radii exclusively below 10 nm within Enceladus. One may expect a broader continuum of sizing if the limiting factor was the ability to be ejected. It is possible then that larger nano-silica grains are not observed simply because they do not have time to grow beyond ~ 10 nm. Alternatively, we posit that larger silica (or silicate) grains derived from other sources, i.e. abraded from the core, may be getting entrained and ejected, but that they result in grains that are too large to escape to altitudes where they could be fully characterized in the spectra.

Using the particle entrainment model, we show that the silica particle sizes observed by Cassini require core heat fluxes of $\geq$ 0.3 W m^{-2}, given our assumed values of thermal expansivity and density contrast. A summary schematic of our dynamical model for convective entrainment in Enceladus' ocean is presented in Fig. 2.4. If we assume that this heat flux is confined to ~10% of the polar core area[24], akin to hotspots, we estimate this heat flux to be ~ 3 GW. Using the parameter space constrained from the particle entrainment model, we find that the turbulent length scale of Enceladus' ocean varies from 100's of meters to a few km, with vertical flow speeds on the order of mm s^{-1} that correspond to transport times of several months. Our derived values compare well to timescale predictions made by ref.[10] and ref.[24]. The analysis shows that convection in the ocean of Enceladus can explain the entrainment, transport, and ultimate delivery of silica particles from Enceladus' core/ocean interface to the ice shell. The physical mechanism proposed in this work can similarly be used to constrain material mixing within other icy satellites with a three-layer internal structure comparable to that of Enceladus, where a silicate core is in contact with a subsurface ocean. Understanding how physical and chemical interactions between the oceans, icy shells, and the cores are central to determine the evolution of icy satellites, which in turn has implications for assessing the habitability of other ocean worlds.

2.4 Methods

2.4.1 Constraining Particle Size from Convective Upwelling

The condition for entrainment of solid particles with a density ρ_P in a thermally convecting fluid with a density ρ_f occurs when the ratio of buoyancy stress to weight per unit area of the particle exceeds some critical value[30,31]:

$$\left(\frac{\eta\alpha g q}{c_p}\right)^{1/2}\frac{1}{\Delta\rho g D} \geq C \quad (1)$$

where C is an empirical constant with a value between 0.1 and 0.2, $\Delta\rho = \rho_P - \rho_f$ is the density contrast between the solid particles and the fluid, α is thermal expansivity of the fluid, η is fluid dynamic viscosity, q is basal heat flux, g is gravitational acceleration, D is particle diameter, and c_p is specific heat capacity.

The thermal expansion coefficient in (1) depends on pressure, temperature, and salinity. Observational inferences for the salinity of Enceladus' ocean remain uncertain, which translates to uncertainty in thermal expansivity. We choose three values of thermal expansivity for our calculations, adhering to the assumption that thermal expansivity is sufficiently positive such that Enceladus possesses a homogeneous and unstratified, convecting subsurface ocean: $\alpha \simeq$ 1x10^{-5}, 5x10^{-5}, 1x10^{-4} K^{-1}. Our reasoning for these values is as follows: a thermal expansivity coefficient of 1x10^{-4} K^{-1} is on the order of what has been used for Europa[28,56] yet is likely unrealistic for Enceladus given different pressure conditions. We also use the value 5x10^{-5} K^{-1}, which is cited for Enceladus in ref.[44] given an ocean salinity of 22 g kg^{-1} and ocean temperature of 274 K at 20 MPa. This pressure is high for Enceladus, so we also use the value 1x10^{-5} K^{-1}, which comes from calculations made with PlanetProfile at 1 MPa and 10 MPa for realistic salinity and temperature conditions within the ocean (Fig. 2.2)[38]. We use a dynamic viscosity of $\eta \simeq$ 8.9x10^{-4} Pa s [57], a thermal heat capacity at constant pressure of $c_p \simeq$ 4200 J kg^{-1} K^{-1} (Fig. 2.2c,f), and the average gravitational acceleration for Enceladus, $g \simeq$ 0.113 m s^{-2}. For simplicity, we also assume that the difference in density between the silica grains and the convecting fluid, Δρ, is constant throughout the ocean column, implying that the salinity of the water does not change significantly with depth (Fig. 2.2a,d), and that the density of the amorphous silica grains does not vary substantially.

2.4.2 Length Scales

In a rotating, low viscosity fluid, buoyant upwellings can become influenced by the effects of rotation, which act to suppress and align plumes along the axis of rotation, creating columnar structures[58-61]. In this work, we assume oceanic flows will be sufficiently influenced by Enceladus' rotation such that fluid structures will be overall aligned with the axis of rotation. This assumption follows with recent work by ref.[28], though it is discussed therein that a low fluid thermal expansivity is likely needed to decrease the effects of bouyancy such that fluid remains organized in columnar-like structures. This finding additionally influences the range of ocean thermal expansivity values explored in this work (see above). Qualitatively, we thus describe the fluid as a series of vertical columns aligned with the axis of rotation[62]. The physical characteristics of the rotating system, such as the width of these columnar structures, depends on the strength of the rotation as well as the amount of energy entering the system[63,64].

We define two end-member length scales of the convecting columns. For a viscosity-dominated system, the horizontal width of the columns (δ_v) may be written as[65-67]:

$$\delta_v \sim E^{1/3} H \qquad (2)$$

where H is the total vertical length of the columns and is equivalent to the ocean thickness; E is the Ekman number defined by $E = \frac{\eta}{2\rho_f \Omega H^2}$, and Ω is the rotational frequency (Fig. 2.1b). Using parameter values listed in Table 2.1, the Ekman number for Enceladus is ~10^{-12} to 10^{-11}, corresponding to δ_v on the order of 1 to 10 m. We also estimate the Rayleigh number for Enceladus, which represents the ratio between buoyancy and viscous and thermal diffusion in a fluid and is defined as $Ra = \alpha g \Delta T H^3/(\nu\kappa)$. We use our range of thermal expansivities, ocean thicknesses, superadiabatic temperatures from (5), and a viscous diffusivity of $\nu = 10^{-6}$ m^2 s-1

to find that *Ra* is on order of 10^{17} to 10^{19}. Taken together, these values suggest that the role of viscosity is not one of leading order[28].

Conversely, for instances of strong thermal forcing, it is expected that inertia will instead play an important role in the dynamics of a rotating convective system. For inertia-dominated systems, the horizontal width of the turbulent convecting columns (δ_t) can be obtained by balancing the Coriolis and inertial forces[68-70]:

$$\delta_t \sim Ro^{\frac{1}{2}} H \quad (3)$$

where $Ro = \frac{U}{2\Omega H}$ is the Rossby number representing the ratio of inertial to Coriolis forces with U as the characteristic velocity of the fluid. Today's most advanced numerical models are only just beginning to probe this turbulent regime, but ref.[71] find fluid structures that agree with (3) in the most rapidly rotating models containing strong thermal forcing. Furthermore, the recent study by ref.[37] finds that the viscous and turbulent length scales scale equivalently over the parameter space explored. Thus, we examine the turbulent scale as a function of heat flux in order to characterize the predicted length scale of our model flow.

2.4.3 Flow Velocities

Rapidly rotating turbulent flows, of which are thought to be relevant to the bulk convection of Enceladus' ocean, are governed by an inviscid balance between the system's rotation, inertia, and buoyancy[28,37,72-74]. Ref.[75] shows that in a rapidly rotating system, the inertial timescale scales equivalently to the convective free-fall time. Thus, the characteristic system velocity can be estimated by the free-fall velocity, which is defined as $u_{ff} \sim \sqrt{\alpha g H \Delta T}$ [76-78]. Here, ΔT is the average superadiabatic temperature contrast across the convective layer.

We note that using the free-fall velocity to define the system scale velocity assumes a balance between buoyancy and inertia in the flow and assumes that viscous diffusion is negligible given that the inertia of the flow outweighs the viscous diffusion[79,80]. This will thus provide an upper-bound on vertical velocity (and conversely a lower bound on transport timescale). We include a pre-factor of 0.1 in our calculations of free-fall velocity, as derived from convection experiments using water[37,81]. The free-fall velocity relates to the non-dimensional free-fall Rossby number, $Ro_{ff,}$ by:

$$Ro_{ff} = \frac{U_{ff}}{2\Omega H} \approx \frac{(0.1)\sqrt{\alpha g H \Delta T}}{2\Omega H}. \quad (4)$$

We note that this parameter is often referred to as the convective Rossby number.

Following ref.[81-83], we use the following scaling relationship to quantify heat transfer in the convecting system:

$$Nu \approx 0.15 Ra^{1.25} 2E^2 \quad (5)$$

where $Nu = qH/(\rho_f c_p \kappa \Delta T)$ is Nusselt number with κ representing thermal diffusivity. Additionally, Ra is Rayleigh number and E is Ekman number. We use (5) to solve algebraically for the superadiabatic temperature and then plug it into our expression for free fall velocity.

2.4.4 Penetrating a Stagnant Fresh Water Layer

The low salinity of Enceladus' ocean implies the existence of a stratified freshwater layer just under the ice, due to water's anomalous thermal expansion. This layer provides a thermally conductive barrier between the convecting ocean and the ice[47]. We can use the heat diffusion equation to calculate the thickness of such a stagnant layer:

$$q = k\frac{\partial T}{\partial z} \approx k\frac{\Delta T_s}{h_s} \rightarrow h_s \approx \frac{k\Delta T}{q} \quad (6)$$

For k = 0.5 W m^{-1} K^{-1} (corresponding to a molecular diffusivity coefficient of κ = 1.3x10^{-7} m^2 s^{-1}), the temperature across the stagnant layer ΔT_s = 0.5 K, and q = 0.3W m^{-2}, the thickness of such a stagnant layer would be h_s = 1 m.

With no convection in the stratified layer, the vertical transport of heat would be primarily achieved by diffusion[48]:

$$\tau_{diff} \sim \frac{{h_s}^2}{\kappa} \tag{7}$$

For h_s = 1 m, and κ = 1.3x10^{-7} m^2 s^{-1}, τ_{diff} ~ 3 months.

Given sufficient momentum, an upwelling fluid parcel may breach this barrier layer. The vertical oscillation of a parcel at neutral density perturbed at the interface is given by the Brunt–Väisälä frequency[62]:

$$N = \sqrt{-\frac{g}{\rho}\frac{\partial \rho}{\partial z}} \tag{8}$$

For g = 0.113 m s^{-2}, ρ = 1000 kg m^{-3}, and $\frac{\partial \rho}{\partial z}$ ~ -5x10^{-4} kg m^{-3} m^{-1} (calculated with Gibbs Seawater)[38], N ~ 0.24 mHz, or a period of ~ 70 minutes. Thus, a parcel encountering the stagnant region needs a velocity of greater than 0.24 mm s^{-1} to traverse the boundary of ~ 1 m.

Lastly, we consider an upward travelling nanometer scale particle subjected to Stokes resistance to provide an additional estimation for penetration timescale. The rise time of the particle is given by:

$$t = \frac{m_p}{6\pi\mu r}\ln\left(1 - \frac{6\pi\mu r}{m_p}\frac{\rho}{\Delta\rho g}\upsilon_0\right) \tag{9a}$$

where m_p = 5.24x10^{-20} kg is the particle mass, r = 10 nm is the particle radius, ρ = 2560 kg m^{-3} is the particle density, μ = 1 mPas is the drag coefficient, and υ_0 = 1 mm s^{-1} is the initial upward velocity. The rise height is then given by:

$$h = (v_0 + v)t = \left(v_0 + \frac{m_p}{6\pi\mu r}\frac{\Delta\rho g}{\rho}\left(1 - e^{-\frac{6\pi\mu r}{m_p}t}\right) + v_0 e^{\frac{-6\pi\mu r}{m_p}t}\right)t \qquad (9b)$$

With (9a) and (9b), we find the rise time to be measured in nanoseconds and the rise height to be sub-atomic. We therefore suggest that Stokes dynamics do not apply to particles of this size.

2.5 Figures and Figure Captions

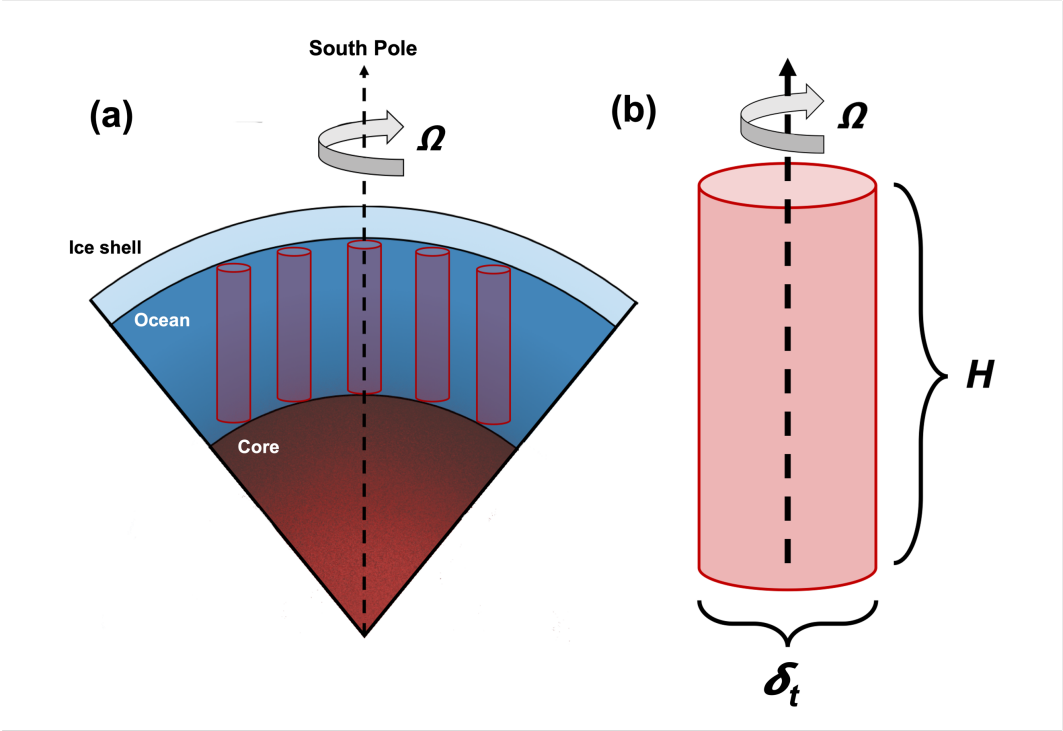

Fig. 2.1: Rotationally dominated convection columns. a) Conceptual representation of rotationally dominated "Taylor" convection columns aligned with the axis of rotation within the ocean underneath Enceladus' south polar terrain, and b) simplified geometry of one such column. *H* represents the vertical length of the fluid system (in this case, the thickness of the ocean), and δ_t represent the width of the column and depends on degree of thermal forcing. Not to scale: for a 60 km thick ocean, the Taylor columns are predicted to have widths of $\delta_t \lesssim 1.6$ km.

Table 2.1 Parameters for Enceladus' ocean used in our calculations[24,28,44,55].

Parameter	Symbol	Value	Unit
Density contrast	$\Delta\rho$	1000	kg m^{-3}

		1200 2000	
Dynamic viscosity	η	10^{-3}	Pa s
Thermal expansion coefficient	α	$1x10^{-4}$ $5x10^{-5}$ $1x10^{-5}$	K^{-1}
Gravitational acceleration	g	0.113	$m\ s^{-2}$
Specific heat capacity	c_p	4200	$J\ kg^{-1}\ K^{-1}$
Thermal diffusivity	κ	$1.3x10^{-7}$	$m^2\ s^{-1}$
Viscous diffusivity	ν	10^{-6}	$m^2\ s^{-1}$
Thermal conductivity	k	0.5	$W\ m^{-1}\ K^{-1}$
Rotation rate	Ω	$5.3x10^{-5}$	$rad\ s^{-1}$
Ocean thickness	H	20 40 60	km

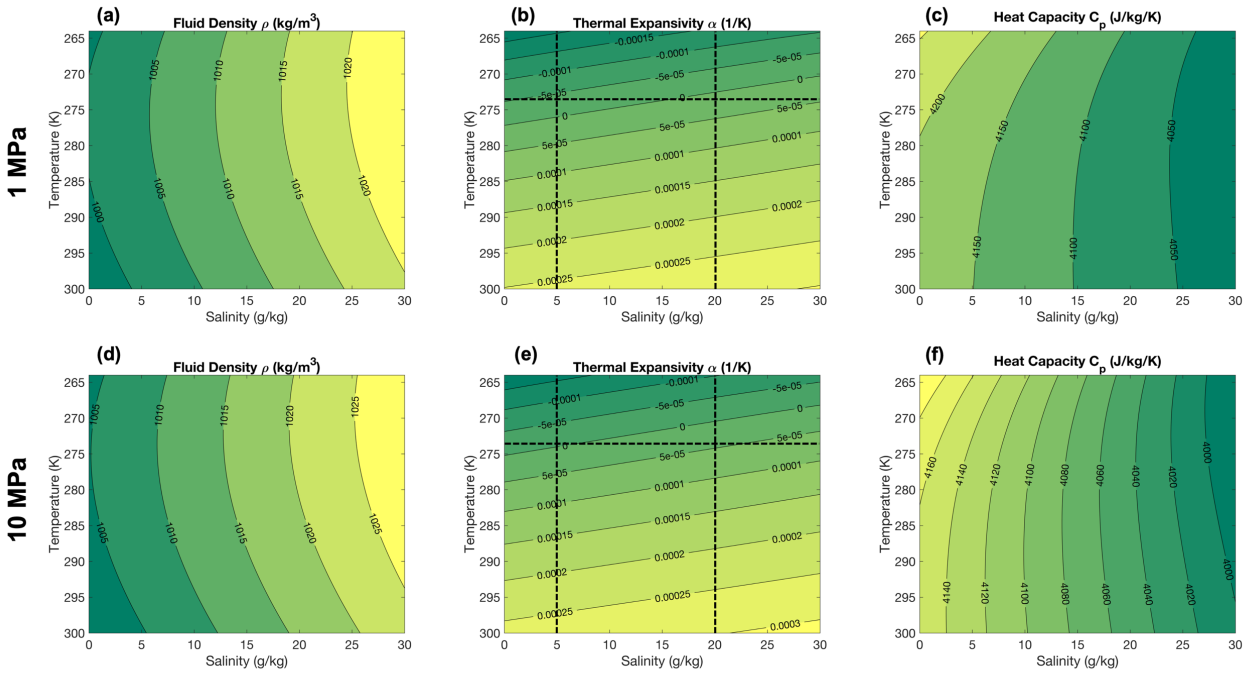

Fig. 2.2: Contours of density, thermal expansivity, and heat capacity vs. ocean salinity and temperatures. Shown at pressures of 1 MPa (a-c) and 10 MPa (d-f). Black dashed lines indicate the lower and upper limits on ocean salinity based on in-situ observations made by Cassini[6,42]. For the ocean temperature, we assume ~274 K [44].

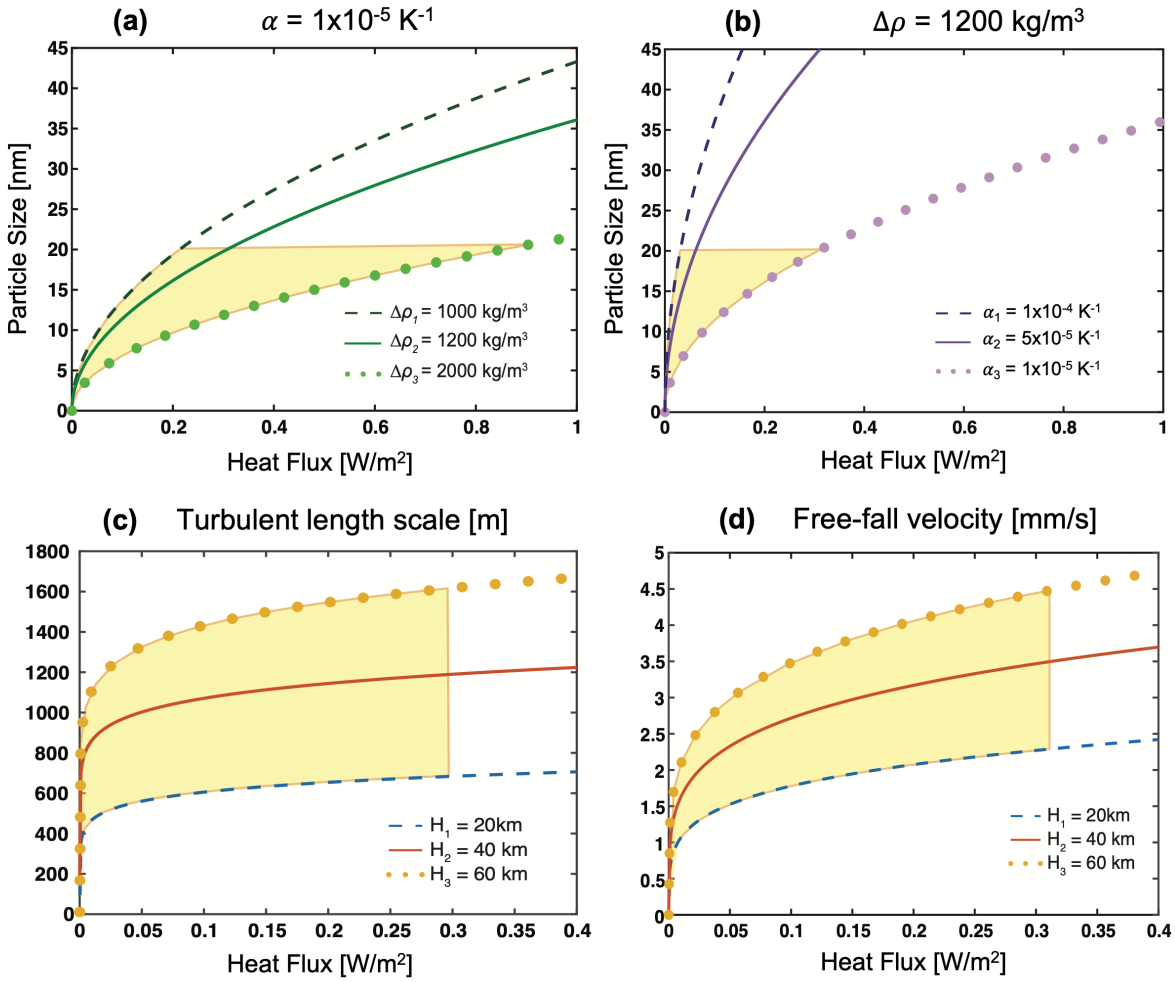

Fig. 2.3: Particle size, length scale, and velocity results. a) Entrained particle size versus heat flux for three different fluid-particle density contrasts of $\Delta\rho$ = 1000, 1200, and 2000 kg m^{-3} (corresponding to amorphous silica particle densities of 2000, 2200, and 3000 kg m^{-3}, respectively) with a constant thermal expansion coefficient of $\alpha \simeq$ 1x10^{-5} K^{-1}. b) Entrained particle size versus heat flux for thermal expansion coefficients of $\alpha \simeq$ 1x10^{-5}, 5x10^{-5}, and 1x10^{-4} K^{-1} with a constant density contrast of $\Delta\rho$ = 1200 kg m^{-3}. Yellow shaded areas represent the range of heat flux values that yield entrainment of particles comparable in size to those detected by Cassini and reported in ref.[10]. c) Plot of turbulent length scale and d) free-fall velocity versus heat flux for constant values of thermal expansivity (α = 1x10^{-5} K^{-1}) and density contrast ($\Delta\rho$ =

1200 kg m^{-3}) within the ocean. Results for three different ocean thicknesses are also shown. Yellow shaded areas represent the range of heat flux values found in (a) and (b) for these α and $\Delta\rho$ values.

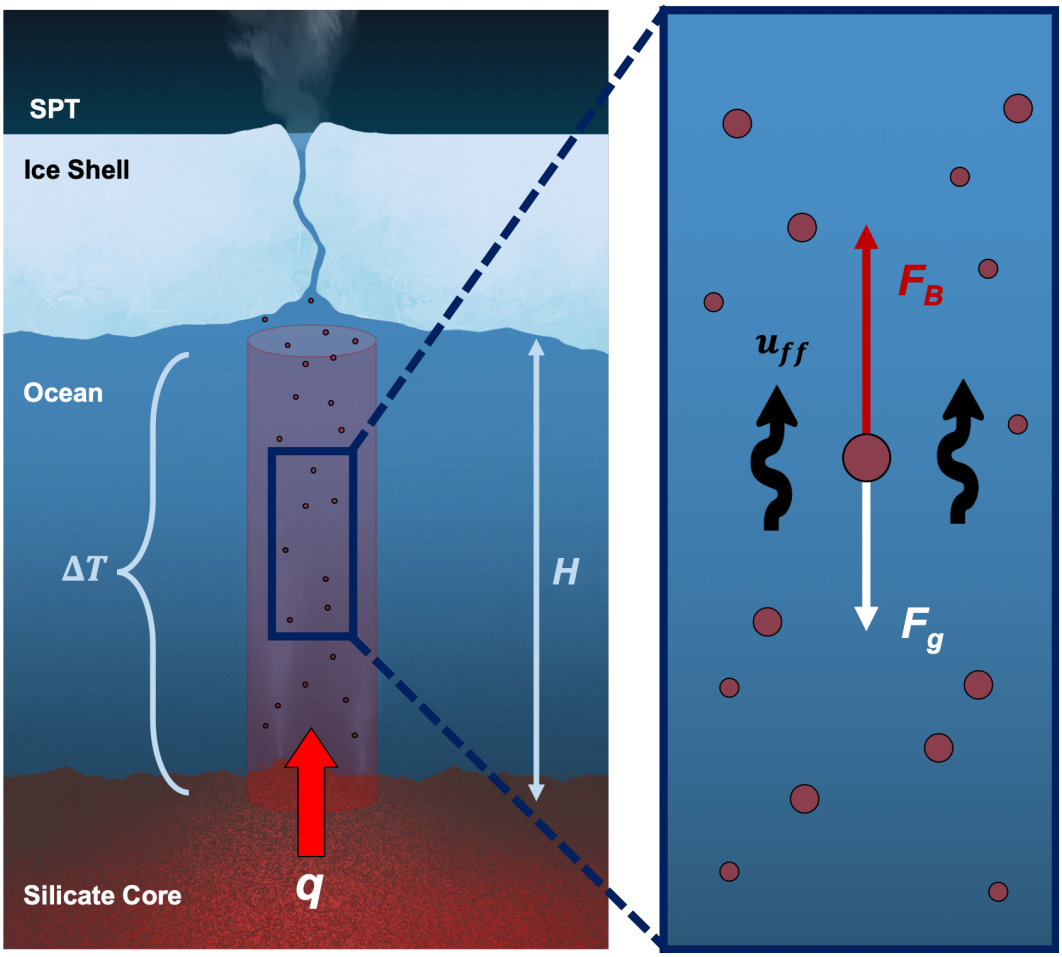

Fig. 2.4: Particle Entrainment in Enceladus' ocean. Conceptual diagram of a columnar vortex entraining particles in Enceladus' ocean (left). Conceptual diagram illustrating the force balance on an entrained silica particle that is traveling vertically upward at velocity u_{ff} (right).

2.6 References

1. Helfenstein, P. & Porco, C. C. Enceladus' geysers: Relation to geological features. *Astron. J.* 150, 96 (2015).
2. Bland, M. T., Singer, K. N., McKinnon, W. B. & Schenk, P. M. Enceladus' extreme heat flux as revealed by its relaxed craters. *Geophy. Res. Lett.* 39, (2012).
3. Crow-Willard, E. N. & Pappalardo, R. T. Structural mapping of Enceladus and implications for formation of tectonized regions. *J. Geophys. Res.* 120, 928–950 (2015).
4. Porco, C. C. *et al.* Cassini observes the active South Pole of enceladus. *Science* 311, 1393–1401 (2006).
5. Postberg, F. *et al.* Sodium salts in E-ring ice grains from an ocean below the surface of Enceladus. *Nature* 459, 1098–1101 (2009).
6. Postberg, F., Schmidt, J., Hillier, J., Kempf, S. & Srama, R. A salt-water reservoir as the source of a compositionally stratified plume on Enceladus. *Nature* 474, 620–622 (2011).
7. Iess, L. *et al.* The gravity field and interior structure of Enceladus. *Science* 344, 78–80 (2014).
8. McKinnon, W. B. Effect of Enceladus's rapid synchronous spin on interpretation of Cassini Gravity. *Geophy. Res. Lett.* 42, 2137–2143 (2015).
9. Thomas, P. C. *et al.* Enceladus's measured physical libration requires a global subsurface ocean. *Icarus* 264, 37–47 (2016).
10. Hsu, H.-W. *et al.* Ongoing hydrothermal activities within Enceladus. *Nature* 519, 207–210 (2015).
11. Sekine, Y. *et al.* High-temperature water–rock interactions and hydrothermal environments in the chondrite-like core of Enceladus. *Nature Commun.* 6, (2015).

12. Waite, J. H. *et al.* Cassini finds molecular hydrogen in the Enceladus Plume: Evidence for hydrothermal processes. *Science* 356, 155–159 (2017).

13. Le Bars, M., Cébron, D. & Le Gal, P. Flows driven by libration, precession, and Tides. *Annu. Rev. of Fluid Mech.* 47, 163–193 (2015).

14. Chen, E. M. A. & Nimmo, F. Obliquity tides do not significantly heat Enceladus. *Icarus* 214, 779–781 (2011).

15. Chen, E. M. A., Nimmo, F. & Glatzmaier, G. A. Tidal heating in icy satellite oceans. *Icarus* 229, 11–30 (2014).

16. Beuthe, M., Rivoldini, A. & Trinh, A. Enceladus's and Dione's floating ice shells supported by minimum stress isostasy. *Geophy. Res. Lett.* 43, (2016).

17. Matsuyama, I., Beuthe, M., Hay, H. C. F. C., Nimmo, F. & Kamata, S. Ocean tidal heating in icy satellites with solid shells. *Icarus* 312, 208–230 (2018).

18. Hay, H. C. F. C. & Matsuyama, I. Nonlinear tidal dissipation in the subsurface oceans of Enceladus and other icy satellites. *Icarus* 319, 68–85 (2019).

19. Rekier, J., Trinh, A., Triana, S. A. & Dehant, V. Internal energy dissipation in Enceladus's subsurface ocean from tides and libration and the role of Inertial Waves. *J. Geophys. Res.* 124, 2198–2212 (2019).

20. Wilson, A. & Kerswell, R. R. Can libration maintain Enceladus's ocean? *Earth Planet. Sci. Lett.* 500, 41–46 (2018).

21. Rovira-Navarro, M. *et al.* Do tidally-generated inertial waves heat the subsurface oceans of Europa and Enceladus? *Icarus* 321, 126–140 (2019).

22. Travis, B. J. & Schubert, G. Keeping Enceladus Warm. *Icarus* 250, 32–42 (2015).

23. Roberts, J. H. The fluffy core of Enceladus. *Icarus* 258, 54–66 (2015).

24. Choblet, G. *et al.* Powering prolonged hydrothermal activity inside Enceladus. *Nature Astron.* 1, 841–847 (2017).

25. Paluszkiewicz, T., Garwood, R. & Denbo, D. Deep convective plumes in the Ocean. *Oceanography* 7, 37–44 (1994).

26. Legg, S., McWilliams, J. & Gao, J. Localization of deep ocean convection by a mesoscale Eddy. *J. of Phys, Oceanogr.* 28, 944–970 (1998).

27. Legg, S. & McWilliams, J. C. Convective modifications of a geostrophic Eddy Field. *J. of Phys, Oceanogr.* 31, 874–891 (2001).

28. Soderlund, K. M. Ocean Dynamics of Outer Solar System Satellites. *Geophy. Res. Lett.* 46, 8700–8710 (2019).

29. Amit, H. *et al.* Cooling patterns in rotating thin spherical shells — application to Titan's Subsurface Ocean. *Icarus* 338, 113509 (2020).

30. Solomatov, V. S., Olson, P., & Stevenson, D. J. Entrainment from a bed of particles by thermal convection. *Earth Planet. Sci. Lett.* 120, 387-393 (1993).

31. Lavorel, G. & Le Bars, M. Sedimentation of particles in a vigorously convecting fluid. *Phys. Rev. E* 80*,* 046324 (2009).

32. Schwaiger, T., Gastine, T., & Aubert, J. Force balance in numerical geodynamo simulations: a systematic study. *Geophys. J. Int.* 219, S101-S114 (2019).

33. Chandrasekhar, S. The Thermal Instability of a Layer of Fluid Heated from Below: The Effect of Rotation, In *Hydrodynamic and Hydromagnetic Stability* (ed. Chandrasekhar, S.) 76-143 (Oxford University Press, 1961).

34. Hide, R. & Mason, P.J. Sloping convection in a rotating fluid. *Adv. Phys.* 24, 47-100 (1975).

35. Grossmann, S. & Lohse, D. Multiple scaling in the ultimate regime of thermal convection. *Phys. Fluids* 23, 045108 (2011).

36. Cheng, J.S., Aurnou, J. M., Julien, K., & Kunnen, R. P. J. A heuristic framework for next-generation models of geostrophic convective turbulence. *Geophys. Astrophys. Fluid Dyn.* 112, 277-300 (2018).

37. Hawkins, E.K., *et al*. Laboratory Models of Planetary Core-Style Turbulence. *Fluids* (in review).

38. Vance, S.D., *et al*. Geophysical investigations of habitability in ice-covered ocean worlds. *J. Geophys. Res.* 123, 180-205 (2018).

39. Zolotov, M.Y. An oceanic composition on early and today's Enceladus. *Geophy. Res. Lett.* 34 (2007).

40. Zolotov, M.Y. & Postberg, F. Can Nano-Phase Silica Originate from Chondritic Fluids? The Application to Enceladus' SiO2 Particles. In *Lunar and Planetary Science Conference Abstracts*, volume 1777, 2496 (2014).

41. Ingersoll, A.P. & Nakajima, M. Controlled boiling on Enceladus. 2. Model of the liquid-filled cracks. *Icarus* 272, 319-326 (2016).

42. Glein, C.R., Postberg, F. & Vance, S.D. The geochemistry of Enceladus: composition and controls. *Enceladus and the icy moons of Saturn* 39 (2018).

43. Kang, W., Mittal, T., Bire, S., Campin, J.M. & Marshall, J. How does salinity shape ocean circulation and ice geometry on Enceladus and other icy satellites? *Sci. Adv.* 8, 4665 (2022).

44. Lobo, A.H., Thompson, A.F., Vance, S.D. & Tharimena, S. A pole-to-equator ocean overturning circulation on Enceladus. *Nat. Geosci.* 14, 185-189 (2021).

45. Čadek, O., Souček, O. & Běhounková, M. Is Airy Isostasy Applicable to Icy Moons? *Geophy. Res. Lett.* 46, 14299-14306 (2019).

46. Hemingway, D.J. & Mittal, T., 2019. Enceladus's ice shell structure as a window on internal heat production. *Icarus* 332, 111-131 (2019).

47. Melosh, H.J., Ekholm, A.G., Showman, A.P. & Lorenz, R.D. The temperature of Europa's subsurface water ocean. *Icarus* 168, 498-502 (2004).

48. Zeng, Y. & Jansen, M.F. Ocean Circulation on Enceladus With a High Versus Low Salinity Ocean. *Planet. Sci. J.* 2, 151 (2021).

49. Kang, W., *et al.* Differing Enceladean ocean circulation and ice shell geometries driven by tidal heating in the ice versus the core. *arXiv preprint arXiv:2008.03764* (2020).

50. Kang, W., Marshall, J., Mittal, T. & Bire, S. Ocean dynamics and tracer transport over the south pole geysers of Enceladus. *Monthly Notices of the Royal Astronomical Society* 517, 3485-3494 (2022).

51. Postberg, F., *et al*. The E-ring in the vicinity of Enceladus: II. Probing the moon's interior—the composition of E-ring particles. *Icarus* 193, 438-454 (2008).

52. Hsu, H.W., *et al*. 2011. Stream particles as the probe of the dust-plasma-magnetosphere interaction at Saturn. *J. Geophys. Res.* 116 (2011).

53. Kempf, S., *et al*. High-velocity streams of dust originating from Saturn. *Nature* 433, 289-291 (2005).

54. Postberg, F., *et al*. Discriminating contamination from particle components in spectra of Cassini's dust detector CDA. *Planet. Space Sci.* 57, 1359-1374 (2009).

55. Goodman, J.C. & Lenferink, E. Numerical simulations of marine hydrothermal plumes for Europa and other icy worlds. *Icarus* 221, 970-983 (2012).

56. Goodman, J.C., Collins, G.C., Marshall, J. & Pierrehumbert, R.T. Hydrothermal plume dynamics on Europa: Implications for chaos formation. *J. Geophys. Res. 109* (2004).

57. Johnson, J. W. & Norton, D. Critical phenomena in hydrothermal systems; state, thermodynamic, electrostatic, and transport properties of H2O in the critical region. *Am. J. of Sci.* **291**, 541–648 (1991).

58. Greenspan, H.P. On the non-linear interaction of inertial modes. *J. Fluid Mech.* **36**, 257-264 (1969).

59. Zhong, F., Ecke, R.E. & Steinberg, V. Rotating Rayleigh–Bénard convection: asymmetric modes and vortex states. *J. Fluid Mech.* **249**, 135-159 (1993).

60. Julien, K., Knobloch, E. & Werne, J. A new class of equations for rotationally constrained flows. *Theoretical and computational fluid dynamics* **11**, 251-261 (1998).

61. Grooms, I., Julien, K., Weiss, J.B., & Knobloch, E. Model of convective Taylor columns in rotating Rayleigh-Bénard convection. *Phys. rev. lett.* **104**, 24501 (2010).

62. Tritton, D.J., Flow in Rotating Fluids, In *Physical fluid dynamics* (ed. Tritton, D.J.) 162-182 (Clarendon, 1988).

63. Aurnou, J., Andreadis, S., Zhu, L. & Olson, P. Experiments on convection in Earth's core tangent cylinder. *Earth Planet. Sci. Lett.* **212**, 119-134 (2003).

64. Panton, R.L. Turbulent Flows, In *Incompressible flow* (ed. Panton, R.L.) 772-825 (John Wiley & Sons, 2013).

65. Jones, C.A. Convection–driven geodynamo models. *Philos. Trans. Royal Soc. A* **358**, 873-897 (2000).

66. Zhang, K. & Schubert, G. Teleconvection: remotely driven thermal convection in rotating stratified spherical layers. *Science* **290**, 1944-1947 (2000).

67. Stellmach, S. & Hansen, U. Cartesian convection driven dynamos at low Ekman number. *Phys. Rev. E* **70**, 056312 (2004).

68. Hide, R., 1974. Jupiter and Saturn. *Proc. Math. Phys. Eng. Sci.* **336**, 63-84 (1974).

69. Ingersoll, A.P. & Pollard, D. Motion in the interiors and atmospheres of Jupiter and Saturn: Scale analysis, anelastic equations, barotropic stability criterion. *Icarus* **52**, 62-80 (1982).

70. Cardin, P. & Olson, P., 1994. Chaotic thermal convection in a rapidly rotating spherical shell: consequences for flow in the outer core. *Phys. Earth Planet. Inter.* **82**, 235-259 (1994).

71. Guervilly, C., Cardin, P., & Schaeffer, N. Turbulent convective length scale in planetary cores. *Nature* **570**, 368-371 (2019).

72. Calkins, M., Julien, K., Tobias, S., & Aurnou, J. A multi-scale dynamo model driven by quasigeostrophic convection. *J. Fluid Mech* **780** (2015).

73. Schwaiger, T., Gastine, T. & Aubert, J., 2021. Relating force balances and flow length scales in geodynamo simulations. *Geophys. J. Int.* **224**, 1890-1904 (2021).

74. Bire, S., Kang, W., Ramadhan, A., Campin, J. M., & Marshall, J. Exploring Ocean Circulation on Icy Moons Heated From Below. *J. Geophys. Res.* **127** (2022).

75. Aurnou, J.M., Horn, S. & Julien, K. Connections between nonrotating, slowly rotating, and rapidly rotating turbulent convection transport scalings. *Phys. Rev. Res.* **2**, 43115 (2020).

76. Julien, K., Legg, S., McWilliams, J. & Werne, J. Rapidly rotating turbulent Rayleigh-Bénard convection. *J. Fluid Mech.* **322**, 243-273 (1996).

77. Horn, S. & Shishkina, O. Rotating non-Oberbeck–Boussinesq Rayleigh–Bénard convection in water. *Phys. Fluids* **26**, 55111 (2014).

78. Plumley, M. & Julien, K. Scaling laws in Rayleigh-Benard convection. *Earth Space Sci.* **6**, 1580-1592 (2019).

79. Chillà, F. & Schumacher, J. New perspectives in turbulent Rayleigh-Bénard convection. *Eur. Phys. J. E* **35**, 1-25 (2012).

80. Qiu, X.L. & Tong, P., 2001. Large-scale velocity structures in turbulent thermal convection. *Phys. Rev. E* **64**, 36304 (2001).

81. Soderlund, K.M., Schmidt, B.E., Wicht, J. & Blankenship, D.D. Ocean-driven heating of Europa's icy shell at low latitudes. *Nat. Geosci.* **7**, 16-19 (2014).

82. Christensen, U.R. & Aubert, J. Scaling properties of convection-driven dynamos in rotating spherical shells and application to planetary magnetic fields. *Geophys. J. Int.* **166**, 97-114 (2006).

83. Gastine, T., Wicht, J. & Aubert, J. Scaling regimes in spherical shell rotating convection. *J. Fluid Mech.* **808**, 690-732 (2016).

- Chapter 3 -

3 Quantifying Tidal versus Non-tidal stresses in driving time-varying fluxes of Enceladus' Plume Eruptions

3.1 Introduction

Endogenic forces due to planetary cooling and radiogenic heating drive tectonic deformation of the terrestrial planets in the solar system (e.g., Watters and Schultz, 2010; Lenardic and Crowley, 2012; O'Neill et al., 2016). On Earth, the motion and deformation of moving plates (McKenzie and Parker, 1967; Morgan, 1968; Le Pichon, 1968) are caused by thermally induced mantle convection (Tackley, 2000; Conrad and Lithgow-Bertelloni, 2002; Bercovici, 2003; Bercovici and Ricard, 2014). In contrast, tidal forces affect only local earthquake triggering and ultimately plays no role in Earth's global tectonics (Knopoff, 1964; Tanaka et al., 2002; Cochran et al., 2004). On Venus, tectonic deformation is expressed as plateaus, rifts, volcanic constructs and coronae, the formation of which has been attributed to endogenic mantle convection, rising plumes, and foundering and viscous spreading of the lithosphere (Phillips, 1990; McKenzie et al., 1992; Solomon et al., 1992; Smrekar and Solomon, 1992; Nimmo and McKenzie, 1998; Piskorz et al., 2014; Weller and Kiefer, 2020; Gülcher et al., 2020; Westall et al., 2023). The global occurrence of wrinkle ridges requires endogenic thermal stresses in the lithosphere as the primary driver of tectonic deformation on Mercury (Solomon, 1977; Hauck et al., 2004; Byrne et al., 2014; Watters et al., 2016), the Moon (Solomon, 1977; Watters et al., 2010a; Watters, 2010b; Watters et al., 2012), and possibly Mars (Schubert et al., 1990; Nahm and Schultz, 2011). Additionally, rising plumes and even local and/or global plate tectonics may have also been generated by endogenic processes in the early history of Mars (e.g., Carr, 1973; Sleep, 1994; Nimmo and Stevenson, 2000; Zhong, 2009; Yin, 2012a; Yin, 2012b). Similar to the Earth, tidal forces do not drive global tectonics (Banerdt et al., 1992; Golombek et al., 2010; Byrne et al., 2014) although they may

contribute to local faulting on Mercury (Melosh and McKinnon, 1988), the Moon (Watters et al., 2015), and Mars (Knapmeyer et al., 2021).

In contrast to the terrestrial planets, the smaller silicate-cores of icy satellites in the solar system make radiogenic heating a less significant energy source to drive tectonic deformation (Collin et al., 2010; Nimmo and Pappalardo, 2016). Instead, tidal forcing has been invoked extensively in the current literature to be the primary driver of icy satellite deformation (Helfenstein and Parmentier, 1983; Helfenstein and Parmentier, 1985; Ojakangas and Stevenson, 1989; Hoppa et al., 1999; Greenberg et al., 1998; Hurford et al., 2007; Beuthe, 2013; Nimmo et al., 2018). Despite this overwhelming consensus, the diverse styles of ice-shell deformation across the solar system require local and global endogenic forcing. Such non-tidal stresses may originate from diapiric flow (Nimmo and Pappalardo, 2006), warm-ice convection (Schenk and Jackson, 1993; Squyres et al., 1983; McKinnon, 1999; Pappalardo et al., 1998; Barr et al., 2004; Green et al., 2021), and lateral viscous spreading of ice shell (Bland et al., 2012; Yin and Pappalardo, 2015; Kang and Flierl, 2020). Invoking non-tidal stresses in driving icy-satellite tectonics thus raise the question of how they may interact with the exogenic tidal stress. In this study, we address this question by quantifying tidal vs. non-tidal stresses in controlling the location and tempo of plume eruptions along the tiger stripes of Enceladus. To this end, we conducted detailed geological mapping using the highest-resolution (up to < 10 m/pixel) satellite images along selected segments of the plume-hosting fault zones. The mapping result allows us to establish the relationship among geometry, kinematics, and stress-states along the plume-erupting faults. As shown below, the unidirectional fault motion determined from our mapping contradicts the bidirectional motion along the plume-erupting faults as predicted by a purely tidal model. Combining the phase delay of the time-varying plume-eruption flux with the diurnal cycle, our new findings can be explained by a simple

mechanical model that assumes the time-dependent stress state along the plume-erupting faults is a superposed result of the exogenic tidal stress and endogenic tectonic stress. The tectonic stress may in turn be related to the spreading of ductile warm ice surrounding the plume-hosting faults.

3.2 Geological Background

With a diameter of ~500 km, Enceladus is a tectonically active icy satellite with consistent geyser eruptions along four parallel troughs located at its south pole (Porco et al., 2006; Spencer and Nimmo, 2013; Nimmo et al., 2018). The satellite is a differentiated body, consisting of a silicate core with a radius of ~190 km and a density of ~ 2400 kg m^{-3}, a 20-50 km global layer of liquid water, and an ice shell that is ~5 km in the southern polar region, ~10 km in the northern polar region, and ~ 30 km in the equatorial region (Hemingway et al., 2018). While a thinner ice shell at the poles is expected for a tidally locked satellite with a global ocean (Ojakangas and Stevenson, 1989; Beuthe, 2013), the cause of the single-pole activity on Enceladus remains unclear. One class of model attributes the hemispheric asymmetry to a giant impact, mode-one warm-ice convection, or a diapiric flow that triggered the true polar wander of the deformed region to the south pole (Nimmo and Pappalardo, 2006; Stegman et al., 2009; Han and Showman, 2010; Běhounková et al., 2012; Rozel et al., 2014; Tajeddine et al., 2017; Roberts and Stickle, 2021). Alternatively, fracture initiation at one pole over the other may have started a positive feedback process for localizing and focusing deformation, which resulted in single-pole tectonics without needing to invoke true polar wander (Hemingway et al., 2020). More recently, Kang and Flierl (2020) demonstrate that the ice-shell thickness instability due to lateral warm-ice flow can amplify ice-shell thinning at one of the two poles. The above mechanical models do not consider the observation that the icy satellite has experienced multiple phases of deformations at different

locations with different styles (Crow-Willard and Pappalardo et al., 2015; Patterson et al. 2018) (**Fig. 3.1**). Geological mapping shows that the surface of Enceladus consists of an ancient cratered-terrain cut by three tectonically deformed provinces, with the plume-hosting South Polar Terrain as the youngest (Spencer et al. 2009; Crow-Willard and Pappalardo et al., 2015; Patterson et al. 2018).

The oldest feature on Enceladus is the Cratered Terrain (CT), which covers a surface area of ~337,000 km^2 (~ 43% of Enceladus) and can be further divided into cratered plains and subdued cratered plains (Crow-Willard and Pappalardo et al., 2015). Tectonic features in this terrain are expressed by morphologically fresh, narrow troughs interpreted as tensile fractures (Crow-Willard and Pappalardo et al., 2015). Cratering statistics assuming either a lunar-like cratering rate or a constant cratering rate yields two surface ages at 4.2 Ga and 1.7 Ga, respectively (Porco et al., 2006). A more detailed study by Kirchoff and Schenk (2009) using the cratering model of Zahnle et al. (2003) shows that the surface age of the terrain is ~ 4.6 Ga +/- 0.9 Ga in the mid-latitude region and 4.4 Ga +/- 0.6 Ga in the equatorial region. The two age estimates for a single region are due to the assumption that (1) the comet population is the same as the shallow-sloped comet population estimated for the Jovian system with fewer small impactors and (2) the comet population has a steeper slope with more small impactors, similar to that for Triton. Interestingly, Schenk and Seddio (2006) show that the southern Cratered Terrain has a lower crater density than that in the northern Cratered Terrain, which they attributed to the effect of younger tectonic activities in the South Polar Terrain. Kirchoff and Schenk (2009) document a relative paucity of craters with diameters less than ~2 km and greater than ~6 km on Enceladus when compared to the other satellites in the Saturnian system. They explain this finding to be a result of viscous relaxation of the larger craters and the burial of the smaller craters by the deposition of the E-ring

materials. Deposition of E-ring materials on Enceladus may also explain the observation that the crater population in the equatorial region is a factor of 3 less than those in the higher latitude and polar regions (Kirchoff and Schenk, 2009).

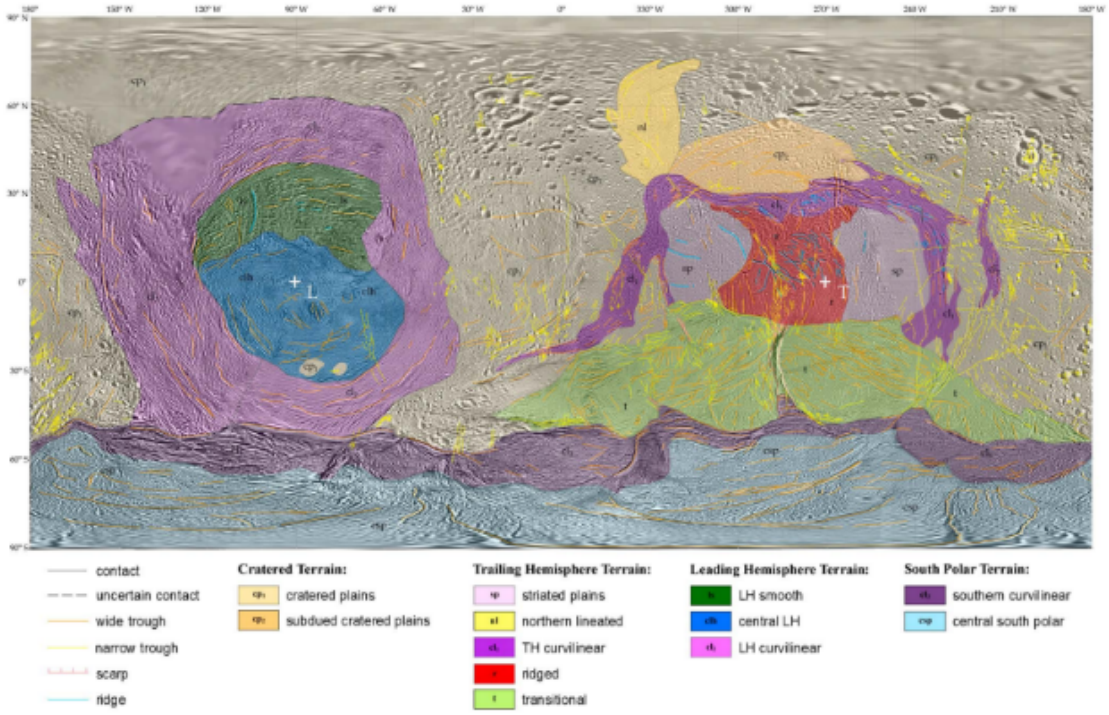

Fig. 3.1 Cylindrical global image mosaic with superimposed geologic map units and structures. Crosses mark the leading point (L) and trailing point (T). After Crow-Willard and Pappalardo (2015).

The Trailing Hemisphere Terrain is considered the second oldest geologic province, a tectonically deformed region covering an area of ~180,000 km^2 (Crow-Willard and Pappalardo, 2015). This terrain is encircled by a circumferential belt that is truncated in the south by the South Polar Terrain (Crow-Willard and Pappalardo, 2015). This region displays striated plains, northern lineated plains, trailing hemisphere curvilinear ridge-groove plains, and ridge systems with multiple trends (Crow-Willard and Pappalardo, 2015). Landform units in this terrain have surface

ages of 3.75 Ga +/- 170 Ma and 980 Ma +/- 10 Ma determined by assuming either the lunar cratering rate or a constant cratering, respectively (Porco et al., 2006). Using the model by Zahnle et al. (2003), the surface age of the landform units in the Trailing Hemisphere Terrain decreases southward: ~2.0 Ga +/- 0.2 Ga in the north towards the sub-saturnian point and ~700 Ma +/- 20 Ma in the south towards the anti-saturnian point. Although the ridge system in this terrain was attributed to cryovolcanism (Spencer et al., 2009), more detailed mapping and comparison against terrestrial analogues suggest that they may have been formed by folding and thrusting during compressional tectonics (Patthoff et al., 2022).

The Leading Hemisphere Terrain covers an area of ~195,000 km^2 and is characterized by ropy and interlaced ridges and troughs and cratered island-like plateaus (up to 35 km across) surrounded by subparallel ridges and troughs (Crow-Willard and Pappalardo, 2015; Leonard et al., 2021). Although the Leading Hemisphere Terrain has not been dated by cratering statistics and has no direct contact with the Trailing Hemisphere Terrain, it appears to be younger because the population of craters with diameters greater than 2 km are a factor of >14 less than those in the Trailing Hemisphere Terrain. Because of this, the surface age of the Leading Hemisphere Terrain is inferred to be younger than that of the Trailing Hemisphere Terrain (Crow-Willard and Pappalardo, 2015; Leonard et al., 2021). Complex deformation involving folding and extension have been proposed for its development (Crow-Willard and Pappalardo, 2015). More detailed mapping by Leonard et al. (2021) shows that the terrain is dominated by broad ductile shear zones that have accommodated strike-slip deformation, suggesting near-surface toroidal ductile-ice flow.

The smallest, quasi-square-shaped South Polar Terrain (SPT) (~80,000 km^2) is the youngest tectonic province because it truncates structures and landform features of three of the other terrains (Porco et al., 2006). The surface age of the terrain is estimated to be ~100 Ma assuming a lunar-

like cratering rate or <0.5 Ma assuming a constant cratering rate with comets as the impactor source (Porco et al., 2006). The SPT has a marginal zone that bounds an interior ridged plain (Porco et al., 2006; Yin and Pappalardo, 2015) (**Fig. 3.2**). This margin displays sharp-crested, round-topped, linear and curvilinear ridges which are interpreted to represent extensional, compressional, and strike-slip zones that have accommodated clockwise rotation of the SPT (Yin and Pappalardo, 2015; also see Rossi et al., 2020). Elongated, Y-shaped structural domains emanate from the marginal zone of the South Polar Terrain and transect neighboring terrains (Porco et al., 2006; Crow-Willard and Pappalardo, 2015; Yin and Pappalardo, 2015). The Y-shaped structures are interpreted as extensional structures (Porco et al., 2006; Gioia et al., 2007; Crow-Willard and Pappalardo, 2015) that trend perpendicular to arcuate-shaped, round-topped ridges that have been interpreted as folds along the trailing-edge side of the SPT margin zone (Yin and Pappalardo, 2015).

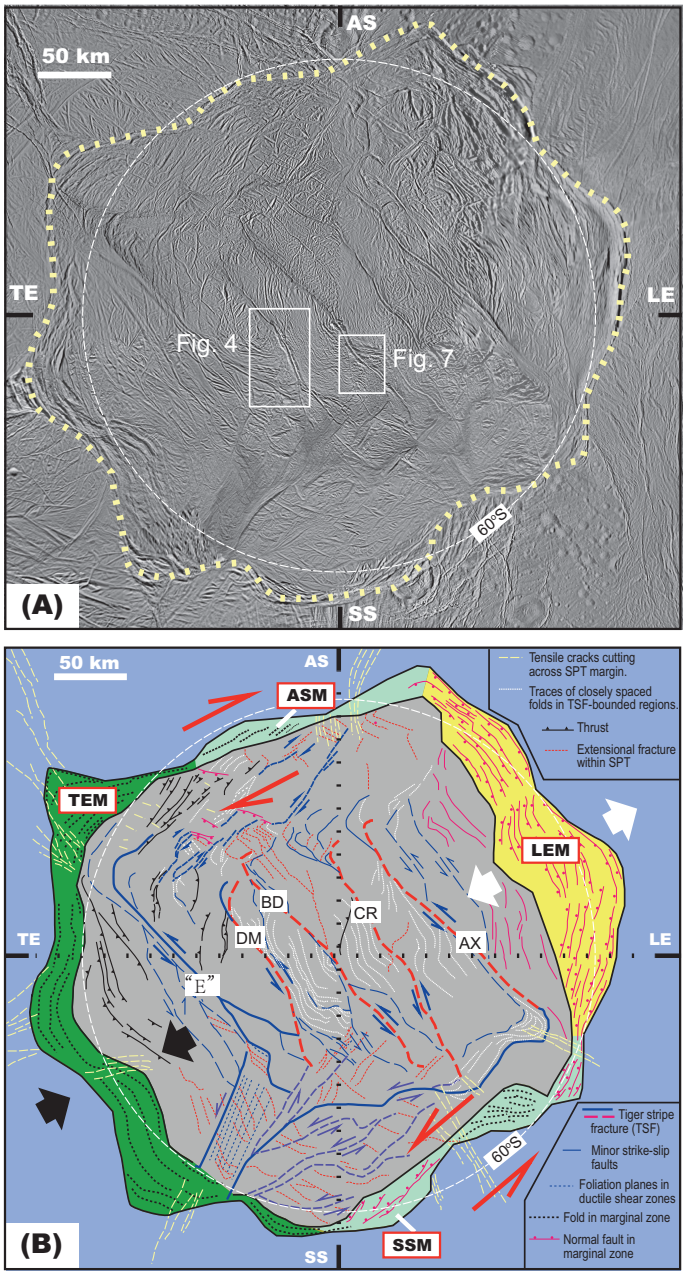

Fig. 3.2 (A) Cassini ISS image mosaic in polar projection. (B) Interpreted structural map of the South Polar Terrain (SPT) from Yin and Pappalardo (2015). The margin zone of the South Polar Terrain consists of four segments with characteristic fault kinematics: (1) anti-saturnian margin (ASM) associated with right-slip shear, (2) leading-edge margin (LEM) associated with extension, (3) sub-saturnian margin (SSM) associated with left-slip shear, and (4) trailing-edge margin (TEM) associated with compression. SS, sub-saturnian direction; LE, leading-edge direction; SS: sub-

saturnian direction; and TE, trailing-edge direction. Abbreviations for tiger-stripe fractures: AX, Alexandria; CR, Cairo; BD, Baghdad; DM, Damascus; ‘‘E” represents a tiger-stripe-like trough zone that does not host active erupting jets. The thin white dashed line represents the small circle of latitude 60°S.

Ridges on the ridged plains within the SPT have 10s to 100s m of relief, 1-2 km spacing, and a ropy surface morphology (Porco et al., 2006). The ridge formation has been related to folding under tectonic compression (Kargel and Pozio, 1996; Barr and Preuss, 2010; Bland et al., 2015; Kay and Dombard, 2023). The interior ridged plains are dissected by five parallel troughs that are ~130 km long and 35 km apart (Yin and Pappalardo, 2015). The troughs themselves are ~100 m wide and are bounded by flank ridges that are each ~2 km wide and ~0.5 km higher than the surrounding ridged plains (Porco et al., 2006; Gioia et al., 2007; Spencer et al., 2009; Spencer and Nimmo, 2013). Four of the five troughs host actively erupting geysers and are informally referred to as tiger-stripe fractures (TSF) (Porco et al., 2006; Spencer et al., 2006; Spitale and Porco, 2007; Porco et al., 2014; Ingersoll et al., 2020). The geyser-hosting tiger stripe troughs are interpreted as faults linking the surface to a subsurface global ocean (Nimmo et al., 2018; Hemingway et al., 2018). Multiple sets of smaller fractures with different trends next to the tiger stripes are interpreted as indicating nonsynchronous rotation of the South Polar Terrain (Patthoff and Kattenhorn, 2011). Deformation directly outside the South Polar Terrain is expressed by viscously relaxed craters (Bland et al. 2012), tensile fracture formation (Porco et al., 2006; Martin, 2016; Patterson et al., 2018), and the development of non-impact basins (Schenk and McKinnon, 2009).

The tiger-stripe troughs coincide with bands of high surface temperatures (114-157 K) (Porco et al., 2006; Spencer et al., 2006). A total thermal emission of ~4.2 GW along the tiger stripes and

~0.5 GW between the tiger stripes have been determined (Spencer et al. 2013). Strong infrared radiation along the tiger stripes may have been induced by shearing along tiger-stripe faults (Nimmo et al., 2007), hot water ejection (Hurford et al., 2007), turbulence-generated heating (Kite and Rubin, 2016), and the latent heat release during vapor condensation (Nakajima and Ingersoll, 2016; Ingersoll and Nakajima, 2016; Pankine, 2023). The ultimate energy source driving the above proposed mechanisms must be tidal dissipation (Meyer and Wisdom, 2007; Travis and Schubert, 2014), which may be distributed among the core, ocean, and the ice shell (Nimmo et al., 2014). Current studies suggest that the ice shell can only accommodate ~20% of the observed thermal output (Beuthe, 2019; Souček et al., 2019; Pleiner Sládková et al., 2021), leaving the ocean (Tyler, 2011) and the core as the primary sites of heat production. While the importance of ocean tides in heating Enceladus remains debated (Nimmo et al., 2018; Tyler, 2020), modeling results show that a mechanically weak core is capable of generating the observed thermal output at the South Polar Terrain (Roberts and Nimmo, 2008; Roberts, 2015; Choblet et al., 2017; Liao et al., 2020; Schoenfeld et al., 2023). However, heating concentrated in a porous core requires a viscosity of ~10^{11} Pa s and frictional sliding between loosely bounded silicate particles (Rovira-Navarro et al., 2022). A major advantage of core heating is that it explains the composition of the erupting geysers, which contain salty water-ice grains, silica nanoparticles, and molecular hydrogen requiring hydrothermal activities within the core (Postberg et al., 2011; Hsu et al., 2015; Waite et al., 2017).

One outstanding issue about Enceladus is that, while the erupting plumes follow the periodicity of the diurnal tide, the observed peak eruption occurs with a ~ 5-hour phase delay past predicted peak eruption (Hurford et al., 2007; Nimmo et al., 2007; Porco et al. 2014; Nimmo et al., 2014; Ingersoll et al., 2020). Possible explanations of the phase delay include viscoelastic relaxation of

the ice shell (Nimmo et al., 2014; Běhounková et al., 2015), physical libration (Hurford et al., 2009; Nimmo et al., 2014), and elastic interactions between tiger-stripe fractures (Kite and Rubin, 2016). A common feature of the above models is the implicit assumption that the non-tidal stress is negligible in driving the opening and closing of the tiger-stripe faults. One exception is the work of Pleiner Sládková (2021) who considered the effect of frictional locking on the tiger-stripe faults in generating a static stress field. Their work shows that the induced time-invariant stress field is insufficient to explain the phase lag of the plume eruption. As shown in Hurford et al. (2007) and Nimmo et al. (2007), the maximum differential stress induced by diurnal tides is on the order of 10^5 Pa. As shown by Yin and Pappalardo (2015), this stress magnitude is comparable to that of the topographic stress induced by gravitational spreading of ice-shell with variable thickness across Enceladus (also see Yin et al., 2016), which is up to >30 km (Hemingway et al., 2018). However, whether this magnitude of stress can explain the phase lag has not been explored.

Quantifying superposed tidal and non-tidal stresses requires the knowledge about the movement direction and movement history of the tiger-stripe fractures (i.e., fault kinematics). Early studies interpreted the tiger stripe fractures to be tensile cracks, assuming that the tiger-stripe troughs were created by extension (Kieffer et al., 2006; Gioia et al., 2007; Patthoff and Kattenhorn, 2011; Kite and Rubin, 2016; Hemingway et al., 2019) (**Fig. 3.3a**). Alternatively, the tiger-stripe fractures are interpreted as time-varying compressional, extensional, left-slip, and right-slip structures governed by diurnal tides (Nimmo et al., 2007; Hurford et al., 2007) (i.e., the tidal walking model; see **Fig. 3.3b**). More recently, the tiger-stripe fractures are interpreted as left-slip faults (Yin and Pappalardo, 2015; Helfenstein and Porco, 2015; Yin et al., 2016) (**Fig. 3.3c**). The above competing models imply different stress states on the tiger-stripe fractures: (1) the tensile-crack model predicts the minimum compressive principal stress will be oriented perpendicular to

the local strike of a tiger-stripe facture, (2) the tidal-walking model predicts the minimum compressive stress that varies in direction and magnitude, and (3) the left-slip model predicts the minimum compressive stress oriented at 45° from the local fault strike (Yin and Pappalardo, 2015) (**Fig. 3**). The three competing models can be tested because the open-crack model predicts minor tensile fractures parallel and next to a tiger-stripe faults, the tidal-walking model predicts net right-slip motion, while the left-slip fault motion is accompanied by a compressive normal-stress component (Hoppa et al., 1999). In this study, we test the above competing models by performing detailed mapping to construct the kinematics of the tiger-stripe faults during plume eruptions. This in turn allows us to develop a self-consistent model capable of decomposing tidal vs. non-tidal stresses. The result of this work has implications for the habitability of Enceladus (Greenberg et al., 2000; McKay et al., 2014; Kalousová and Sotin, 2020; Mackenzie et al., 2023) because the competing models are ultimately related to the evolution of the satellite (Howell and Pappalardo, 2020; Cable et al., 2021; Mackenzie et al., 2021).

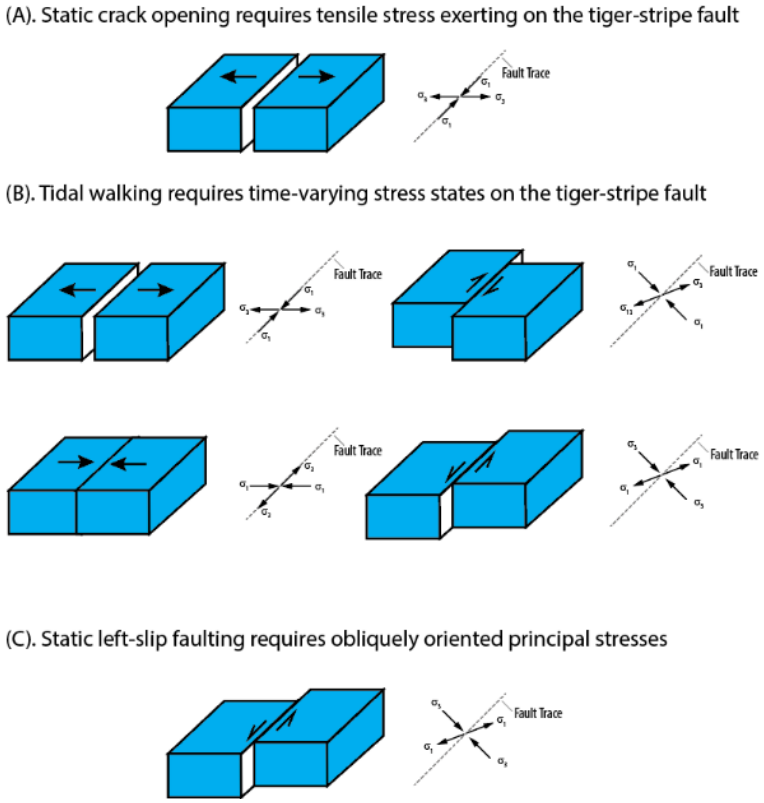

Fig. 3.3 Three competing models for the mechanics of the tiger-stripe fault evolution. (A) The tiger-stripe fractures are static open cracks, and their widths may vary with time. (B) The motion and the stress state vary with time due to diurnal tides. (C) Static left-slip faulting along the tiger-stripe fractures. Principal stresses: σ_1, maximum compressive normal stress; σ_3, minimum compressive principal stress.

3.3 Data and Methods

Data used in this study are images obtained by the Image Science Subsystem (ISS) instrument aboard the Cassini-Huygen spacecraft (Porco et al., 2006) and available publicly from United States Geological Survey (USGS) Astropedia (PDS Annex) at astrogeology.usgs.gov. The ISS consisted of a wide-angle and narrow-angle digital camera sensitive to visible light, as well as parts of the infrared and ultraviolet spectrum. The regional tectono-geomorphological map as shown in **Fig. 3.2** was constructed from an ISS mosaic of Enceladus's south pole. The controlled mosaic is assembled from NAC images that have been photometrically corrected for limb-to-terminator brightness gradients. It has a spatial resolution of ~100 m/pixel. The images used in this mosaic have a spatial resolution between 50 m/pixel and 500 m/pixel and phase angles of < 120° to create consistency across the global mosaic. The images used in our detailed mapping and structural analysis range in resolution from 3 to 30 m/pixel, which are among the highest-resolution images collected by Cassini-Huygen spacecraft (Porco et al., 2006; Helfenstein and Porco, 2015). All high-resolution mosaics used are publicly available from NASA Photojournal (photojournal.jpl.nasa.gov with photo ID numbers starting with PIA). Jet locations used in our study are taken from Porco et al. (2014) and Helfenstein and Porco (2015). Note that we only use

86 out of the 101 jets identified; we do not use jet locations in our model calculations where image resolution was too poor to establish the proper relationship among the jets, fault traces, and local geologic context.

The mapping method adopted in this study is that widely used in the study of tectonic geomorphology. On Earth, active geologic structures that have not been modified by erosion can be correlated directly with the shape of landforms (Burbank and Anderson, 2011). For example, active and recently formed folds can be expressed by warping of fluvial terraces and the development of round-topped ridges (Lavé and Avouac, 2000; Burgess et al., 2012). Similarly, normal and strike-slip faults display planar topographic scarps and sharp-crested ridges whereas thrusts show curvilinear fault traces (Wesson et al., 1975; Armijo et al., 1986; Armijo et al., 1989). This general technique has been widely applied in planetary mapping with the focus on determining the tectonic history of a planetary surface (Pappalardo and Greeley, 1995; Yin and Pappalardo, 2015).

3.4 Structural Mapping

Early structural mapping by Patthoff and Kattenhorn (2011) across the South Polar Terrain focused exclusively on groove-like landforms, which they interpret as tensile fractures. The larger geologic context of the South Polar Terrain was established by Crow-Willard and Pappalardo (2015), who recognized a marginal zone bounding the south polar lowland basin. Yin and Pappalardo (2015) performed systematic structural mapping across the marginal zone and basin floor of the southern polar depression. Their work established for the first time the kinematic framework of all major fracture zones in the area. Specifically, Yin and Pappalardo (2015) showed that the tiger-stripe faults, their hemisphere asymmetry, and their spatial relationship to folding-

generated curvilinear ridges can be explained by a unified bookshelf fault model. In this model, the tiger-stripe faults are left-slip and motion across the four parallel faults accommodate a clockwise rotation of the South Polar Terrain relative to its bounding terrain; the rotation axis is about the spinning axis of the satellite and the rotation direction is prograde. Yin and Pappalardo (2015) did not examine the spatial relationship between the jet locations identified by Porco et al. (2014) and local geologic structures along the nonlinear traces of the tiger-stripe faults, including releasing and restraining bends where local extension and compression occur along a strike-slip fault. Some of the best examples of restraining and releasing bends on Earth are the Transverse Range and Salton Sea in southern California (Crowell, 1974); the Transverse Range is a positive landform created by local compression (Crowell, 1979) whereas the Salton Sea is a negative landform associated with active volcanism and plutonic intrusion due to local extension (Robinson et al., 1976; Brothers et al., 2009).

In contrast to the larger-scale structural mapping by Yin and Pappalardo (2015), Helfenstein and Porco (2015) performed a detailed and systematic investigation using the highest-resolution images available to establish the relationship between structures along tiger-strip fault zones and known jet locations. The purpose of the work by Helfenstein and Porco (2015) is to address (1) why the jets are mostly tilted and (2) why jets with the same titling direction tend to be clustered along specific segments of the tiger-stripe. The main finding of their work is that the jet locations can be correlated with crack-like features surrounded by light-toned boulders and streaks that may represent ejecta from the erupting plumes. These authors also show that the jects are spaced about 5 km apart along the tiger-stripe fractures, which they interpret as tensile cracks created by left-slip faulting; their left-slip faulting interpretation follows that first suggested by Yin and Papppalardo (2015). Despite the detailed analysis, Helfenstein and Porco (2015) did not analyze

the exact structural setting of the jet locations they examined. Below, we address this issue by conducting structural mapping using the highest-resolution images in areas where the locations of jets identified by Porco et al. (2014) are best determined. This approach allows us to gain insights into the mechanical control on plume eruptions along the tiger-stripe fractures.

3.4.1 Damascus Sulcus

Locations of jets identified by Porco et al. (2014) were systematically plotted on an ISS image mosaic along tiger-stripe fault zones by Helfenstein and Porco (2015). These authors used the best-known jet locations on the highest-resolution image mosaics available, at a resolution of 30 m/pixel. **Fig. 3.4** shows jet locations and the tilting direction of the jets (i.e., azimuths) along the central stretch of Damascus Sulcus (i.e., Damascus tiger-stripe trough) by Helfenstein and Porco (2015). The following observations can be made from **Fig. 3.4**: (1) the tiger-stripe fault is not a straight line but a curvilinear feature with many bends and local strikes that deviate from the average regional trend, (2) the jets are located along both straight segments and kink points, and jets are regularly spaced at ~5 km. Below we map an area at the southern end of a straight segment of the Baghdad tiger-stripe fault to elucidate the structural control on jet location.

Fig. 3.5A is a perspective view of a segment along Damascus Sulcus, which is the easternmost tiger-stripe trough towards the leading-edge point (see **Fig. 3.2** for location). The image has a resolution of 12-30 m/pixel, and its relief is exaggerated by a factor of ~10. The location of jet 66 identified by Porco et al. (2014) and examined by Helfenstein and Porco (2015) is also shown with the uncertainty as a dashed white ellipse in **Fig. 3.5A**. The interpreted geological structures are shown in **Fig. 3.5B**. The tiger-tripe fault zone is expressed as a V-shaped trough (*feature 1* in **Fig. 3.5A** and unit *vw* in **Fig. 3.5B**) round-topped or sharp-crested flanking ridges (feature 2 in **Fig.**

3.5A and unit *VR* in **Fig. 3.5B**). The trend of the northern trough zone (segment *ab* in **Fig. 3.5A**) deviates ~ 40° from the trend of the southern trough zone (segment *bc* in **Fig. 3.5A**) as displayed by the perspective image. The southern trough-segment contains a chain of six quasi-circular, steep-walled pits along the deepest portion of the trough floor (*feature 3* in **Fig. 3.5A** and unit *pt* in **Fig. 3.5B**). The western trough wall of the southern trough segment is planar (feature 4 in **Fig. 5A**), whereas its wall consists of two sheet-like landforms (*features 5* and *6* in **Fig. 3.5A**). The trough-bounding ridges are draped over by a ridge-surfaced mantling landform (*feature D* in **Fig. 3.5A** and unit *dr* in **Fig. 3.5B**); the draped ridge segments exhibit rounded crests that contrast against the sharp-crested ridge segment where the draping unit is absent. The draping unit hosts trough-perpendicular ridges superposed over pre-existing topographic lows and highs (*feature 7* in **Fig. 3.5A**).

The tiger-stripe trough zone is bounded by the lower-relief, lower-elevation ridged (unit *rp*) and pitted (unit *pp*) plains (i.e., funiscular terrain of Barr and Preuss, 2010) in the west and east, respectively (**Figs. 3.5A and 3.5B**). Lower-elevation ridges and knobs in the plain terrains are truncated by the tiger-stripe trough zone (*features TR* and *TK* in **Fig. 3.5A**). The trough-bounding ridged plains are characterized by parallel, round-topped ridges (unit *rp* in **Fig. 3.5B**). Note that the ridge marked as *feature R1* in **Fig. 3.5A** is bounded in the west by a continuous groove (*feature G*) and a discontinuous groove (*feature P*) disrupted by the presence of the draping unit (*feature 7* in **Fig. 3.5A**). Note also that the ridge R1 is deflected by a left-lateral bend. Similarly, the two parallel ridges to the west (*features R2* and *R3* in **Fig. 3.5A**) also show a left-lateral bend.

Rectangular-shaped depressions bounded at least on one side by steep walls are present next to the southern trough segment (*feature sq* in **Fig. 3.5A**). Because none of the characteristic landforms are present in the rectangular depressions (**Fig. 3.5A**), the ridged and pitted plains next to the tiger-stripe trough must predate the formation of the depressions. Subtle linear scarps trending obliquely to the trough zone occur next to the rectangular-shaped depressions (*feature scp* in **Fig. 5A**). The linear scarps crosscut the round-topped ridges in the ridged plains terrain, which is consistent with a younger formation age for the depressions.

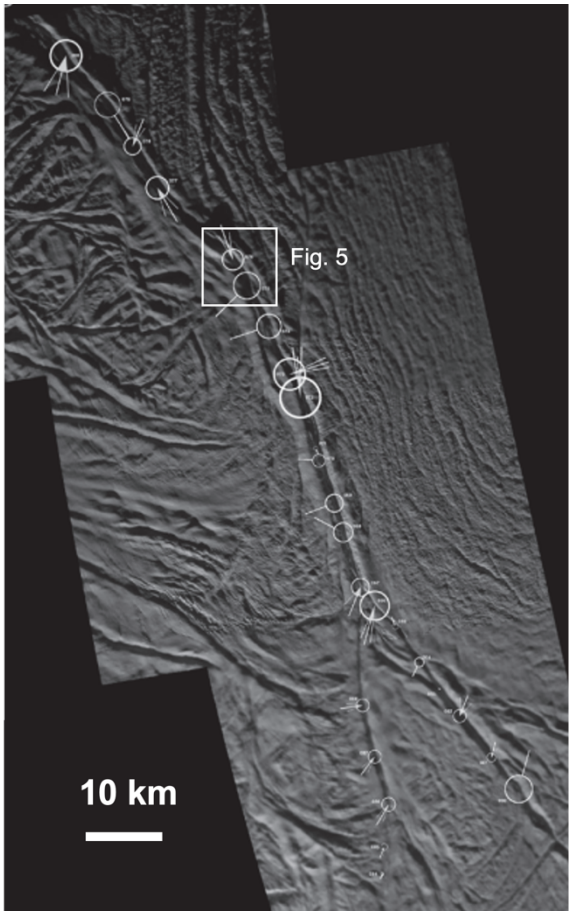

Fig. 3.4 Locations and jet azimuths (direction of tilt) of geysers along Damascus Sulcus superposed on ISS NAC mosaic map (polar stereographic projection at 30 m/pixel) from Helfenstein and Porco (2015). Circles centered at geyser locations are scaled to 2-sigma position uncertainty, whereas white radial line extending outward from the circle indicate jet azimuth.

Interpretation. The cross-cutting relationship indicates the emplacement of the ridged and pitted plains to be the oldest event, which was followed then by the coeval formation of the tiger-stripe trough with (a) the emplacement of the draping unit over the trough-bounding ranges, (b) the formation of the pit chains along the trough floor, (c) the development of the rectangular depressions and linear scarps trending obliquely to the trough zone, and (d) left-lateral bending of the parallel round-topped ridges. Following earlier interpretation that the ridged plains were generated by ductile folding (Barr and Preuss, 2010), the late formation of the tiger-stripe trough, interpreted as a brittle left-slip fault zone by Yin and Pappalardo (2015) and Helfenstein and Porco (2015), implies that the ice-shell deformation changes in style from ductile to brittle, requiring a gradual cooling of the ice shell. The circular pits (*feature 3* in **Fig. 3.5A**) along the valley floor are discrete and spaced regularly at ~2 km. The pits are interpreted as the conduits of the erupting jets. To maintain the pits under a strike-slip fault setting, the melting rate of the upwelling water must be higher than the freezing rate of the pit wall. Turbulence-generated heating, as suggested by Kite and Rubin (2009), may provide the needed heating. However, this mechanism requires the tensile stress to be applied constantly on the wall of the tiger-stripe trough, which would predict a zone of eruption rather than discrete pits. Alternatively, the pit opening may be maintained by obliquely oriented minimum compressive stress (i.e., maximum tensile normal stress) along the left-slip shear zone, such that the pits represent *en echelon* tensile cracks as proposed by Helfenstein and Porco (2015). The draping landform next to the valley-floor pits are characterized by parallel ridges and grooves trending at high angles to the crest of the valley-bounding flanking ridges; the draping materials are interpreted as ejecta deposits from jet eruptions. The planar surface bounding the western side of the V-shaped valley in **Fig. 3.5A** represents the fault plane

exhumed by the trough-forming faulting process. The convex ridges in map view west of the tiger-stripe trough are interpreted as drag folds due to left-slip motion along the tiger-stripe fault zone. The tiger-stripe valley was created by explosive eruption that removed the wall rocks of the valley.

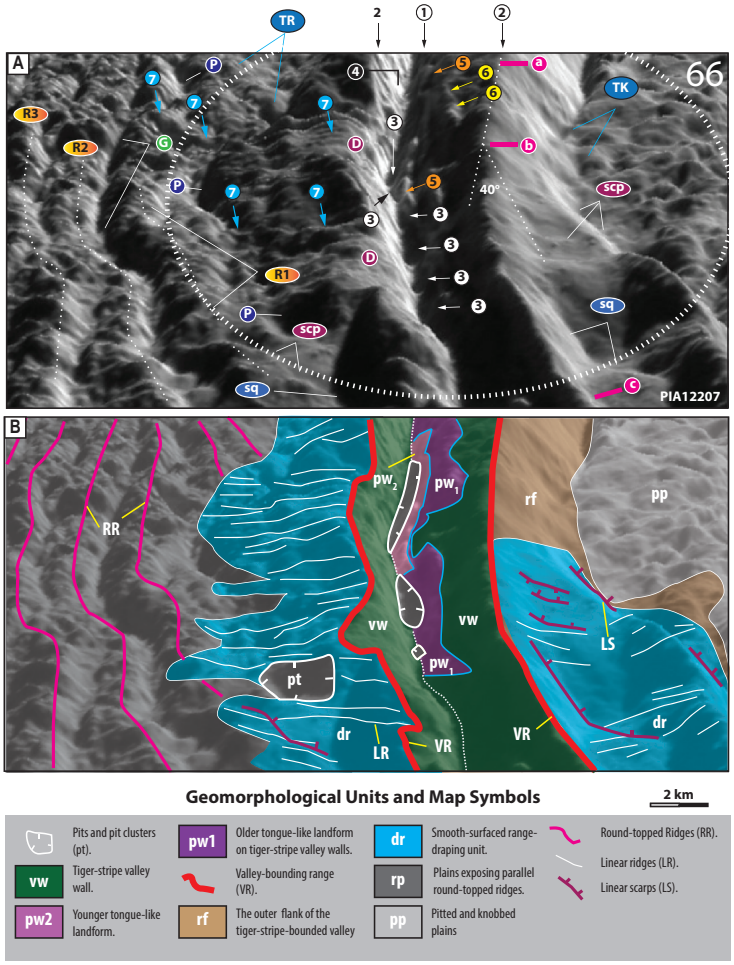

Fig. 3.5 (A) Perspective image of a segment of Damascus Sulcus. The image ID is PIA12207. See Fig. 2 for location; numbers and letters are features discussed in the text. (B) Same perspective image overlain by the interpreted geological structures. Map symbols and the scale of the image are shown below the image. The white ellipse represents the location of jet 66 with the uncertainty that was identified by Porco et al. (2014).

The mechanical condition for the development of tensile cracks in a strike-slip shear zone can be expressed as the fault zone reaching tensile and shear failure simultaneously. This condition is shown in **Fig. 3.6,** in which the Mohr circle represents the stress state and two tangent lines represent the Coulomb fracture criterion: $\tau_n = S_0 + \mu\sigma_n$; τ_n is the critical shear stress above which shear failure occurs along the tiger-stripe fault, μ is the coefficient of internal friction, S_0 is the cohesive stress, and σ_n is the normal stress on the tiger-stripe fault (Jaeger et al., 2009). The formation of tensile cracks in the shear zone during left-slip faulting can be written as $\sigma_3 = T_0$, where σ_3 is the minimum compressive principal stress, and T_0 is the tensile strength of the tiger-strike fault-zone material (Jaeger et al., 2009).

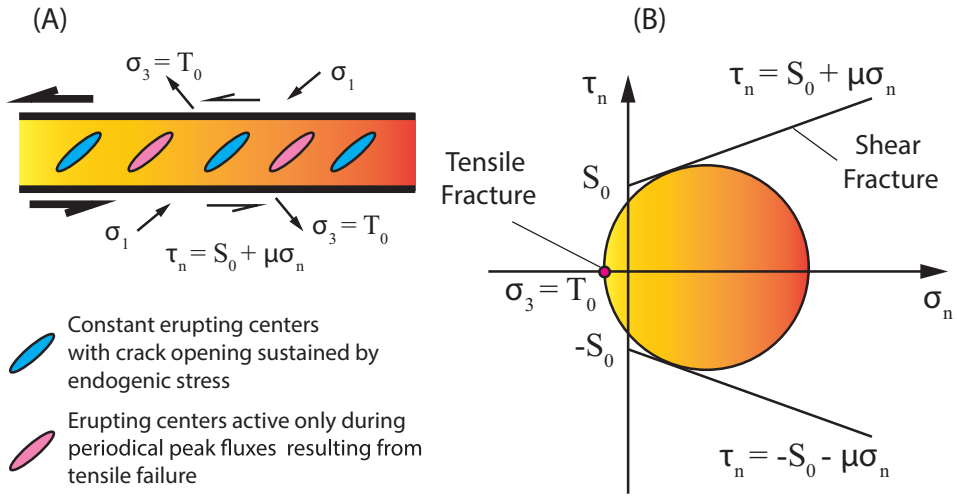

Fig. 3.6. Interpreted stress state for coeval development of a left-slip fault and the formation of tensile cracks within the shear zone. (A) Relationship between tensile cracks and the left-slip fault zone. Note that the tensile cracks may not be open all the time because they may have different tensile strengths. Because of this, the cracks may be opened and enlarged as stress magnitude

increases such as during seismic slip, injection of pore-fluids, and tidally driven stressing. (B) A Mohr circle representation of the stress state within a fault zone that is capable of both shear and tensile failures.

3.4.2 Baghdad Sulcus

Fig. 3.7 shows jet locations and the tilt direction of the jets along the central stretch of Baghdad Sulcus (i.e., Baghdad tiger-stripe trough) by Helfenstein and Porco (2015). Similar to features along the Damascus trough, the Baghdad tiger-stripe fault is a curvilinear feature with local kinks and bends with discrete jets located along both straight and kinking segments of the fault zone.

Fig. 3.8A shows a segment of the Baghdad tiger-tripe fault zone. The resolution of this image is 12 m/pixel. The location of jet 43 identified by Porco et al. (2014) and examined by Helfenstein and Porco (2015) is also shown with the uncertainty as a dashed white ellipse in **Fig. 3.8A**. The tiger-stripe fault zone is a single strand (*feature 1*) in the upper part of the image, which splits into two branches towards the lower part of the image (*features 2* and *3*) shown in **Fig. 3.8A**. A lenticular-shaped opening lies at the center of brighter-toned materials that drape over a darker background (*feature 4* in **Fig. 3.8A**). V-shaped valleys trending at high angles against the tiger-stripe fault zone (*feature 5* in **Fig. 3.8A**) either bound curvilinear ridges (*feature 6* in **Fig. 3.8A**) or are themselves curvilinear in trace (*feature 7* in **Fig. 3.8A**). A prominent linear ridge locally bounding linear grooves trends at lower angles towards the tiger-stripe fault zone (*feature 8* in **Fig. 3.8A**). Oblique ridges curve into and eventually merge with this linear ridge (*features 9* and *10* in **Fig. 3.8A**). The linear ridge (i.e., *feature 8* in **Fig. 3.8A**) together with another planar scarp (*feature 11* in **Fig. 3.8A**) bounds a V-shaped depression at its southern termination. A larger and more

obliquely trending curvilinear ridge bends into and merges with the eastern branch of the southern tiger-stripe fault zone (*feature 12* in **Fig. 3.8A**).

Interpretation. Interpreted structural and geomorphological features are shown in **Fig. 3.8B**. The fundamental assumption of the interpreted map is that the V-shaped valleys characterized by planar walls and grooves bounded by sharp-crested, linear ridges indeed represent faults. This assumption is consistent with the deflection geometry of round-topped ridges, interpreted to be pre-faulting drag folds, as they approach the V-shaped valleys and linear grooves/ridges. The proposed kinematic relationship between faults and drag folds yields a self-consistent structural pattern that can be explained by overall left-slip shear deformation across the mapped area (**Fig. 3.8C**). Specifically, our interpreted structural system consists of *P*-, *R*-, and *R*'-shears, which are the characteristic structural elements in a strike-slip fault system on Earth (Sylvester, 1988). The fault system also displays a releasing bend (see Sylvester, 1988 for definition) that links the northern fault-zone segment with the eastern branch of the southern fault-zone segment. The pit located at the center of the bright mantling materials lies along this interpreted releasing band. As such, we suggest that this pit as an eruption center for plume material and that the bright mantling materials as fallback material from plume. This interpretation implies obliquely trending maximum and minimum compressive stresses relative to the tiger-stripe fault zone (**Fig. 8C**), consistent with a transtensional left-slip fault system (Sylvester, 1988). In **Fig. 9**, we compare a terrestrial fault system along the marginal zone of the Ross Sea ice shelf in Antarctica against the feature we mapped along the Baghdad fault zone. The Ross Sea ice shelf is actively deforming and moving, which is dominated by clockwise rotation (Kwok, 2005; Holland and Kwok, 2012). The ice-shelf deformation is wind-driven, and the ice-shelf rotation creates the left-slip shear along its eastern margin against the Transantarctic Mountains (Holland and Kwok, 2012). We note that both

shear zones display *en echelon* folds next to the fault zones, and the fault zones themselves are bounded by double ridges. Additionally, both fault systems have locally developed releasing bends. The above similarities further support the left-slip fault interpretation for the Baghdad shear zone.

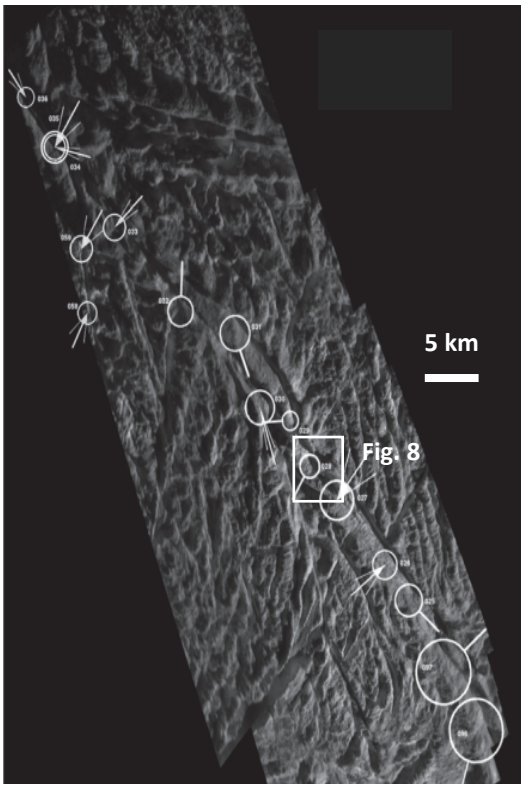

Fig. 3.7 Locations and jet azimuths (direction of tilt) of Baghdad Sulcus geysers superposed on ISS NAC mosaic map (polar stereographic projection at 30 m/pixel) from Helfenstein and Porco (2015). Circles centered at geyser locations are scaled to 2-sigma position uncertainty, whereas white radial line extending outward from the circle mark the azimuths of the geysers.

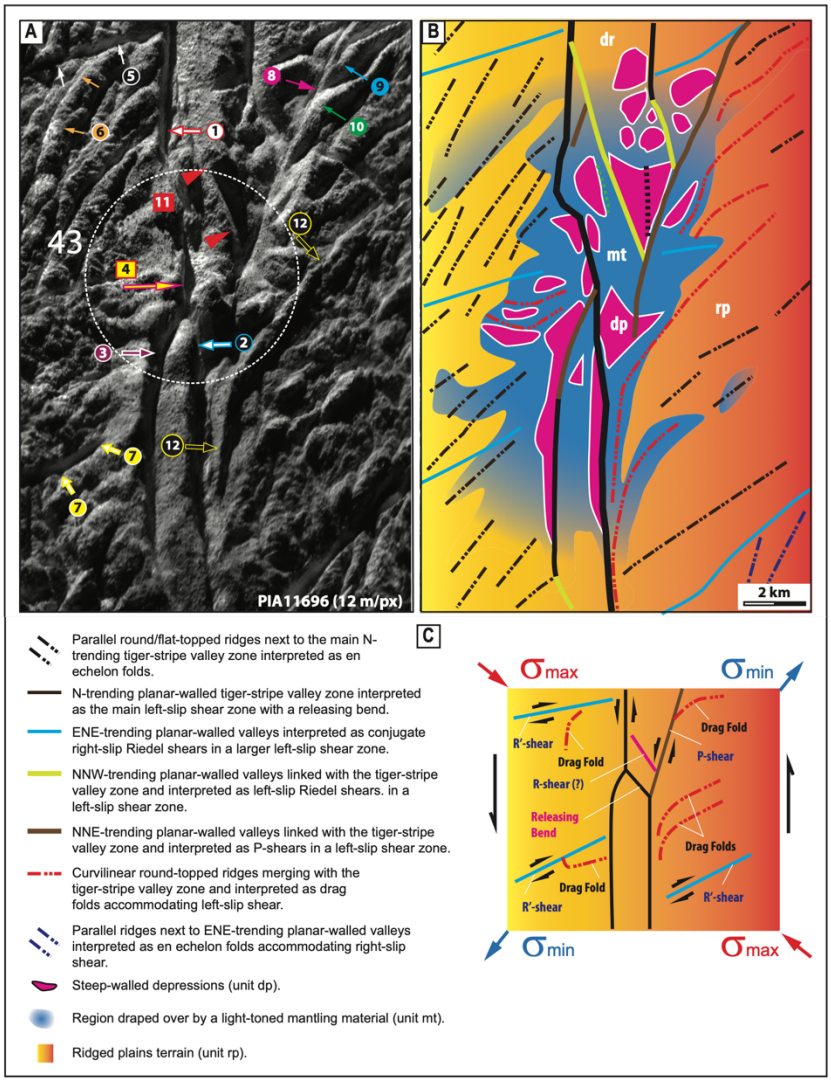

Fig. 3.8 (A) High resolution ISS image of a segment along Baghdad Sulcus. The image ID is PIA11696. See Fig. 2 for location; numbers are features discussed in the text. (B) Same perspective image but overlain with detailed structural mapping and associated symbology and unit description. (C) Interpreted structural system based on mapping from (B), which consists of characteristic strike-slip fault elements as found on Earth (P-, R-, and R'-shears).

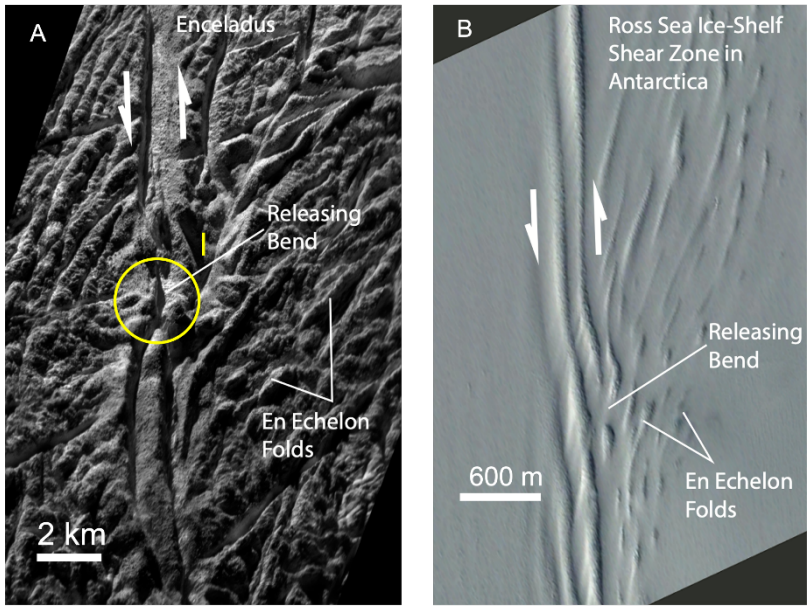

Fig. 3.9 Side-by-side comparison of (A) the Baghdad tiger-stripe fault zone from Fig. 6 and (B) the marginal shear zone of the Ross Sea ice shelf in Antarctica. Image is (B) is from Google Earth ™ at 77°33'32.16"S 169°18'46.55"E. Both structural systems show *en echelon* folds, double ridges bounding the main shear zone, and releasing bends.

The stress state that governs coeval left-slip faulting and the development of tensile cracks along releasing bends of the overall strike-slip fault zone is shown in **Fig. 3.10**. Although the detailed spatial pattern of the fault and the extensional cracks differ from the situation shown in **Fig. 3.6**, the stress state and its relationship to shear and tensile failures are the same: $\tau_n = S_0 + \mu\sigma_n$ and $\sigma_3 = T_0$.

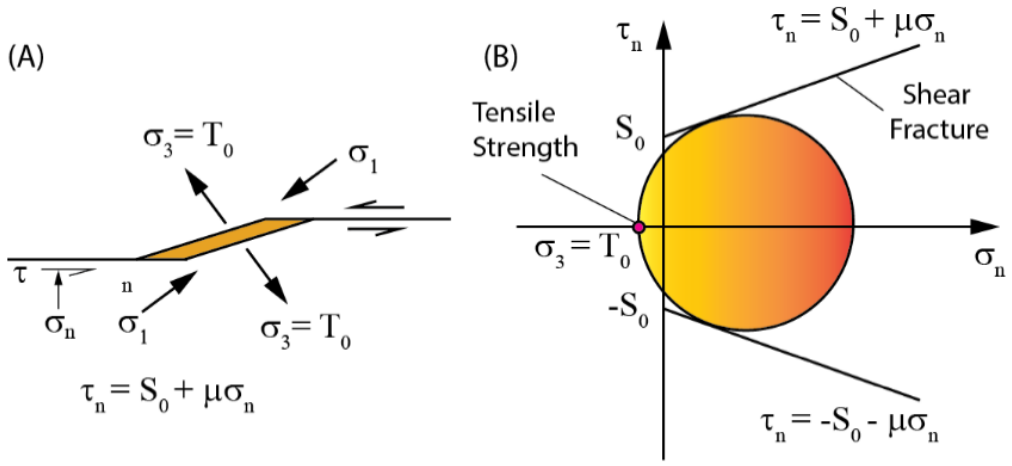

Fig. 3.10 Interpreted stress state for the coeval motion on a left-slip fault and the formation of a tensile crack along its releasing bend. (A) Relationship between a tensile crack in a releasing bend (marked by yellow) and the motion on a left-slip fault. (B) A Mohr circle representation of the stress state within a strike-slip fault zone that is capable of creasing both shear and tensile failures.

3.5 Superposition of Tectonic and Tidal Stresses

3.5.1 Defining the stress state along segments of the tiger-stripe faults

Our mapping shows the feasibility of a tectonic model for the location and continuous eruption of geysers. More detailed and systematic work is required to evaluate all sites where the jets have been observed, as well as associated structural setting. With the above limitations in mind, we ask the question: what is the magnitude for non-tidal tectonic stress in the ice shell, the stress that not only drives left-slip motion along the tiger-stripe fractures but also causes the phase delay of the peak plume eruption? To answer this question, we postulate that the total stress along any segment of the tiger-stripe fault zones is the sum of the tectonic and tidal stresses and can be written as

$$\begin{pmatrix} \sigma_{xx}^{\mathrm{sum}} & \sigma_{xy}^{\mathrm{sum}} & \sigma_{xz}^{\mathrm{sum}} \\ \sigma_{yx}^{\mathrm{sum}} & \sigma_{yy}^{\mathrm{sum}} & \sigma_{yz}^{\mathrm{sum}} \\ \sigma_{zx}^{\mathrm{sum}} & \sigma_{zy}^{\mathrm{sum}} & \sigma_{zz}^{\mathrm{sum}} \end{pmatrix} = \begin{pmatrix} \sigma_{xx}^{\mathrm{TD}} & \sigma_{xy}^{\mathrm{TD}} & \sigma_{xz}^{\mathrm{TD}} \\ \sigma_{yx}^{\mathrm{TD}} & \sigma_{yy}^{\mathrm{TD}} & \sigma_{yz}^{\mathrm{TD}} \\ \sigma_{zx}^{\mathrm{TD}} & \sigma_{zy}^{\mathrm{TD}} & \sigma_{zz}^{\mathrm{TD}} \end{pmatrix} + \begin{pmatrix} \sigma_{xx}^{\mathrm{TT}} & \sigma_{xy}^{\mathrm{TT}} & \sigma_{xz}^{\mathrm{TT}} \\ \sigma_{yx}^{\mathrm{TT}} & \sigma_{yy}^{\mathrm{TT}} & \sigma_{yz}^{\mathrm{TT}} \\ \sigma_{zx}^{\mathrm{TT}} & \sigma_{zy}^{\mathrm{TT}} & \sigma_{zz}^{\mathrm{TT}} \end{pmatrix} \quad (1)$$

In the above equation, the superscripts "sum", "TD", and "TT" denote the total, tidal, and tectonic stresses respectively. Following Hurford et al. (2009) and using the thin-shell approximation, the time-varying tidal stress components at any latitude δ and longitude λ are given by:

$$\sigma_{\theta\theta} = -\frac{3Mh_2\mu}{8\pi\rho_{av}a^3}\left(\frac{1+\nu}{5+\nu}\right)(5+3cos2\theta) \quad (2a)$$

$$\sigma_{\phi\phi} = \frac{3Mh_2\mu}{8\pi\rho_{av}a^3}\left(\frac{1+\nu}{5+\nu}\right)(1-9cos2\theta) \quad (2b)$$

where θ is the angular distance of a point on the satellite surface from the axis of symmetry with respect to the tidal deformation (Melosh, 1977; Leith and McKinnon, 1996; Greenberg et al., 1998). In the above equations, μ and ν are rigidity and Poisson's ratio of the ice shell, *M* is the mass of Saturn, h_2 is the tidal love number, ρ_{av} is the average density of Enceladus, and a is the semi-major axis (see Table 1 for all model input values). The stress component in the radial direction to the axis of symmetry is given by $\sigma_{\theta\theta}$, while $\sigma_{\phi\phi}$ is the stress component orthogonal to $\sigma_{\theta\theta}$. The sign convention used here is that a positive sign is for compressional stresses and a negative sign is for tensile stresses. Transforming the above solution to the local coordinate system of *x* and *y* yields the three stress components in the spherical ice shell as:

$$\sigma_{xx} = \frac{1}{2}\left(\sigma_{\phi\phi}+\sigma_{\theta\theta}\right) - \frac{1}{2}\left(\sigma_{\phi\phi}-\sigma_{\theta\theta}\right)cos2\beta \quad (3a)$$

$$\sigma_{yy} = \frac{1}{2}\left(\sigma_{\phi\phi}+\sigma_{\theta\theta}\right) + \frac{1}{2}\left(\sigma_{\phi\phi}-\sigma_{\theta\theta}\right)cos2\beta \quad (3b)$$

$$\sigma_{xy} = \sigma_{yx} = -\frac{1}{2}\left(\sigma_{\phi\phi}-\sigma_{\theta\theta}\right)sin2\beta \quad (3c)$$

where β is the angle between the principal-stress axis in the tidal-deformation coordinate and the local reference framework that can be obtained by:

$$\beta = cos^{-1}\left[-\frac{sin\delta sin\theta}{cos\delta sin\theta}\right] \quad (4)$$

The principal components of the instantaneous tidal stresses, $\sigma(t)$, caused by the change in tidal figure due to optical and physical librations at any point in the orbit, valid for small eccentricity *e*, are given by:

$$\sigma(t)_{\theta\theta} = \frac{3M\mu h_2}{8\pi\rho_{av}a^3}\left(\frac{1+\nu}{5+\nu}\right)(5 + 3cos2\theta(t))(1 + 3ecosnt) \quad (5a)$$

$$\sigma(t)_{\phi\phi} = -\frac{3M\mu h_2}{8\pi\rho_{av}a^3}\left(\frac{1+\nu}{5+\nu}\right)(1 - 9cos2\theta(t))(1 + 3ecosnt) \quad (5b)$$

In the above equations, the angular position in the orbit is defined by *nt*, where *n* is the mean motion and *t* is time in seconds after pericenter passage. The instantaneous angular distance $\theta(t)$ between any point on the surface and the instantaneous location of the tidal bulge is time-dependent and given by:

$$\theta(t) = cos^{-1}[sin\delta\,\sin(\varepsilon\,\sin(nt-\omega)) + cos\delta\,\cos(\varepsilon\,\sin(nt-\omega))\cos\big(\lambda + 2esin(nt) - Fsin(nt+\psi)\big)\} \quad (6)$$

where ε is the obliquity, ω is the angle between the direction of the ascending node and the direction of pericenter, and *F* is the amplitude of the physical libration with phase ψ. The components of the stress tensor $\sigma(t)$ referenced to the local coordinate system are given by

$$\sigma_{xx} = \frac{1}{2}\left(\sigma_{\phi\phi}(t) + \sigma_{\theta\theta}(t)\right) - \frac{1}{2}\left(\sigma_{\phi\phi}(t) - \sigma_{\theta\theta}(t)\right)cos2\beta(t) \quad (7a)$$

$$\sigma_{yy} = \frac{1}{2}\left(\sigma_{\phi\phi}(t) + \sigma_{\theta\theta}(t)\right) + \frac{1}{2}\left(\sigma_{\phi\phi}(t) - \sigma_{\theta\theta}(t)\right)cos2\beta(t) \quad (7b)$$

$$\sigma_{xy} = \sigma_{yx} = -\frac{1}{2}\left(\sigma_{\phi\phi}(t) - \sigma_{\theta\theta}(t)\right) sin2\beta(t) \tag{7c}$$

where $\beta(t)$ is defined as

$$\beta(t) = cos^{-1}\left[\frac{\sin(\varepsilon \sin(nt-\omega)) - sin\delta cos\theta(t)}{cos\delta sin\theta(t)}\right] \tag{8}$$

Now that σ and $\sigma(t)$ are in similar reference frames, the diurnal tidal stress tensor σ^{TD} can be written by their principal stress components as

$$\sigma^{D} = \begin{vmatrix} \sigma_1^{TD} & 0 \\ 0 & \sigma_2^{TD} \end{vmatrix} \tag{9}$$

where

$$\sigma_1^{TD} = \sigma_{xx}^{TD} cos^2\gamma_D + \sigma_{xx}^{TD} sin^2\gamma_D + \sigma_{xy}^{TD} sin^2\gamma_D \tag{10a}$$

$$\sigma_2^{TD} = \sigma_{xx}^{TD} sin^2\gamma_D + \sigma_{xx}^{TD} cos^2\gamma_D - \sigma_{xy}^{TD} sin^2\gamma_D \tag{10b}$$

In the above equation, γ_D describes the orientation of the principal axis in the local *x*-*y* coordinate system and is measured from the σ_{xx}^{TD} direction to the σ_1^{TD} direction. We can obtain γ_D from the general tidal stress components as

$$\gamma_D = \frac{1}{2} tan^{-1}\left[\frac{2\sigma_{xy}^{TD}}{\sigma_{xx}^{TD} - \sigma_{yy}^{TD}}\right] \tag{11}$$

Following the interpretation that the segment of a tiger-stripe fault hosting an erupting jet experiences simultaneous shear and tensile failure, we have the following relationship:

$$\begin{pmatrix} \sigma_{x'x'}^{\text{sum}} & \sigma_{x'y'}^{\text{sum}} = \tau_f & 0 \\ \sigma_{y'x'}^{\text{sum}} = \tau_f & \sigma_{y'y'}^{\text{sum}} & 0 \\ 0 & 0 & 0 \end{pmatrix} = \begin{pmatrix} \sigma_{x'x'}^{\text{TD}} & \sigma_{x'y'}^{\text{TD}} & 0 \\ \sigma_{y'x'}^{\text{TD}} & \sigma_{y'y'}^{\text{TD}} & 0 \\ 0 & 0 & 0 \end{pmatrix} + \begin{pmatrix} \sigma_{x'x'}^{\text{TT}} = -\frac{1}{2}\rho g h & \sigma_{x'y'}^{\text{TT}} & 0 \\ \sigma_{y'x'}^{\text{TT}} & \sigma_{y'y'}^{\text{TT}} & 0 \\ 0 & 0 & 0 \end{pmatrix}$$

(12)

In the above equation, τ_f is the frictional strength of a segment of a tiger-stripe fault collocated with an erupting jet, ρ is the density of the ice shell, g is the surface gravity of Enceladus, and h is the average ice shell thickness. Because the trace of a single tiger-stripe fault is not a perfect straight line, defining normal and shear stresses on the fault surface at any point requires the use of a local coordinate system referenced to the local fault strike. Here, we use x'-y' coordinates referenced to the local fault orientation when defining local stress components on a fault. For the regional coordinate system, we use the axes pointing towards the sub-saturnian and trailing-edge points as the ***x*** and ***y*** directions. The relationship between the regional and local coordinate systems is shown in **Fig. 3.11**. In this study, we assume that all segments of the tiger-stripe faults experience simultaneous tensile and shear failure. As discussed above, the tensile failure does not follow the left-slip fault surface/fault zone, but along an oblique direction (also see **Fig. 3.11**). The tensile failure can be written as

$$\sigma_{3'}^{\text{sum}}(x', y', t_p) = \frac{\sigma_{x'x'}^{\text{sum}} + \sigma_{y'y'}^{\text{sum}}}{2} - \sqrt{\left(\frac{\sigma_{x'x'}^{\text{sum}} - \sigma_{y'y'}^{\text{sum}}}{2}\right)^2 + \sigma_{x'y'}^{\text{sum}}} = T_0 \qquad (13)$$

where $\sigma_{3'}^{\text{sum}}(x', y', t_p)$ is the minimum compressive stress at a location (x', y') on a segment of a tiger-stripe fault when the peak plume flux occurs at time t_p, i.e. ~ 5 hours past apoapsis (Nimmo et al., 2014). In the above equation, T_0 is the tensile strength of a tiger-stripe fault assuming it is constant for all fault segments, and $\sigma_{x'y'}^{\text{sum}} = \tau_f$ is the critical shear stress for shear failure to occur, which we also assume to be constant along all tiger-stripe faults. The choice T_0 at the time of the peak flux implies that cracks in the shear zone may have different tensile strengths; the strongest

can only be opened when the tensile stress reaches its maximum value at the time of the peak eruption flux. Using the thin-shell approximation, we use the vertically averaged frictional strength $\bar{\tau}_f$ for shear failure

$$\left[\bar{\tau}_f\right] = S_0 + \frac{1}{2}\mu_f \rho g h \tag{14}$$

Here, μ_f is the *effective* coefficient of friction of the tiger-stripe fault zone, ρ is the ice-shell density, g is the gravitational acceleration of Enceladus, and h is the fault depth assuming to be the same as the ice-shell thickness. Note that the effective coefficient of friction depends on the pore fluid pressure in the tiger-stripe fault zone, which is poorly known. Equations (3), (4) and (5) together with equation (1) yield four equations with four unknowns highlighted in bold:

$$\boldsymbol{\sigma}^{\mathbf{sum}}_{\boldsymbol{y'y'}}(\boldsymbol{x_i},\ \boldsymbol{y_i}) = \sigma^{\mathrm{TD}}_{y'y'}(x_i,\ y_i) - \frac{1}{2}\rho g h \tag{15a}$$

$$\frac{1}{2}\mu\rho g h + S_0 = \sigma^{\mathrm{TD}}_{x'y'} + \boldsymbol{\sigma}^{\mathbf{TT}}_{\boldsymbol{x'y'}}(\boldsymbol{x_i},\ \boldsymbol{y_i}) \tag{15b}$$

$$\boldsymbol{\sigma}^{\boldsymbol{sum}}_{\boldsymbol{x'x'}} = \sigma^{\mathrm{TD}}_{x'x'}(x_i,\ y_i) + \boldsymbol{\sigma}^{\mathbf{TT}}_{\boldsymbol{x'x'}}(\boldsymbol{x_i},\ \boldsymbol{y_i}) \tag{15c}$$

$$\frac{\boldsymbol{\sigma}^{\mathbf{sum}}_{\boldsymbol{x'x'}} + \boldsymbol{\sigma}^{\mathbf{sum}}_{\boldsymbol{y'y'}}}{2} - \sqrt{\left(\frac{\boldsymbol{\sigma}^{\mathbf{sum}}_{\boldsymbol{x'x'}} - \boldsymbol{\sigma}^{\mathbf{sum}}_{\boldsymbol{y'y'}}}{2}\right)^2 + \sigma^{\mathrm{sum}}_{x'y'}} = T_0 \tag{15d}$$

where x_i and y_i represent a point along the tiger-stripe faults (latitude, longitude). The maximum tidal (τ_{TD}) and tectonic (τ_{TT}) stresses can be obtained by

$$\tau_{TT} = \sqrt{\left(\frac{\sigma^{TT}_{x'x'} - \sigma^{TT}_{y'y'}}{2}\right)^2 + \left(\sigma^{TT}_{x'y'}\right)^2} \tag{16a}$$

$$\tau_{TD} = \sqrt{\left(\frac{\sigma_{x'x'}^{TD} - \sigma_{y'y'}^{TD}}{2}\right)^2 + \left(\sigma_{x'y'}^{TD}\right)^2} \quad (16b)$$

To assess their relative importance in driving ice-shell deformation expressed by spatial location and temporal evolution of the erupting jets along, we define a dimensionless factor: $\tau_0 = \frac{\tau_{TT}}{\tau_{TD}}$. See Table 1 for all values used in the model.

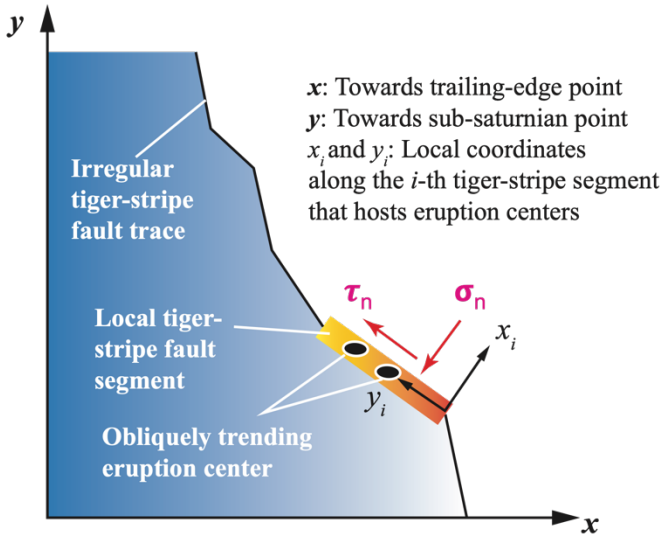

Fig. 3.11 Relationship between regional and local coordinates. The local coordinates x' and y' are defined by the strike and normal of the fault segment, where the regional coordinates ***x*** and ***y*** point towards the sub-saturnian and trailing-edge points, respectively.

Table 3.1 Input parameters and values used in this study **(**Schulson, 2002; Hurford et al., 2009; Schulson and Fortt, 2012; Thomas et al., 2016).

Parameter	Meaning	Value	Unit
e	Eccentricity	0.0047	-

n	Mean motion	5.29×10^{-5}	rad/s
ψ	Phase of optical libration	0	degrees
g	gravity	0.113	m/s^2
ρ_{av}	Average density of Enceladus	1608	kg/m^3
M	Mass of Saturn	5.683×10^{26}	kg
μ	Rigidity of ice	3.52×10^{9}	Pa
$2e$	Amplitude of optical libration	0.541	degrees
h_2	Tidal love number	0.32	-
ν	Poisson ratio	0.33	-
a	Semi-major axis	2.38×10^{8}	m
F	Amplitude of physical libration	0.12	-
ω	Argument of periapsis	0	degrees
ε	Obliquity	0	degrees
μ_f	Coefficient of friction	0.4	-

ρ	Density of ice	1000	kg/m^3

3.5.2 Model results

Our model results depend critically on the choice of model parameters, including cohesive strength, tensile strength, and effective coefficient of friction of the tiger-stripe shear zones. The results are also sensitive to the choice of ice-shell thickness but less so to the ice-shell density. The lack of direct measurements of the mechanical properties of the ice shell from Enceladus requires that we adopt values derives from experimental results for this work. It is well known that the mechanical behavior of ice, such as the stress-strain relationship, is similar to that of rocks (e.g., Sinha, 1978; Hutter, 1983; Schulson, 2001). Under low stress magnitudes, the induced strain of deforming ice is elastic and linearly proportional to stress as described by Hooke's law (e.g., Sinha, 1978). When the applied stress is higher than the elastic limit, the corresponding strain varies nonlinearly with stress, and the induced deformation is irreversible (i.e., plastic) (Sinha, 1978; Hutter, 1983; Mellor and Cole, 1983). A further increase in the stress magnitude leads to brittle failure expressed by fracturing and frictional sliding (Schulson, 2001).

Ice samples (<10 cm in size) measured under laboratory conditions typically have cohesive strengths in the range of 1.7 to 5.7 MPa at temperatures of -10° to -40° (Schulson, 2001). However, larger sea-ice blocks ~10s of meters in size appear to have smaller cohesive strengths at ~11-38 kPa (Dempsey et al., 1999; Dempsey, 2000). This difference has been attributed to the presence of air bubbles inside sea-ice slabs (Dempsey et al., 1999; Dempsey, 2000). Because the average temperature of the ice shell for Enceladus is much lower than the experiments performed on Earth, the above estimates for the cohesive strength of the ice should be regarded as minimum values when used in our model. We note that the mechanical model of Yin et al. (2016) shows the spacing

of the tiger-stripe faults in a 5-km thick ice shell requires a cohesive strength of 1 MPa (see their fig. 8). This estimate should serve as the upper bound, as it applies to the ice shell bounding the tiger-stripe faults, which should be weaker. Experimental studies show that the cohesive and tensile strengths of rocks are similar in magnitude (Jaeger et al., 2009). This conclusion is also confirmed by experiments on ice as shown by Dempsey et al. (1999). Because of this, we assume that the cohesive and tensile strengths of the tiger-stripe fault zones are similar in magnitude. As shown below, this assumption is well justified by our model results, as the effect of varying the two parameters on the magnitude of the induced tectonic stresses is quite similar. The coefficient of friction for ice as determined under laboratory conditions ranges from 0.4 to 0.6 (Schulson, 2002; Schulson and Fortt, 2012). Because the magnitude and distribution of pore fluid pressure in the tiger-stripe fault zones is unknown, we use the lower value of 0.4 for the friction coefficient in all our calculations. As shown in Yin et al. (2016), the shear strength of ice in a low-gravity environment such as Enceladus is dominated by the cohesive term rather than the gravity dependent term involving the friction-coefficient. Hence, we expect the choice of the friction coefficient value does not affect our general conclusions made in this study.

Using the above constraints as bounds, we present our model results in two formats. First, we plot the ratio of the maximum tectonic stress vs. maximum tidal stress as functions of the cohesive (**Fig. 3.12A**) and tensile strengths (**Fig. 3.12B**) of the tiger-stripe fault zone using ice-shell thicknesses of 20 km, 10 km, and 5 km, respectively. Second, we show the direction of the minimum principal compressive stress along the tiger-stripe shear zones (**Fig. 3.13**) where jets have been identified and where we assume a simultaneous tensile and shear failure of the fault zones at the peak-flux of the plumes.

The plot in **Fig. 3.12A** shows that the ratio of the maximum tectonic stress to the maximum tidal stress, expressed as $\log(\tau_0)$, varies from ~0.5 to ~1.8 for the shell thickness of 5, 10, and 20 km and for a cohesive strength less than 10^5 Pa, which we consider to the upper bound for the strength of the tiger-stripe fault zones. For a cohesive strength of 10^3 Pa and a shell thickness of 5 km, the $\log(\tau_0)$ value is about 0.58, which means that the maximum tectonic stress is greater than the tidal stress, but the two types of stresses are on the same order of magnitude at ~10^4 Pa. Using a cohesive strength of 10^6 Pa as the upper bound, the required maximum tectonic stress must be less than two orders of magnitude higher than that of the maximum tidal stress.

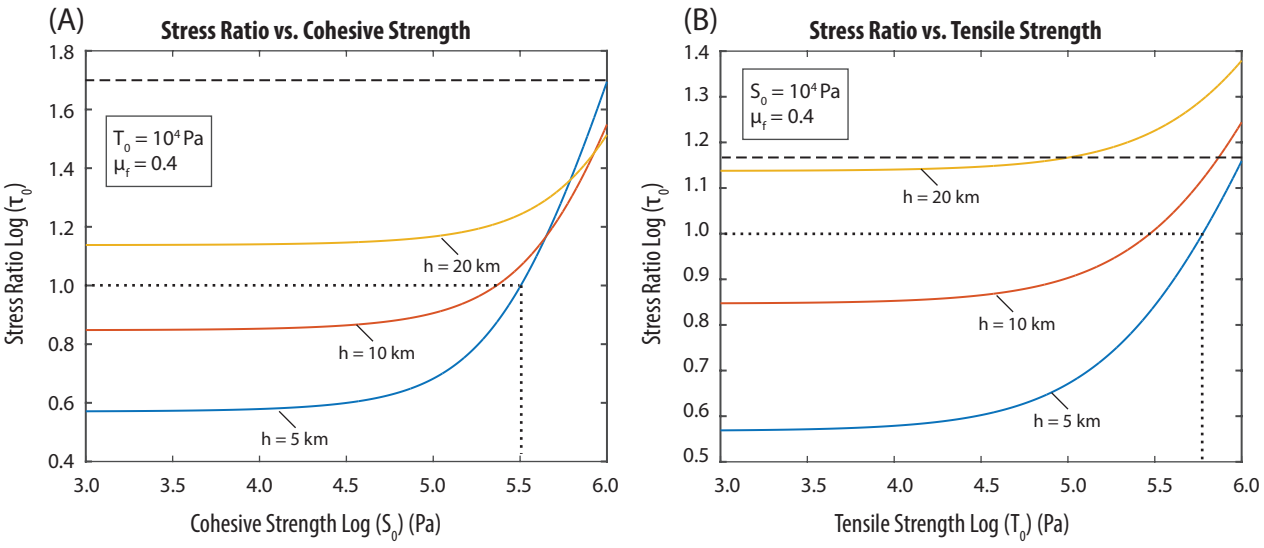

Fig. 3.12. (A) Ratio of tectonic stress vs. tidal stress as a function of the tiger-stripe fault zone cohesive strength with varying ice-shell thickness at 5 km, 10 km, and 20 km, respectively. (B) Ratio of tectonic stress vs. tidal stress as a function of the tensile strength of the tiger-stripe fault zone with varying ice-shell thickness at 5 km, 10 km, and 20 km, respectively.

The directions of the minimum principal compressive stress for the total stress along the tiger-stripe faults are determined at each jet location identified by Porco et al. (2014). As stated in our

model assumption, this result is obtained by assuming a simultaneous shear and tensile failure at the jet location when the peak plume flux occurs. We find that the stress-direction pattern as shown in **Fig. 3.13** changes little within the range of permissible model parameters: the tensile and cohesive strengths are on the order of 10^4 to 10^6 Pa and the ice-shell thickness from 5 to 20 km. We note that the principal-stress directions displayed in **Fig. 3.13** require left-slip motion on all tiger-stripe faults, a prediction consistent with our mapping results. Note that left-slip faulting is not assumed in our model, but a natural consequence of the assumption from the phase lag for the tidal stress. The averaged total shear stress on the tiger-stripe faults is on the order of ~ $7x10^5$ Pa given the inputted parameters (see figure caption).

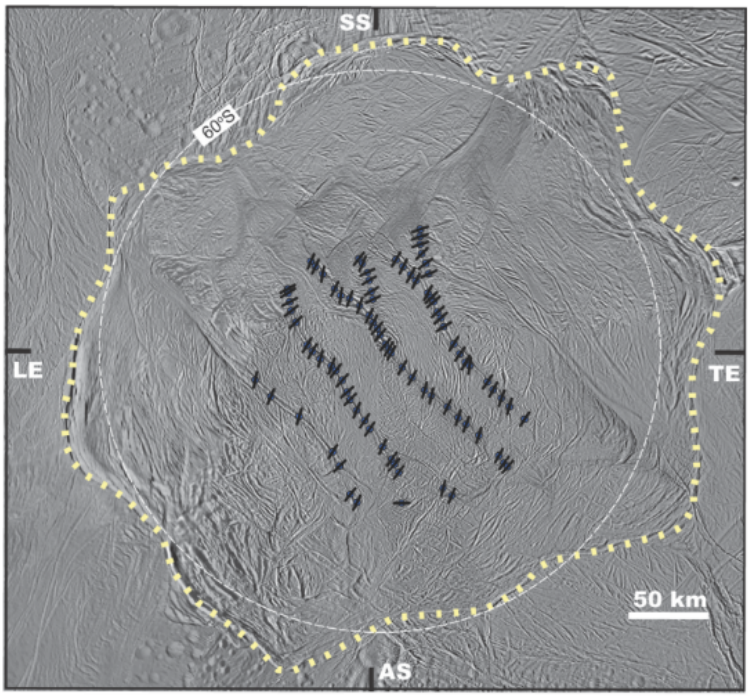

Fig. 3.13 Directions of the minimum principal compressive stress for the total stress field determined from this study at the jet locations identified by Porco et al. (2014). The results are

based on the assumption that simultaneous shear and tensile failure occurs at the time of peak plume flux at these locations. Model parameters used for this plot are h = 20 km, $T_0 = 10^4$ Pa, $S_0 = 10^4$ Pa, and $\mu_f = 0.4$. Note that the orientations of the principal stresses require left-slip motion on all tiger-stripe faults, consistent with our geological observations. The averaged total shear stress on the tiger-stripe fault planes is on the order of ~ 7×10^5 Pa.

3.6 Discussion

Although our mapping is restricted only to two sites where the location of active erupting jets is well known, our work nevertheless demonstrates for the first time that the jet locations can be related to local extensional structures along overall left-slip fault zones. Because the extensional structures lie within or are linked to the left-slip fault zones, coeval shear and tensile failure due to a combination of both an endogenic stress field and the exogenic tidal stress may be the cause of the eruption phase delay relative to the diurnal tide. Under this assumption, we are able to superpose the tidal stress at the time of the phase delay along various segments of the tiger-stripe fault zones where erupting jets are well located. Our modeling work shows that the inferred tectonic stress has a magnitude (~10^4 to ~10^5 Pa) comparable to or slightly greater than the maximum magnitude of the tidal stress when model parameters as determined by laboratory experiments. Below, we discuss the implications and limitations of our work.

3.6.1 Mechanism of plume eruption and future work

Our mapping results allows us to differentiate between the three competing models for jet eruptions as shown in **Fig. 3.3**: (1) the tensile-crack model (Kieffer et al., 2006; Gioia et al., 2007; Pathoff and Kattenhorn, 2011; Kite and Rubin, 2016; Hemingway et al., 2019), (2) the tidal

walking model (Nimmo et al., 2007; Hurford et al., 2007), and (3) the left-slip-fault model (Yin and Pappalardo, 2015; Helfenstein and Porco, 2015; Yin et al., 2016). The open-crack model predicts parallel tensile fractures next to the tiger-stripe faults, which are not observed by our detailed mapping. Similarly, we do not observe geological features supporting the tidal-walking model. This is because the model predicts net right-slip displacement along the tiger-stripe faults (Nimmo et al., 2007; Hurford et al., 2007), but the secondary geological structures directly next to the tiger-stripe faults in our mapped areas are all consistent with them being created by left-slip motion rather than right-slip motion along the tiger-stripe faults. Although our work remains limited in the spatial coverage of the tiger-stripe faults across the SPT, the available data lead us to favor a strike-slip fault model for controlling the locations of the active erupting plumes. Specifically, the eruption centers occur at local extensional structures such as releasing bends/pull-apart basins as shown in **Fig. 3.14**. Magmatic intrusion and volcanic eruption can be facilitated by strike-slip faulting that creates local dilation; this process is well known on Earth (e.g., Tikoff and Teyssier, 1992) and has been documented on the Moon (Zhang et al., 2023) where strike-slip faults in an overall compressional tectonic setting may have served as conduits for volcanic eruptions.

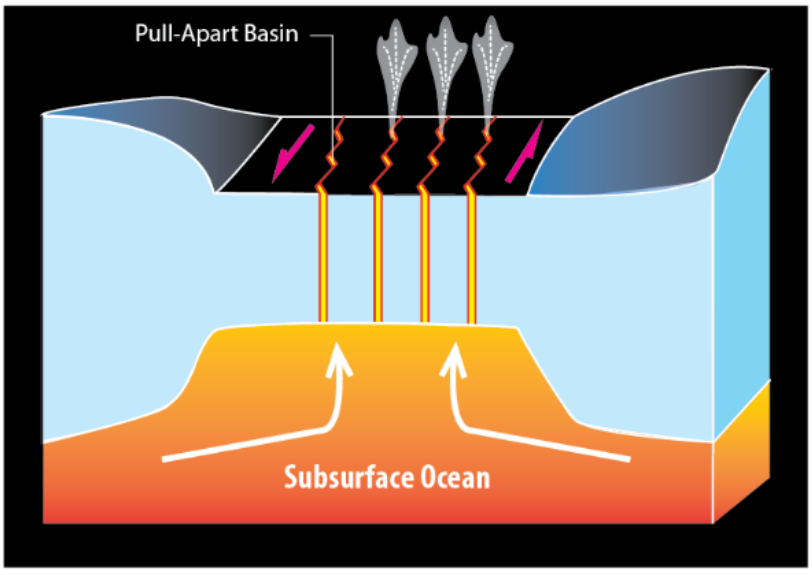

Fig. 3.14 A conceptual model for the structural control on the spatially discrete and temporally continuous erupting plumes. In this model, eruption centers are located at local extensional structures, such as pull-apart basins/releasing bends, in an overall strike-slip fault zone.

Despite the preliminary interpretation of our results favoring a strike-slip origin of the jet eruption centers, more systematic and detailed studies along all segments of the tiger-stripe faults are needed. Based on the existing work, we envision additional sites can be used to test our conceptual model. First, widely spaced (>1 km), parallel fractures with consistent left-lateral offsets have been identified and mapped along segments of Baghdad Sulcus (see figure 13B in Yin and Pappalardo, 2015; also see Patthoff and Kattenhorn, 2011). Local curvature of these strike-slip faults may have created extensional cracks favorable for plume eruptions. Obliquely oriented *en echelon* tensile cracks representing components typical of an extensional strike-slip duplex system (e.g., Woodcock and Fischer, 1986) were identified and mapped along Baghdad Sulcus (see figure 13A in Yin and Pappalardo, 2015) and along Damascus Sulcus (see figure 14A in Yin and Pappalardo, 2015). These extensional structures in the tiger-stripe strike-slip fault systems are likely associated with the locations of erupting jets if our conceptual model is valid. Interestingly, Helfenstein and Porco (2015) document regularly spaced jet centers a cadence of ~ 5 km along all the tiger-stripe fault zones, but these authors did not examine the exact structural setting of the regularly spaced jet locations. Detailed studies addressing this issue can shed a light on the mechanics of the tiger-stripe faults.

3.6.2 Endogenic stresses and their relative magnitudes to the diurnal tidal stress

As stated in the introduction, one of the biggest ongoing problems in the study of icy satellites is whether ice-shell deformation is controlled by tidal stresses, and under what conditions. Addressing this issue requires quantification of the magnitude of stresses sourced from endogenic and exogenic sources. Non-tidal stresses in the ice shell of Enceladus and icy satellites in general may be generated by warm-ice convection (Barr and McKinnon, 2007; Barr and Showman, 2009), true polar wander (Nimmo and Pappalardo, 2006), non-synchronous rotation (Patthoff and Kattenhorn, 2011), laterally varying gravitational potential induced by uneven ice-shell thickness (Schenk and McKinnon, 2009; Yin and Pappalardo, 2015; Kang and Flierl, 2020), or diapiric flow (Nimmo and Pappalardo, 2006). Whether solid-state convection can occur in the ice shell of Enceladus depends critically on the assumed ice flow law and ice-shell thickness. For example, Barr and McKinnon (2007) should that convection may occur in a pure water ice shell of Enceladus if the ice grain size is 0.1 to 0.3 mm and the ice-shell thickness is 40-100 km. The required ice-shell thickness is too thick for the South Polar Terrain that has a shell thickness of only ~5 km thick (Hemingway et al., 2018). Even if convection occurred in the past when the ice shell was much thicker, the anticipated stress magnitude is ~100s of Pa (Collins et al., 2010), which is ~2 orders of magnitude smaller than the tidal stress magnitude operated within the ice shell of Enceladus, as well as the predicted tectonic stress from our model.

Larger stress magnitudes on the order of ~10 MPa can be generated by reorientation of the ice shell for Enceladus (Nimmo and Pappalardo, 2006), which is two orders of magnitude greater than the tidal stress. The dominance of this type of stress is expected to overwhelm the cyclic tidal stress such as the case on Earth. Hence, the cyclic eruption of plumes may become either completely muted if the stress is compressive or erupting with little changes in flux if the stress is tensile. Non-synchronous rotation is a consequence of net-torque exerted on a tidally locked

satellite (Goldreich, 1966; Greenberg and Weidenschilling, 1984), which is expressed by slow changes in the sub-planet point and hence ice-shell deformation. Modeling of the effects of non-synchronous rotation on the ice shell deformation of Enceladus suggests a stress magnitude on the order of ~5 MPa at the south polar terrain (Patthoff et al., 2019), which is an order of magnitude higher that required from our modeling result.

Schenk and McKinnon (2009) recognized several large depressions on Enceladus, varying from 90 to 175 km across and from 800 to 1500 m in depth. The SPT itself is a larger depression that is 0.5-1.5 km below its bounding regions. Combined analysis of topographic and gravity data show that the Enceladus ice shell is in Airy isostasy (Schenk and McKinnon, 2009; Besserer et al., 2013; Hemingway et al., 2018), which means that the shell has negligible elastic strength and may behave more like viscous fluid. Meanwhile, the large variation in surface elevation requires ice-shell thickness to vary from ~ 5 km to > 35 km (Giese et al., 2008; Iess et al., 2014; Čadek et al., 2016; Hemingway et al., 2018). This variation in ice shell thickness should have induced lateral viscous flow driven by the gradient of gravitational potential energy stored in the ice, which was anticipated by Ojakangas and Stevenson (1989) and Collins and Goodman (2007) and was modelled by Wang and Flierl (2020). Yin and Pappalardo (2015) estimated the stress magnitude across the SPT as induced the varying ice-shell thickness in surrounding regions to be on the order of ~0.1 MPa, which is comparable in magnitude to the diurnal tidal stress field and the stress magnitude predicted by our model when using model parameters as determined by laboratory experiments.

3.7 Conclusions

In this study, we investigated the relative importance of endogenic vs. exogenic stresses in governing the active tectonics of Enceladus, which is expressed by cyclic plume eruptions along four parallel faults. Our geologic mapping shows that the faults have experienced left-slip motion, and that local extensional structures owing to fault-trace irregularities host plume eruption centers. The geometric and kinematic relationships between left-slip fault segments and local extensional structures within the left-slip fault zones lead us to hypothesize that the peak plume eruption is generated when the superposed tidal and tectonic stress cause simultaneous shear and tensile failure along plume hosting segments of the tiger-stripe fault zones. We quantified this hypothesis using a stress decomposition model that allows us to assess (1) the relative importance of tectonic stress vs. tidal stress and (2) the role of ice-shell properties (strength and thickness) in controlling the phase delay of the cyclic plume eruptions along the tiger-stripe fractures with respect to the diurnal tide. Using laboratory-determined ice strengths and constrained ice-shell thickness for the South Polar Terrain of Enceladus, our model results predict that the endogenic tectonic stress and the diurnal-tide-induced stress are comparable in magnitude on the order of $\sim 10^4$ Pa. When comparing the predicted stress magnitudes from our model against those induced by warm-ice convection, true polar wander, non-synchronous rotation, and variation of ice-shell thickness, we find that the most plausible generator of the endogenic stress in the ice is that produced by the lateral gradient of gravitational potential energy stored in an ice shell with uneven thickness, ranging from 5 km to >35 km.

3.8 References

Armijo, R., Tapponnier, P., Mercier, J. L., & Han, T. L., 1986. Quaternary extension in southern Tibet: Field observations and tectonic implications. *Journal of Geophysical Research: Solid Earth*, *91*(B14), 13803-13872.

Armijo, R., Tapponnier, P., & Han, T., 1989. Late Cenozoic right-lateral strike-slip faulting in southern Tibet. *Journal of Geophysical Research: Solid Earth*, *94*(B3), 2787-2838.

Banerdt, W. B., Golombek, M. P., & Tanaka, K. L., 1992. Stress and tectonics on Mars. *Mars*, 249-297.

Barr, A. C., Pappalardo, R. T., & Zhong, S., 2004. Convective instability in ice I with non-Newtonian rheology: Application to the icy Galilean satellites. *Journal of Geophysical Research: Planets*, *109*(E12).

Barr, A.C. and McKinnon, W.B., 2007. Convection in ice I shells and mantles with self-consistent grain size. *Journal of Geophysical Research: Planets*, *112*(E2).

Barr, A.C. and Preuss, L.J., 2010. On the origin of south polar folds on Enceladus. *Icarus*, *208*(1), pp.499-503.

Běhounková, M., Tobie, G., Choblet, G. and Čadek, O., 2012. Tidally-induced melting events as the origin of south-pole activity on Enceladus. *Icarus*, *219*(2), pp.655-664.

Běhounková, M., Tobie, G., Čadek, O., Choblet, G., Porco, C. and Nimmo, F., 2015. Timing of water plume eruptions on Enceladus explained by interior viscosity structure. *Nature Geoscience*, *8*(8), pp.601-604.

Bercovici, D., 2003. The generation of plate tectonics from mantle convection. *Earth and Planetary Science Letters*, *205*(3-4), 107-121.

Bercovici, D., & Ricard, Y., 2014. Plate tectonics, damage and inheritance. *Nature*, *508*(7497),

513-516.

Besserer, J., Nimmo, F., Roberts, J.H. and Pappalardo, R.T., 2013. Convection-driven compaction as a possible origin of Enceladus's long wavelength topography. *Journal of Geophysical Research: Planets*, *118*(5), pp.908-915.

Beuthe, M., 2013. Spatial patterns of tidal heating. *Icarus*, *223*(1), pp.308-329.

Beuthe, M., 2019. Enceladus's crust as a non-uniform thin shell: II tidal dissipation. *Icarus*, *332*, pp.66-91.

Bland, M.T., Singer, K.N., McKinnon, W.B. and Schenk, P.M., 2012. Enceladus' extreme heat flux as revealed by its relaxed craters. Geophysical Research Letters 39.

Bland, M. T., McKinnon, W. B., & Schenk, P. M., 2015. Constraining the heat flux between Enceladus' tiger stripes: Numerical modeling of funiscular plains formation. *Icarus*, *260*, 232-245.

Brothers, D. S., Driscoll, N. W., Kent, G. M., Harding, A. J., Babcock, J. M., & Baskin, R. L., 2009. Tectonic evolution of the Salton Sea inferred from seismic reflection data. *Nature Geoscience*, *2*(8), 581-584.

Burgess, W. P., Yin, A., Dubey, C. S., Shen, Z. K., & Kelty, T. K., 2012. Holocene shortening across the Main Frontal Thrust zone in the eastern Himalaya. *Earth and Planetary Science Letters*, *357*, 152-167.

Byrne, P. K., Klimczak, C., Celâl Şengör, A. M., Solomon, S. C., Watters, T. R., & Hauck, II, S. A., 2014. Mercury's global contraction much greater than earlier estimates. *Nature Geoscience*, *7*(4), 301-307.

Cable, M.L., Porco, C., Glein, C.R., German, C.R., MacKenzie, S.M., Neveu, M., Hoehler, T.M.,

Hofmann, A.E., Hendrix, A.R., Eigenbrode, J. and Postberg, F., 2021. The science case for a return to Enceladus. *The planetary science journal*, *2*(4), p.132.

Čadek, O., Tobie, G., Van Hoolst, T., Massé, M., Choblet, G., Lefèvre, A., Mitri, G., Baland, R.M., Běhounková, M., Bourgeois, O. and Trinh, A., 2016. Enceladus's internal ocean and ice shell constrained from Cassini gravity, shape, and libration data. *Geophysical Research Letters*, *43*(11), pp.5653-5660.

Carr, M. H., 1973. Volcanism on mars. *Journal of Geophysical Research*, *78*(20), 4049-4062.

Choblet, G., Tobie, G., Sotin, C., Běhounková, M., Čadek, O., Postberg, F. and Souček, O., 2017. Powering prolonged hydrothermal activity inside Enceladus. *Nature Astronomy*, *1*(12), pp.841-847

Cochran, E. S., Vidale, J. E., & Tanaka, S., 2004. Earth tides can trigger shallow thrust fault earthquakes. *Science*, *306*(5699), 1164-1166.

Collins, G.C. and Goodman, J.C., 2007. Enceladus' south polar sea. *Icarus*, *189*(1), pp.72-82.

Collins, G. C., McKinnon, W. B., Moore, J. M., Nimmo, F., Pappalardo, R. T., Prockter, L. M., & Schenk, P. M. (2010). Tectonics of the outer planet satellites. *Planetary tectonics*, *11*(264), 229.

Conrad, C. P., & Lithgow-Bertelloni, C., 2002. How mantle slabs drive plate tectonics. *Science*, *298*(5591), 207-209.

Crow-Willard, E.N. and Pappalardo, R.T., 2015. Structural mapping of Enceladus and implications for formation of tectonized regions. Journal of Geophysical Research: Planets 120, 928-950.

Crowell, J.C., 1974. Origin of late Cenozoic basins in southern California. In *Tectonics and*

sedimentation (Vol. 22, pp. 190-204). Tulsa, Okla.: Society of Economic Paleontologists and Mineralogists.

Crowell, J. C., 1979. The San Andreas fault system through time. *Journal of the Geological Society*, *136*(3), 293-302.

Dempsey, J.P., 2000. Research trends in ice mechanics. Int. J. Solids Struct. 37 (1), 131–153.

Dempsey, J.P., Adamson, R.M., Mulmule, S.V., 1999. Scale effects on the in-situ tensile strength and fracture of ice. Part II: First-year sea ice at resolute, NWT. Int. J. Fract. 95 (1–4), 347–366.

Giese, B., Wagner, R., Hussmann, H., Neukum, G., Perry, J., Helfenstein, P. and Thomas, P.C., 2008. Enceladus: An estimate of heat flux and lithospheric thickness from flexurally supported topography. *Geophysical Research Letters*, *35*(24).

Gioia, G., Chakraborty, P., Marshak, S. and Kieffer, S.W., 2007. Unified model of tectonics and heat transport in a frigid Enceladus. *Proceedings of the National Academy of Sciences*, *104*(34), pp.13578-13581.

Goldreich, P., 1966. History of the lunar orbit. *Reviews of Geophysics*, *4*(4), pp.411-439.

Golombek, M. P., Phillips, R. J., Watters, T. R., & Schultz, R. A., 2010. Mars tectonics. *Planetary tectonics*, *11*, 183-232.

Green, A. P., Montesi, L. G. J., & Cooper, C. M., 2021. The growth of Europa's icy shell: Convection and crystallization. *Journal of Geophysical Research: Planets*, *126*(4), e2020JE006677.

Greenberg, R. and Weidenschilling, S.J., 1984. How fast do Galilean satellites spin?. *Icarus*, *58*(2), pp.186-196.

Greenberg, R., Geissler, P., Hoppa, G., Tufts, B. R., Durda, D. D., Pappalardo, R., ... & Carr, M.

H., 1998. Tectonic processes on Europa: Tidal stresses, mechanical response, and visible features. *Icarus*, *135*(1), 64-78.

Greenberg, R., Geissler, P., Tufts, B.R. and Hoppa, G.V., 2000. Habitability of Europa's crust: The role of tidal-tectonic processes. *Journal of Geophysical Research: Planets*, *105*(E7), pp.17551-17562.

Gülcher, A. J., Gerya, T. V., Montési, L. G., & Munch, J., 2020. Corona structures driven by plume–lithosphere interactions and evidence for ongoing plume activity on Venus. *Nature Geoscience*, *13*(8), 547-554.

Hauck II, S. A., Dombard, A. J., Phillips, R. J., & Solomon, S. C., 2004. Internal and tectonic evolution of Mercury. *Earth and Planetary Science Letters*, *222*(3-4), 713-728.

Han, L. and Showman, A.P., 2010. Coupled convection and tidal dissipation in Europa's ice shell. *Icarus*, *207*(2), pp.834-844.

Helfenstein, P., & Parmentier, E. M., 1983. Patterns of fracture and tidal stresses on Europa. *Icarus*, *53*(3), 415-430.

Helfenstein, P., & Parmentier, E. M., 1985. Patterns of fracture and tidal stresses due to nonsynchronous rotation: Implications for fracturing on Europa. *Icarus*, *61*(2), 175-184.

Helfenstein, P. and Porco, C.C., 2015. ENCELADUS'GEYSERS: RELATION TO GEOLOGICAL FEATURES. *The Astronomical Journal*, *150*(3), p.96.

Hemingway, D., Iess, L., Tajeddine, R. and Tobie, G., 2018. The interior of Enceladus. *Enceladus and the icy moons of Saturn*, pp.57-77.

Hemingway, D.J. and Mittal, T., 2019. Enceladus's ice shell structure as a window on internal heat production. *Icarus*, *332*, pp.111-131.

Hemingway, D.J., Rudolph, M.L. and Manga, M., 2020. Cascading parallel fractures on

Enceladus. *Nature Astronomy*, *4*(3), pp.234-239.

Holland, P. R., & Kwok, R., 2012. Wind-driven trends in Antarctic sea-ice drift. *Nature Geoscience*, *5*(12), 872-875.

Hoppa, G., Tufts, B. R., Greenberg, R., & Geissler, P., 1999. Strike–slip faults on Europa: Global shear patterns driven by tidal stress. *Icarus*, *141*(2), 287-298.

Howell, S.M. and Pappalardo, R.T., 2020. NASA's Europa Clipper—a mission to a potentially habitable ocean world. *Nature Communications*, *11*(1), p.1311.

Hsu, H.W., Postberg, F., Sekine, Y., Shibuya, T., Kempf, S., Horányi, M., Juhász, A., Altobelli, N., Suzuki, K., Masaki, Y. and Kuwatani, T., 2015. Ongoing hydrothermal activities within Enceladus. *Nature*, *519*(7542), pp.207-210.

Hurford, T. A., Helfenstein, P., Hoppa, G. V., Greenberg, R., & Bills, B. G., 2007. Eruptions arising from tidally controlled periodic openings of rifts on Enceladus. *Nature*, *447*(7142), 292-294.

Hurford, T.A., Bills, B.G., Helfenstein, P., Greenberg, R., Hoppa, G.V. and Hamilton, D.P., 2009. Geological implications of a physical libration on Enceladus. *Icarus*, *203*(2), pp.541-552.

Hutter, K., 1983. Theoretical Glaciology: Material Science of Ice and the Mechanics of Glaciers and Ice Sheets, vol. 1. Springer.

Iess, L., Stevenson, D.J., Parisi, M., Hemingway, D., Jacobson, R.A., Lunine, J.I., Nimmo, F., Armstrong, J.W., Asmar, S.W., Ducci, M. and Tortora, P., 2014. The gravity field and interior structure of Enceladus. Science 344, 78-80.

Ingersoll, A.P. and Nakajima, M., 2016. Controlled boiling on Enceladus. 2. Model of the liquid-filled cracks. *Icarus*, *272*, pp.319-326.

Ingersoll, A.P., Ewald, S.P. and Trumbo, S.K., 2020. Time variability of the Enceladus plumes: Orbital periods, decadal periods, and aperiodic change. *Icarus*, *344*, p.113345.

Jaeger, J. C., Cook, N. G., & Zimmerman, R., 2009. *Fundamentals of rock mechanics*. John Wiley & Sons.

Kalousová, K. and Sotin, C., 2020. The insulating effect of methane clathrate crust on Titan's thermal evolution. *Geophysical Research Letters*, *47*(13), p.e2020GL087481.

Kang, W., & Flierl, G., 2020. Spontaneous formation of plumes at only one pole on Enceladus's ice shell. *Proceedings of the National Academy of Sciences*, *117*(26), 14764-14768.

Kargel, J. S., & Pozio, S., 1996. The volcanic and tectonic history of Enceladus. *Icarus*, *119*(2), 385-404.

Kay, J. P., & Dombard, A. J., 2023. Simulating spatial variations of lithospheric folding in the south polar terrain of Enceladus. *Icarus*, 115431.

Kieffer, S.W., Lu, X., Bethke, C.M., Spencer, J.R., Marshak, S. and Navrotsky, A., 2006. A clathrate reservoir hypothesis for Enceladus' south polar plume. *Science*, *314*(5806), pp.1764-1766.

Kirchoff, M.R. and Schenk, P., 2009. Crater modification and geologic activity in Enceladus' heavily cratered plains: Evidence from the impact crater distribution. *Icarus*, *202*(2), pp.656-668.

Kite, E.S. and Rubin, A.M., 2016. Sustained eruptions on Enceladus explained by turbulent dissipation in tiger stripes. *Proceedings of the National Academy of Sciences*, *113*(15), pp.3972-3975.

Knapmeyer, M., Stähler, S. C., Daubar, I., Forget, F., Spiga, A., Pierron, T., ... & Banerdt, B.,

2021. Seasonal seismic activity on Mars. *Earth and Planetary Science Letters*, *576*, 117171.

Knopoff, L., 1964. Earth tides as a triggering mechanism for earthquakes. *Bulletin of the Seismological Society of America*, *54*(6A), 1865-1870.

Kwok, R., 2005. Ross Sea ice motion, area flux, and deformation. *Journal of climate*, *18*(18), 3759-3776.

Lavé, J., & Avouac, J. P., 2000. Active folding of fluvial terraces across the Siwaliks Hills, Himalayas of central Nepal. *Journal of Geophysical Research: Solid Earth*, *105*(B3), 5735-5770.

Leith, A.C. and McKinnon, W.B., 1996. Is there evidence for polar wander on Europa?. *Icarus*, *120*(2), pp.387-398.

Lenardic, A., & Crowley, J. W., 2012. On the notion of well-defined tectonic regimes for terrestrial planets in this solar system and others. *The Astrophysical Journal*, *755*(2), 132.

Leonard, E.J., Yin, A. and Pappalardo, R.T., 2021. Forming Relic Cratered Blocks: Left-Lateral Shear on Enceladus Inferred From Ice-Shell Deformation in the Leading Hemisphere. *Journal of Geophysical Research: Planets*, *126*(2), p.e2020JE006499.

Le Pichon, X., 1968. Sea-floor spreading and continental drift. *Journal of geophysical research*, *73*(12), 3661-3697.

Liao, Y., Nimmo, F. and Neufeld, J.A., 2020. Heat production and tidally driven fluid flow in the permeable core of Enceladus. *Journal of Geophysical Research: Planets*, *125*(9), p.e2019JE006209.

MacKenzie, S. M., Neveu, M., Davila, A. F., Lunine, J. I., Craft, K. L., Cable, M. L., ... &

Spilker, L. J., 2021. The Enceladus Orbilander mission concept: balancing return and resources in the search for life. *The Planetary Science Journal*, *2*(2), 77.

MacKenzie, S.M., Neveu, M., Davila, A.F., Lunine, J.I., Craft, K.L., Cable, M.L., Phillips-Lander, C.M., Hofgartner, J.D., Eigenbrode, J.L., Waite, J.H. and Glein, C.R., 2021. The Enceladus Orbilander mission concept: balancing return and resources in the search for life. *The Planetary Science Journal*, *2*(2), p.77.

Martin, E. S., 2016. The distribution and characterization of strike-slip faults on Enceladus. *Geophysical Research Letters*, *43*(6), 2456-2464.

McKay, C.P., Anbar, A.D., Porco, C. and Tsou, P., 2014. Follow the plume: the habitability of Enceladus. *Astrobiology*, *14*(4), pp.352-355.

McKenzie, D. P., & Parker, R. L., 1967. The North Pacific: an example of tectonics on a sphere. *Nature*, *216*(5122), 1276-1280.

McKenzie, D., Ford, P. G., Liu, F., & Pettengill, G. H., 1992. Pancakelike domes on Venus. *Journal of Geophysical Research: Planets*, *97*(E10), 15967-15976.

McKinnon, W.B., 1999. Convective instability in Europa's floating ice shell. *Geophysical Research Letters*, *26*(7), pp.951-954.

Mellor, M., Cole, D.M., 1983. Stress/strain/time relations for ice under uniaxial compression. Cold Reg. Sci. Technol. 6 (3), 207–230.

Melosh, H.J., 1977. Global tectonics of a despun planet. *Icarus*, *31*(2), pp.221-243.

Melosh, H. J. & McKinnon, W. B. in Mercury (eds Vilas, F., Chapman, C. R. & Matthews, M. S.) 374–400 (Univ. Arizona Press, 1988).

Meyer, J. and Wisdom, J., 2007. Tidal heating in Enceladus. *Icarus*, *188*(2), pp.535-539.

Morgan, W. J., 1968. Rises, trenches, great faults, and crustal blocks. *Journal of Geophysical*

Research, *73*(6), 1959-1982.

Nakajima, M. and Ingersoll, A.P., 2016. Controlled boiling on Enceladus. 1. Model of the vapor-driven jets. *Icarus*, *272*, pp.309-318.

Nahm, A. L., & Schultz, R. A., 2011. Magnitude of global contraction on Mars from analysis of surface faults: Implications for martian thermal history. *Icarus*, *211*(1), 389-400.

Nimmo, F., & McKenzie, D., 1998. Volcanism and tectonics on Venus. *Annual Review of Earth and Planetary Sciences*, *26*(1), 23-51.

Nimmo, F., & Stevenson, D. J., 2000. Influence of early plate tectonics on the thermal evolution and magnetic field of Mars. *Journal of Geophysical Research: Planets*, *105*(E5), 11969-11979.

Nimmo, F., & Pappalardo, R. T., 2006. Diapir-induced reorientation of Saturn's moon Enceladus. *Nature*, *441*(7093), 614-616.

Nimmo, F., Spencer, J.R., Pappalardo, R.T. and Mullen, M.E., 2007. Shear heating as the origin of the plumes and heat flux on Enceladus. *Nature*, *447*(7142), pp.289-291.

Nimmo, F., Porco, C. and Mitchell, C., 2014. Tidally modulated eruptions on Enceladus: Cassini ISS observations and models. The Astronomical Journal 148, 46.

Nimmo, F., & Pappalardo, R. T., 2016. Ocean worlds in the outer solar system. *Journal of Geophysical Research: Planets*, *121*(8), 1378-1399.

Nimmo, F., Barr, A. C., Behounková, M., & McKinnon, W. B., 2018. The thermal and orbital evolution of Enceladus: observational constraints and models. *Enceladus and the icy moons of Saturn*, *475*, 79-94.

Ojakangas, G. W., & Stevenson, D. J., 1989. Thermal state of an ice shell on Europa. *Icarus*, *81*(2), 220-241.

O'Neill, C., Lenardic, A., Weller, M., Moresi, L., Quenette, S., & Zhang, S., 2016. A window for plate tectonics in terrestrial planet evolution?. *Physics of the Earth and Planetary Interiors*, *255*, 80-92.

Pankine, A.A., 2023. Numerical simulations of heat exchange and vapor flow in ice fractures on Enceladus. *Icarus*, *401*, p.115584.

Pappalardo, R.T. and Greeley, R., 1995. A review of the origins of subparallel ridges and troughs: Generalized morphological predictions from terrestrial models. *Journal of Geophysical Research: Planets*, *100*(E9), pp.18985-19007.

Pappalardo, R. T., Head, J. W., Greeley, R., Sullivan, R. J., Pilcher, C., Schubert, G., ... & Goldsby, D. L., 1998. Geological evidence for solid-state convection in Europa's ice shell. *Nature*, *391*(6665), 365-368.

Patterson, G.W., Kattenhorn, S.A., Helfenstein, P., Collins, G.C. and Pappalardo, R.T., 2018. The geology of Enceladus. *Enceladus and the icy moons of Saturn*, p.95.

Patthoff, D.A. and Kattenhorn, S.A., 2011. A fracture history on Enceladus provides evidence for a global ocean. *Geophysical Research Letters*, *38*(18).

Patthoff, D.A., Kattenhorn, S.A. and Cooper, C.M., 2019. Implications of nonsynchronous rotation on the deformational history and ice shell properties in the south polar terrain of Enceladus. *Icarus*, *321*, pp.445-457.

Patthoff, D. A., Pappalardo, R. T., Golombek, M., Chilton, H., Crow-Willard, E., & Thomas, P. C., 2022. Thrust faulting as the origin of dorsa in the trailing hemisphere of Enceladus. *Icarus*, *375*, 114815.

Phillips, R. J., 1990. Convection-driven tectonics on Venus. *Journal of Geophysical Research: Solid Earth*, *95*(B2), 1301-1316.

Pleiner Sládková, K., Souček, O., & Běhounková, M., 2021. Enceladus' tiger stripes as frictional faults: Effect on stress and heat production. *Geophysical Research Letters*, *48*(19), e2021GL094849.

Piskorz, D., Elkins-Tanton, L. T., & Smrekar, S. E., 2014. Coronae formation on Venus via extension and lithospheric instability. *Journal of Geophysical Research: Planets*, *119*(12), 2568-2582.

Porco, C.C., Helfenstein, P., Thomas, P.C., Ingersoll, A.P., Wisdom, J., West, R., Neukum, G., Denk, T., Wagner, R., Roatsch, T. and Kieffer, S., 2006. Cassini observes the active south pole of Enceladus. Science 311, 1393-1401.

Porco, C., DiNino, D. and Nimmo, F., 2014. How the geysers, tidal stresses, and thermal emission across the south polar terrain of Enceladus are related. The Astronomical Journal 148, 45.

Postberg, F., Schmidt, J., Hillier, J., Kempf, S. and Srama, R., 2011. A salt-water reservoir as the source of a compositionally stratified plume on Enceladus. Nature 474, 620-622.

Roberts, J.H. and Nimmo, F., 2008. Tidal heating and the long-term stability of a subsurface ocean on Enceladus. *Icarus*, *194*(2), pp.675-689.

Roberts, J.H., 2015. The fluffy core of Enceladus. *Icarus*, *258*, pp.54-66.

Roberts, J.H. and Stickle, A.M., 2021. Breaking the symmetry by breaking the ice shell: An impact origin for the south polar terrain of Enceladus. *Icarus*, *359*, p.114302.

Robinson, P. T., Elders, W. A., & Muffler, L. P., 1976. Quaternary volcanism in the Salton Sea geothermal field, Imperial Valley, California. *Geological Society of America Bulletin*, *87*(3), 347-360.

Rossi, C., Cianfarra, P., Salvini, F., Bourgeois, O., & Tobie, G., 2020. Tectonics of Enceladus'

South Pole: Block Rotation of the Tiger Stripes. *Journal of Geophysical Research: Planets*, *125*(12), e2020JE006471.

Rovira-Navarro, M., Katz, R.F., Liao, Y., van der Wal, W. and Nimmo, F., 2022. The tides of Enceladus' porous core. *Journal of Geophysical Research: Planets*, *127*(5), p.e2021JE007117.

Rozel, A., Besserer, J., Golabek, G.J., Kaplan, M. and Tackley, P.J., 2014. Self-consistent generation of single-plume state for Enceladus using non-Newtonian rheology. *Journal of Geophysical Research: Planets*, *119*(3), pp.416-439.

Schenk, P., & Jackson, M. P. A., 1993. Diapirism on Triton: A record of crustal layering and instability. *Geology*, *21*(4), 299-302.

Schenk, P., & Seddio, S., 2006. Geologic and cratering history of Enceladus. Bull. Am. Astron. Soc. 38. Abst. #18.01

Schenk, P. M., & McKinnon, W. B., 2009. One-hundred-km-scale basins on Enceladus: Evidence for an active ice shell. *Geophysical research letters*, *36*(16).

Schoenfeld, A.M., Hawkins, E.K., Soderlund, K.M., Vance, S.D., Leonard, E. and Yin, A., 2023. Particle entrainment and rotating convection in Enceladus' ocean. Communications Earth & Environment 4, 28.

Schubert, G., Soloman, S. C., Turcotte, D. L., Drake, M. J., & Sleep, N. H., 1990. *Origin and thermal evolution of Mars* (No. NAS 1.26: 188095).

Schulson, E.M., 2001. Brittle failure of ice. Eng. Fract. Mech. 68, 1839–1887.

Schulson, E.M., 2002. Compressive shear faults in ice: Plastic vs. Coulombic faults. Acta Mater. 50 (13), 3415–3424.

Schulson, E.M., Fortt, A.L., 2012. Friction of ice on ice. J. Geophys. Res.: Solid Earth 117 (B12).

Sinha, N.K., 1978. Rheology of columnar-grained ice. Exp. Mech. 18 (12), 464–470.

Sleep, N. H., 1994. Martian plate tectonics. *Journal of Geophysical Research: Planets*, *99*(E3), 5639-5655.

Smrekar, S. E., & Solomon, S. C., 1992. Gravitational spreading of high terrain in Ishtar Terra, Venus. *Journal of Geophysical Research: Planets*, *97*(E10), 16121-16148.

Solomon, S. C., 1977. The relationship between crustal tectonics and internal evolution in the Moon and Mercury. *Physics of the Earth and Planetary Interiors*, *15*(2-3), 135-145.

Solomon, S. C., Smrekar, S. E., Bindschadler, D. L., Grimm, R. E., Kaula, W. M., McGill, G. E., ... & Stofan, E. R., 1992. Venus tectonics: An overview of Magellan observations. *Journal of Geophysical Research: Planets*, *97*(E8), 13199-13255.

Souček, O., Běhounková, M., Čadek, O., Hron, J., Tobie, G. and Choblet, G., 2019. Tidal dissipation in Enceladus' uneven, fractured ice shell. *Icarus*, *328*, pp.218-231.

Spencer, J.R., Pearl, J.C., Segura, M., Flasar, F.M., Mamoutkine, A., Romani, P., Buratti, B.J., Hendrix, A.R., Spilker, L.J. and Lopes, R.M.C., 2006. Cassini encounters Enceladus: Background and the discovery of a south polar hot spot. Science 311, 1401-1405.

Spencer, J.R., Barr, A.C., Esposito, L.W., Helfenstein, P., Ingersoll, A.P., Jaumann, R., McKay, C.P., Nimmo, F. and Waite, J.H., 2009. Enceladus: An active cryovolcanic satellite. Saturn from Cassini-Huygens, 683-724.

Spencer, J.R. and Nimmo, F., 2013. Enceladus: An active ice world in the Saturn system. Annual Review of Earth and Planetary Sciences 41, 693-717.

Spencer, J.R., Howett, C.J.A., Verbiscer, A., Hurford, T.A., Segura, M. and Spencer, D.C., 2013. Enceladus heat flow from high spatial resolution thermal emission observations. *EPSC Abstracts*, *8*, pp.840-1.

Spitale, J.N. and Porco, C.C., 2007. Association of the jets of Enceladus with the warmest regions on its south-polar fractures. Nature 449, 695-697.

Squyres, S. W., Reynolds, R. T., Cassen, P. M., & Peale, S. J., 1983. The evolution of Enceladus. *Icarus*, *53*(2), 319-331.

Stegman, D.R., Freeman, J. and May, D.A., 2009. Origin of ice diapirism, true polar wander, subsurface ocean, and tiger stripes of Enceladus driven by compositional convection. *Icarus*, *202*(2), pp.669-680.

Sylvester, A.G., 1988. Strike-slip faults. *Geological Society of America Bulletin*, *100*(11), pp.1666-1703.

Tackley, P. J., 2000. Self-consistent generation of tectonic plates in time-dependent, three-dimensional mantle convection simulations. *Geochemistry, Geophysics, Geosystems*, *1*(8).

Tajeddine, R., Soderlund, K.M., Thomas, P.C., Helfenstein, P., Hedman, M.M., Burns, J.A. and Schenk, P.M., 2017. True polar wander of Enceladus from topographic data. *Icarus*, *295*, pp.46-60.

Tanaka, S., Ohtake, M., & Sato, H., 2002. Spatio-temporal variation of the tidal triggering effect on earthquake occurrence associated with the 1982 South Tonga earthquake of Mw 7.5. *Geophysical Research Letters*, *29*(16), 3-1.

Thomas, P.C., Tajeddine, R., Tiscareno, M.S., Burns, J.A., Joseph, J., Loredo, T.J., Helfenstein, P. and Porco, C., 2016. Enceladus's measured physical libration requires a global subsurface ocean. Icarus 264, 37-47.

Tikoff, B. and Teyssier, C., 1992. Crustal-scale, en echelon" P-shear" tensional bridges: A possible solution to the batholithic room problem. *Geology*, *20*(10), pp.927-930.

Travis, B.J. and Schubert, G., 2015. Keeping Enceladus warm. *Icarus*, *250*, pp.32-42.

Tyler, R., 2011. Tidal dynamical considerations constrain the state of an ocean on Enceladus. *Icarus*, *211*(1), pp.770-779.

Tyler, R.H., 2020. Heating of Enceladus due to the dissipation of ocean tides. *Icarus*, *348*, p.113821.

Waite, J.H., Glein, C.R., Perryman, R.S., Teolis, B.D., Magee, B.A., Miller, G., Grimes, J., Perry, M.E., Miller, K.E., Bouquet, A. and Lunine, J.I., 2017. Cassini finds molecular hydrogen in the Enceladus plume: evidence for hydrothermal processes. *Science*, *356*(6334), pp.155-159.

Watters, T. R., Johnson, C. L., & Schultz, R. A., 2010a. Lunar tectonics. *Planetary Tectonic,* Watters, T. R. & Schultz, R. A. (Eds.) (Vol. 11). Cambridge University Press, 121.

Watters, T. R., Robinson, M. S., Beyer, R. A., Banks, M. E., Bell III, J. F., Pritchard, M. E., ... & Williams, N. R., 2010b. Evidence of recent thrust faulting on the Moon revealed by the Lunar Reconnaissance Orbiter Camera. *Science*, *329*(5994), 936-940.

Watters, T. R., Robinson, M. S., Collins, G. C., Banks, M. E., Daud, K., Williams, N. R., & Selvans, M. M., 2015. Global thrust faulting on the Moon and the influence of tidal stresses. *Geology*, *43*(10), 851-854.

Watters, T. R., Robinson, M. S., Banks, M. E., Tran, T., & Denevi, B. W., 2012. Recent extensional tectonics on the Moon revealed by the Lunar Reconnaissance Orbiter Camera. *Nature Geoscience*, *5*(3), 181-185.

Watters, T. R., Daud, K., Banks, M. E., Selvans, M. M., Chapman, C. R., & Ernst, C. M., 2016.

Recent tectonic activity on Mercury revealed by small thrust fault scarps. *Nature Geoscience*, *9*(10), 743-747.

Weller, M. B., & Kiefer, W. S., 2020. The physics of changing tectonic regimes: Implications for the temporal evolution of mantle convection and the thermal history of Venus. *Journal of Geophysical Research: Planets*, *125*(1), e2019JE005960.

Wesson, R. L., Helley, E. J., Lajoie, K. R,, and Wentworth, C. M., 1975, Faults and future earthquakes, in Borchardt, R. D., ed., Studies for seismic zonation of the San Francisco Bay region: U.S. Geological Survey Professional Paper 941 A, p. 5-30.

Westall, F., Höning, D., Avice, G., Gentry, D., Gerya, T., Gillmann, C., ... & Wilson, C., 2023. The habitability of Venus. *Space Science Reviews*, *219*(2), 17.

Woodcock, N.H. and Fischer, M., 1986. Strike-slip duplexes. *Journal of structural geology*, *8*(7), pp.725-735.

Yin, A., 2012a. Structural analysis of the Valles Marineris fault zone: Possible evidence for large-scale strike-slip faulting on Mars. *Lithosphere*, *4*(4), 286-330.

Yin, A., 2012b. An episodic slab-rollback model for the origin of the Tharsis rise on Mars: Implications for initiation of local plate subduction and final unification of a kinematically linked global plate-tectonic network on Earth. *Lithosphere*, *4*(6), 553-593.

Yin, A. and Pappalardo, R.T., 2015. Gravitational spreading, bookshelf faulting, and tectonic evolution of the South Polar Terrain of Saturn's moon Enceladus. Icarus 260, 409-439.

Yin, A., Zuza, A.V. and Pappalardo, R.T., 2016. Mechanics of evenly spaced strike-slip faults and its implications for the formation of tiger-stripe fractures on Saturn's moon Enceladus. *Icarus*, *266*, pp.204-216.

Zahnle, K., Schenk, P., Levison, H. and Dones, L., 2003. Cratering rates in the outer Solar

System. *Icarus*, *163*(2), pp.263-289.

Zhang, F., Pizzi, A., Ruj, T., Komatsu, G., Yin, A., Dang, Y., ... & Zou, Y., 2023. Evidence for structural control of mare volcanism in lunar compressional tectonic settings. *Nature Communications*, *14*(1), 2892.

Zhong, S., 2009. Migration of Tharsis volcanism on Mars caused by differential rotation of the lithosphere. *Nature Geoscience*, *2*(1), 19-23.

- Chapter 4 -

4 Geomorphological Map of the South Belet Region of Titan

4.1 Introduction

Saturn's largest moon Titan is the only natural satellite known to have a substantial atmosphere, a dense veil of nitrogen and methane obscuring the surface below. It was not until the Cassini-Huygens mission arrived in 2004 that Titan was revealed to be a geologically complex world, one characterized by mountains (Radebaugh et al., 2007; Cook-Hallet et al., 2015; Liu et al., 2016a, 2016b), dune fields (Lorenz et al., 2006; Radebaugh et al., 2008), lakes and seas (Stofan et al., 2007; Mitri et al., 2007; Brown et al., 2008; Hayes et al., 2008), channels (Perron et al., 2006; Lorenz et al., 2008a; Burr et al., 2013a), putative cryovolcanism (Lopes et al., 2007, 2013; Le Corre et al., 2009; Mitri et al., 2019; Wood and Radebaugh, 2020), and other strikingly terrestrial-like features. Evidence for impact processes have also been identified, but their relative scarcity attest to a geologically young surface (Wood et al., 2010; Neish and Lorenz, 2012, Neish et al., 2013; Hedgepeth et al., 2020).

These familiar landforms inspire comparisons between terrestrial surface processes and processes currently or previously operating on Titan. A departure is found when considering their vastly different formation conditions. For example, Titan's surface is blanketed in organic materials, the result of long-term photochemical processing of methane and nitrogen in the upper atmosphere (e.g. Wilson and Atreya, 2004; Lavvas et al., 2008; Krasnopolsky, 2009). Titan's thick, nitrogen-dominated atmosphere allows for aeolian processes to shape the surface by transporting photochemically derived organic debris analogously to how silica or gypsum grains are transported on Earth (e.g. Barnes et al., 2015). Titan's equatorial zones are dominated by massive organic sand seas, whereas the mid-latitudes are dominated by "undifferentiated plains",

a terrain interpreted as either vast aeolian deposits (Lopes et al., 2016) or vast lag deposits (Birch et al., 2016).

Titan also exhibits an active hydrological cycle, one where the precipitating fluid is methane and dissolved nitrogen, as opposed to water (Lorenz, 1993, 2000; Atreya 2006; Hayes et al., 2018). Titan's surface temperature and pressure conditions are such that liquid methane is stable on the surface, and many observations suggest that liquid hydrocarbons have flowed energetically across Titan's surface, carving a variety of channel networks and fluvial valleys (Burr et al., 2009, 2013a, 2013b; Langhans et al., 2012; Birch et al., 2016; Radebaugh et al., 2018). Images taken from the Huygens probe, as it descended through Titan's atmosphere and after it landed, confirmed that liquids have modified the moon's surface, revealing a dense network of branching channels reminiscent of terrestrial river networks (Perron et al. 2006; Jaumann et al., 2008; Lunine and Lorenz, 2009; Langhans et al., 2012; Burr et al., 2013b). Numerous lakes and vast seas of liquid hydrocarbons are also found at high latitudes (Stofan et al., 2007; Mitri et al., 2007; Hayes et al., 2008; Birch et al., 2017).

In this paper, we describe our mapping of Titan's South Belet region and associated geomorphological terrain units. This region spans longitude 60°E to 120°E and from latitude 60°S to 0°, which includes part of the equatorial and mid-latitude region of the moon's southern hemisphere; our mapping thus characterizes the type and extent of terrains and geological processes representative of this locale. We used Cassini's RADAR data, acquired in the Synthetic Aperture Radar (SAR) mode as our basemap, supplemented by secondary datasets such as microwave emissivity and topography from RADAR-derived datasets, and infrared reflectance from the Imaging Science Subsystem (ISS) and the Visual and Infrared Mapping Spectrometer (VIMS) to provide additional constraints on our terrain assignment.

This study is a continuation of the detailed geomorphological mapping effort introduced in Malaska et al. (2016a). In Lopes et al. (2020), we present a global Titan map that is related to the detailed mapping of Malaska et al. (2016) and the work presented here, but at a coarser scale. The characterization and description of mapping units discussed in this paper will follow previously established conventions. We chose to follow up our detailed mapping of the Afekan Crater region with a detailed map of the South Belet region for several reason. First, the South Belet region, which spans Titan's equatorial and southern mid-latitudes, works as a natural corollary to the characterization of Titan's equatorial and northern mid-latitude regions performed with the Afekan map; questions of latitudinal dependence, symmetry, and regional variations can be readily investigated and expanded towards broader conclusions of Titan's geologic history. Second, this first detailed map of South Belet leads to the identification of new terrain units and to the discussion of previously unidentified geologic processes characteristic of the equatorial and mid-latitude regions. Third, South Belet features interaction between dune and non-dune units, especially at the sand sea boundaries, that allows for investigating the connection between these units, and can be compared to northern hemisphere mapping in Afekan.

4.2 Geologic Setting

The areal extent of South Belet amounts to 9.5×10^6 km^2, or 11.3 % of Titan's surface. SAR swaths provide 31.8% coverage of the region at high resolution (260-500 m/pixel), which accounts for about 3.6% of Titan's surface. From initial examination of the global map presented in Lopes et al., (2020), and much like the Afekan Crater region of Titan as discussed in Malaska et al. (2016a), South Belet appears typical of Titan's mid-latitude and equatorial regions. The region most notably contains the Belet Sand Sea, located on Titan's trailing hemisphere between

30°S and 25°N latitude and 60° and 120°E longitude, and is in a topographically low basin with an average elevation of approximately -300 m (Le Gall et al., 2011; Corlies et al., 2017). As mentioned, Belet is the largest sand sea on Titan, with an estimated area of 3.3 ± 0.6 million km^2 and estimated sand volume of 610,000 to 1,270,000 km^3 (Le Gall et al., 2011). The South Belet region contains one unnamed crater of suitable certainty (Hedgepeth et al., 2020). Like Titan's Afekan Crater region, South Belet's equatorial sand sea is in contact with large swaths of the featureless plains, where the transition from dunes to plains starts roughly at the 20°S latitude line. Lopes et al. (2020) shows that plains dominate Titan's mid-latitudes globally; the conspicuous lack of SAR coverage beyond this latitude line (notably from 25°S to 60°S; see Fig. 4.2) may result in the underestimation of the total area of the plains (and associated subunits) in this region.

The detailed mapping was predominately performed using the SAR dataset on areas where coverage is available. We follow the procedure described in Malaska et al. (2016a) and distinguish between discrete units based on radar backscatter and overall morphology. We also considered feature geometry, sharpness of boundaries, internal texture, degree of dissection, and overall context when ultimately assigning a terrain classification. Differences in Cassini SAR images represent differences in signal returned to the spacecraft. The returned signal, or "backscatter", can be a result of a change to any of a number of properties, such as incidence angle of the beam, slope angle orthogonal to the beam, surface roughness, volume scattering, structural properties, subsurface inhomogeneities, and dielectric constant of the material. A

difference in backscatter can be a result of a change to any one of these properties. Other RADAR modes, such as radiometry (e.g., Wye et al., 2007; Janssen et al., 2009; 2011; 2016) and altimetry (e.g., Kirk et al., 2005; Stiles et al., 2009), provide supplementary information about the surface. We use data from these modes, in addition to observations of visual reflectance from ISS and infrared from VIMS, to further refine our mapping delineations and make final terrain assignments.

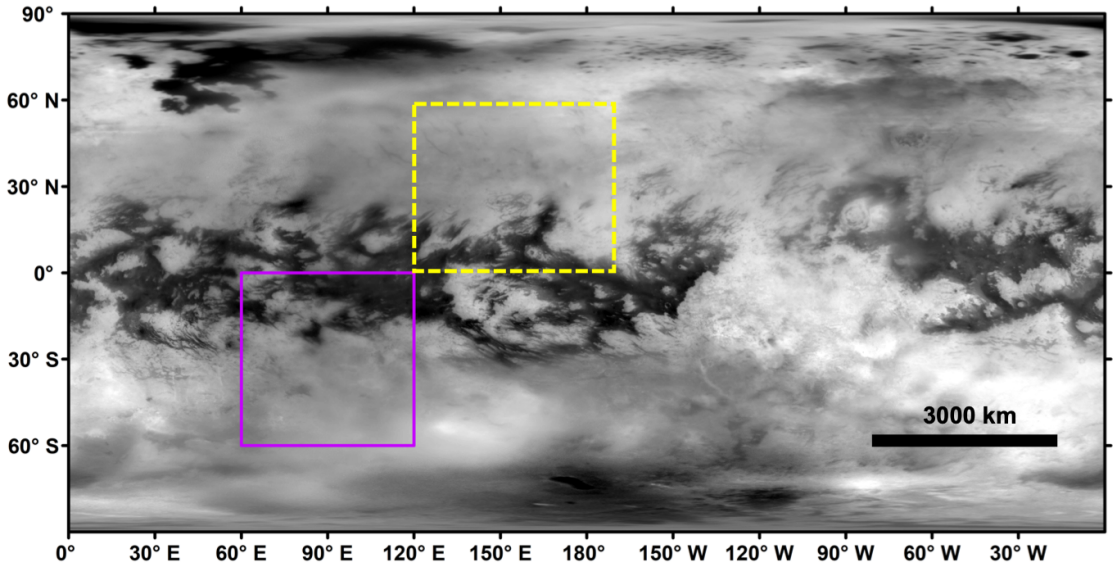

Fig. 4.1 Global context of the South Belet Region (purple box) on an Imaging Science Subsystem (ISS) mosaic (Karkoschka et al., 2017, LPSC). The Afekan Crater region (Malaska et al., 2016a) is also indicated for reference (yellow, dashed box).

4.3 Methods

4.3.1 Datasets and Instruments

4.3.1.1. SAR

Due to the absorptive and scattering nature of Titan's atmosphere, the efficacy of detailed visual and infrared spectro-imaging, normally used in planetary remote sensing, is limited. Methane absorbs mostly in the infrared, while Titan's haze layers scatter light at the visible to near-infrared parts of the spectrum. As a result, the multimode RADAR instrument (Ku-band, 13.78 GHz, λ=2.17 cm; Elachi et al., 2005a, 2006) was the main instrument used to study Titan's geomorphology. We used data from the SAR mode as our primary basemap, using backscatter return to define the boundaries and create the main categorization schema for our terrain units.

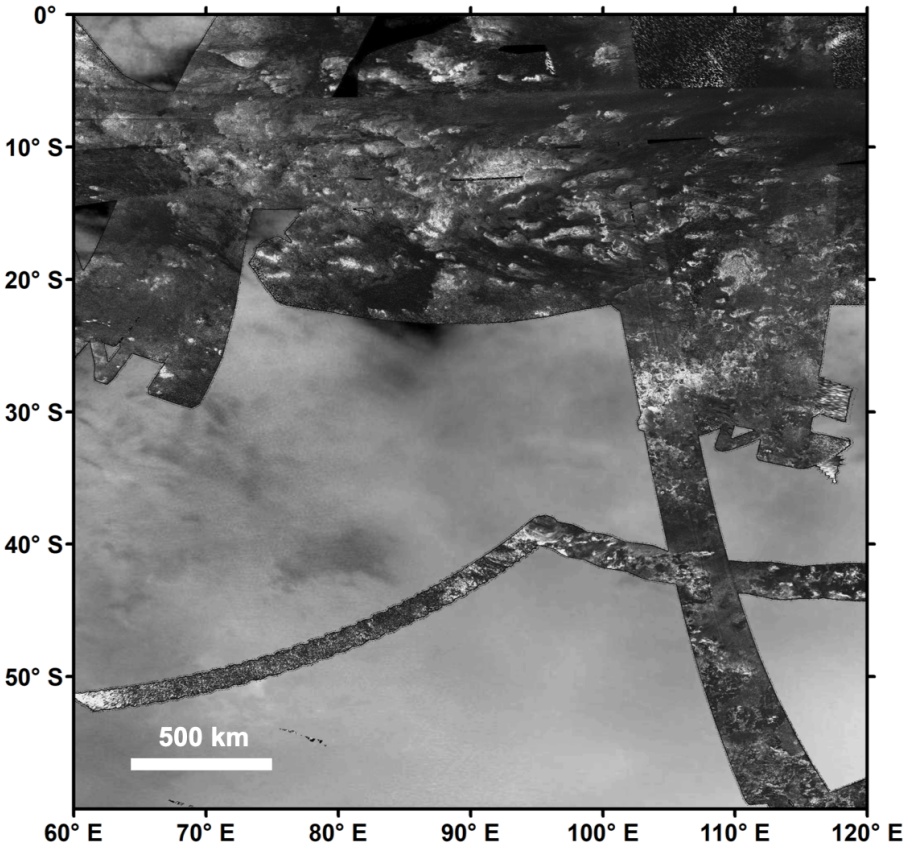

Fig. 4.2 The South Belet Region as seen in our SAR mosaic base map. The SAR mosaic is superposed on a globally controlled ISS mosaic. See text for details.

The SAR mode operates mostly at altitudes under ~4000 km, yielding image resolutions from 260 m/pixel to 500 m/pixel, with the best resolution acquired in the center of the swath during closest approach. SAR data cover about 46% of Titan's surface at less than 1 km resolution, while the higher-altitude SAR data cover an additional 24% at less than 5 km resolution (Lopes et al., 2020). Each swath is 120 to 450 km wide, and 1000 to 5000 km long. For mapping purposes, we used incidence angle corrected SAR swaths to minimize geometric variations. A SAR mosaic of the South Belet region is shown in Fig. 4.2, and includes SAR swaths from flyby's T8, T19, T21, T49, T50, T57, T61, T84, and T92. Materials having high-backscatter appear lighter in the images, while materials having low-backscatter appear darker.

4.3.1.2. Topography

Topographic information can be obtained from overlapping SAR beams by SARTopo (Stiles et al. 2009). SARTopo provides 1 to 3 profile strips per SAR pass. Each strip is 10 km wide and thousands of kilometers long with vertical uncertainties of < 75 m. Relative elevation information is, in general, only valid along the same SARTopo strip, and thus we refrain from comparing strips generated from different SAR swaths. The Cassini RADAR instrument also had a dedicated altimetry mode that provided limited, but higher-resolution (~35 m), elevation data. However, altimetry cannot be obtained simultaneously with SAR and thus covers relatively small segments of the surface. For our purposes, we use an updated topographic map of Titan generated by Corlies et al. (2017) that includes all SARTopo, altimetry, and stereophotogrammetry topographic data available at the end of the Cassini mission. A SAR mosaic coverage with superimposed SARTopo strips for South Belet is shown in Fig. 4.3.

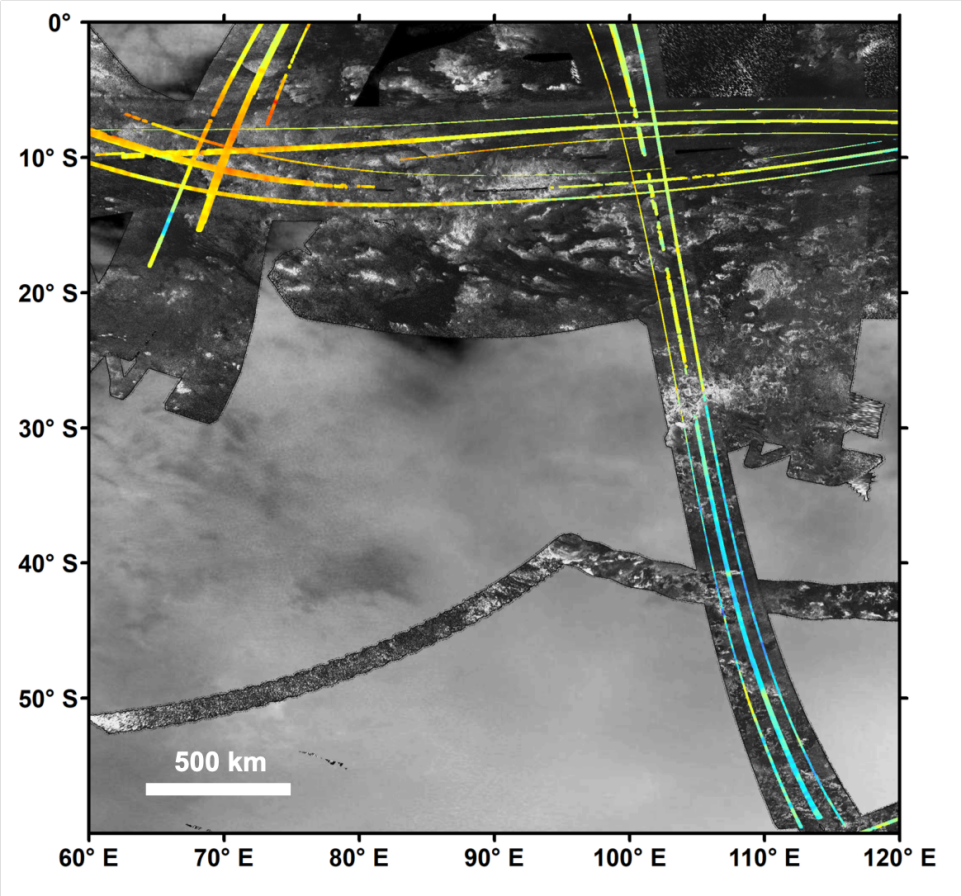

Fig. 4.3 SAR plus ISS mosaic with SARTopo overlay for the South Belet Region with data obtained from Corlies et al. (2017).

4.3.1.3. Emissivity

The RADAR instrument had a passive radiometry mode that measured the brightness temperature of the surface of Titan (Janssen et al. 2009, 2016). The brightness temperature is converted to emissivity (E) using Titan's surface temperature (~95 K in the equatorial regions) (Fulchignoni et al., 2005; Jennings et al., 2016). Radiometry resolution varies from 5 to 500 km, with higher resolution data corresponding directly to SAR swaths (i.e. when the spacecraft was closest to Titan). Materials having low emissivity are interpreted as fractured water ice, whereas materials having high emissivity are interpreted as organic (Janssen et al., 2016). An emissivity map of the South Belet region is shown in Fig. 4.4.

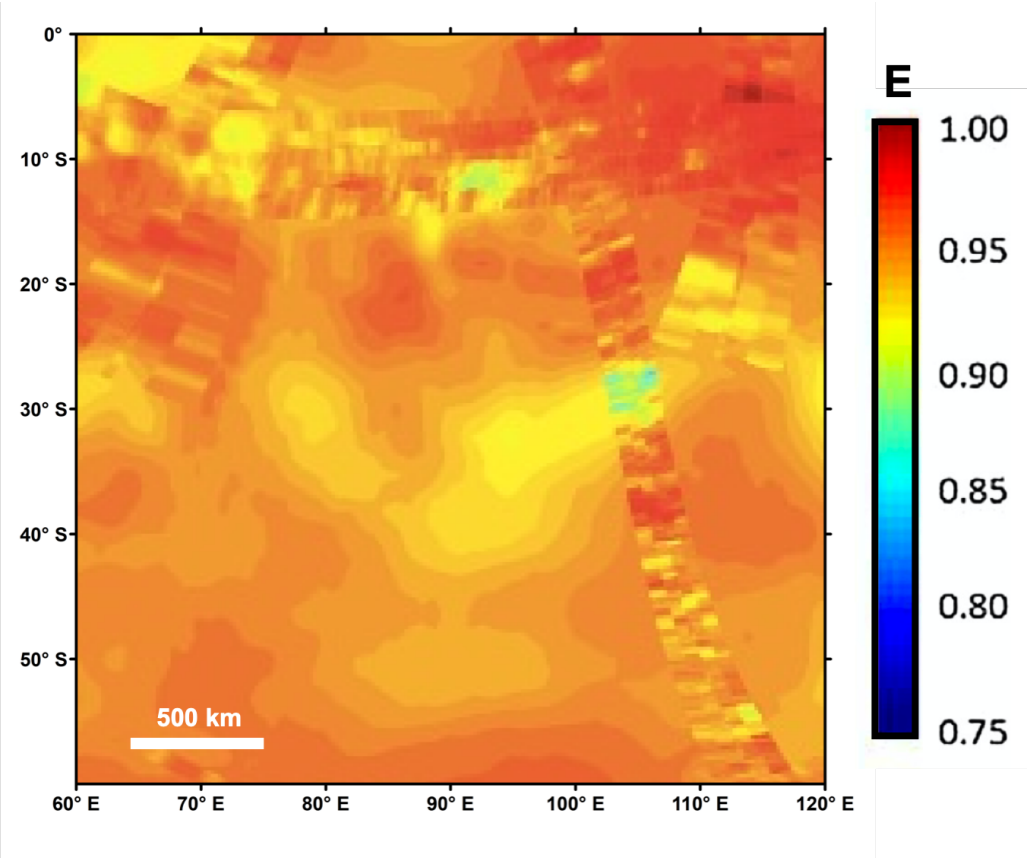

Fig. 4.4 Emissivity map of the South Belet region. From Janssen et al. (2016).

4.3.1.4. ISS and VIMS

Cassini's Imaging Science Subsystem (Porco et al., 2004) had Wide and Narrow Angle Cameras that included 0.938-micron filters and infrared polarizing filters capable of imaging Titan's surface through an atmospheric transmission window. At best, the theoretical spatial resolution of these images is several hundred meters, but this theoretical resolution is severely degraded by the strong scattering of the atmosphere. We used a global controlled and corrected

ISS mosaic at ~ 1km resampled pixel-scale for our mapping (Karkoschka et al., 2017, LPSC; Fig. 4.5).

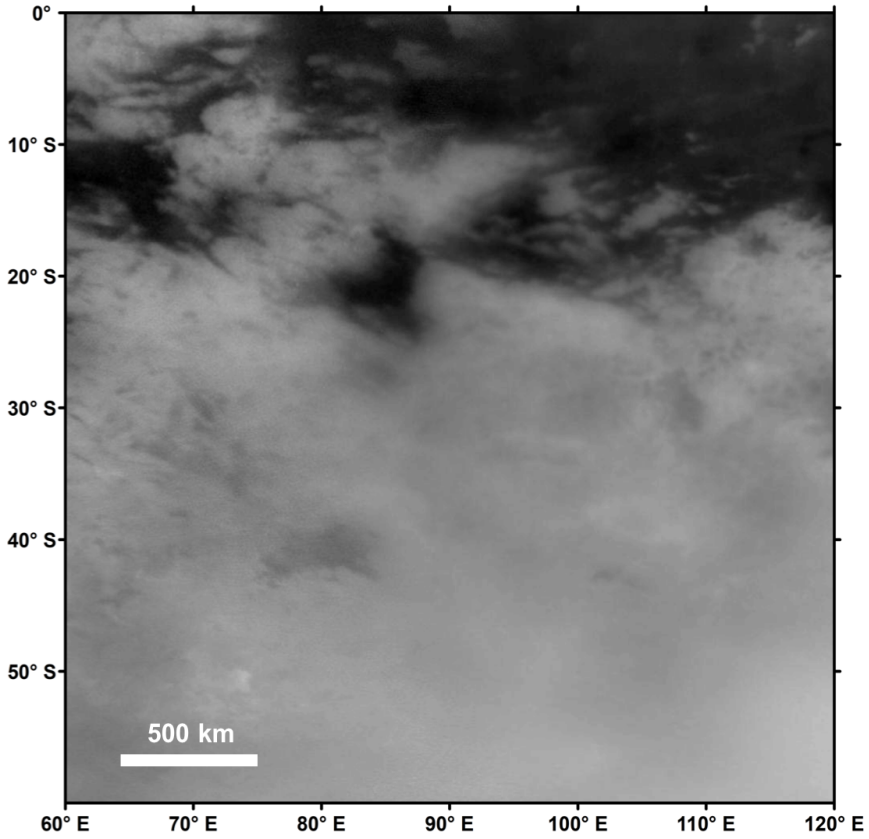

Fig. 4.5 ISS mosaic of the South Belet region.

Cassini's VIMS instrument (Brown et al., 2004) was a hyperspectral mapping spectrometer that then observed Titan's surface through atmospheric transmission windows at 0.94, 1.08, 1.28, 1.58, 2.03, 2.69, 2.79, and 5.0 microns (Sotin et al., 2005; Barnes et al., 2007a). VIMS data provide constraints on the composition of the surface (e.g., Soderblom et al., 2007; Brown et al., 2008; Clark et al., 2010; Solomonidou et al., 2014; 2018; 2020a; Brossier et al., 2018; Griffith et al., 2019). VIMS pixel-scale typically ranges from a 0.5 km to tens of km, but only 5% of the surface was observed by VIMS at a resolution of < 5 km/pixel (Le Mouélic et al., 2019). For a very small number of targeted areas observed during closest approach, the scale can

be as high as 500 m/pixel (Jaumann et al., 2009). The global VIMS mosaic described in Le Mouélic et al. (2019) and locally merged with ISS (Seignovert et al., 2019), cropped for South Belet, is shown in Fig. 4.6.

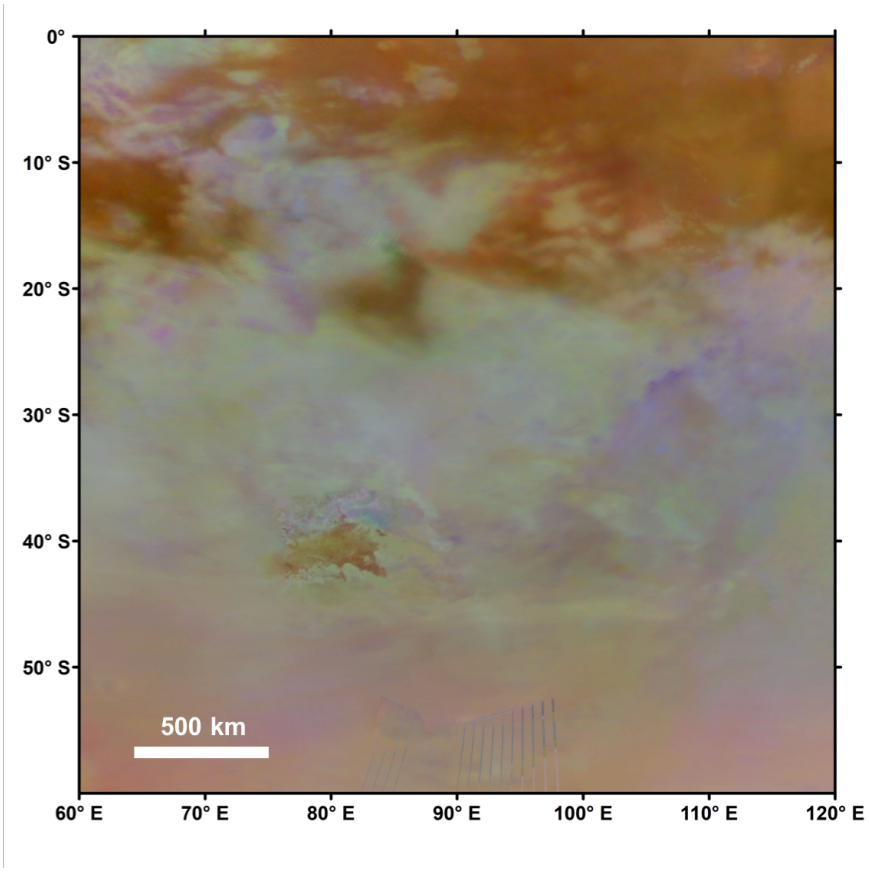

Fig. 4.6 VIMS mosaic of South Belet. The mosaic is made from a combination of a VIMS haze corrected dataset (at first order, see Le Mouélic et al., 2019) and ISS (from Seignovert et al., 2019). RGB composite is 1.59/1.27 µm (red), 2.03/1.27 (green) and 1.27/1.08 µm (blue) corrected from atmospheric scattering as described in Le Mouélic et al. (2019).

4.3.2. Mapping Technique

SAR mosaics were loaded into ArcGIS™ 10.6 (ESRI) software package, then used as the base layer data for morphological classification. We drew contacts between terrains of different

radar backscatter or morphological texture. We determined terrain boundaries following previous studies (e.g., Stofan et al., 2007; Lopes et al., 2010; Williams et al., 2011; Malaska et al. 2016a). In general, we only use the higher-resolution SAR swaths for mapping and mapped at an image scale of 1:800,000 (Greeley and Batson, 1990). However, in certain areas, HiSAR (a high-altitude SAR imaging mode with km to multi-km scale resolution) of sufficient quality was included in the base map and used for mapping. We determined if a HiSAR swath was of suitable quality based on the capacity to distinguish terrain units with the same level of detail as with a regular SAR swath. For example, a HiSAR swath was included in our mapping if we were able to distinguish between "undifferentiated plains", "variable featured plains", "hummocky", and "linear" or "featureless" dunes; an example area mapped with HiSAR is centered on 18.1°S, 89.5°E. In total, 4.6% of the mapped area was done so with HiSAR. SAR or HiSAR swaths that were too low resolution, either because of noise or large pixel-scale, were not used for primary identification. We defined gradational contacts between units if a clear delineation could not be made at the resolution of the SAR images. Polygons were generated from the drawn contacts using ArcGIS functionalities; these polygons were then assigned a terrain unit classification based on feature morphology and radar backscatter. Data from SARTopo, radiometry, ISS, and VIMS were used to refine terrain classification as outlined in Malaska et al. (2016a).

4.4. Description of Map Units

The terrain classes and units in the South Belet region were identified using the SAR mosaic basemap. While there are six major terrain classes on Titan, four of these are found in the South Belet region. These are: plains, dunes, hummocky/mountains, and craters. We did not observe any terrain units belonging to the Lake and Basin or Labyrinth terrain classes. Each

terrain class was subdivided into terrain units by characteristic morphology (texture, border geometry, and general appearance) and radar backscatter. Radar backscatter is broadly classified as “high”, “medium”, “low”, and in some cases as “variable”. Physical features such as crater rims and channels were added as separate polyline layers to our map. Channel mapping is based on procedure described in Burr et al. (2013a). The map is shown in Fig. 4.7, and a graphic of physical features is shown in Fig. 4.8.

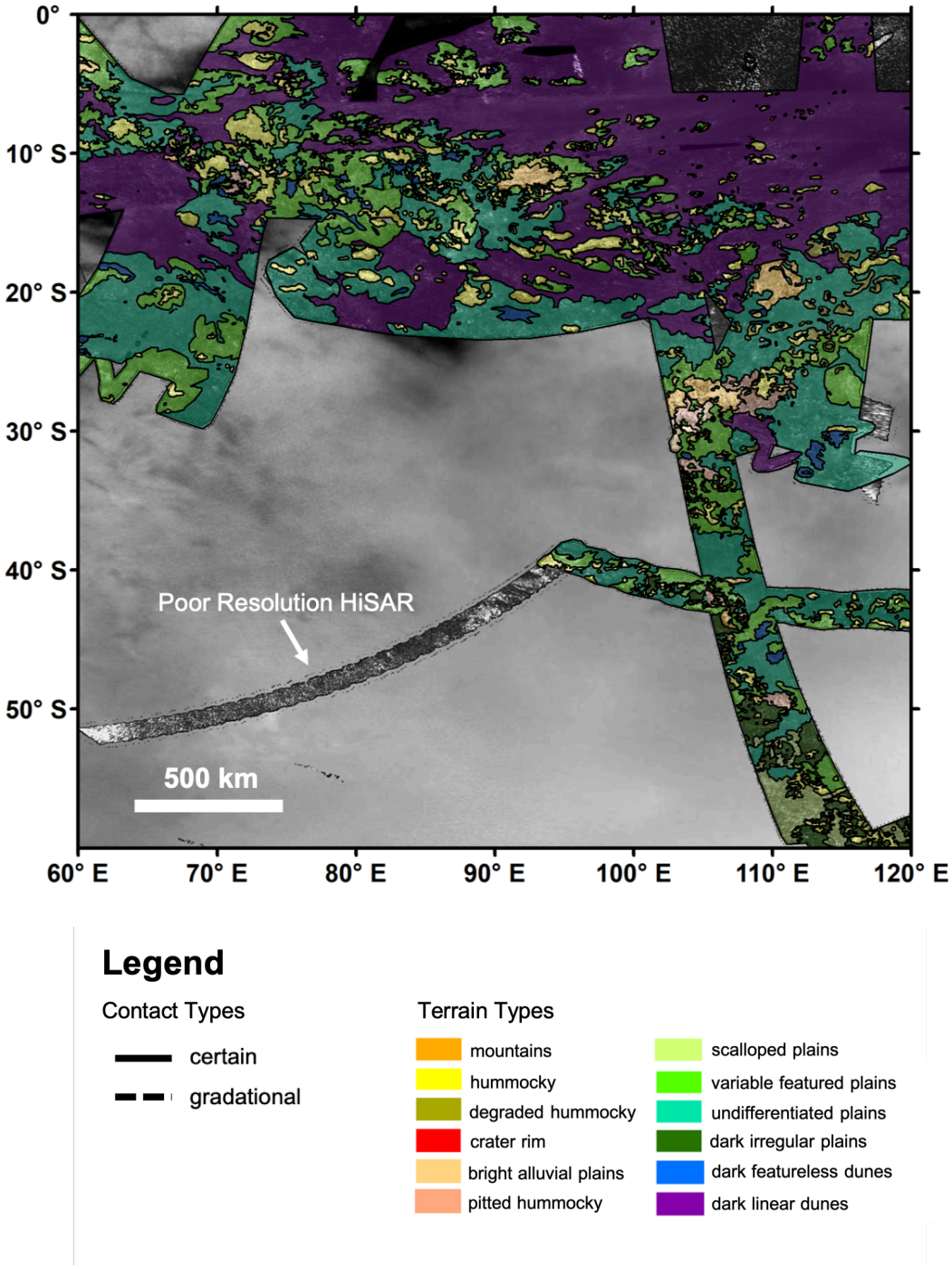

Fig. 4.7 Geomorphological map of the South Belet region, including the major geomorphological units.

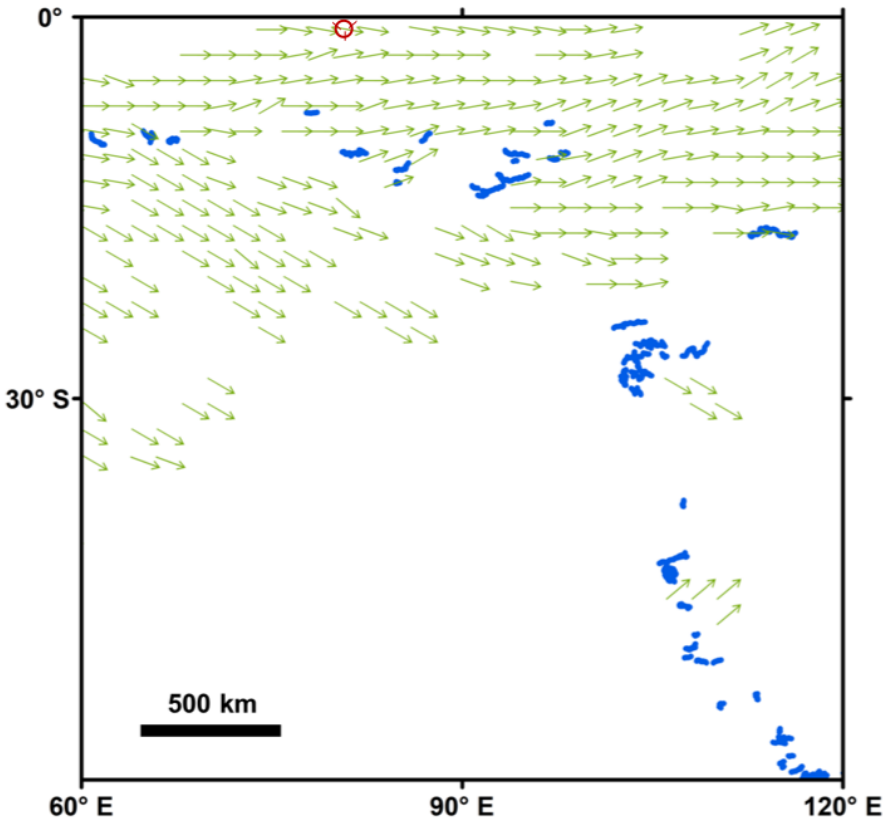

Fig. 4.8 Potential valleys, channels, and crater rims of the South Belet region and possible material transfer on the surface. The green arrows represent inferred material transport directions from Malaska et al. (2016b). Blue lines indicate valley and channels, while red solid circles indicate crater rims, respectively.

Many of the units identified in the South Belet map are described in detail in Malaska et al. (2016a) and have been used for the VIMS analysis of various Titan areas in Solomonidou et al. (2018); rather than repeat those descriptions here, we provide a summary in Table 4.1. The three-letter terrain unit abbreviations refer to the broad terrain class (e.g., p for plains), a descriptor letter for the terrain type (e.g., u for undifferentiated), and a letter indicative of relative radar backscatter (e.g., l for low) (Malaska et al., 2016a). We also present local examples for each unit in SAR, which are shown in Fig. 4.9.

Table 4.1 Terrain units identified in Titan's South Belet region. Unit description and interpretations, with the exception of *hph* and *pah*, summarized from Malaska et al. (2016a). The three-letter terrain unit abbreviations refer to the broad terrain class (e.g., p for plains), a descriptor letter for the terrain type (e.g., u for undifferentiated), and a letter indicative of relative radar backscatter (e.g., l for low).

Terrain class	Terrain Unit Name	Terrain Unit Code	Local type location	Terrain Unit Description	Interpretation
Crater	Crater rim	*crh*	0.023°N, 79.51°W	High-backscatter hummocky or mountainous terrain in a circle with clear dissection on inside edge	Impact crater rim
	Crater ejecta	*ceh*	0.039°S, 80.03°E	Rough, radar-bright to radar-medium material that grades away	Impact crater ejecta

				radially from a rim	
Mountains/Hummocky	Mountain	*hm*	11.55°S, 92.52°E	Elongated features with evident SAR bright/dark pairing	Rugged mountainous areas of ancient crust
	Hummocky	*hh*	3.54°S, 72.72°E	Radar-bright "blob" like exposures; unclear bright/dark pairing	Highland areas of ancient crust
	Degraded hummocky	*hdm*	19.57°S, 116.56°E	Small exposures of hummocky-like materials with comparatively lower backscatter return	Small remnants of hummocky terrains eroded or partially buried by organics

	Pitted hummocky	*hph*	11.7°S, 71.4°E.	Radar-bright hummocks populated by radar-dark, pit-like structures	Fine grained, low backscatter materials deposited in pre-existing depressions in the exposed icy crust
Plains	Bright alluvial deposit	*pah*	28.23°S, 105.01°E	Radar-bright, triangular shaped regions typically found at the terminus of channel; backscatter decreases away from apex of triangle	Alluvial deposits originating from fluvial activity

Undifferentiated plains	*pul*	22.85°S, 65.78°E	Low backscatter nearly featureless plains; most extensive unit on Titan, dominate the mid-latitudes	Deposits of organic, aeolian-transported materials
Variable featured plains	*pfv*	13.21°S, 74.48°E	Plains of variable backscatter, with characteristic internal texture. Terminates at diffuse boundaries.	Deposits of eroded materials from mountain and hummocky units
Dark irregular plains	*pil*	50.97°S, 108.63°E	Irregular patches of radar-dark, lobate terrain	Low-lying basins dampened by

				set in a low-to-medium backscatter substrate	liquids or muds
	Scalloped plains	*psv*	56.85°S, 111.45°E	Extensive units mostly at high latitudes; medium backscatter, with scalloped borders and patchy internal structure	Eroded hummocky terrains partially covered by organic materials or potentially evaporitic remnants of previously filled lake basins
Dunes	Featureless sand sheets	*ds*	11.93°S, 84.32°E	Featureless radar-dark areas extending in patches consistent	Sand deposits that may contain dune structures below the

			with aeolian transport direction	resolution of radar
Linear dunes	*dl*	7.64°S, 93.03°E	Parallel to sub-parallel radar-dark lineations on a variable backscatter substrate	Dunes, mostly longitudinal, composed of organic materials

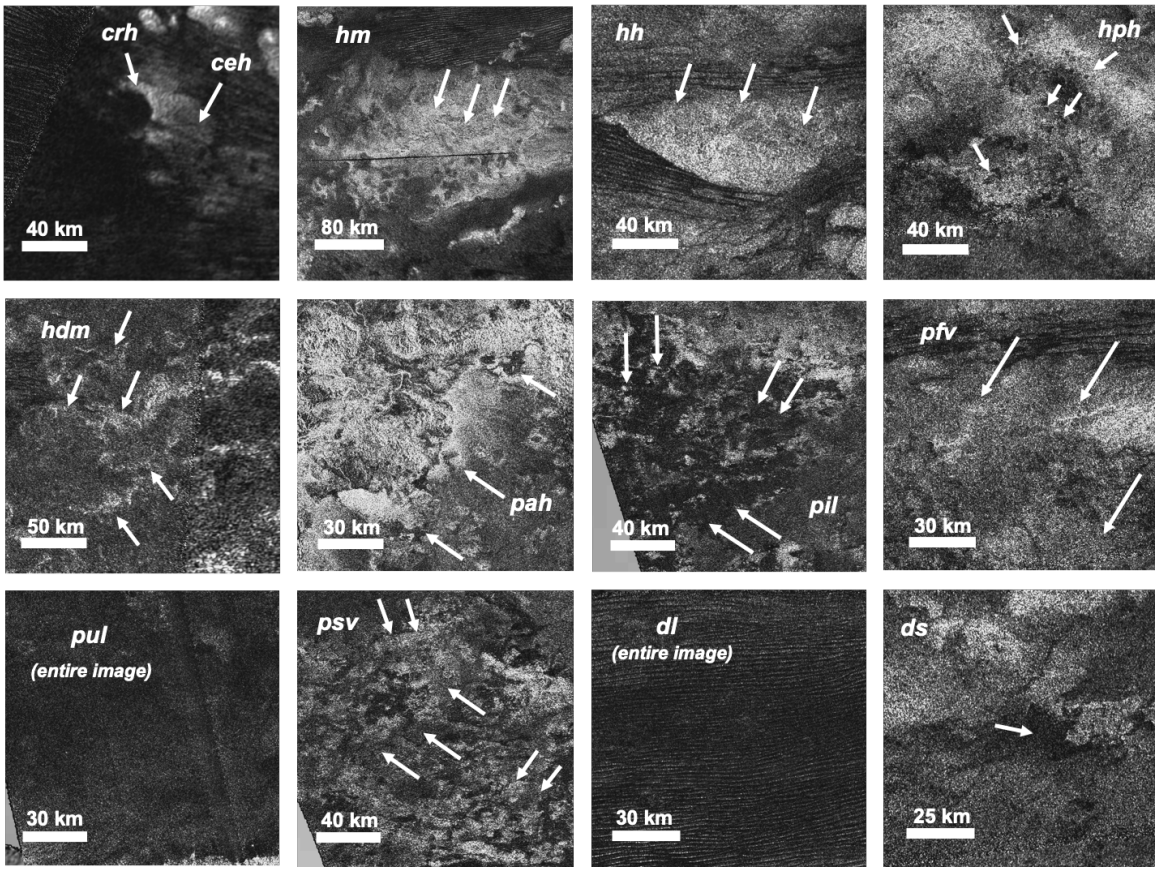

Fig. 4.9 Example of units identified in South Belet, presented as SAR images. White arrows point to the representative feature. With the exception of the *pah* and *hph* units, all units, including local type examples, are previously discussed in Malaska et al. (2016a). Units are: *crh* = crater rim, *ceh* = crater ejecta, *hm* = mountain, *hh* = hummocky, *hph* = pitted hummocky, *hdm* = degraded hummocky, *pah* = bright alluvial plains, *pil* = dark irregular plains, *pfv* = variable featured plains, *pul* = undifferentiated plains, *psv* = scalloped plains, *dl* = linear dunes, *ds* = featureless sand sheets.

There are two terrain units that were not included in Malaska et al. (2016a) that were identified in our mapping of South Belet. In the following section we describe and discuss these terrain units.

4.4.1 Bright Alluvial Plains (pah)

Description. The bright alluvial plains (*pah*) are radar bright, triangular shaped features typically found at the terminus of observable channel structure (Fig. 4.10). These features have sharp to diffuse boundaries, with backscatter tending to decrease away from the apex of the triangle. These regions have low emissivity, much lower than other plains units like variable (*pfv*), undifferentiated (*pul*), and scalloped (*psv*). In some cases, the *pah* unit appears to have microwave emissivity characteristics similar to the mountain/hummocky units. They are more commonly found at higher latitudes and are commonly associated with nearby mountainous terrain or other local topographic highs. *Type area:* 28.6°S, 105.2°E.

Interpretation. These features are interpreted as alluvial deposits of high backscatter materials emplaced by fluvial activity. A global survey of Titan's alluvial fans is given in Birch et al. (2016) and Radebaugh et al. (2018) and includes the fans identified here. Fans on Earth similarly show higher backscatter compared to their surroundings as well as radar darkening away from the fan apex (Schaber et al., 1976; Birch et al., 2016). High backscatter of the fans in SAR images may be due to either grains with a size comparable to the SAR wavelength, 2.17 cm (Le Gall et al., 2010; Schaber et al., 1976), or to high porosity in the top few meters of the deposit causing additional scattering (Birch et al., 2016). Grains (pebbles and cobbles) of this size were imaged at the Huygens landing site (Tomasko et al., 2005).

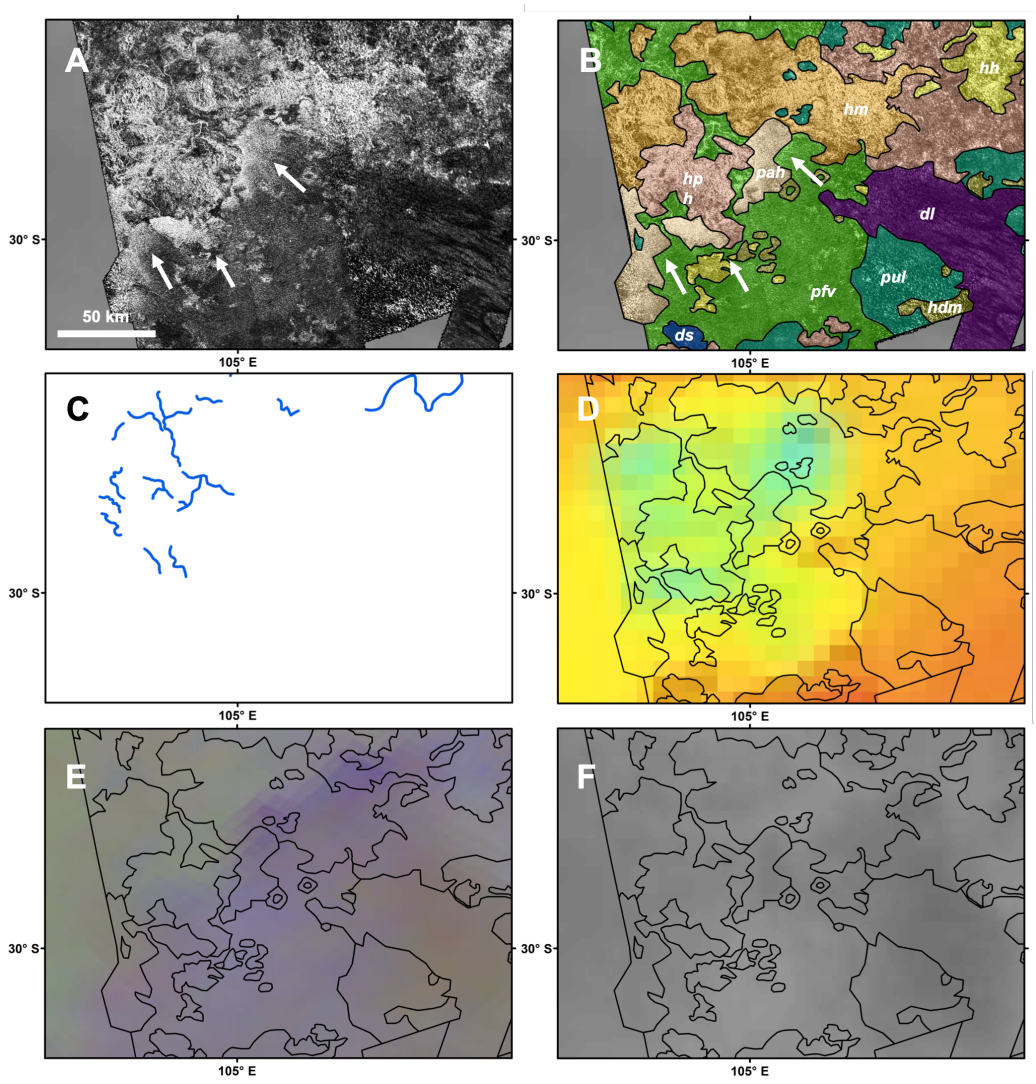

Fig. 4.10 Instances of bright alluvial plains (28.6°S, 105.2°E): (A) SAR mosaic, bright alluvial plains indicated by white arrows. (B) Annotated terrain unit mapping on the SAR mosaic. (C) Channels that terminate in the bright alluvial plains indicated via a blue line (detail from Fig. 4.8). (D) Emissivity map with contacts between terrain units shown. See Fig. 4.4 for color scale. (E) VIMS RGB mosaic with contacts between terrain units outlined. (F) ISS mosaic with contacts between terrain units shown.

The low microwave emissivity response (Fig. 4.10d) is likewise consistent with volume scattering from subsurface inhomogeneities (Paganelli et al., 2008), such as a loosely

consolidated mix of water ice and organic sediments. Both the VIMS and ISS maps (though more pronounced in VIMS) show albedo differences between the area southeast of the mountainous unit (*hm*) and adjacent terrain (Fig. 4.10e,f). This area corresponds to the location of the bright alluvial plains and the channels. The dark-blue unit in VIMS has been associated with channels (e.g. Barnes et al., 2007b; Langhhans et al., 2012). We thus find that the VIMS observation may be showing an "icy sediment" transport direction for the highlighted region, consistent with the presence of the channels and alluvial plain unit. Similarly, Brossier et al. (2018) recently showed trends in water ice content and grain size properties of the VIMS blue unit within transition zones between infrared bright-blue-brown units that support the fluvial origin of these deposits.

4.4.2 Pitted Hummocky (*hpm*)

Description. Pitted hummocky terrain (*hpm*) units are similar to hummocky (*hh*) terrain in that they are high-backscatter areas with rounded boundaries and internal textures varying from uniform to "lumpy". They are different from hummocky terrains in that they are "pitted" by dark circular features 1 to 6 km in diameter (Fig. 4.11). However, smaller, sub-resolution pits may be present. A pitted hummocky feature maybe be partially or completely marked by these dark features. The microwave emissivity is somewhat higher than that of the hummocky terrain unit (*hh*), but lower than the surrounding plain units, and the SARTopo is consistent with these being terrains that are locally elevated. Similar features of this specific morphology (Fig. 4.11f), assumed to be depressions or pits, were first identified by Lopes et al. (2007) within Cassini's T8 swath. *Type area:* 11.7°S, 71.4°E.

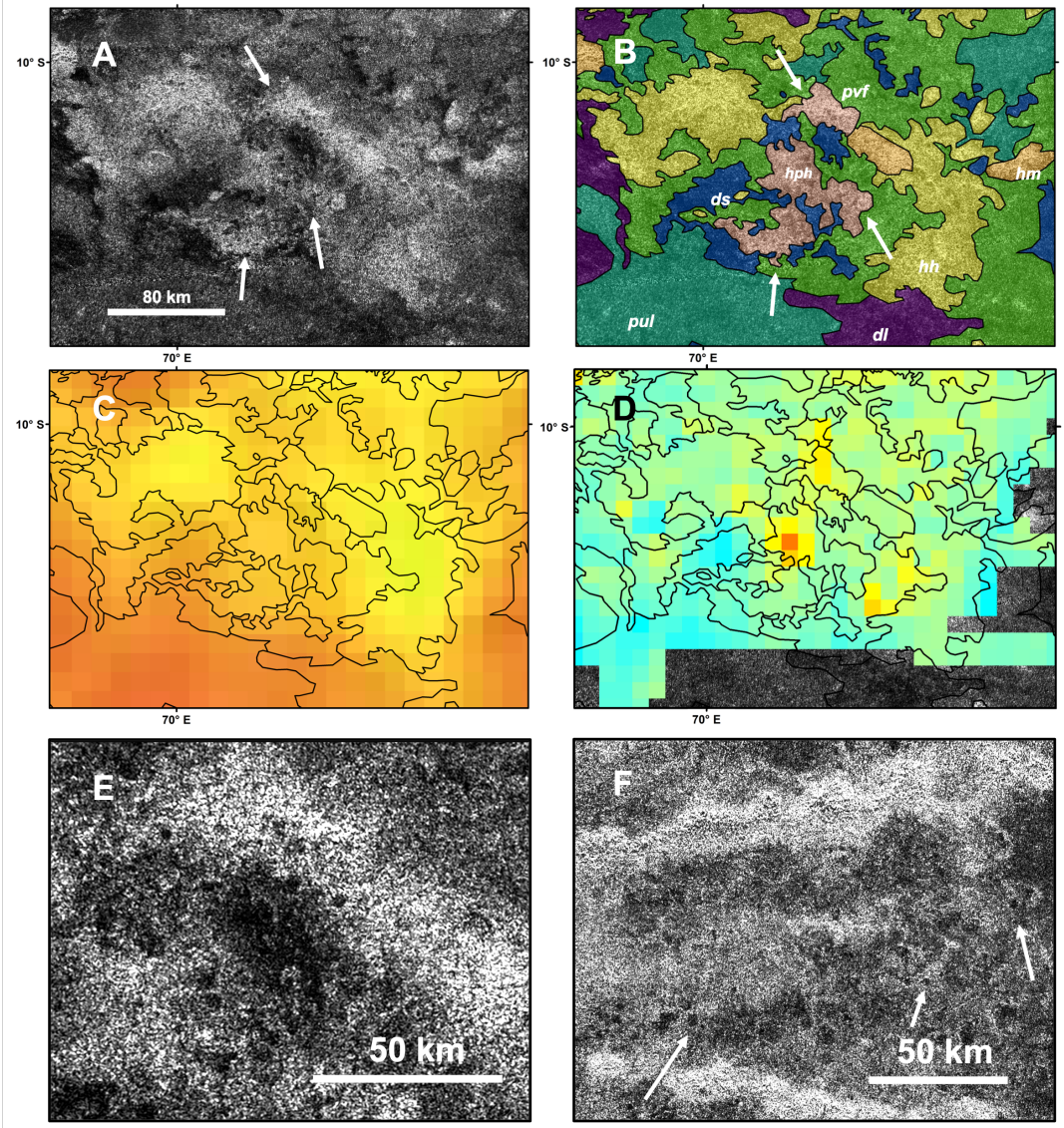

Fig. 4.11 Example of pitted hummocky terrain (*hph*) (11.7°S, 71.4°E): (A) SAR mosaic, pitted hummocks indicated via white arrows. (B) Annotated terrain unit mapping on a SAR mosaic. (C) Emissivity map overlain with contacts between terrain units. See Fig. 4.4 for color scale. (D) Topography of the pitted hummocky terrain interpolated from closely overlapping SARTopo bands. (E) Zoom-in on the pitted hummocky patch indicated by the topmost white arrow in A. (F) SAR mosaic of pitted hummocky terrain (*hph*) in Adiri, indicated by white arrows (8.8°S, 138.8°E).

Interpretation. We interpret this unit as elevated areas of ancient crust, similar to our interpretation of the hummocky terrain unit. However, we speculate that the dark quasi-circular features within these exposures are topographic depressions filled with low backscatter materials, though we have no detailed topographic information that supports this. The microwave emissivity data of this terrain is similar to that of the hummocky terrain and suggests that the pitted hummocky terrains consist of fractured water ice or water ice and organic material mixtures. It is not possible, given the resolution of the microwave emissivity dataset, to determine if the dark pits are radiometrically distinct from their host hummocky structures. In addition, the low resolution of VIMS compared to the other data does not allow for an individual study of the dark quasi-circular features. The topographic expression of the pits likewise cannot be resolved given the resolution of the SARTopo data. A more detailed discussion of the pits, including possible formation scenarios, is explored in section 4.5.5.

4.5. Geologic Synthesis

4.5.1 Comparing South Belet to Afekan and the Global Map

Table 4.2 quantifies the mapping done in South Belet, and table 4.3 compares the areal extent of the terrain units in South Belet to Afekan and to the global map. Much like in the case of the Afekan region, our mapping shows that plains are the most widespread type of terrain unit in South Belet, comprising 46.6% of the mapped area (Table 4.2). Unlike Afekan, the dunes closely rival the dominance of plains, making up 43.0% of the mapped area. The areal extent of dunes for Afekan (18.6%) is comparable to the spatial extent of dunes from the global map (17.0%), making South Belet uncharacteristically dominated by dune units. However, this may

be an observational bias caused by lack of SAR coverage beyond South Belet's equatorial belt, underrepresenting the plains units that are more likely to be found south of the 30-degree latitude line. At the same time, South Belet hosts a large portion of the Belet Sand Sea, so it is reasonable to expect a larger representation of the dune units.

The next most prominent unit are the mountains/hummocky terrains (10.4%), percent-wise similar to Afekan (11.5%) and the global map (14.0%). And finally, the crater terrain units (0.01%) are the least prominent unit in South Belet. There are no labyrinth units identified in South Belet, whereas labyrinths make up 2.3% of area coverage in Afekan, and 1.5% areal coverage of the global map. South Belet also contains no basin and lake units. The Malaska et al. (2016a) paper reported no basin and lake units in Afekan. However, after reevaluating the map post-publication, we revised mapping in the higher latitudes to include "sharp-edged depressions" (*bse*) and have since identified 5 *bse* units within existing units, mainly the undifferentiated plains and the scalloped plains.

Table 4.2 Terrain unit statistics in the South Belet region.

Terrain class	**Terrain Unit Name**	**Total Area (km^2)**	**Number of Feature**	**Average Size (km^2)**	**% of mapped area**	**% mapped of each class**
Crater	Crater rim (*crh*)	78	2	39	<0.1	0.01
	Crater ejecta (*ceh*)	213	2	106	<0.1	

Mountains/hummocky	Mountain (*hm*)	50,160	25	2,006	1.6	10.36
	Hummocky(*hh*)	251,347	582	431.87	8.1	
	Degraded hummocky (*hdm*)	19,747	88	224	0.6	
	Pitted hummocky (*hph*)	779	3	260	<0.1	
Plains	Bright alluvial deposit	2,841	2	1,420	0.1	46.63
	Undifferentiated plains	852,917	99	8,615	27.5	
	Variable featured plains	521,826	221	2,361	16.8	
	Dark irregular plains	38,774	69	38,774	1.3	
	Scalloped plains	25,278	8	3,160	0.8	
Dunes	Featureless sand sheets	47,207	110	429	1.5	43
	Linear dunes	1,286,125	16	80,383	41.5	

Table 4.3 Percentage of areal extent of units in South Belet compared to Afekan (Malaska et al., 2016a) and the global map (Lopes et al., 2020).

Terrain Unit	**South Belet**	**Afekan**	**Global Map**
Crater	*<0.1*	*0.8*	*0.4*
Crater rim (crh)	<0.1	0.3	
Crater ejecta (ceh)	<0.1	0.5	
Crater fill 2	-	<0.1	
Crater fill 1	-	<0.1	
Central peak	-	<0.1	
Hummocky	*10.36*	*11.5*	*14*
Mountain (hm)	1.6	4.2	
Hummocky (hh)	8.1	4.9	
Degraded hummocky (hdm)	0.6	1.3	
Pitted hummocky (hph)	0.1	-	
Cross-cut hummocky	-	1.1	
Labyrinth	-	*2.3*	*1.5*
Plains	*46.63*	*66.8*	*65*
Bright alluvial deposit	0.1	-	
Undifferentiated plains	27.5	46	
Variable featured plains	16.8	13.4	
Dark irregular plains	1.3	0.5	

Scalloped plains	0.8	1.5	
Lineated Plains	-	0.4	
Dunes	*43.0*	*18.6*	*17*
Featureless sand sheets	1.5	2.2	
Linear dunes	41.5	16.1	
Reticulated dunes	-	0.3	

In South Belet, the undifferentiated plains (*pul*) comprise 27.5% of the entire mapped area and are spatially the most dominant of the plain units, though not as dominant as the undifferentiated plains in Afekan, which comprise 46.0% of the entire area in that region. Variable featured plains (*pfv*) are the second most widespread plains unit, making up 16.8% of the entire mapped area, followed by "dark irregular plains" (*pil*; 1.3%), "scalloped plains" (*psv*; 0.8%), and then "bright alluvial deposit" (*pah*; 0.1%). "Lineated plains" (*plh*) and "streak-like plains" (*psh*), which were identified in Afekan, are not seen in South Belet. In the case of the dunes units, linear dunes (*dl*), primarily from the Belet dune seas, make up the majority (41.5%), whereas featureless sand sheets (*ds*) covers a relatively small area (1.5%). There were no mapped occurrences of the reticulated dune units (*dt*), whereas 0.3% of mapped dunes in Afekan are reticulated.

The hummocky (*hh*) unit (582 identified) make up the bulk of terrain exposures. Variable feature plains (*pfv*) were also widespread (221 identified), followed by featureless sand sheets (*ds*; 110 identified). Hummocky terrain units are widespread yet fairly small in areal extent, with an average size under 500 km^2. However, the linear dunes, mainly part of the contiguous Belet

sand sea, are extensive, with the average size of an individually mapped dune area being roughly 81,000 km^2 (about 1 ½ times larger than the average size of linear dune terrain units in Afekan). The average size of an individual unit of undifferentiated plains (~ 8600 km^2, compared to 21,000 km^2 for Afekan) may be an underestimate, especially because greater radar coverage in the southern half of the South Belet region would likely connect isolated units in individual swaths into larger expanses of the unit.

Crater units, limited to crater rim and ejecta, comprise less than 0.1% of the mapped surface in South Belet, compared to 0.8% for Afekan. Crater units are interpreted as the direct result of impact processes. Previous work (Werynski et al., 2019; Solomonidou et al., 2020a) suggests that evidence of impacts have been erased by other geological processes, likely those that form dunes and plains. When compared to Afekan, which features 17 exposures of crater related units, South Belet is particularly deficient, featuring only 4. This is likely owing to both spatial coverage bias (especially in areas away from dunes) and burial or fill potential within the Belet sand sea (e.g. Neish et al., 2013; Hedgepeth et al., 2020). While it is possible to use the ISS or VIMS mosaic to identify crater rims, none are found in either within the South Belet region. If there are any craters outside the SAR boundaries, it is possible that they are too small or too low contrast to be seen in ISS or VIMS. There is only one identified crater in South Belet that is unnamed; we identify 4 crater-like features with potential impact origins as well, but they are insufficiently resolved to confidently describe as such.

South Belet is likewise deficient in the “labyrinth” terrain unit described in Malaska et al. (2016a; 2020) suggesting either that the process behind the formation of these units has not taken place in this area, or that they have since been completely eroded/buried. It is also possible, given the preferential distribution of labyrinth at high latitudes (Malaska et al., 2020), that the

aforementioned lack of SAR coverage in these latitude regions has left these units unidentified. The SAR in this region is largely deficient south of the 30° latitude line, and labyrinths are normally found north of the 30°N line or south of the 30°S line (Malaska et al., 2020). However, ISS images will sometimes show a subtle darkening that corresponds to the presence of labyrinth terrains within surrounding plains units, although this was not considered a defining characteristic due to the fact that not all labyrinths are visible in ISS. Similarly, darkening in ISS images can correlate to other terrains, and none of that seen in South Belet region outside the bounds of the SAR can be assuredly labeled as labyrinth.

Next, we briefly discuss the characteristics of South Belet's mid-latitude-to-pole transition region (~50°S to 60°S) and compare it to the transition regions of Afekan and Soi, both of which are located in Titan's northern hemisphere. There are two units in particular that seem to define the morphology of Titan's transitional zones and have been identified in our mapping in the northern hemispheres (Malaska et al., 2016a; Lopes et al., 2020) and here in the southern hemisphere: the scalloped plains (*psv*) and the dark irregular plains (*pil*). For descriptions of these two units, see table 4.1.

In the Afekan region, a small portion of scalloped plains is observed in the northwest region of that study area (Fig. 4.12), making up 1.5% of the mapped area (Malaska et al., 2016a). In the Soi region, a similarly sized portion of scalloped plains is also observed in the northernmost part of the study area (Lopes et al., 2019) and makes up 1.6% of that mapped area. VIMS analysis showed the scalloped plains as one of the highest in albedo on Titan (Solomonidou et al., 2018). Following Malaska et al. (2016a), we have interpreted this terrain unit as composed of either organic materials that are slightly higher in backscatter than the undifferentiated plains, or else as eroded hummocky materials that have been covered by a

relatively thin layer of organics. The scalloped plains begin to appear around latitudes of 50°S and extend toward the poles; they correlate well with the mottled plains (Vm_b) and uniform SAR-bright plains (Vu_b) described in Birch et al. (2017). In higher latitude regions, small, empty depressions can be seen within this unit (Lopes et al., 2020) that are similar in morphology to the empty sharp-edged depressions (SEDs) (Birch et al., 2017; Hayes et al., 2017) (Fig. 4.12E and F). Identification of SEDs is more ambiguous in South Belet; there are some features reminiscent of SEDs, such as topographic lows (relative to surrounding terrain) corresponding to radar bright floors, but the quality of the SAR in this area makes it difficult to definitively label it as such.

South Belet's scalloped plains are also patchier when compared to Afekan and Soi; South Belet has a smaller average size for the feature (3200 km^2) when compared to Afekan (22,000 km^2) and Soi (98,000 km^2). This may also be due to a bias in spatial coverage for the higher latitudes, and the scalloped plains we are observing may be skewing small due to an insufficient sample size. South Belet's transitional latitude similarly differs from that of Afekan and Soi in that there are more channels in contact with the scalloped plains and dark irregular plains units within the latitude zones under consideration (Fig. 4.12d); there is 1 channel mapped north of the 50°N latitude line in Soi, zero channels mapped north of the 50°N latitude line in Afekan, and 17 mapped channels south of the 50°S latitude in in South Belet. One explanation as to the prevalence of channels in the South Belet high latitudes, compared to Afekan and Soi, is that more of the scalloped plains material has been eroded and removed via fluvial action, which would explain the patchiness of South Belet's scalloped plains. Other possibilities include less deposition in this area, thus allowing for more channels to remain unburied and exposed. Alternatively, it could be a difference in the material properties of the excavated substrate, or comparatively different trends in precipitation.

The dark irregular plains are often found in contact with the scalloped plains. They are not extensive and occur only at higher mid-latitudes, but are found in Afekan, Soi, and South Belet. Like the scalloped plains, they appear around 50°S and extend toward the poles. The dark irregular plains correlated well with the low flat plains (Lf_d) unit from Birch et al. (2017). South Belet has comparatively more dark irregular plains than the other two regions, making up 1.3 % of the mapped area in South Belet, 0.5% of the mapped area in Afekan, and 1% of the mapped area in Soi. We interpret this unit as composed of local basins that are dampened by liquid hydrocarbons either on the surface or within the top ~10's of centimeters of the surface (Janssen et al. 2016). However, the overall elevation with respect to the regional liquid table and surrounding terrains is unknown and may be variable. An alternative explanation is that this unit may contain finer grained materials than the surrounding terrain. They could also be small isolated areas of undifferentiated plains that have been identified as dark irregular terrains due to their smaller areal extent.

The 50° to 60° latitude zones, in both the northern and southern hemispheres, seem to represent a transitional region of sorts. The change in characteristic surface morphologies likely reflect a change from the aeolian dominated equatorial regions to the fluvially and lacustrine dominated poles.

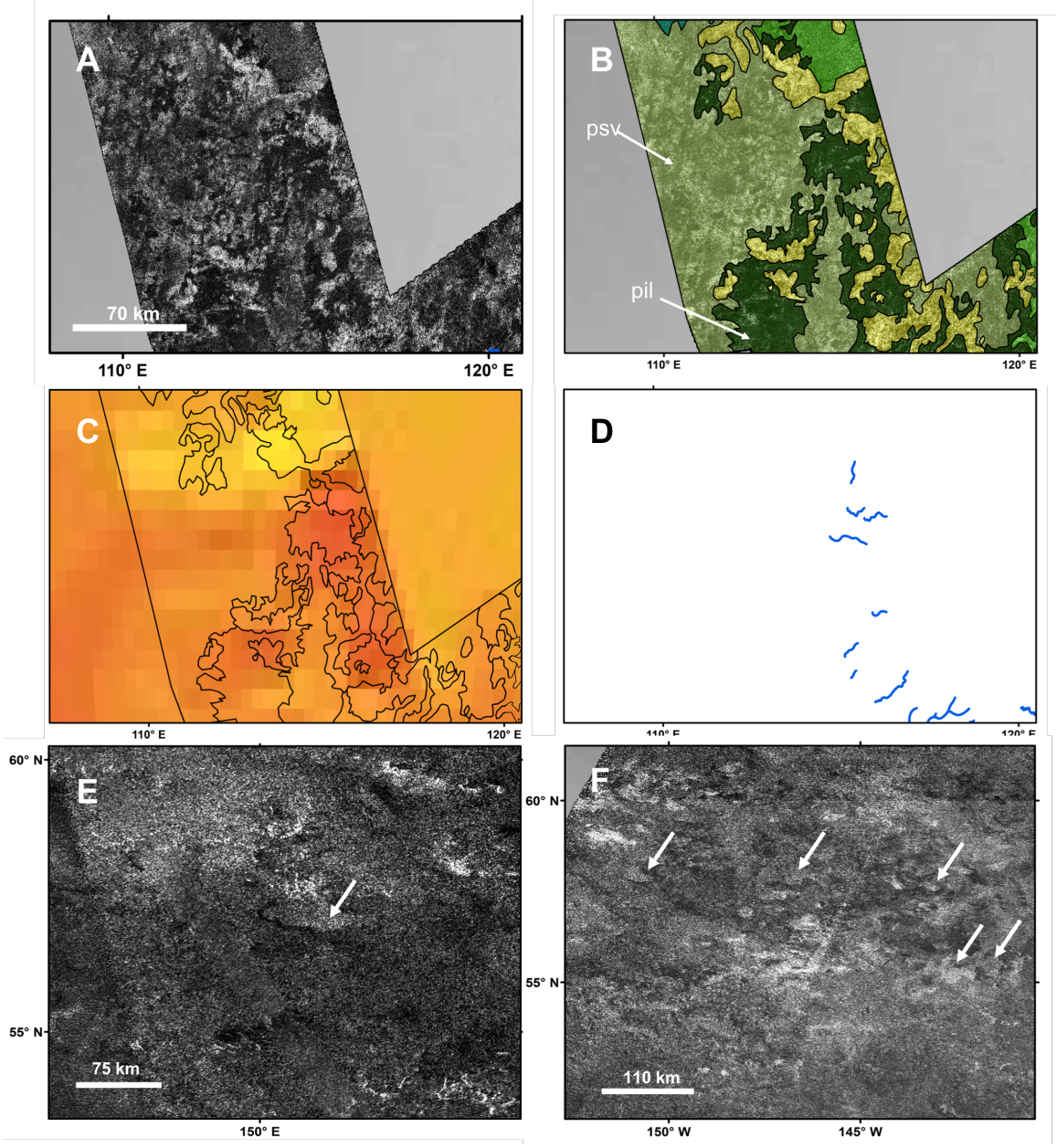

Fig. 4.12 Region south of the 50°S line in South Belet, presented in sinusoidal projection. (A) SAR mosaic. (B) Annotated terrain map on the SAR mosaic with scalloped plains (*psv*) and dark irregular plains (*pil*). (C) Microwave emissivity map. (D) Location of channels in area, marked in blue. (E) SAR mosaic of the transition zones in Afekan, and (F) Soi. White arrows indicate sharp edge depressions (*bse*), interpreted as empty lakes.

4.5.2 The Belet Sand Sea

The majority of South Belet's linear dunes (*dl*) are located in the Belet Sand Sea (Fig 4.13). Linear (or longitudinal) dunes appear as parallel, SAR-dark lines against a variable backscatter substrate and are similar in morphology to terrestrial dunes, such as

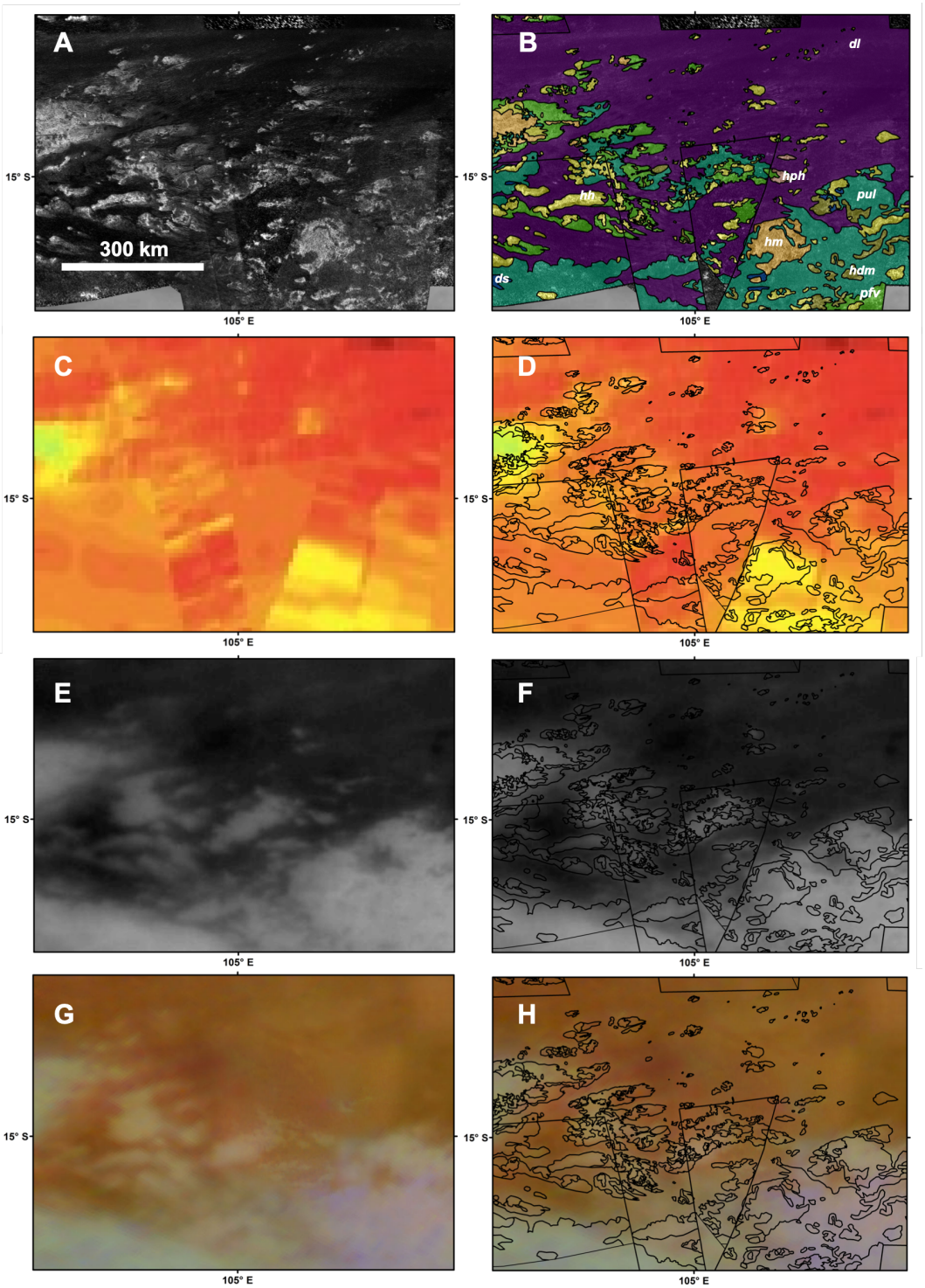

Fig. 4.13 Belet Sand Sea close-up (image centered at 13.7°S, 106.6°E): (A) SAR mosaic. (B) Annotated terrain map on the SAR mosaic. (C) Emissivity map. (D) Emissivity map showing contacts between terrain units. (E) ISS mosaic. (F) ISS mosaic showing contacts between terrain units. (G) VIMS RGB color ratio mosaic. (H) VIMS RGB color ratio mosaic showing contacts between terrain units.

Namibia, the Sahara, and Saudi Arabia (Lorenz et al., 2006; Radebaugh et al., 2010). The Belet Sand Sea consists of a wide belt of linear dunes with a sand transport direction inferred to be from west to east (Radebaugh et al., 2010; Malaska et al., 2016b).

Compared to other Titan sand seas, the dune forms in Belet are tightly spaced, straight, and very long (Radebaugh et al. 2008; Le Gall et al. 2012). Microwave emissivity data shows high emissivity for dune areas, but Belet is particularly emissive when compared to Titan's other dune fields, suggesting a low interdune to dune area ratio (Le Gall et al., 2012). The sum of these characteristics point to the Belet Sand Sea having a comparatively thick dune layer fed by a rich sand supply, perhaps with contributions from surface winds with particularly competent transport capacity (Kocurek and Lancaster, 1999). On Earth, dune fields commonly form within topographic basins where flow entering the basin expands, decelerates and results in the deposition of sediment (Wilson, 1971). Belet sits a few hundreds of meters below its surroundings, occupying a depression on Titan's trailing edge hemisphere (Stiles et al., 2009) that can readily concentrate windward materials.

Analysis by Bishop et al. (2017) found that dune widths in the Belet Sand Sea confirm a global correlation between decreasing dune width and increasingly northern latitudes (Le Gall et al., 2011; 2012). Additionally, they find that dune width and spacing correlate somewhat with

longitude and decreases to the east. However, dune width and spacing typically increase in the migration direction, where dunes originate at the upwind margin of a field (Kocurek and Ewing, 2005), thus an opposite trend for dune width would be expected in a system where sand transport is from west to east, as is the case for Titan. It could be possible that the observed westward dipping regional slope is responsible for the field's observed spatial trends (Lorenz et al., 2013; Bishop et al., 2017; Telfer et al., 2019). However, latitudes roughly between 10°S and 20°S have been shown to be zones of sediment flux divergence (Lucas et al., 2014). This suggests that the transport is not solely eastward and thus could be affecting the width and spacing of the dunes. The observed dune patterns may be a result of the two factors combined.

4.5.3 Alluvial Fans

In South Belet, areas of interpreted fluvial deposition are observed, but are not widespread (e.g., Fig. 4.8); these observations are similar to those made of the Afekan region and seem characteristic of Titan's mid-latitude and equatorial regions. However, SAR data were not able to resolve the networks visible in the Descent Imager / Spectral Radiometer (DISR) Huygens landing images (Jaumann et al., 2009), suggesting that the apparent scarcity of fluvial features in Cassini images should not be taken as evidence of their absence (Burr et al., 2013a). Channels that we do see are typically associated with the hummocky (*hh*) or mountain (*hm*) units. Such an association is well illustrated by an extensive system of channels found centered at 104.4°E, 28.29°S. While most of these channels terminate before the plains, some visibly extend from mountainous areas out onto the plains. The disappearance of channels into the plains could be due to several factors, including infiltration capacity of the undifferentiated plains, or also plain formation outpacing (burying or covering) channel incision (Lopes et al., 2016).

Alternatively, the downstream portion of such channels may be less observable due to losses in contrast with their surroundings. The fact that some channels are seen within the undifferentiated plains unit suggests that these properties may be inhomogeneous within a given region.

In some instances, channels terminate into the *bright alluvial plains* (*pah*) unit (Fig. 4.10). Based on their triangular morphology and association with channel termini (section 4.4.1), we interpreted this unit as alluvial fan-like deposits of high backscatter materials. Channels emerging from highland regions onto flat, low-lying plains deposit sediment into a cone-shaped fan, a consequence of the carrying capacity of the flow being suddenly reduced (Bull, 1977; Stock, 2013). Unlike fans on Earth and Mars, which are primarily composed of silicate rocks and transported by water, the mobilized materials on Titan's surface are most likely made of water ice and organics (Soderblom, 2007; Barnes et al., 2007a; Birch et al., 2016) and are transported by liquid hydrocarbon runoff (Lunine and Atreya, 2008; Birch et al., 2016). The similarity between Earth's and Titan's alluvial fans suggest similar underlying physical processes despite drastically different compositions of both fluids and sediments (Collins, 2005; Soderblom, 2007; Burr et al., 2013a; Birch et al., 2016).

We identify a total of three "bright alluvial plains" units in the South Belet region, all within the same ~28,000 km^2 region centered on 104.4°E, 28.29°S (Fig. 4.10b). SAR coverage in this area is limited, and thus the prevalence of alluvial fans in South Belet may be underestimated. Similarly, we are likely underestimating the number of fans in South Belet, and likely the whole moon, due to the coarse resolution of the Cassini SAR. Likewise, it is possible that any of the three fans identified here are actually a series of overlapping fans, or bajada-like structures, emanating from a single elevated region (Birch et al., 2016; Radebaugh et al., 2018).

Regardless, no fans were identified within South Belet's well-imaged equatorial zone (<25°S) despite inferred observations of a large rainstorm at the equatorial regions (Turtle et al., 2011).

Birch et al. (2016) attributed the lack of fans in the equatorial regions to three factors. First, the landscape may have eroded to the point where sharp slope breaks are no longer available to generate fans at the observable resolution, despite a sufficiently energetic flow event. Second, precipitation at the equator may not be reaching headwater channels, instead infiltrating through a highly porous surface layer (Hayes et al., 2008; Birch et al., 2016). Third, equatorial fans are capable of forming at the observed scale but have subsequently been buried by aeolian sediments (Birch et al., 2016). Furthermore, Malaska et al. (2016a and 2016b) suggest that sediment transport in these areas is dominated by aeolian transport mechanisms, although some degree of recent equatorial fluvial activity is possible.

The global survey of Titan's alluvial fans presented in Birch et al. (2016) include the fans identified here. Their survey found that most fans are at latitudes between ± 50-80°, with few observed fans seen within or in proximity to any of the equatorial dune fields. They also found a strong correlation between the latitudes of highest precipitation rates as predicted by Titan GCMs (e.g. Lora et al. 2014) and the latitudinal concentration of fans, suggesting a causal relationship. A study by Faulk et al. (2017) similarly found that storms capable of sediment transport and erosion occur at all latitudes in their simulations, consistent with the observed global coverage of fluvial features. However, the most extreme, high discharge storm events tend to occur in Titan's mid-latitudes, which are far more capable of transporting gravel-sized sediment than persistent low-magnitude precipitation. Consequently, such discharge events can leave geomorphic signatures in the form of large alluvial fans (e.g. Blair and McPherson, 1994; Leier et al., 2005; Borga et al., 2014). Furthermore, the Birch et al. (2016) study evaluates the fan

area-drainage area relationships for Titan and finds that it supports a transport-limited sedimentary environment.

4.5.4 Impact Processes

We have identified one (unnamed) crater in the South Belet region with confidence. The crater is ~26 km in diameter and is visible in HiSAR (Fig. 4.14).

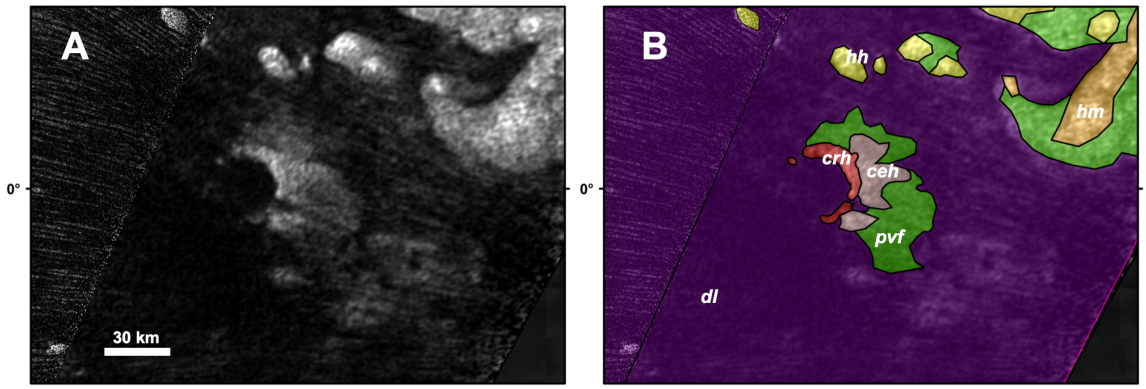

Fig. 4.14 Unnamed crater in South Belet (0.023°N, 79.51°W). (A) Unnamed crater in SAR. (B) Terrain unit mapping, including annotations of units.

Despite the lower resolution data, the morphology of this feature is semi-circular in nature, with a distinguishable rim and morphology similar to that of other Titan craters. The crater rim (*crh*) is seen to have been breached or overrun on the westward facing side, with linear dunes (*dl*) consequently invading the crater interior. There is a small zone of crater ejecta featured only on the eastward side of the rim, the rim presumably protecting the eastward ejecta from burial by the encroaching dunes. We interpret this crater as resulting from an impact into Titan's surface, bringing up deep crustal materials likely enriched in water ice. The crater rim was then eroded by aeolian and/or fluvial processes, creating a major breach on the western side of the rim and burying the western ejected deposits. Locations to the east of the crater were

partially protected from dune transport and deposition, leaving a partially intact ejecta blanket. The breach of the rim is substantial, and thus the crater floor materials are likely aeolian materials transported from the west to the east. Other as-of-yet unidentified craters in the South Belet region have more than likely undergone a similar fate. Complete burial of craters, especially in and around the Belet Sand Sea, may explain the dramatic lack of craters in this region.

4.5.5 Equatorial Pits in South Belet

Throughout South Belet, but specifically within the equatorial latitudes, there are numerous radar dark, circular features with diameters ranging in size from about 1-6 km. In total, 171 of these features were identified (Fig. 4.15). Similar features of this specific morphology, assumed to be depressions or pits, were first identified by Lopes et al. (2007) within Cassini's T8 swath. We primarily found these pits within a radar bright substrate resembling the "lumpy" internal texture of hummocky terrain; this association is the qualitative basis behind distinguishing "pitted hummocky" (*hpm*) from "hummocky" (*hh*). Pitted hummocky is also found in contact with mountainous (*hm*) and hummocky (*hh*) terrains (Fig. 4.11b). We interpret

the radar-dark and smooth internal appearance of these features to be wind-blown organic sands deposited and concentrated into pre-existing depressions within exposure of the ancient ice crust.

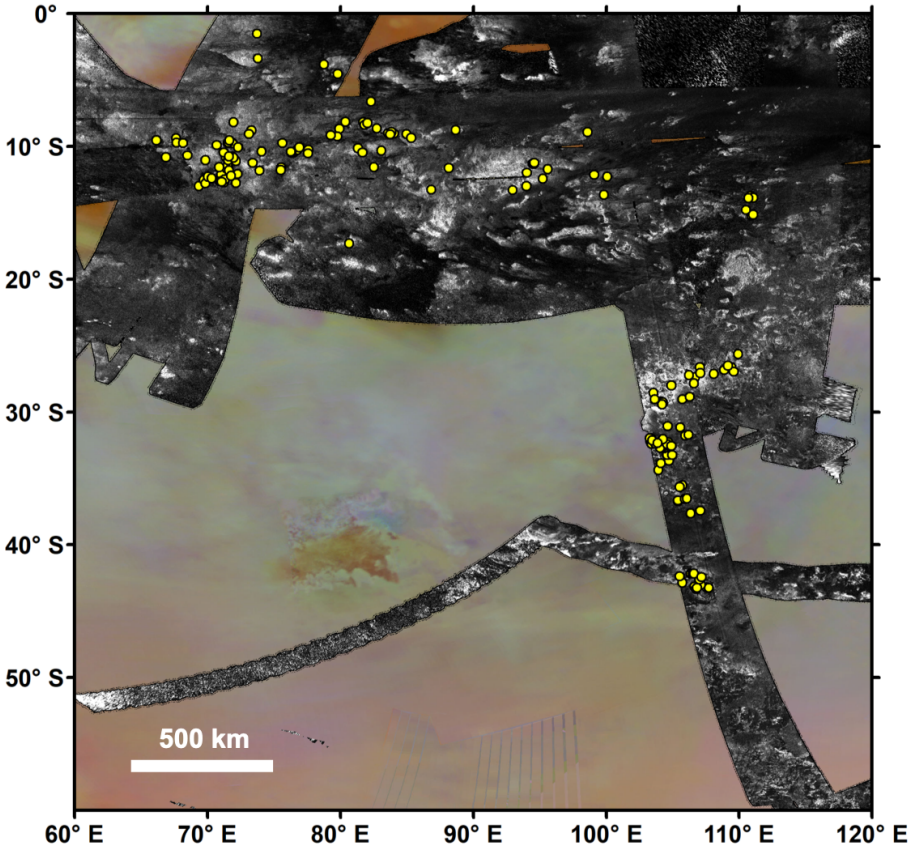

Fig. 4.15 SAR mosaic of the South Belet region. Location of individual pits marked in yellow.

The association between pits and Titan's mountainous units is compelling. It could be that, being locally elevated to the surrounding terrain, pitted depressions are preserved from complete burial by windward sediments and incidentally become associated with mountains and hummocks. Alternatively, the contrast in backscatter afforded by the radar bright substrate of the hummocky terrain makes the pits easier to identify; pits that may or may not be in the undifferentiated plains, for example, would be difficult to identify due to their comparable backscatters.

Based on morphological similarities, and their similar association with a radar-bright substrate, we interpret the pits found in South Belet to have formed in the same manner as the pits found in the T8 SAR swath between 6°–12° south and 212°–230° west (Fig. 4.11f). As discussed in Lopes et al. (2007) and Lunine et al. (2008), the morphologies of these pits are not consistent with those of impact craters (e.g. Wood et al., 2010; Neish et al., 2013; Hedgepeth et al., 2020), lacking associated features such as a rim or ejecta blanket. Similarly, these pits have a modal diameter of 1–6 km, and do not have a size distribution consistent with impact craters. Regardless, any impactor that could be responsible for craters of this size would be too small (< 2km) to pass through the atmosphere without breaking up (Lunine et al., 2005; Lunine et al., 2008). Secondary craters forming the pits is a possibility, but the distribution of the South Belet pits, very similar to the quasi-random distribution of pits within the mountain ranges of T8 (Adams and Jurdy, 2012), is not characteristic of chains of secondary craters. The general lack of a large primary impactor is likewise problematic. We hypothesize several alternative formation mechanisms and described them below.

4.5.5.1. Hypothesis #1: Cryovolcanism

Cryovolcanism has been suggested as a method for pit formation on Titan by Lopes et al. (2007). Cryovolcanism is defined as eruptions of icy-cold aqueous solutions, or partly crystallized slurries, derived by partial melting of ice-bearing materials (Kargel, 1995). Lopes et al. (2007) suggests that the pits identified in the T8 SAR swath may be collapse or explosion pits, common in volcanic regions and thus may be related to cryovolcanism. While there is no morphological evidence of volcanic features such as flow fronts or calderas, in planform view the pits appearances are not unlike that of maar on Earth. Maar pits form via phreatomagmatic

eruptions, or an explosion that is generated when ground water comes in contact with hot magma or lava, an example of which is Ubehebe Crater in Death Valley National Park, CA. A model for an analogous but Titan-appropriate process has been proposed by Mitri et al. (2019) and Wood and Radebaugh (2020) (see section 4.5.6).

4.5.5.2. Hypothesis #2: "Sinkhole" Formation via Volatile Loss

Pits observed on the Martian south polar cap have been attributed to sublimation (Thomas et al., 2000; Malin et al., 2001; Byrne and Ingersoll, 2003). In addition, pit formation on planetary surfaces is expected to form via collapse due to a cavity forming beneath the surface (Wyrick et al., 2004), such as through dissolution. Dissolution and/or sublimation processes requires an icy regolith that contains a sufficient fraction of volatile material to permit formation of pits several kilometers in size. However, water ice is both stable in Titan's atmosphere and insoluble in liquid methane/ethane (Lorenz & Lunine, 1996; Perron et al., 2006) and thus cannot be eroded by dissolution or sublimation. Small organic molecules such as acetylene, ethylene, propene, propyne (methylacetylene), cyclopropane, cyclopropene, all of which have been recently resolved in Titan's stratosphere (Thelen et al., 2019), are potentially volatile at Titan temperatures in the surface or near subsurface. However, these volatiles would likewise be soluble at the surface; relative rates of processing via either dissolution or sublimation of said volatiles have yet to be constrained.

If there were a volatile or semi-volatile substrate, however, then we can hypothesize that these pits formed via a type of sinkhole collapse, i.e. when the ceiling of a subsurface cavity can no longer support itself and fails, producing circular depressions aligned with the local gravity vector (Waltham et al., 2005). A potentially analogous process to the one proposed here is the

outgassing of Mercury's volatile-rich (or at least historically volatile-rich) crust; on-going investigations indicate that Mercury's chaotic terrains and associated kilometer-scale "hollows" may have formed due to large-scale upper crustal devolatilization via various exogenic processes (Blewett et al., 2011; Blewett et al., 2013) . Another analogous collapse mechanism to consider is pit formation on cometary nuclei, where removal of subsurface volatiles generates a void (Belton and Melosh, 2009; Vincent et al., 2015; Mousis et al., 2015). Failure of the cavity's ceiling propagates upward, resulting in quasi-circular depressions few tens to a few hundreds of meters in diameter, such as the pits observed by Rosetta on comet 67P (Vincent et al., 2015). Because the size of sinkholes depends on the material strength of the top layers, sinkholes in a given terrain are all of similar size (Waltham et al., 2005) and may explain the similarity in size of South Belet's pits, though it is possible that smaller pits exist beyond the scale of Cassini resolution.

4.5.5.3. Hypothesis #3: Clathrate De-stabilization via Tectonic Shear Heating

The presence of a large quantity of pits in proximity to the radar-bright mountains suggests the two may be related (Adams and Jurdy, 2012). Both extension fracturing and dilation faulting result in subsurface voids into which loose material on the surface can drain, creating linear assemblages of pits known as "pit chains" (Tanaka and Golombek, 1989; Ferrill et al., 2003; Wyrick et al., 2004; Martin et al., 2017). Radebaugh et al., (2007) describe the sub-parallel mountain ranges of T8 as possible extension features, although Liu et al. (2016) supersedes this idea and calls for contraction using methane ground fluids as lubricant. Adams and Jurdy (2012) explore an extensional origin for the T8 pits in more detail and finds statistical evidence of

clustering throughout the entire pit field yet finds only a hint of linearity within those pit clusters when compared with a same-sized random set.

Whether from extensional or compressive tectonics, large scale mountain building in these areas will mechanically generate heat via the motion of faults, producing frictional heat from both shallow brittle deformation and deep plastic deformation in ductile shear zones (e.g. Scholz, 1980; Brewer, 1981). Transient shear heating during dynamic rupture of faults also can produce melting within a fault zone, given sufficiently large slip (e.g. McKenzie and Brune, 1972; Scholz, 1980; Lachenbruch, 1980). Methane stored as clathrate hydrates (Lunine et al., 1987) are highly stable in Titan's interior and thus their dissociation can occur only when the internal temperature reaches sufficiently high values (e.g. Grasset and Pargamin, 2005; Choukroun et al., 2010). It is worth considering the possibility that mechanical heating during a sufficiently large slip event (e.g. Mackenzie and Brune, 1972) may facilitate the release of methane clathrates in the crust; gas generated in such an event may induce over-pressures required for creating cracks (Choukron et al., 2010) that can be exploited and widened by erosion later.

4.5.5.4. Hypothesis 4: Collapse via loss of fluid pressure

Pit collapse could be explained by the depletion of liquid methane in Titan's upper icy crust, which may lead to caprock collapse as a result of overburden pressures no longer being supported. Some sinkholes on Earth result from loss of buoyant support following a decline of the water table in the interior terrane, leading to the immediate collapse of the roofs of cavities in bedrock and unconsolidated deposits (e.g. Newton and Hyde, 1971; Spigner 1978; Sinclair, 1982; Newton, 1987). The strong association between pits and mountainous terrains may be a

factor, where highland topography is sufficiently removed from a receding ground-methane table, facilitating collapse. While the depth and extent of such a subsurface methane reservoir is unknown, liquid methane in Titan's crust is thought to have played an important role in mountain building on Titan (e.g. Liu et al., 2016b).

4.5.5.5. Hypothesis #5: Formation via Dissolution

Lastly, sinkhole-like collapse could be driven by dissolution of an organics/ice mixture. As previously discussed (Section 4.5.5.2.), the association of pits with the hummocky terrain suggests that they preferentially develop within an icy substrate. Water ice is insoluble in a landscape shaped by nonpolar solvents (Cornet et al., 2015), but this does not necessarily preclude the possibility of sinkhole collapse via dissolution. Though not constrained, a certain degree of mixing likely exists between the transition from surface organic regolith to buried icy crust, evoking the possibility of a heterogeneous media where dissolvable substrates can be dissolved in an otherwise insoluble matrix (e.g. Neish et al. 2019). Laboratory work has demonstrated dissolution of Titan's organic materials under cryogenic conditions (e.g. Malaska and Hodyss, 2014). Likewise, compelling geomorphologic interpretations exist for organic karstic processes on Titan, including evidence for karstic lakes, poljes, polygonal karst, fluviokarst, tower karst and corrosion plains (Malaska et al., 2010; 2011; 2020; Cornet et al., 2015; Solomonidou et al., 2020b;). In addition, interpretations of evaporites (Barnes et al., 2011; MacKenzie et al., 2014), although not classically thought of as karstic landforms, provide observational evidence that dissolution and re-deposition has occurred on a large scale.

The pits seen in South Belet are larger than the largest sinkholes on Earth (~500 m; Waltham et al., 2005). Tectonic quiescence in more recent Titan epochs, as well as lower gravity,

may allow Titan's voids to grow larger before finally collapsing (Mitchell et al., 2011). In contrast, the largest pits observed on cometary nuclei such as 67P are an order of magnitude smaller (max ~300 m). This difference in size may be owing to a dramatic difference in strength of weakly bounded cometary materials (e.g. Groussin et al., 2019) when compared to ice at Titan conditions, despite a much smaller gravity field. Regardless, a more detailed analysis into the likelihood of sinkhole collapse on planetary bodies and the controls dominating size and distribution is warranted.

It is possible that the South Belet pits are more ubiquitous than suggested by the radar. For example, smaller, sub-resolution pits may be present yet remain unaccounted for. The pits identified, after all, are several kilometers in size, and possibly represent the extreme end member of the pit formation process, or the result of smaller pits coalescing into a larger one. It is also possible that the association between pit and hummocks are a result of locally high areas preferentially preserving the pits from complete burial by wind-ward sediments. Lastly, pits of similar morphological character are not restricted to the T8 swath nor South Belet and have been identified elsewhere in Titan's mid-latitudes. Titan's pits may represent a poorly understood erosional process with potential implications for methane replenishment of the atmosphere, as well as implications for sediment sources and sinks.

4.5.6 "Crescents" of East South Belet

East of the Belet Sand Sea are radar bright "crescent" features (Fig. 4.16) 15 to 35 km in diameter that have thus far not been described in the Titan literature. These features are also seen in other areas of Titan, including Afekan where they were mapped as "degraded hummocky

terrain" (*hdm*). The number and spatial coverage of these features is extensive enough that the "crescent" may present a significant geologic process for Titan.

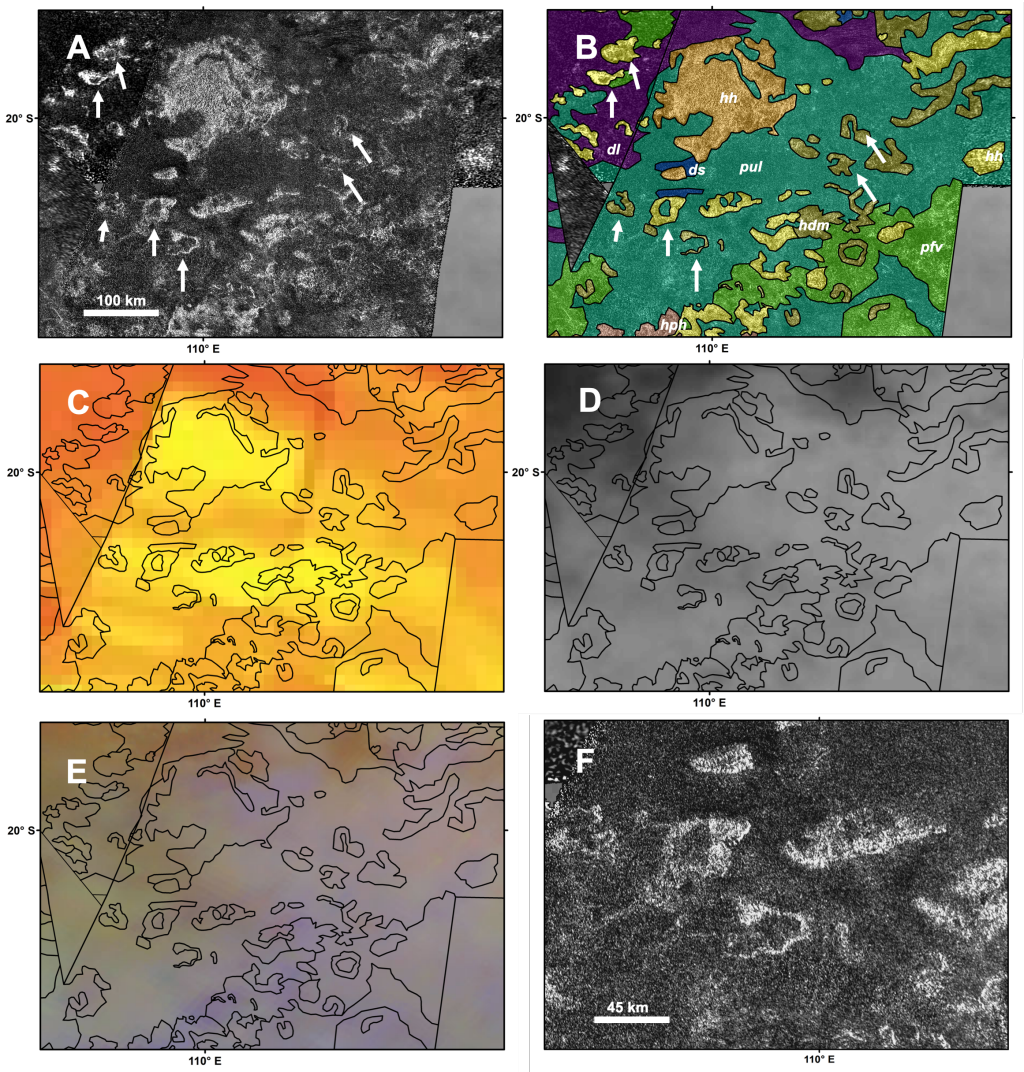

Fig. 4.16 Example area with "crescents". (A) SAR mosaic, crescents indicated with white arrows. (B) Terrain unit mapping, including annotations of units. White arrows indicate crescents. (C) Microwave emissivity map shown with contacts between terrain units. (D) ISS mosaic shown with contacts between terrain units. (E) VIMS RGB mosaic overlain with contacts between terrain units. (F) Zoom-in of several "crescents" that are indicated by the bottommost white arrows in (A).

For the purposes of our mapping, we continue to label the crescents as "degraded hummocky" owing to their radar-bright appearance with a certain amount of dissection and burial. The degraded hummocky terrain (*hdm*) units are described in Malaska et al. (2016a) as small exposures of high-backscatter regions and are interpreted as remnants of hummocky terrain that have been eroded, and in some cases, partially buried by plains materials. What distinguishes the crescents from other "degraded hummocky" features are their irregular, pseudo-circular shape that partially encloses parts of the plains.

The irregular shape and rounded edges of the crescents are similar in morphology and size to many of the empty and filled sharp edged depressions (Hayes et al., 2017; Birch et al., 2018). Likewise, these crescents appear to have radar-bright "rims". These rims appear thicker in width than the raised rims (Birch et al., 2018) normally associated with the SEDs (~5km here versus < 1 km at the poles), but similar in thickness to the "ramparts" discussed in Solomonidou et al. (2020b) (which can be up to 10's of kms) and appear radar-bright and crenulated, closely resembling breached and partially eroded crater rims. Despite their crater-like appearance, their irregular shape presents a problem. Impact craters can lose their circular shape via tectonic processes, however there is not an obvious directional trend in deformation that could be associated with a regional process. In addition, the irregularity of the crescents does not resemble the tectonically deformed craters of other icy satellites (e.g. Pappalardo and Collins, 2005; Crow-Willard and Pappalardo, 2015; Kinczyk et al., 2019).

If not impact in origin, the crescent features may represent some evolutionary relationship between the pits described in the previous sections and the crescents discussed here. The crescents differ from the pits in that they are larger (15 to 35 km in diameter), more irregularly shaped, have a radar bright rim (though this may be a resolution effect), and in some

cases are breached by plains material on one side. The crescents may represent the end stages of the pit formation process, a result of pits growing via lateral scarp retreat, ultimately coalescing together and creating irregular features. Alternatively, the crescent features may be analogous to that of explosion craters from magma–water interaction on Earth. Such a process has been proposed by Mitri et al. (2019) and Wood and Radebaugh (2020) to explain the formation of Titan's polar SEDs.

We make a final morphological comparison here in order to understand the origin of the crescent features. It is possible that the crescents represent remnant exposures of a large icy substrate similar in morphology to northwestern Xanadu (Fig 4.17) but that has been buried and breached by plains materials. The emissivity of this area is notably lower than the surrounding plains (Fig. 4.17c), suggesting near surface burial of a volume scattering material such as ice. The size and spacing of the crescents are also similar to that of the pseudo-circular depressions of Xanadu, which range in size from 7 to 27 km in diameter. Wall et al. (2009) and Nelson et al. (2009) proposed that the large depressions of western Xanadu are associated with cryovolcanic eruption and may be source vents, however other features related to volcanism such as flow fronts and depositions are lacking (Moore and Pappalardo, 2011). In a future study, it would be worthwhile to conduct a more detailed morphological analysis of Western Xanadu for comparison with the crescents in South Belet (and Afekan), as well as extend comparisons to other regions of cryovolcanic interest within Xanadu, such as Hotei and Tui Regio.

Regardless of origin, the preponderance of pseudo-circular features, whether as pits or crescents, on the surface of Titan suggest a complex erosional process that necessitates a more developed understanding of atmosphere/surface interactions, of the role of fluids in Titan's icy

substrate and organic regolith, as well as of the role of endogenic activity in Titan's evolutionary history beyond mountain building.

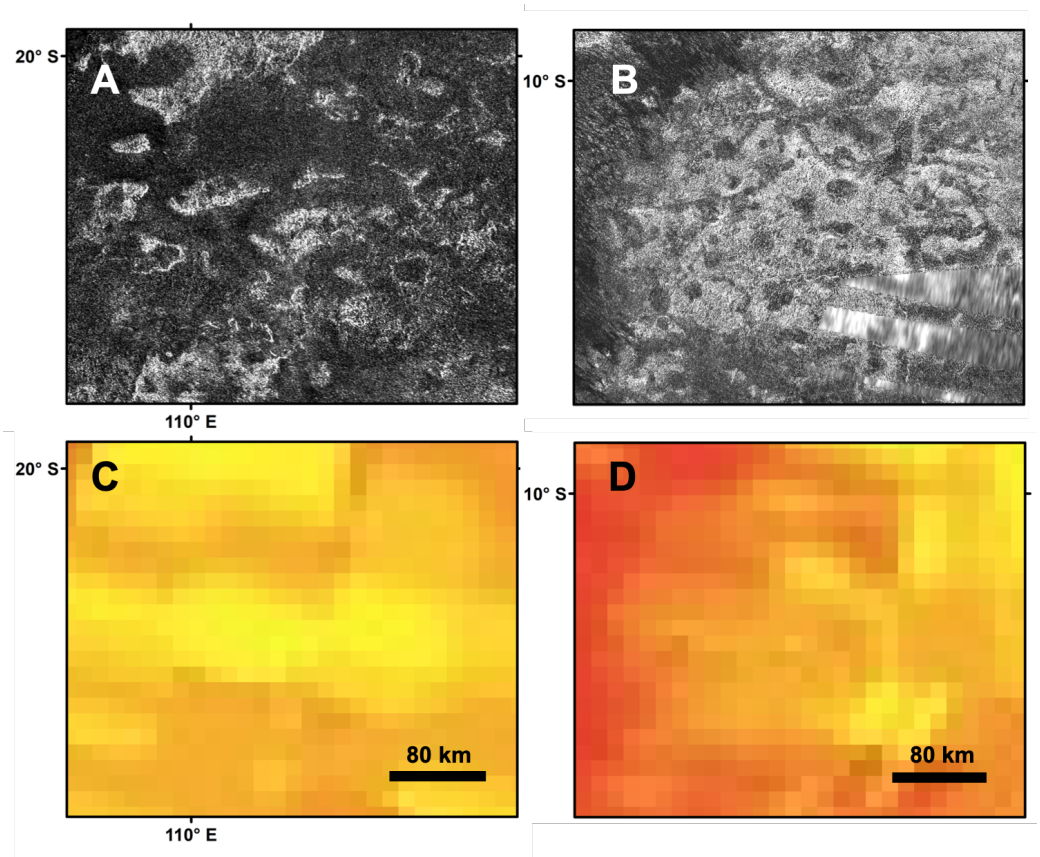

Fig. 4.17 (A) SAR mosaic of the "crescents" in South Belet. (B) SAR mosaic of western Xanadu. (C) Microwave emissivity map of the crescents in South Belet. (D) Microwave emissivity map of Western Xanadu.

4.5.7 Likely Compositions

The surface diversity of Titan seen in ISS, VIMS, and RADAR observations provides evidence that Titan is not uniformly buried in organic dust (Barnes et al., 2007a), although the low contrast of surface images from the Huygens Landing Site analyzed in Karkoschka and Schröder (2016) indicate a uniform coating of materials. The likely surface composition of

Titan's midlatitudes and equatorial regions are discussed in detail in Malaska et al. (2016a); based on the similarity of unit distribution and quantity, we suggest that the likely composition of South Belet is comparable to that of Afekan. For example, the radiometric and spectral signatures of the mountains, hummocky, and crater rim units are more consistent with materials containing water ice. Similarly, microwave emissivity data (Janssen et al. 2009, 2016) and spectral analysis (Solomonidou et al., 2018) suggests that the dunes and plains, which make up the majority of Titan's surface materials, are consistent with organic materials.

This picture is more complicated for the undifferentiated plains, where observations suggest latitudinal variations in composition within otherwise identical units. Using infrared surface reflectance with the Cassini VIMS instrument, Solomonidou et al. (2018) shows that plains closer to the equator have spectral similarities to that of the dunes, whereas water ice appears to be a major constituent of the plains beyond 30°N and 30°S. However, significant amounts of water ice are not expected to be present in these regions, given the lack of detection of high-dielectric constant material (Janssen et al., 2016). Results from Solomonidou et al. (2020a) also show that craters in Titan's midlatitude plains are enriched in water ice in an organic based mixture, whereas equatorial dune craters appear to be purely composed of organic material. VIMS and radar probe different depths: a thin top layer in the case of VIMS, and a thicker layer in the case of radar. The existence of a thin layer of water ice (or of a material with a similar spectral response) covering organic material of low-dielectric constant is possible. Solomonidou et al. (2018) suggest that if this interpretation is correct, then more dark material is deposited from the atmosphere onto the equatorial regions compared to the higher latitudes and polar regions. Alternatively, atmospheric deposition is similar in the low and midlatitudes, but more rainfall may have been occurring for the higher latitudes causing additional modification of

materials. The dark unknown material at higher latitudes could be either washed away or modified by rain so that it is no longer detectable.

Fig. 4.18 presents an inferred composition map of the South Belet region, similar to that presented in Malaska et al. (2016). Based on radiometric signatures and analyses of VIMS data (Jaumann et al., 2009; Lopes et al., 2016; Solomonidou et al., 2018), we determine that terrain units likely composed of organic materials include all dune units (*ds, dl*), the undifferentiated plains (*pul*), and the dark irregular plains (*pil*). Terrain units that are consistent with water ice materials (or other materials with similar emissivity and spectral properties) include the crater rim (*crh*), crater ejecta (*ceh*), mountain (*hm*), hummocky (*hh*), degraded hummocky (*hdm*), the pitted hummocky (*hph*) terrain units, and the bright alluvial plains (*pah*). Terrain units that are of indeterminate composition or may represent a mix of water ice and organic materials include the variable plains terrains (*pfv*, which by definition, are variable in composition) and scalloped plains (*psv*). The area percentages for South Belet show that the likely organic-rich terrains make up over 71.8 % of Titan's surface in this area. Areas that are consistent with being rich in water–ice materials make up 10.6 % of South Belet's surface, suggesting that, at least by areal coverage, Titan's uppermost surface is primarily composed of organic materials, a result similarly found for Afekan.

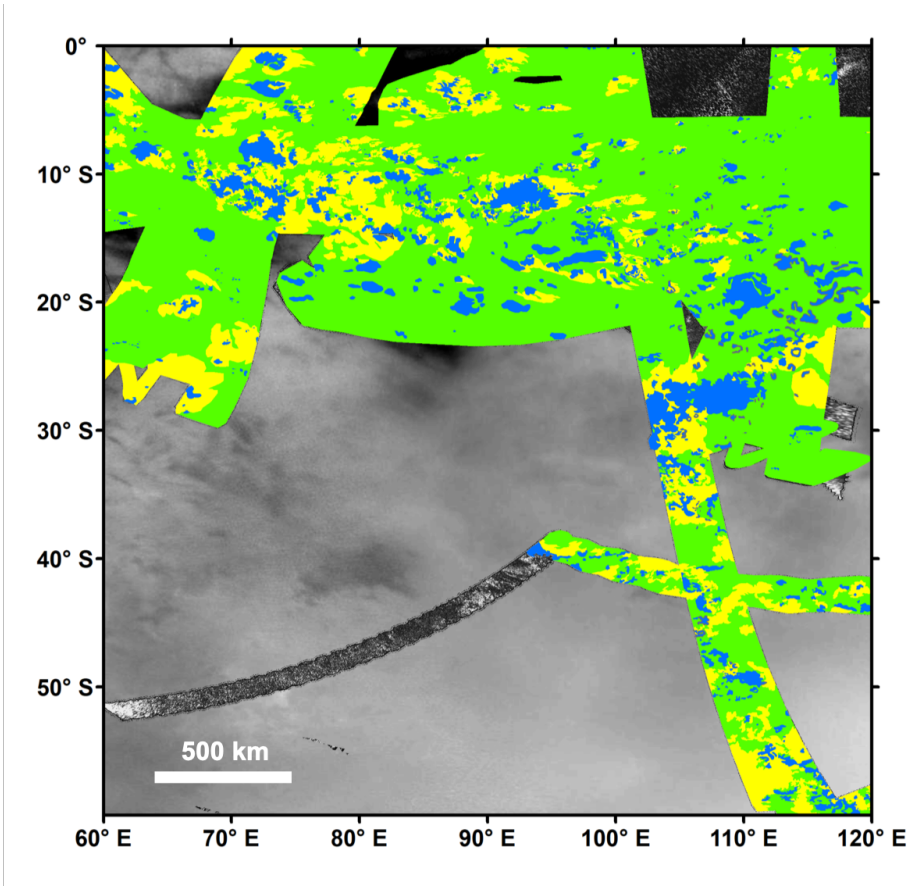

Fig. 4.18 Composition map of the South Belet region. Terrain types with properties consistent with organic materials are colorized in green, while those consistent with water ice are colorized in blue. Terrains of uncertain or mixed composition are colorized in yellow.

4.6 Geologic History

We update the relative stratigraphic relations established in Malaska et al. (2016a) for the South Belet region and graphically show their correlation in Fig. 4.19. Relative superposition of terrain units were used to determine a relative sequence in Afekan and now in South Belet. Topographic data, where available, was used to confirm relations between terrain units. See Malaska et al. (2016a) for a more detailed discussion.

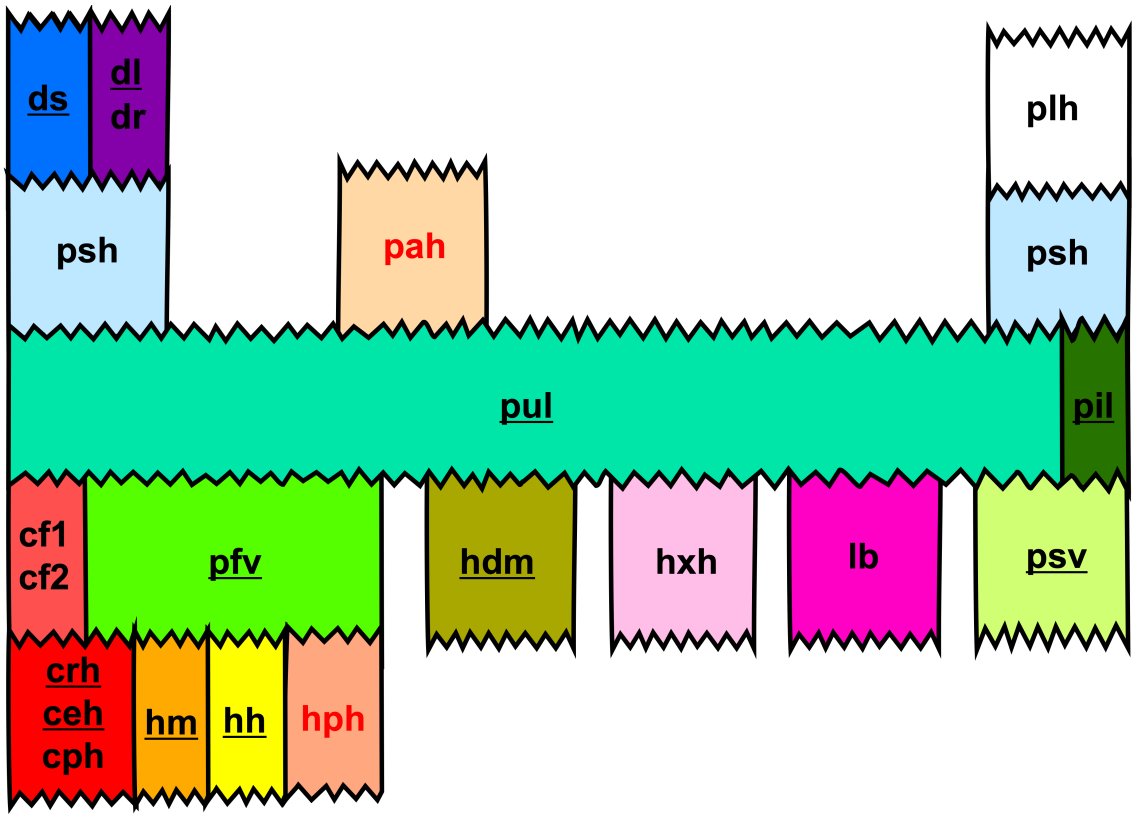

Fig. 4.19 Relative stratigraphy of terrain units from Afekan and South Belet. Red text indicates new units introduced in this paper, whereas underlined units indicate units that appear both in Afekan and South Belet. Units adjacent in the graphics represent direct contact seen in SAR. Units that do not touch in the graphic represent where superposition could not be determined from the SAR. The main units used to determine relative stratigraphy is the undifferentiated plains (*pul)*. Units are: *crh* = crater rim, *ceh* = crater ejecta, *cph* = central peak, *cf1* = crater fill 1, *cf2* = crater fill 2, *hm* = mountain, *hh* = hummocky, *hph* = pitted hummocky, *hdm* = degraded hummocky, *hxh* = cross-cut hummocky, *lb* = labyrinth, *pah* = bright alluvial plains, *pil* = dark irregular plains, *pfv* = variable featured plains, *pul* = undifferentiated plains, *psv* = scalloped plains, *psh* = streak-like plains, *plh* = lineated plains, *dl* = linear dunes, *ds* = featureless sand sheets, *dr* = reticulated dunes.

Following previous interpretations, South Belet's geologic history presents a story familiar to that of Afekan, but with some notable differences. The hummocky (*hh*) and mountainous terrain (*hm*) of South Belet are likely remnant exposures of Titan's ancient icy crust. The crust may originally have been impact-scarred, but subsequent erosion and depositional processes have erased any record of these impacts. Pits within the icy crust, constituting the pitted hummocky terrain (*hph*), may have formed via dissolution or sublimation processes, or may have some connections to Titan's tectonic past. The linear orientation of some of Titan's mountains suggest some underlying tectonic fabric, whether from extension or compression, led to their uplift (Mitri et al., 2010; Cook- Hallett et al., 2015; Liu et al., 2016a, 2016b). Plains and dune materials have more recently been deposited onto, and subsequently buried, the eroded landscape, partially filling or embaying craters and pits alike (e.g. Werynski et al., 2019).

Studies of surface material transport directions (Malaska et al., 2016b) and analysis of spectral data from VIMS (Lopes et al., 2016; Solomonidou et al., 2018) suggest that the materials from the dune terrains (*ds* and *dl*) eventually evolve into the materials making up the mid-latitude undifferentiated plains (*pul*; Lopes et al., 2016; Malaska et al., 2016b; Solomonidou et al., 2018). Solomonidou et al., (2018) show that the undifferentiated plains have a much stronger 2-μm absorption than the dunes, suggesting there is a constituent in the mix that ultimately plays a role in differentiating the two units.

In the equatorial regions and mid-latitudes, materials eroded from the mountains likely mix with adjacent organic materials, eventually resulting in the variable featured plains (*pfv*). This is consistent with results from VIMS that show that the surface albedo values of variable plains are intermediate between equatorial undifferentiated plains and dunes, as if some process

mixed the two (Solomonidou et al., 2018). In the equatorial region, the dunes eventually bury these deposits as they migrate in a predominantly west to east direction. In the mid-latitudes, sediments derived from erosion of the mountains are embayed by wind-ward undifferentiated plains (Lopes et al., 2016). Otherwise, fluvial channels may have abraded and transported material from the mountains, delivering sediment and depositing it as the fan-shaped bright alluvial plains (*pah*).

4.7. Summary

Here we have presented and described a geomorphologic map of the South Belet region of Titan. We used Cassini SAR as our basemap, supplemented with other datasets such as radiometry, topography, ISS, and VIMS. This entire region makes up 11.3% of Titan's areal surface, whereas the parts of the region imaged by SAR make up 3.6% of Titan's surface. This area represents the main geological processes that have occurred in Titan's equatorial and the southern mid-latitudes. We identified and described two new terrain units, the "bright alluvial plains" and the "pitted hummocky", adding to the mapping units discussed in Malaska et al. (2016a). Following previous interpretations, South Belet's geologic history presents a story familiar to that of Afekan, but with some notable differences. Similar to the Afekan region, there are four major classes of terrain units in South Belet: dunes, plains, mountain/hummocky, and crater. Noticeably missing from South Belet is the fifth and sixth major class of unit, the labyrinths and the basin and lake units. We find that plains dominate the make-up of this region, accounting for 47.0% of the mapped area, followed by dunes (43.0%), mountains/hummocky terrains (11.0%), and crater terrains (<<1%). The emissivity and spectral properties of the undifferentiated plains and dunes have emissivity and spectral properties consistent with organic

materials, whereas the emissivity and spectral properties of the mountain/hummocky and crater terrains are more consistent with water ice. Only one crater has been identified in South Belet with confidence, which may be a consequence of both spatial coverage bias (especially in areas away from dunes) and burial capacity of the Belet Sand Sea.

We only observe small instances of fluvial transport in South Belet, such as the alluvial plains. Instead, material transport patterns are more consistent with widespread aeolian deposition of dunes and plains units. If fluvial activity was once more present in this region, it has since been buried by aeolian deposits. We identified three "bright alluvial plains" that we interpret to be alluvial fans. Fans, like the equatorial dunes, are part of a limited set of depositional features identified on Titan. Likely alluvial in origin (e.g. Birch et al., 2016), the identification of fans on Titan's surface indicate that discharges and slopes are such that sediment can be mobilized and ultimately deposited. We additionally introduce another unit not previously discussed in Malaska et al., (2016a): pitted hummocky (*hph*). We interpret this unit to be an icy substrate with 1-6 km sized "pits" and hypothesize that these pits may have formed as a result of either cryovolcanism, the removal of methane (either from outgassing or the retreat of a ground reservoir) in the near surface, or as a result of the dissolution of soluble organics in an otherwise icy matrix. Given our proposed origins, pit formation was either coeval with the uplift of Titan's mountains or formed subsequently via atmospheric or ground fluid interactions with Titan's near subsurface. Eventually, the pits were infilled with windward dune material. The introduction of these two new units are necessary to capture the full range of morphologies seen in South Belet, and likewise indicate a morphological departure from Afekan. We also discussed Titan's "crescents", radar bright features 15 to 35 km in diameter that have thus far not been described in the Titan literature. We find that the crescents are morphologically similar to polar

SEDs as well as to the icy exposures of northwestern Xanadu. We propose that these pseudo-circular features may represent the end-stage evolution of the aforementioned pits or are perhaps relics of past cryovolcanism.

Our geomorphological mapping results for South Belet is consistent with the narrative of Titan's equatorial and mid-latitudes being dominated by organic materials that have been deposited and emplaced by aeolian activity. This is likewise the conclusion we arrived at through our mapping and analysis of the Afekan region. Additionally, the presence of similar units found in both Afekan and South Belet suggests latitudinal symmetry in Titan's surface processes and their evolution.

4.8 References

Adams, K.A. and Jurdy, D.M., 2012. Pit distribution in the equatorial region of Titan. Planetary and Space Science, 65, 58-66.

Atreya, S.K., Adams, E.Y., Niemann, H.B., Demick-Montelara, J.E., Owen, T.C., Fulchignoni, M., Ferri, F. and Wilson, E.H., 2006. Titan's methane cycle. Planetary and Space Science, 54, 1177-1187.

Barnes, J.W., Brown, R.H., Soderblom, L., Buratti, B.J., Sotin, C., Rodriguez, S., Le Mouèlic, S., Baines, K.H., Clark R., Nicholson, P., 2007a. Global-scale surface spectral variations on Titan seen from Cassini/VIMS. Icarus 242, 258. doi: 10.1016/j.icarus.2006.08.021.

Barnes, J.W., Radebaugh, J., Brown, R.H., Wall, S., Soderblom, L., Lunine, J., Burr, D., Sotin, C., Le Mouélic, S., Rodriguez, S., Buratti, B.J., Clark, R., Baines, K.H., Jaumann, R., Nicholson, P.D., Kirk, R.L., Lopes, R., Lorenz, R.D., Mitchell, K., Wood, C.A., 2007b. Near-infrared spectral mapping of Titan's mountains and channels. Journal of Geophysical Research 112, E11006. doi: 10.1029/2007JE002932.

Barnes, J.W., Bow, J., Schwartz, J., Brown, R.H., Soderblom, J.M., Hayes, A.G., Vixie, G., Le Mouélic, S., Rodriguez, S., Sotin, C. and Jaumann, R., 2011. Organic sedimentary deposits in Titan's dry lakebeds: Probable evaporite. Icarus, 216, 136-140.

Barnes, J.W., Lorenz, R.D., Radebaugh, J., Hayes, A.G., Arnold, K. and Chandler, C., 2015. Production and global transport of Titan's sand particles. Planetary Science, 4, 1-19.

Belton, M.J. and Melosh, J., 2009. Fluidization and multiphase transport of particulate cometary material as an explanation of the smooth terrains and repetitive outbursts on 9P/Tempel 1. Icarus, 200, 280-291.

Blair, T.C., McPherson, J.G., 2009. Processes and Forms of Alluvial Fans. In: Abrahams, A.D., Parsons, A.J. (Eds.), Geomorphology of Desert Environments, 2nd ed. Chapman & Hall, pp. 454–456.

Blewett, D.T., Chabot, N.L., Denevi, B.W., Ernst, C.M., Head, J.W., Izenberg, N.R., Murchie, S.L., Solomon, S.C., Nittler, L.R., McCoy, T.J. and Xiao, Z., 2011. Hollows on Mercury: MESSENGER evidence for geologically recent volatile-related activity. Science, 333, 1856-1859.

Blewett, D.T., Vaughan, W.M., Xiao, Z., Chabot, N.L., Denevi, B.W., Ernst, C.M., Helbert, J., D'Amore, M., Maturilli, A., Head, J.W. and Solomon, S.C., 2013. Mercury's hollows: Constraints on formation and composition from analysis of geological setting and spectral reflectance. Journal of Geophysical Research: Planets, 118, 1013-1032.

Birch, S.P.D., Hayes, A.G., Howard, A.D., Moore, J.M., Radebaugh, J., 2016. Alluvial Fan Morphology, distribution and formation on Titan. Icarus 270, 238-247. 10.1016/j.icarus.2016.02.013.

Birch, S.P.D., Hayes, A.G., Dietrich, W.E., Howard, A.D., Bristow, C.S., Malaska, M.J., Moore, J.M., Mastroguiseppe, M., Hofgartner, J.D., Williams, D.A., White, O.L., Soderblom, J.M., Barnes, J.W., Turtle, E.P., Lunine, J.I., Wood, C.A., Neish, C.D., Kirk, R.L., Stofan, E.R., Lorenz, R.D., Lopes, R.M.C., 2017. Geomorphologic mapping of Titan's polar terrains: Constraining surface processes and landscape evolution. Icarus 282, 214-236. doi: 10.1016/j.icarus.2016.08.003.

Birch, S.P.D., Hayes, A.G., Corlies, P., Stofan, E.R., Hofgartner, J.D., Lopes, R.M.C., Lorenz,

R.D., Lunine, J.I., MacKenzie, S.M., Malaska, M.J. and Wood, C.A., 2018. Morphological evidence that Titan's southern hemisphere basins are paleoseas. Icarus, 310, 140-148.

Bishop, B., Lewis, R.C., Radebaugh, J. and Christiansen, E.H., 2017. Spatial variations of dune parameters and relationship to elevation and geographic position within the Belet sand sea. LPI, (1964), 2425.

Borga, M., Stoffel, M., Marchi, L., Marra, F. and Jakob, M., 2014. Hydrogeomorphic response to extreme rainfall in headwater systems: flash floods and debris flows. Journal of Hydrology, *518*, 194-205.

Brossier, J.F., Rodriguez, S., Cornet, T., Lucas, A., Radebaugh, J., Maltagliati, L., Le Mouélic, S., Solomonidou, A., Coustenis, A., Hirtzig, M. and Jaumann, R., 2018. Geological evolution of Titan's equatorial regions: possible nature and origin of the dune material. *Journal of Geophysical Research: Planets*, *123*(5), pp.1089-1112.

Brewer, J., 1981. Thermal effects of thrust faulting. *Earth and Planetary Science Letters*, *56*, pp.233-244.

Brown, R.H., Baines, K.H., Bellucci, G., Bibring, J.-B., Buratti, B.J., Capaccioni, F., Cerroni, P., Clark, R.N., Coradini, A., Cruikshank, D.P., Drossart, P., Formisano, V., Jaumann, R., Langevin, Y., Matson, D.L., McCord, T.B., Mennella, V., Miller, E., Nelson, R.M., Nicholson, P.D., Sicardy, B., Sotin, C., 2004. The Cassini Visual and Infrared Mapping Spectrometery (VIMS) investigation. Space Science Reviews 115, 111-168. doi: 10.1007/s11214-004-1453-x.

Brown, R.H., Soderblom, L.A., Soderblom, J.M., Clark, R.N., Jaumann, R., Barnes, J.W., Sotin,

C., Buratti, B., Baines, K.H. and Nicholson, P.D., 2008. The identification of liquid ethane in Titan's Ontario Lacus. Nature, 454, 607-610.

Bull, W.B., 1977. The alluvial-fan environment. Progress in Physical geography, 1, 222-270.

Burr, D.M., Jacobsen, R.E., Roth, D.L., Phillips, C.B., Mitchell, K.L., Viola, D., 2009. Fluvial network analysis on Titan: Evidence for subsurface structures and west to east wind flow, southwestern Xanadu. Geophysical Research Letters 36, L22203. doi: 10.1029/2009GL040909.

Burr, D.M., Perron, J.T., Lamb, M.P., Iriwin, R.P. III, Collins, G.C., Howard, A.D., Sklar, L.S., Moore, J.M., Ádámkovics, M., Baker, V.R., Drummond, S.A., Black, B.A., 2013a. Fluvial features on Titan: Insights from morphology and modeling. Geological Society of America Bulletin 125, 299-321. doi: 10.1130/B30612.1

Burr, D.M., Drummond, S.A., Cartwright, R., Black, B.A. and Perron, J.T., 2013b. Morphology of fluvial networks on Titan: Evidence for structural control. *Icarus*, *226*(1), pp.742-759.

Byrne, S. and Ingersoll, A.P., 2003. A sublimation model for Martian south polar ice features. Science, 299, 1051-1053.

Choukroun, M., Grasset, O., Tobie, G. and Sotin, C., 2010. Stability of methane clathrate hydrates under pressure: Influence on outgassing processes of methane on Titan. Icarus, 205, 581-593.

Clark, R.N., Curchin, J.M., Barnes, J.W., Jaumann, R., Soderblom, L., Cruikshank, D.P., Brown, R.H., Rodriguez, S., Lunine, J., Stephan, K., Hoefen, T.M., Le Mouelic, S., Sotin, C., Baines, K.H., Buratti, B.J., Nicholson, P.D., 2010. Detection and mapping of hydrocarbon deposits on Titan. Journal of Geophysical Research 115, E10005. doi: 10.1029/2009JE003369.

Collins, G.C., 2005. Relative rates of fluvial bedrock incision on Titan and Earth. Geophys. Res. Lett. 32 L22202.

Cook-Hallett, C., Barnes, J.W., Kattenhorn, S.A., Hurford, T., Radebaugh, J., Stiles, B.,Beuthe, M., 2015. Global contraction/expansion and polar lithospheric thinning on Titan from patterns of tectonism, Journal of Geophysical Research: Planets, 120, 1220–1236. doi:10.1002/2014JE004645.

Corlies, P., Hayes, A.G., Birch, S.P.D., Lorenze, R., Stiles, B.W., Kirk, R., Poggiali, V., Zebker, H., Iess, L., 2017. Titan's Topography and Shape at the End of the Cassini Mission. Geophysical Research Letters 44, 11754-11761. doi: 10.1002/2017GL075518.

Cornet, T., Cordier, D., Bahers, T.L., Bourgeois, O., Fleurant, C., Mouélic, S.L. and Altobelli, N., 2015. Dissolution on Titan and on Earth: Toward the age of Titan's karstic landscapes. Journal of Geophysical Research: Planets, 120, 1044-1074.

Crow-Willard, E.N. and Pappalardo, R.T., 2015. Structural mapping of Enceladus and implications for formation of tectonized regions. Journal of Geophysical Research: Planets, 120, 928-950.

Elachi, C., Allison, M., Anderson, Y., Boehmer, R., Callahan, P., Encrenaz, P., Flameni, E., Francescetti, G., Gim, Y., Hamilton, G., Hensley, S., Janssen, M., Johnson, W., Kelleher, K., Kirk, R., Lopes, R., Lorenz, R., Lunine, J., Muhleman, D., Ostro, S., Paganelli, F., Picardi, G., Posa, F., Roth, L., Seu, R., Shaffer, S., Soderblom, L., Stiles, B., Stofan, E., Vetrella, S., Wall, S., West, R., Wood, C., Wye, L., Zebker, H., 2005a. Cassini RADAR's First View of the Surface of Titan. Science 13, 970-974.

Elachi, C., Allison, M.D., Borgarelli, L., Encrenaz, P., Im, E., Janssen, M.A., Johnson, W.T.K., Kirk, R.L., Lorenz, R.D., Lunine, J.I., Muhleman, D.O., Ostro, S.J., Picardi, G., Posa, F., Rapley, C.G., Roth, L.E., Seu, R., Soderblom, L.A., Vetrella, S., Wall, S.D., Wood, C.A., Zebker, H.A., 2005b. RADAR: The Cassini Titan Radar Mapper, Space Sci. Rev. 117, 71-110.

Elachi, C., Wall, S., Janssen, M., Stofan, E., Lopes, R., Kirk, R., Lorenz, R., Lunine, J. Paganelli, F., Soderblom, L., Wood, C., Wye, L., Zebker, H., Anderson, Y., Ostro, S., Allison, M., Boehmer, R., Callahan, P., Encrenaz, P., Flamini, E., Francescetti, G., Gim, Y., Hamilton, G., Hensley, S., Johnson, W., Kelleher, K., Muhleman, D., Picardi, G., Posa, F., Roth, L., Seu, R., Shaffer, S., Stiles, B., Vetrella, S., West, R., 2006. Titan Radar Mapper observations from Cassini's T3 fly-by. Nature 441, 709-713, doi:10.1038/nature04786.

Faulk, S.P., Mitchell, J.L., Moon, S. and Lora, J.M., 2017. Regional patterns of extreme precipitation on Titan consistent with observed alluvial fan distribution. Nature Geoscience, 10, 827-831.

Ferrill, D.A., Morris, A.P., Waiting, D.J., Franklin, N.M. and Sims, D.W., 2003, March. Influence of gravity on the geometry of Martian normal faults. In Lunar and Planetary Science Conference (Vol. 34).

Fulchignoni, M., Ferri, F., Angrilli, F., Ball, A.J., Bar-Nun, A., Barucci, M.A., Bettanini, C., Bianchini, G., Borucki, W., Colombatti, G., Coradini, M., Coustenis, A., Debei, S., Falkner, P., Fanti, G., Flamini, E., Gaborit, V., Grard, R., Hamelin, M., Harri, A.M., Hathi, B., Jernej, I., Leese, M.R., Lehto, A., Lion Stoppato, P.F., López-Moreno, J.J., Mäkinen, T., McDonnell, J.A.M., McKay, C.P., Molina-Cuberos, G., Neubauer, F.M.,

Pirronello, V., Rodrigo, R., Saggin, B., Schwingenschuh, K., Seiff, A., Simões, F., Svedhem, H., Tokano, T., Towner, M.C., Trautner, R., Withers, P., Zarnecki, J.C., 2005. In situ measurements of the physical characteristics of Titan's environment. Nature 438, 785-791. doi: 10.1038/nature04314.

Grasset, O. and Pargamin, J., 2005. The ammonia–water system at high pressures: Implications for the methane of Titan. Planetary and Space Science, 53, 371-384.

Greeley R. and Batson, R.M., 1990. Planetary Mapping. New York: Cambridge University Press.

Griffith, C.A., Penteado, P.F., Turner, J.D., Neish, C.D., Mitri, G., Montiel, N.J., Schoenfeld, A. and Lopes, R.M., 2019. A corridor of exposed ice-rich bedrock across Titan's tropical region. Nature Astronomy, 3, 642-648.

Groussin, O., Attree, N., Brouet, Y., Ciarletti, V., Davidsson, B., Filacchione, G., Fischer, H.H., Gundlach, B., Knapmeyer, M., Knollenberg, J. and Kokotanekova, R., 2019. The thermal, mechanical, structural, and dielectric properties of cometary nuclei after Rosetta. Space Science Reviews, 215, 29.

Hayes, A., Aharonson, O., Callahan, P., Elachi, C., Gim, Y., Kirk, R., Lewis, K., Lopes, R., Lorenz, R., Lunine, J., Mitchell, K., Mitri, G., Stofan, E., Wall, S., 2008. Hydrocarbon lakes on Titan: Distribution and interaction with a porous regolith. Geophysical Research Letters 35, L09204. doi: 10.1029/2008GL033409.

Hayes, A.G., Birch, S.P.D., Dietrich, W.E., Howard, A.D., Kirk, R.L., Poggiali, V., Mastrogiuseppe, M., Michaelides, R.J., Corlies, P.M., Moore, J.M. and Malaska, M.J., 2017. Topographic constraints on the evolution and connectivity of Titan's lacustrine basins. Geophysical Research Letters, 44, 11-745.

Hayes, A.G., Lorenz, R.D. & Lunine, J.I. A post-Cassini view of Titan's methane-based hydrologic cycle, 2018. Nature Geoscience 11, 306–313. doi: 10.1038/s41561-018-0103-y

Hedgepeth, J.E., Neish, C.D., Turtle, E.P., Stiles, B.W., Kirk, R. and Lorenz, R.D., 2020. Titan's impact crater population after Cassini. Icarus, 113664.

Hörst, S.M., 2017. Titan's atmosphere and climate. Journal of Geophysical Research: Planets, 122, 432-482.

Janssen, M.A., Lorenz, R.D., West, R., Paganelli, F., Lopes, R.M., Kirk, R.L., Elachi, C., Wall, S.D., Johnson, W.T.K., Anderson, Y., Boehmer, R.A., Callahan, P., Gim, Y., Hamilton, G.A., Kelleher, K.D., Roth, L., Stiles, B., Le Gall, A., Cassini RADAR Team, 2009. Titan's Surface at 2.2-cm wavelength imaged by the Cassini RDAR radiometer: Calibration and first results. Icarus 200, 222-239. doi: 10.1016/j.icarus.2008.10.017.

Janssen, M.A., Le Gall, A. and Wye, L.C., 2011. Anomalous radar backscatter from Titan's surface? Icarus, 212, 321-328.

Janssen, M.,A., Le Gall, A., Malaska, M.J., Lopes, R.M., Lorenz, R.D., Malaska, M.J., Hayes, A.G., Neish, C.D., Solomonidou, A., Mitchell, K.L., Radebaugh, J., Keihm, S.J., Choukroun, M., Leyrat, C., Encrenaz, P.J., Mastroguiseppe, M., 2016. Titan's Surface at 2.218-cm Wavelength wavelength imaged by the Cassini RADAR radiometer: Results and interpretation through the first ten years of observations. Icarus 270, 443-459. doi: 10.1016/j.icarus.2015.09.027.

Jaumann, R., Brown, R.H., Stephan, K., Barnes, J.W., Soderblom, L.A., Sotin, C., Le Mouélic,

S., Clark, R.N., Soderblom, J., Buratti, B.J., Wagner, R., McCord, T.B., Rodriguez, S., Baines, K.H., Cruikshank, D.P., Nicholson, P.D., Griffith, C.A., Langhans, M., Lorenz, R.D., 2008. Fluvial erosion and post-erosional processes on Titan. Icarus 197, 526-538. doi: 10.1016/j.icarus.2008.06.002.

Jaumann, R., Kirk, R. L. Lorenz, R. D., Lopes, R. M.C., Stofan, E. Turtle, E. P. Keller, H. U. Wood, C. A., Sotin, C. Soderblom, L. A., Tomasko, M. G., 2009. Geology and Surface Processes on Titan. In: Brown, R. H., Leberton, J.-P., Waite, J. H. (Eds.), Titan from Cassini-Huygens. Springer, New York, pp 75–140.

Jennings, D.E., Cottini, V., Nixon, C.A., Achterberg, R.K., Flasar, F.M., Kunde, V.G., Romani, P.N., Samuelson, R.E., Mamoutkine, A., Gorius, N.J.P., Coustenis, A., , Tokano, T., 2016. Surface temperatures on Titan during northern winter and spring. The AstroPhysical Journal Letters, 816, L17. doi: 10.3847/2041-8205/816/1/L17

Kargel, J.S., 1995. Cryovolcanism on the icy satellites. In Comparative planetology with an Earth perspective. Springer, Dordrecht, 101-113.

Karkoschka, E. and Schröder, S.E., 2016. Eight-color maps of Titan's surface from spectroscopy with Huygens' DISR. Icarus, 270, 260-271.

Karkoschka E., McEwen A., Perry J., 2017. Producing the Best Global Mosaic of Titan's Surface Albedo Using Cassini Images. LPSC 48, #2518.

Kirk, R.L., Callahan, P., Seu, R., Lorenz, R.D., Paganelli, F., Lopes, R. and Elachi, C., 2005. RADAR reveals Titan topography.

Kinczyk, M.J., Byrne, P.K., Collins, G.C., Patterson, G.W. and Bohnenstiehl, D.R., 2019. Stress Risers in Enceladus' Cratered Terrain. LPI, (2132), 1446.

Kocurek, G. and Lancaster, N., 1999. Aeolian system sediment state: theory and Mojave Desert Kelso dune field example. Sedimentology, 46, 505-515.

Kocurek, G. and Ewing, R.C., 2005. Aeolian dune field self-organization–implications for the formation of simple versus complex dune-field patterns. Geomorphology, 72, 94-105.

Krasnopolsky, V.A., 2009. A photochemical model of Titan's atmosphere and ionosphere. Icarus 201, 226-256. doi: 10.1016/j.icarus.2008.12.038.

Krasnopolsky, V., 2014. Chemical composition of Titan's atmosphere and ionosphere: Observations and the photochemical model. Icarus 236 (2014), 83-91. doi: 10.1016/j.icarus.2014.03.041.

Lachenbruch, A.H., 1980. Frictional heating, fluid pressure, and the resistance to fault motion. Journal of Geophysical Research: Solid Earth, 85, 6097-6112.

Langhans, M.H., Jaumann, R., Stephan, K., Brown, R.., Buratti, B.J., Clark, R.N., Baines, K.H., Nicholson, P.D., Lorenz, R.D., Soderblom, L.A., Soderblom, J.M., Sotin, C., Barnes, J.W., Nelson, R., 2012. Titan's fluvial valleys: Morphology, distribution, and spectral properties. Planetary and Space Science 60, 34-51. doi: 10.1016/j.pss.2011.01.020.

Lavvas, P.P., Coustenis, A., Vardavas, I.M., 2008. Coupling photochemistry with haze formation in Titan's atmosphere, Part II: Results and validation with Cassini/Huygens data. Planetary and Space Science 56, 67-99. doi: 10.1016/j.psss.2007.05.027.

Le Corre, L., Le Mouélic, S., Sotin, C., Combe, J.P., Rodriguez, S., Barnes, J.W., Brown, R.H., Buratti, B.J., Jaumann, R., Soderblom, J. and Soderblom, L.A., 2009. Analysis of a cryolava flow-like feature on Titan. Planetary and Space Science, 57, 870-879.

Le Gall, A., Janssen, M.A., Paillou, P., Lorenz, R.D. and Wall, S.D., 2010. Radar-bright channels on Titan. Icarus, 207, 948-958.

Le Gall, A., Janssen, M.A., Wye, L.C., Hayes, A.G., Radebaugh, J., Savage, C., Zebker, H., Lorenz, R.D., Lunine, J.I., Kirk, R.L. and Lopes, R.M.C., 2011. Cassini SAR, radiometry, scatterometry and altimetry observations of Titan's dune fields. Icarus, 213, 608-624.

Le Gall, A., Hayes, A.G., Ewing, R., Janssen, M.A., Radebaugh, J., Savage, C. and Encrenaz, P., 2012. Latitudinal and altitudinal controls of Titan's dune field morphometry. Icarus, 217, 231-242.

Leier, A.L., DeCelles, P.G. and Pelletier, J.D., 2005. Mountains, monsoons, and megafans. Geology, 33, 289-292.

Le Mouélic, S., Paillou, P., Janssen, M.A., Barnes, J.W., Rodriguez, S., Sotin, C., Brown, R.H., Baines, K.H., Buratti, B.J., Clark, R.N. and Crapeau, M., 2008. Mapping and interpretation of Sinlap crater on Titan using Cassini VIMS and RADAR data. Journal of Geophysical Research: Planets, 113.

Le Mouélic, S., Cornet, T., Rodriguez, S., Sotin, C., Seignovert, B., Barnes, J.W., Brown, R.H., Baines, K.H., Buratti, B.J., Clark, R.N. and Nicholson, P.D., 2019. The Cassini VIMS archive of Titan: From browse products to global infrared color maps. Icarus, 319, 121-132.

Lewis, R.C., Radebaugh, J., Christiansen, E.H., Tass, E.S. and Le Gall, A., 2018, March. A Comparative Analysis of Sediment Transport and Deposition Trends of the Namib Sand Sea and Belet on Titan. In *Lunar and Planetary Science Conference* (Vol. 49).

Liu, Z.Y., Radebaugh, J., Harris, R.A., Christiansen, E.H., Neish, C.D., Kirk, R.L., Lorenz, R.D.,

the Cassini RADAR team, 2016a. The tectonics of Titan: global structural mapping from Cassini RADAR. Icarus 270, 14–29.

Liu, Z.Y.C., Radebaugh, J., Harris, R.A., Christiansen, E.H. and Rupper, S., 2016b. Role of fluids in the tectonic evolution of Titan. Icarus, 270, 2-13.

Lopes, R.M., Mitchell, K.L., Stofan, E.R., Lunine, J.I., Lorenz, R., Paganelli, F., Kirk, R.L., Wood, C.A., Wall, S.D., Robshaw, L.E. and Fortes, A.D., 2007. Cryovolcanic features on Titan's surface as revealed by the Cassini Titan Radar Mapper. Icarus, 186, 395-412.

Lopes, R.M.C., Stofan, E.R., Pecyno, R., Radebaugh, J., Mitchell, K.L., Mitri, G., Wood, C.A., Kirk, R.L., Wall, S.D., Lunine, J.L., Hayes, A., Lorenz, R., Farr, T., Wye, L., Craig, J., Ollerenshaw, R., Janssen, M., LeGall, A., Paganelli, F., West, R., Stiles, B., Callahan, P., Anderson, Y., Valora, P., Soderblom, L., and the Cassini RADAR Team, 2010. Distribution and interplay of geologic processes on Titan from Cassini radar data. Icarus 205, 540–558. doi: 10.1016/j.icarus.2009.08.010.

Lopes, R.M.C., Kirk, R.L.; Mitchell, K.L., Le Gall, A., Barnes, J.W., hayes, A., Kargel, J., Wye, L., Radebaugh, J., Stofan, E.R., Janssen, M., Neish, C., Wall, S., Wood, C.A., Lunine, J.I., Malaska, M.J., 2013. Cryovolcanism on Titan: New results from Cassini RADAR and VIMS. Journal of Geophysical Research: Planets 118, 1-20. doi: 10.1002/jgre.20062.

Lopes, R.M.C., Malaska, M.J., Solomonidou, A., Le Gall, A., Janssen, M.A., Neish, C.D., Turtle, E.P., Birch, S.P.D., Hayes, A.G., Radebaugh, J., Coustenis, A., Schoenfeld, A, Stiles, B.W., Kirk, R.L., Mitchell, K.L., Stofan, E.R., Lawrence, K.,J. and the Cassini RADAR Team, 2016. Nature, distribution, and origin of Titan’s Undifferentiated Plains. Icarus 270, 162-182. doi: 10.1016/j.icarus.2015.11.034.

Lopes, R.M., Malaska, M., Schoenfeld, A., Solomonidou, A., Williams, D.D., Birch, S., Le Gall, A.A. and Radebaugh, J., 2019, December. Geomorphological map of the Soi crater region on Titan. In AGU Fall Meeting 2019. AGU.

Lopes, R.M.L., Malaska, M.J., Schoenfeld, A.M., Solomonidou, A., Birch, S.P.D., Florence, M., Hayes, A.G., Williams, D.A., Radebaugh, J., Verlander T., Turtle, E.P., Le Gall, A., Wall, S., and the Cassini RADAR Team, 2020. A Global Geomorphological Map of Saturn's Moon Titan. Nature Astronomy 4, 228-233.

Lora, J.M., Lunine, J.I., Russell, J.L., 2014. GCM Simulations of Titan's Middle and Lower Atmosphere and Comparison to Observations. Available from: <arXiv: 1412.7995> [astro-ph.EP].

Lorenz, R. D., 1993. The Life, Death and Afterlife of a Raindrop on Titan, Planetary and Space Science, 41, 647-655.

Lorenz, R.D., Lunine, J.I., 1996. Erosion on Titan: Past and Present. Icarus 196, 79-91.

Lorenz, R.D., 2000. The Weather on Titan. Science 290, 467-468.

Lorenz , R.D., Wall, S., Radebaugh, J., Boubin, G., Reffet, E., Janssen, M., Stofan, E., Lopes, R., Kirk, R., Elachi, C., Lunine, J., Mitchell, K., Paganelli, F., Soderblom, L., Wood, C., Wye, L., Zebker, H., Anderson, Y., Ostro, S., Allison, M., Boehmer, R., Callahan, P., Encrenaz, P., Ori, G.G., Francescitti, G., Gim, Y., Hamilton, G., Hensley, S., Johnson, W., Kelleher, K., Muhleman, D., Picardi, G., Posa, F., Roth, L., Seu, R., Shaffer, S., Stiles, B., Vetrella, S., Flamini, E., West, R., 2006. The Sand Seas of Titan: Cassini RADAR Observations of Longitudinal Dunes. Science 312, 724-727. doi: 10.1126/science.1123257.

Lorenz, R.D., Wood, C.A, Lunine, J.I., Wall, S.D., Lopes, R.M., Mitchell, K.L., Paganelli, F., Anderson, Y.Z., Wye, L., Tsai, C., Zebker, H., Stofan, E.R., 2007. Titan's young surface: Initial impact crater survey by Cassini RADAR and model comparison. Geophysical Research Letters 34, L07204. doi: 10.1029/2006GL028971.

Lorenz, R.D., Lopes, R.M., Paganelli, F., Lunine, J.I., Kirk, R.L., Mitchell, K.L., Soderblom, L.A., Stofan, E.R., Ori, G., Myers, M. and Miyamoto, H., 2008a. Fluvial channels on Titan: initial Cassini RADAR observations. Planetary and Space Science, 56, 1132-1144.

Lorenz, R.D., Mitchell, K.L., Kirk, R.L., Hayes, A.G., Aharanson, O., Zebker, H.A., Paillou, P., Radebaugh, J., Lunine, J.I., Janssen, M.A., Wall, S.D., Lopes, R.M., Stiles, B., Ostro, S., Mitri, G., Stofan, E.R., 2008b. Titan's inventory of organic surface materials. Geophysical Research Letters 35, L02206. doi: 10.1029/2007GL032118.

Lorenz, R.D., Radebaugh, J., 2009. Global pattern of Titan's dunes: Radar survey from the Cassini prime mission. Geophysical Research Letters 36, L03202. doi: 10.1029/2008GL036850.

Lorenz, R.D., Stiles, B.W., Aharonson, O., Lucas, A., Hayes, A.G., Kirk, R.L., Zebker, H.A., Turtle, E.P., Neish, C.D., Stofan, E.R., Barnes, J.W., and the Cassini RADAR Team, 2013. A global topographic map of Titan. Icarus 225, 367-377. doi: 10.1016/j.icarus.2013.04.002

Lucas, A., Rodriguez, S., Narteau, C., Charnay, B., Du Pont, S.C., Tokano, T., Garcia, A., Thiriet, M., Hayes, A.G., Lorenz, R.D. and Aharonson, O., 2014. Growth mechanisms and dune orientation on Titan. *Geophysical Research Letters*, *41*(17), pp.6093-6100.

Lunine, J.I. and Stevenson, D.J., 1987. Clathrate and ammonia hydrates at high pressure: Application to the origin of methane on Titan. Icarus, 70, 61-77.

Lunine, J., Artemieva, N., Lorenz, R., Flamini, E., 2005. Numerical modeling of impact cratering on Titan with implications for the age of Titan's surface.Lunar Planet. Sci. 36. Abstract 1504.

Lunine, J.I., Elachi, C., Wall, S.D., Janssen, M., Allison, M.D., Anderson, Y., Boehmer, R., Callahan, P., Encrenaz, P., Flamini, E., Franceschetti, G., Gim, Y., Hamilton, G., Hensley, S., Johnson, W.T.K., Kelleher, K., Kirk, R.L., Lopes, R.M., Lorenz, R., Muhlemen, D.O., Orosei, R., Ostro, S.J., Paganelli, F., Paillou, P., Picardi, G., Posa, F., Radebaugh, J., Roth, L.E., Seu, R., Shaffer, S., Soderblom, L.A., Stiles, B., Stofan, E.R., Vetrella, S., West, R., Wood, C.A., Wye, L., Zebker, H., Alberti, G., Karkoschka, E., Rizk, B., McFarlane, E., See, C., Kazeminejad, B., 2008. Titan's diverse lanscapes as evidenced by Cassini RADAR's third and fourth looks at Titan. Icarus 195, 415-433. doi: 10.1016/j.icarus.2007.12.022.

Lunine, J.I. and Atreya, S.K., 2008. The methane cycle on Titan. Nature Geoscience, 1, 159-164.

Lunine, J.I. and Lorenz, R.D., 2009. Rivers, lakes, dunes, and rain: crustal processes in Titan's methane cycle. Annual Review of Earth and Planetary Sciences, 37, 299-320.

MacKenzie, S.M., Barnes, J.W., Sotin, C., Soderblom, J.M., Le Mouélic, S., Rodriguez, S., Baines, K.H., Buratti, B.J., Clark, R.N., Nicholson, P.D. and McCord, T.B., 2014. Evidence of Titan's climate history from evaporite distribution. Icarus, 243, 191-207.

Malaska, M., Radebaugh, J., Lorenz, R., Mitchell, K., Farr, T., Stofan, E., 2010. Identification of Karst-like Terrain on Titan from Valley Analysis. Lunar and Planetary Science Conference XLI, Abstract #1544.

Malaska, M., Radebaugh, J., Mitchell, K., Lopes, R., Wall, S., Lorenz, R., 2011. Surface dissolution model for Titan karst. Oral presentation at the First International Planetary Cave Research Workshop, Carlsbad, NM, October 2011. Abstract 8018.

Malaska, M.J., Hodyss, R., 2014. Dissolution of benzene, naphthalene, and biphenyl in a simulated Titan lake. Icarus 242, 74-81. doi: 10.1016/j.icarus.2014.07.022.

Malaska, M.J., Lopes, R.M.C., Williams, D.A., Neish, C.D., Solominidou, A., Soderblom, J.M., Schoenfeld, A.M., Birch, S.P.D., Hayes, A.G., Le Gall, A., Janssen, M.A., Farr, T.G., Lorenz, R.D., Radebaugh, J.,Turtle, E.P., 2016a. Geomorphological map of the Afekan Crater region, Titan: Terrain relationships in the equatorial and mid-latitude regions. Icarus 270, 130-161. doi: 10.1016/j.icarus.2016.02.021.

Malaska, M.J., Lopes, R.M., Hayes, A.G., Radebaugh, J., Lorenz, R.D., Turtle, E.P., 2016b. Material transport map of Titan: the fate of dunes. Icarus 270, 183-196. doi: 10.1016/j.icarus.2015.09.029.

Malaska, M.J., Radebaugh, J., Lopes, R.M., Mitchell, K.L., Verlander, T., Schoenfeld, A.M., Florence, M.M., Le Gall, A., Solomonidou, A., Hayes, A.G. and Birch, S.P., 2020. Labyrinth terrain on Titan. Icarus, 113764.

Malin, M.C., Caplinger, M.A. and Davis, S.D., 2001. Observational evidence for an active surface reservoir of solid carbon dioxide on Mars. Science, 294, 2146-2148.

Martin, E.S., Kattenhorn, S.A., Collins, G.C., Michaud, R.L., Pappalardo, R.T. and Wyrick, D.Y., 2017. Pit chains on Enceladus signal the recent tectonic dissection of the ancient cratered terrains. Icarus, 294, 209-217.

McKenzie, D. and Brune, J.N., 1972. Melting on fault planes during large earthquakes. Geophysical Journal International, 29, 65-78.

Mitchell, J.L., 2012. Titan's transport-driven methane cycle. The Astrophysical Journal Letters, 756, L26.

Mitri, G., A.P. Showman, J.I. Lunine, and R.D. Lorenz, 2007. Hydrocarbon lakes on Titan. Icarus 186, 385-394.

Mitri, G., Showman, A.P., Lunine, J.I. and Lopes, R.M., 2008. Resurfacing of Titan by ammonia-water cryomagma. Icarus, 196, 216-224.

Mitri, G., Bland, M.T., Showman, A.P., Radebaugh, J., Stiles, B., Lopes, R.M.C., Lunine, J.I., Pappalardo, R.T., 2010. Mountains on Titan: Modeling and observations. Journal of Geophysical Research: Planets 115, E10002. doi: 10.1029/2010/JE003592

Mitri, G., Lunine, J.I., Mastrogiuseppe, M. and Poggiali, V., 2019. Possible explosion crater origin of small lake basins with raised rims on Titan. Nature Geoscience, 12, 791-796.

Moore, J.M. and Pappalardo, R.T., 2011. Titan: An exogenic world? Icarus, 212, 790-806.

Mousis, O., Guilbert-Lepoutre, A., Brugger, B., Jorda, L., Kargel, J.S., Bouquet, A., Auger, A.T., Lamy, P., Vernazza, P., Thomas, N. and Sierks, H., 2015. Pits formation from volatile outgassing on 67P/Churyumov–Gerasimenko. The Astrophysical Journal Letters, 814, L5.

Neish, C.D., Lorenz, R.D., Kirk, R.L. and Wye, L.C., 2010. Radarclinometry of the sand seas of Africa's Namibia and Saturn's moon Titan. Icarus, 208, 385-394.

Neish, C.D., Lorenz, R.D., 2012. Titan's global crater population: A new assessment. Planetary and Space Science 60, 26-33. doi: 10.1016/j.psss.2011.02.016.

Neish, C.D., Kirk, R.L., Lorenz, R.D., Bray, V.J., Schenk, P., Stiles, B.W., Turtle, E., Mitchell,

K., Hayes, A. and Cassini RADAR Team, 2013. Crater topography on Titan: Implications for landscape evolution. Icarus, 223, 82-90.

Neish, C.D., Barnes, J.W., Sotin, C., MacKenzie, S., Soderblom, J.M., Le Mouélic, S., Kirk,R.L., Stiles, B.W., Malaska, M.J., Le Gall, A., Brown, R.H., Baines,K.H., Buratti, B., Clark, R.N., Nicholson, P.D., 2015. Spectral properties of Titan's impact craters imply chemical weathering of its surface. Geophysical Research Letters 42, 3746–3754. doi: 10.1002/2015GL063824.

Neish, C.D., Molaro, J.L., Lora, J., Howard, A.D., Kirk, R.L., Schenk, P., Bray, V.J, Lorenz, R.D., 2016. Fluvial erosion as a mechanism for crater modification on Titan. Icarus 270, 114-182.

Nelson, R.M., Kamp. L.W., Lopes, R.M.C., Matson, D.L., Kirk, R.L., Hapke, B.W., Wall, S.D., Boryta, M.D., Leader, F.E., Smythe, W.D., Mitchell, K.L., Baines, K.H., Jaumann, R., Sotin, C., Clark, R.N., Cruikshank, D.P., Drossart, P., Lunine, J.I., Combes, M., Bellucci, G., Bibring, J-P., Capaccioni, F., Cerroni, P., Coradini, A., Formisano, V., Filacchione, G., Langevin, Y., McCord, T.B., Mennella, V., Nicholson, P.D., Sicardy, B., Irwin, P.G.J. (2009). Photometric Changes on Saturn's Moon Titan: Evidence for Cryovolcanism. Geophys. Res. Lett., 36, L04202, doi:10.1029/2008GL036206.

Newton, J. G., and L. W. Hyde, 1971. Sinkhole problem in and near Roberts Industrial Subdivision, Birmingham, Alabama. Alabama Geological Survey Circ. 68, 49.

Newton, J.G., 1987. Development of sinkholes resulting from man's activities in the eastern United States (No. 968-969). US Geological Survey.

Paganelli, F., Janssen, M.A., Lopes, R.M., Stofan, E., Wall, S.D., Lorenz, R.D., Lunine, J.I.,

Kirk, R.L., Roth, L., Elachi, C. and Team, T.C.R., 2008. Titan's surface from the Cassini RADAR radiometry data during SAR mode. Planetary and Space Science, 56, 100-108.

Pappalardo, R.T. and Collins, G.C., 2005. Strained craters on Ganymede. Journal of structural geology, 27, 827-838.

Perron, J.T., Lamb, M.P., Koven, C.D., Fung, I.Y., Yager, E., Ádámkovics, M., 2006. Valley formation and methane precipitation rates on Titan. Journal of Geophysical Research 111, E11001. doi: 10.1029/2005JE002602.

Porco, C.C., West, R.A., Squyres, S., McEwen,A., Thomas, P., Murray, C.D., Delgenio, A., Ingersoll, A.P., Johnson, T.V, Neukum, G., Veverka, J., Dones, L., Brahic, A., Burns, J.A., Haemmerle, V., Knowles, B., Dawson, D., Roatsch, T., Beurle, K., Owen, W., 2004. Cassini Imaging Science: Instrument characteristics and anticipated scientific investigations at Saturn. Space Science Reviews 115, 363-497. doi: 10.1007/s11214-004-1456-7

Radebaugh, J., Lorenz, R.D., Kirk, R.L., Lunine, J.I., Stofan, E.R., Lopes, R.M.C., Wall, S.D., 2007. Mountains on Titan as observed by Cassini Radar. Icarus 192, 77-91. doi: 10.1016/j.icarus.2007.026.020.

Radebaugh, J., Lorenz, R.D., Lunine, J.I., Wall, S.D., Boubin, G., Reffet, E., Kirk, R.L., Lopes, R.M., Stofan, E.R., Soderblom, L., Allison, M., Janssen, M., Paillouo, P., Callahan, P., Spencer, C., Cassini RADAR Team, 2008. Dunes on Titan observed by Cassini Radar. Icarus 194, 690-703. doi: 10.1016/j.icarus.2007.10.015.

Radebaugh, J., Lorenz, R., Farr, T., Paillou, P., Savage, C., Spencer, C., 2010. Linear dunes on Titan and earth: Initial remote sensing comparisons. Geomorphology 121, 122-132. doi: 10.1016/j.geomorph.2009.09.02.022.

Radebaugh, J., Ventra, D., Lorenz, R.D., Farr, T., Kirk, R., Hayes, A., Malaska, M.J., Birch, S., Liu, Z.Y.C., Lunine, J. and Barnes, J., 2018. Alluvial and fluvial fans on Saturn's moon Titan reveal processes, materials and regional geology. Geological Society, London, Special Publications, 440, 281-305.

Schaber, G.G., Berlin, G.L. and Brown Jr, W.E., 1976. Variations in surface roughness within Death Valley, California: Geologic evaluation of 25-cm-wavelength radar images. Geological Society of America Bulletin, 87, 29-41.

Scholz, C.H., 1980. Shear heating and the state of stress on faults. Journal of Geophysical Research: Solid Earth, 85, 6174-6184.

Seignovert, B., Le Mouélic, S., Brown, R.H., Joseph, E., Karkoschka, E., Pasek, V., Sotin, C. and Turtle, E.P., 2019. Titan’s global map combining VIMS and ISS mosaics. EPSC, 2019, EPSC-DPS2019.

Sinclair, W.C., 1982. Sinkhole development resulting from ground-water withdrawal in the Tampa area, Florida (81-50). US Geological Survey, Water Resources Division.

Soderblom, L.A., Kirk, R.L., Lunine, J.I., Anderson, J.A., Baines, K.H., Barnes, J.W., Barrett, J.M., Brown, R.H., Buratti, B.J., Clark, R.N., Cruikshank, D.P., Elachi, C., Janssen, M.A., Jaumann, R., Karkoschka, E., Le Mouélic, S., Lopes, R.M., Lorenz, R.D., McCord, T.B., Nicholson, P.D., Radebaugh, J., Rizk, B., Sotin, C., Stofan, E.R., Sucharski, T.L., Tomasko, M.G., Wall, S.D., 2007. Correlations between Cassini VIMS spectra and RADAR SAR images: Implications for Titan's surface composition and the character of the Huygens Probe Landing Site. Planetary and Space Science 55, 2025-2036. doi: 10.1016/j.pss.2007.04.014.

Solomonidou, A., Hirtzig, M., Coustenis, A., Bratisolis, E., le Mouelic, S., Rodriguez, S., Stephan, K., Drossart, P., Sotin, C., Jaumann, R., Bornw, R.H., Kyriakopoulos, K., Lopes, R.M.C., Bampasidis, G., Stamatelopoulou-Seymour, K., Moussas, X., 2014. Surface albedo properties of geologicaly interesting areas on Titan. Journal of Geophysical Research 119, 1729-1747. doi: 10.1002/2014JE004634.

Solomonidou, A., Coustenis, A., Lopes, R.M., Malaska, M.J., Rodriguez, S., Drossart, P., Elachi, C., Schmitt, B., Philippe, S., Janssen, M. and Hirtzig, M., 2018. The spectral nature of Titan's major geomorphological units: constraints on surface composition. Journal of Geophysical Research: Planets, 123, 489-507.

Solomonidou, A., Neish, C., Coustenis, A., Malaska, M., Le Gall, A., Lopes, R., Werynski, A., Lawrence, K., Altobelli, N., Witasse, O., Schoenfeld, A. and Matsoukas, C., Baziotis, I., Drossart, P., 2020a. The chemical composition of impact craters on Titan: Implications for exogenic processing. Astronomy & Astrophysics.

Solomonidou, A., Le Gall, A., Malaska, M.J., Birch, S.P.D., Lopes, R.M.C., Coustenis, A., Rodriguez, S., Wall, S.D., Michaelides, R.J., Nasr, M.R. and Elachi, C., 2020b. Spectral and emissivity analysis of the raised ramparts around Titan's northern lakes. Icarus, 344, p.113338.

Sotin, C., Jaumann, R., Buratti, B.J., Brown, R.H., Clark, R.N., Soderblom, L.A., Baines, K.H., Bellucci, G., Bibring, J.P., Capaccioni, F. and Cerroni, P., 2005. Release of volatiles from a possible cryovolcano from near-infrared imaging of Titan. Nature, 435, 786-789.

Spigner, B.C., 1978. Review of Sinkhole-collapse Problems in a Carbonate Terrane. The Commission.

Stock, J.D., 2013. 9.23 Waters Divided: A History of Alluvial Fan Research and a View of Its Future.

Stiles, B.W., Hensley, S., Gim, Y., Bates, D.M., Kirk, R.L., Hayes, A., Radebaugh, J., Lorenz, R.D., Mitchell, K.L., Callahan, P.S., Zebker, H., Johnson, W.T.K., Wall, S.D., Wood, C.A., Janssen, M., Pelletier, F., West, R.D., Veramacheneni, C., Cassini RADAR Team, 2009. Determining Titan Surface Topography from Cassini SAR data. Icarus 202, 584-598. doi: 10.1016/j.icarus.2009.03.032.

Stofan, E.R., Elachi, C., Lunine, J.I., Lorenz, R.D., Stiles, B., Mitchell, K.L., Ostro, S., Soderblom, L., Wood, C., Zebker, H., Wall, S., Janssen, M., Kirk, R., Lopes, R., Paganelli, F., Radebaugh, J., Wye, L., Anderson, Y., Allison, M., Boehmer, R., Callahan, P., Encrenaz, P., Flamini, E., Francescetti, G., Gim, Y., Hamilton, G., Hensley, S., Johnson, W.T.K., Kelleher, K., Muhlman, D., Paillou, P., Picardi, G., Posa, F., Roth, Seu, R., Shaffer, S., Vetrella, S., West, R., 2007. The lakes of Titan. Nature 445, 61-64. doi: 10.1038/nature05438.

Tanaka, K.L. and Golombek, M.P., 1989. Martian tension fractures and the formation of grabens and collapse features at Valles Marineris. In Lunar and Planetary Science Conference Proceedings (Vol. 19, pp. 383-396).

Telfer, M.W., Radebaugh, J., Cornford, B. and Lewis, C., 2019. Long-Wavelength Sinuosity of Linear Dunes on Earth and Titan and the Effect of Underlying Topography. Journal of Geophysical Research: Planets, 124, 2369-2381.

Thelen, A.E., Nixon, C.A., Chanover, N.J., Cordiner, M.A., Molter, E.M., Teanby, N.A., Irwin,

P.G.J., Serigano, J. and Charnley, S.B., 2019. Abundance measurements of Titan's stratospheric HCN, HC3N, C3H4, and CH3CN from ALMA observations. Icarus, 319, 417-432.

Thomas, P.C., Malin, M.C., Edgett, K.S., Carr, M.H., Hartmann, W.K., Ingersoll, A.P., James, P.B., Soderblom, L.A., Veverka, J. and Sullivan, R., 2000. North–south geological differences between the residual polar caps on Mars. Nature, 404, 161-164.

Tomasko, M.G., Archinal, B., Becker, T., Bézard, B., Bushroe, M., Combes, M., Cook, D., Coustenis, A., De Bergh, C., Dafoe, L.E. and Doose, L., 2005. Rain, winds and haze during the Huygens probe's descent to Titan's surface. Nature, 438, 765-778.

Turtle, E.P., Perry, J.E., Hayes, A.G., Lorenz, R.D., Barnes, J.W., McEwen, A.S., West, R.A., Del Genio, A.D., Barbara, J.M., Lunine, J.I., Schaller, E.L., Ray, T.L., Lopes, R.M.C., Stofan, E.R., 2011. Rapid and Extensive Surface Changes Near Titan's Equator: Evidence of April Showers. Science 331, 1414-1417. doi: 10.1126/science.1201063.

Vincent, J.B., Bodewits, D., Besse, S., Sierks, H., Barbieri, C., Lamy, P., Rodrigo, R., Koschny, D., Rickman, H., Keller, H.U. and Agarwal, J., 2015. Large heterogeneities in comet 67P as revealed by active pits from sinkhole collapse. Nature, 523, 63-66.

Wall, S.D., Lopes, R.M., Stofan, E.R., Wood, C.A., Radebaugh, J.L., Hörst, S.M., Stiles, B.W., Nelson, R.M., Kamp, L.W., Janssen, M.A. and Lorenz, R.D., 2009. Cassini RADAR images at Hotei Arcus and western Xanadu, Titan: Evidence for geologically recent cryovolcanic activity. Geophysical Research Letters, 36.

Waltham, A.C., Bell, F.G. and Culshaw, M.G., 2005. Sinkholes and subsidence: karst and cavernous rocks in engineering and construction. Springer Science & Business Media.

Werynski, A., Neish, C.D., Le Gall, A., Janssen, M.A. and Cassini RADAR Team, 2019. Compositional variations of Titan's impact craters indicates active surface erosion. Icarus, 321, 508-521.

Willacy, K., Allen, M. and Yung, Y., 2016. A new astrobiological model of the atmosphere of Titan. The Astrophysical Journal, 829, 79.

Williams, D.A., Radebaugh, J., Lopes, R.M.C., Stofan, E., 2011. Geomorphologic mapping of the Menrva region of Titan using *Cassini* RADAR data. Icarus 212, 744-750. doi: 10.1016/j.icarus.2011.01.014.

Wilson, I.G., 1971. Desert sand flow basins and a model for the development of ergs. Geographical Journal, 180-199.

Wilson, E.H., Atreya, S.K., 2004. Current state of modeling the photochemistry of Titan's mutually dependent atmosphere and ionosphere. Journal of Geophysical Research 109, E06002. doi: 10.1029/2003JE002181.

Wood, C.A., Lorenz, R., Kirk, R., Lopes, R., Mitchell, K., Stofan, E., and the Cassini RADAR Team, 2010. Impact craters on Titan. Icarus 206 (2010) 334-344. doi: 10.1016/j.icarus.2009.08.021.

Wood, C.A. and Radebaugh, J., Morphologic Evidence for Volcanic Craters near Titan's North Polar Region May 28, 2020. Journal of Geophysical Research: Planets, e2019JE006036.

Wye, L.C., Zebker, H.A., Ostro, S.J., West, R.D., Gim, Y., Lorenz, R.D. and Cassini RADAR Team, 2007. Electrical properties of Titan's surface from Cassini RADAR scatterometer measurements. *Icarus*, *188*(2), pp.367-385.

Wyrick, D., Ferrill, D.A., Morris, A.P., Colton, S.L. and Sims, D.W., 2004. Distribution,

morphology, and origins of Martian pit crater chains. Journal of Geophysical Research: Planets, 109.

- Chapter 5 -

5 Geomorphological map of the Soi crater region on Titan

5.1 Introduction

The Cassini-Huygens' mission revealed the once enigmatic moon Titan to be a geologically complex world, modified by both exogenic and putative endogenic processes. The largest moon of Saturn, Titan has a dense atmosphere and active hydrocarbon cycle that enables aeolian, fluvial, pluvial, and lacustrial processes. Relatively few impact craters are found (Wood et al., 2010; Neish and Lorenz, 2012, Neish et al., 2013; 2015; Werynski et al., 2019; Hedgepeth et al., 2020), confirming a geologically young surface. Organic materials, produced by long-term photochemical processing of methane and nitrogen in the upper atmosphere, cover much of Titan (Wilson and Atreya, 2004; Soderblom et al., 2007; Barnes et al., 2008, 2011; Lavvas et al., 2008; Krasnopolsky, 2009; Clark et al., 2010; Mackenzie et al., 2014; Brossier et al., 2018**;** Solomonidou et al., 2018; 2020a). Titan's equatorial zones are dominated by massive organic sand seas (Lorenz et al., 2006a; Radebaugh et al., 2008; Lopes et al., 2010; Rodriguez et al., 2014), whereas the mid-latitudes are dominated by "undifferentiated plains": patterns of wind deposition on Titan show that, for both northern and southern hemispheres, winds transport material from both the equatorial regions and high latitudes towards the mid-latitudes (a belt at ~35º), where materials are eventually concentrated and deposited as undifferentiated plains (Lopes et al., 2016; Malaska et al., 2016b; Solomonidou et al., 2020a). A variety of channel networks and fluvial valleys have been seen by both the Cassini orbiter and by the Huygens probe during its descent, suggesting that liquid hydrocarbons have flowed energetically across Titan's surface (Burr et al., 2009, 2013a, 2013b; Langhans et al., 2012; Birch et al., 2016; Radebaugh et al., 2018). Some channels even still contain liquids (Poggiali et al., 2016). Lakes and seas are found at high latitudes and the poles (Stofan et al., 2007; Mitri et al., 2007; Hayes et

al., 2008; Birch et al., 2016). Studies based on morphology have also constrained location and areal extent for polar paleoseas (e.g. Birch et al., 2018), with additional evidence for paleolakes at low latitudes (e.g. Moore and Howard, 2010). Evidence for evaporites on Titan, in particular within or around dry lakes and seas, is suggested by water-ice-poor, 5-μm bright material (e.g. Barnes et al. 2011; Michaelides et al., 2016). These evaporitic features cover's 1% of the moon's surface, with the greatest areal concentration in the equatorial basins Tui Regio and Hotei Regio, and not in the poles (MacKenzie et al., 2014). Taken together, the morphology and spectral studies suggest a historically wetter Titan with a larger inventory of surface liquid hydrocarbons, with the possibility of fossil seas or lakes at low latitudes. Evidence for tectonism and possible cryovolcanism have also been identified, similarly contributing to surface modification (Jaumann et al., 2008, 2009; Mitri et al., 2008, 2010; Radebaugh et al., 2007; Lopes et al., 2007, 2013; Wall et al., 2009; Nelson et al., 2009; Sohl et al., 2014; Solomonidou et al., 2013; 2016). Mountains and hummocky materials are mostly exposed at equatorial latitudes (e.g. Radebaugh et al., 2011), but also appear in smaller areas all over the surface and are thought to be remnants of the ancient ice crust (Lopes et al. 2010; 2016; 2019; 2020; Williams et al., 2011; Malaska et al., 2016a; 2020; Birch et al., 2017; Schoenfeld et al, 2021).

Planetary geologic mapping is a tool that helps us inventory and interpret the regional or global geologic history of planets and moons. For Saturn's moon Titan, we inventory the landscape using geomorphological terrain units defined by common radar backscatter and morphological characteristics (e.g. Lopes et al., 2016; Malaska et al., 2016a; Lopes et al., 2020; Schoenfeld et al., 2021), which may or may not correspond to true geological units (which are defined by rock composition, age, and history). We therefore refer to the map presented in this study as a geomorphologic map, which nonetheless allows us to infer geologic relationships. As such, the

goal of this endeavor is to reconstruct the geologic history of the Soi crater region, which is representative of the transition between the equatorial, mid-latitude, and high latitude northern regions of Titan, through detailed geomorphological mapping.

Our completed map details the types and extents of geomorphologic units present in the Soi crater region. We use the map infer relative stratigraphy between units and the possible geological processes responsible for their formation and evolution. The mapping presented here follows the general principles of previous Titan mapping (e.g., Stofan et al., 2006) and is a continuation of the detailed geomorphological mapping effort presented in Malaska et al. (2016a) and Schoenfeld et al. (2021). For this paper, we are particularly interested in examining the transition between the equatorial and mid-latitude terrains (such as mapped by Lopes et al., 2010; Malaska et al., 2016a; Schoenfeld et al., 2021) and the high latitude regions mapped by Birch et al. (2017). We used the Cassini's Synthetic Aperture Radar (SAR) data as the basemap, but we also incorporated information from non-SAR datasets, including microwave emissivity, topography, visible and infrared reflectance. A better understanding of such geologic processes will aid in the science return of Dragonfly, where new, high-resolution data can be used to test terrain evolution models derived from the detail mapping, and additionally guide the science objectives for future missions (e.g., Tobie et al., 2014; Lorenz et al., 2021; Rodriguez et al., 2022; Sulaiman et al., 2021).

5.2 Location and Geologic Setting

Our mapping encompasses the Soi crater region (Fig. 5.1), which we define as the area spanning from longitude 110º W to 180º W (from right to left, covering 70 degrees longitudinally;

see green square in Fig. 5.S1; all tables, figures, and additional text in supplementary material will be symbolized by 'S'). and from latitude 0 to 60º N. A portion of this area, from 170º W to 180º W, was previously examined in Malaska et al. (2016a) as part of the Afekan crater region map (yellow square in Fig. 5.S1). However, for our mapping purposes going forward we define Afekan as the area spanning the region from longitude 110º E to 180º W and from latitude 0 to 60º N. We expanded the Soi crater region to 180º W in order to include western features in our analysis. Figure 1 shows the Soi crater regional map with location of subsequent figures within this paper indicated in green. Figure S1 shows a context map of where the region is located as well as the overlap area previously published in Malaska et al. (2016a) and the South Belet region (magenta square in Fig. 5.S1) published by Schoenfeld et al. (2021).

The area contained in this region amounts to ~8×10^6 km^2 (~10% of Titan's surface). However, detailed mapping was only done for the areas within the Soi crater region covered at high resolution by SAR (4.7×10^6 km^2) and therefore, the fraction of Titan's total surface that was mapped at high-resolution is ~5.6%. The rest of the area was covered by non-SAR data (emissivity, ISS, VIMS), and mapped at lower resolution (see section 5.3.1.2). The Soi crater region contains a wide variety of terrain units and, when compared to the Afekan (Malaska et al., 2016a) and South Belet regions (Schoenfeld et al., 2021), appears to be representative of Titan's midlatitudes and equator. The region contains the NE section of Shangri-La dune field, a vast field of equatorial dunes at lower latitudes, ten impact craters we identify with confidence (including Soi), a large number of empty lakes, part of the Xanadu region, and large expanses of plains at midlatitudes.

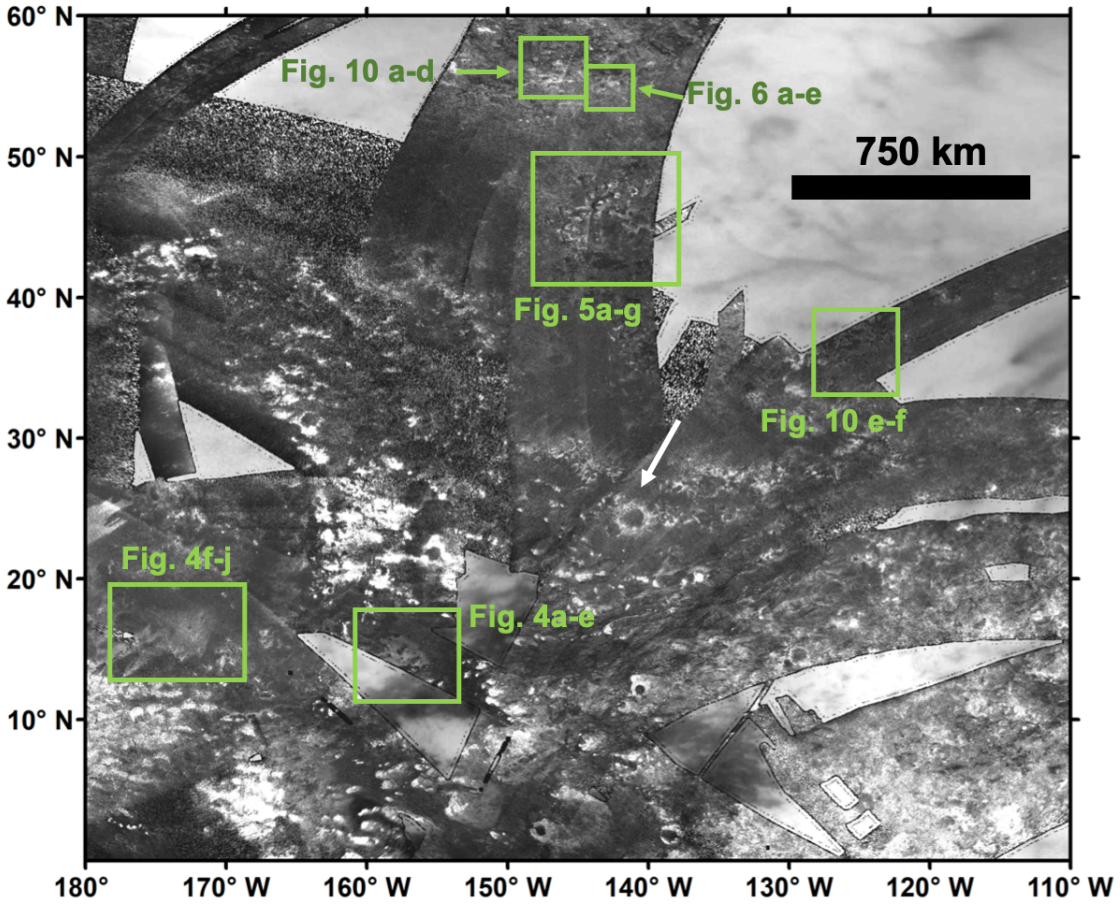

Fig. 5.1 SAR map of the Soi crater region. Locations of figure subsets included in this paper indicated with green boxes. The white arrow points to the Soi crater. The total area of the Soi crater region is 8×10^6 km^2. Scale bar applies to equatorial latitudes. North is at the top.

5.3 Geomorphological Mapping

To extract morphological information, Titan's hazy atmosphere limits the usefulness of visible and infrared data, as it scatters light at these wavelengths. RADAR is therefore the primary Cassini instrument used for studying Titan's geology since the longer wavelengths of microwave radiation interacts with the surface with negligible atmospheric interference. We recognize that,

from SAR images alone, the interpretation can be limited (e.g., Bratsolis et al., 2012). We therefore used SAR as the base data set, from which we drew the contacts between units, but also used data from other modes of the RADAR instrument (altimetry, SARTopo, radiometry) and data from VIMS and ISS to provide additional constraints on the terrain assignment.

5.3.1 Datasets

5.3.1.1 SAR

Cassini's RADAR is a multimode Ku-band (13.78 GHz, λ=2.17 cm) instrument (Elachi et al., 2005; Elachi et al., 2006; Stiles, 2017a,b) that operates in four modes: SAR, altimetry, scatterometry, and radiometry. We used data from the RADAR in its SAR mode to perform our initial geomorphological mapping and define the boundaries of the terrain contacts (Fig. 5.2a;b). Radar data is incidence angle corrected to be the same globally and for all terrains (Stiles et al., 2006); relative backscatter is then used to evaluate terrain brightness. Some terrain types are more sensitive to incidence angle than others (e.g. Malaska et al., 2016a), so a uniformly applied incidence angle correction introduces some uncertainty in our mapping, although we use overlapping SAR swaths (when available) to mitigate this uncertainty. Radar backscatter returned from the surface depends on roughness, incidence angle of the beam, dielectric constant of the material, slope angle orthogonal to the beam, volume scattering, structural properties, and subsurface inhomogeneities (such as layers of varying dielectric constant). A change of any one of these properties can produce a different radar backscatter; for example, a rough surface and a smooth surface of the same composition could present different properties to radar, and terrains of different compositions, but similar backscatter functions, could be undistinguishable in SAR

images. Details on the SAR and HiSAR nature of the data can be found in section 5.S1 and Table 5.S1 in the supplementary material.

5.3.1.2 Non-SAR

We also used data from the RADAR's radiometry mode and altimeter, in addition to VIMS and ISS observations (section 5.S1). Fig. 5.2 shows the different types of data used for the geomorphological mapping:

(a) SAR swaths were used as a basemap for geomorphological mapping. Underlying the SAR mosaic is the globally-controlled ISS mosaic, from Karkoschka et al. (2017, LPSC). Atmospheric scattering limits the usefulness of this mosaic. Soi crater is located near the center of the image (24.3ºN, -140.9ºW) and a portion of Xanadu is seen on the lower right.

(b) SAR and HiSAR coverage, where light green indicates the HiSAR swaths and blue indicates the high-resolution SAR swaths, as listed in Table 5.S1. Small parts of HiSAR that are not colored green in the figure were not used in our mapping due to significant noise. The background is VIMS RGB color ratio mosaic that complements the SAR swaths to cover the entire Soi crater region (description in Le Mouélic et al., 2019; Seignovert et al., 2019), and has been manually georeferenced to the SAR base mosaic. The RGB composite is 1.59/1.27 μm (R), 2.03/1.27 μm (G), and 1.27/1.08 μm (B).

(c) Elevation data. SARTopo data were obtained by the method described in Stiles et al. (2009). For SARTopo (along the SAR swath), colors represent relative elevations within each swath. Cooler colors are lower (to -800 m), and warmer tones are higher (to + 200 m) relative to the nominal 2,575 km radius sphere. Because of relatively large errors involved in SARTopo when compared across swaths, we only use the relative elevations along an individual swath track to help mapping; they do not provide an absolute scale. Digital Terrain Models (DTMs) are also

available with a typical error of ~100 m (Kirk et al., 2012; Corlies et al., 2017). Altimetry data are consistent across passes as shown by the overlap in the lower left of the region.

(d) Emissivity map from Janssen et al. (2016). Comparison with panel (a) shows that Xanadu has relatively low emissivity (cold colors), while the undifferentiated plains and dunes have higher (warm colors) emissivity.

(e) VIMS mosaic of the region prepared from a global VIMS mosaic (same details as for (b)).

(f) The ISS mosaic without the overlayed SAR mosaic.

More information on these instruments and their data can be found in the supplementary material in section 5.S1.

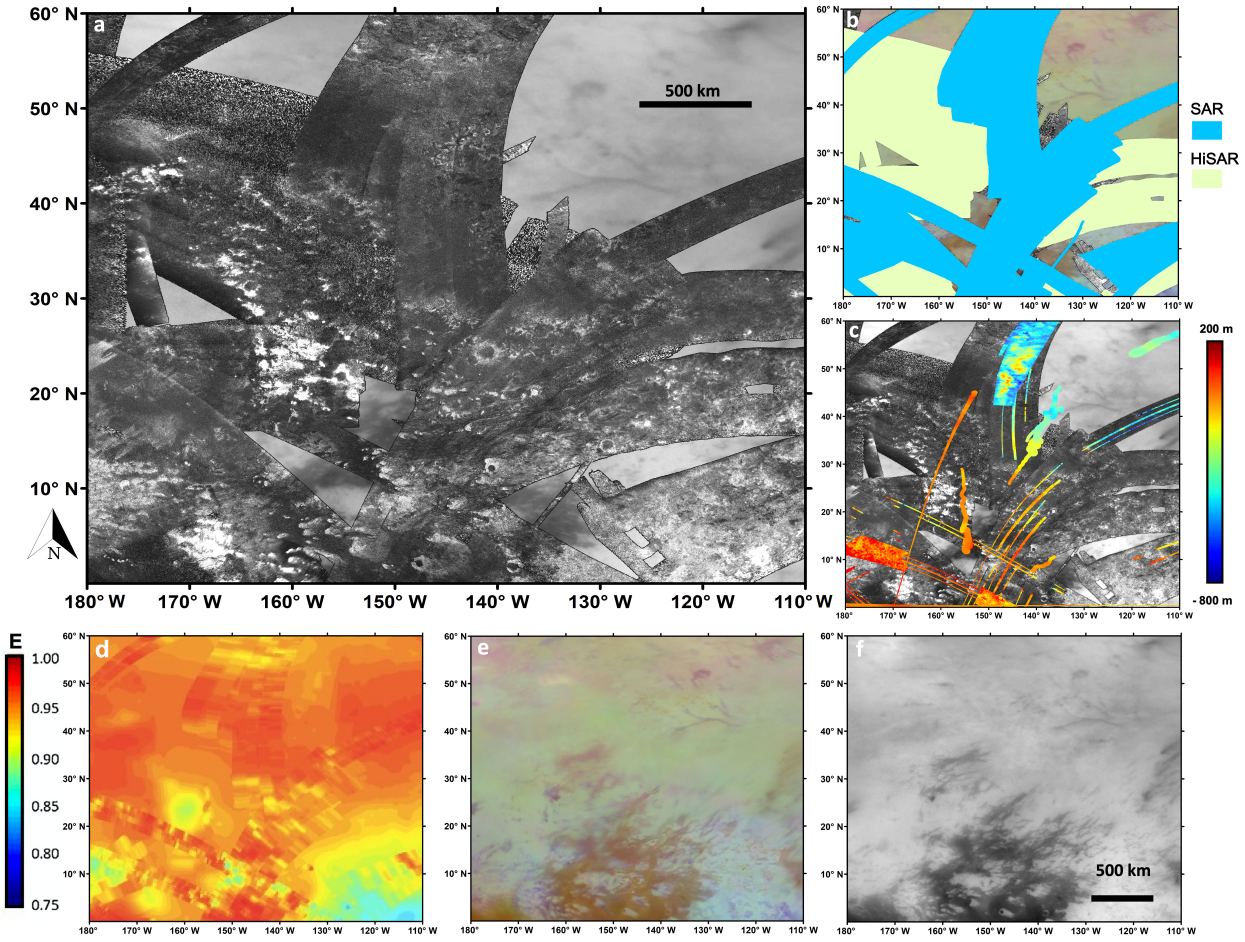

Fig. 5.2 Different types of Cassini data covering the Soi crater region. (a) SAR, (b) SAR and HiSAR, (c) SARTopo and DTM, (d) Emissivity, (e) VIMS, and (f) ISS.

5.3.2 Mapping area and technique

In general, we follow the technique outlined in Malaska et al. (2016a; 2020), Lopes et al. (2020), and Schoenfeld et al. (2021), and use SAR swaths as our primary basemap for conducting our geomorphological mapping. However, in this study we describe in greater detail the technique we developed for mapping beyond the boundaries of the SAR, i.e., non-SAR mapping, that makes use of lower resolution datasets such as ISS, VIMS, radiometry, and HiSAR in order to provide a more complete picture of Titan's surface characteristics (Lopes et al., 2020).

5.3.2.1 SAR mapping

The SAR swaths were mosaicked and loaded into the ArcGIS™ 10.6 (ESRI) software package and then used to categorize the surface based on morphological and backscatter properties. Contacts between terrains of different radar backscatter or morphological signatures were drawn, the boundaries being determined by following procedures described in previous studies (e.g., Stofan et al., 2007; Lopes et al., 2010; 2016; Williams et al., 2011; Malaska et al., 2016a; Birch et al., 2017; Schoenfeld et al., 2021). We defined gradational contacts between units if a clear delineation could not be made at the resolution of the SAR images (~1 km). Using the drawn contacts, we built polygons and assigned a terrain unit classification based on feature morphology and radar backscatter. Data from SARTopo, radiometry, ISS, and VIMS, while not used to delineate units in the high-resolution contact mapping, were used to refine terrain classification as outlined in Malaska et al. (2016a).

In general, we only use the higher-resolution SAR swaths for mapping at an image scale of 1:800,000 (Greeley and Batson, 1990). However, in certain areas, HiSAR (a high-altitude SAR imaging mode with multi-km scale resolution) of sufficient quality were included in the base map mosaic and used for mapping. We determined if a HiSAR swath was of suitable quality based on the capacity to distinguish terrain units and subunits with the same level of detail as with a regular SAR swath; for example, if we were able to distinguish between "degraded hummocky terrains", "hummocky", and "mountainous". In total ~32% of the Soi crater region was mapped using the high-resolution SAR, while ~26% of the mapped area was done so with "good" HiSAR. Some data (particularly HiSAR with degraded resolution) were considered not to be of sufficient quality to map at the scale of 1:800,000, though these could potentially be mapped at larger scales (see section 3.2.2).

5.3.2.2 Non-SAR mapping

The mapping procedure outlined in Malaska et al. (2016a), Lopes et al. (2020), and Schoenfeld et al. (2021) involves correlating the SAR mapping units with characteristic signal return in radiometry, VIMS, and ISS. For example, the "featureless sand sheets" appear dark in radar, but they also appear dark in ISS, brown-purple in RGB VIMS false colors (1.59/1.27 μm (R), 2.03/1.27 μm (G), and 1.27/1.08 μm (B)), and have high emissivity in radiometry. This combination of characteristics is part of the definition established for the "featureless sand sheets" unit. Similarly, undifferentiated plains appear bland and dark in SAR and HiSAR but appear bright in ISS and have high emissivity in radiometry. We leveraged previously established correlations and used them to extend the mapping to the areas not imaged by SAR or HiSAR. The non-SAR areas were mapped at a much lower resolution than the SAR area, at a scale of 1:20,000,000 (Lopes

et al., 2020), and make up ~42% of the mapped region. We identify this larger scale mapping by labelling contacts drawn using the ISS, VIMS, as “approximate”.

Finally, for areas where HiSAR exists but is of insufficient quality, i.e. unable to distinguish between “degraded hummocky terrains”, “hummocky”, “mountainous”, etc, we still rely primarily on the radar backscatter for unit delineation, but use the NonSAR units for terrain assignment. For example, a unit that is both radar dark in the HiSAR and elongated in the E-W direction we assign as “undivided dunes”, whereas a radar bright unit with globular morphology we assign as “undivided hummocky/mountainous”. Contacts are drawn as “inferred” for the low-resolution HiSAR.

5.4 Geomorphologic mapping results

5.4.1 SAR units

The terrain classes and units, including the three new mapping units, in the Soi crater region were initially identified using the SAR mosaic basemap. The main terrain classes are Craters, Hummocky/mountainous, Labyrinth, Plains, dunes, and Lake and Basin. Each main terrain class is subdivided into terrain units based on morphology (general shape, texture, and basic appearance) and radar backscatter. In general, the radar backscatter is broadly classified as “high”, “medium”, “low”, or “variable” for each of the units. The main terrain units are described in Table 5.1 and local examples of each unit are shown in Fig. 5.3. The terrain unit abbreviations are a concatenation where the first letter refers to the broad terrain class (e.g., *p* for plains), the second letter stands for a finer descriptor for the terrain type (e.g., *u* for undifferentiated), and the last letter indicates the relative radar backscatter compared to the other units (e.g., *l* for low). Therefore, the undifferentiated plains abbreviation “*pul*”, refers to “plains-undifferentiated-low”, indicating a

plains unit with no distinct features and with a radar backscatter that is relatively lower (darker) than other units on Titan. For detailed description of the units, see Malaska et al. (2016a) (section 4), Lopes et al. (2020) (Methods), and Schoenfeld et al. (2021) (section 4). As with the Afekan and South Belet maps, we additionally include physical features (such as channels, impact features, and putative cryovolcanic features (Lopes et al., 2013) as a polyline or additional shape layer on the geomorphological map**.** However, the Soi crater region does not contain any putative cryovolcanic feature. See section 4.3 for the resulting geomorphology map and section 5.1.2 for the physical feature map.

In this study, we describe in detail three new mapping units not previously discussed in our mapping investigations: the bright gradational plains (*pgh*), the sharp-edged depressions (*bse*), and the ramparts (*brh*). It should be noted, that the sharp-edged depressions and the ramparts are features that have been identified and described for Titan, and are "new" only in the context of our mapping schema, but not new in the literature (e.g. Birch et al., 2017, 2019; Solomonidou et al., 2020b). Similarly, bright gradational plains (*pgh*) are consisted with features discussed in existing literature, but were not labeled as such (e.g. Radebaugh et al., 2018). We describe the characteristics of the units below as well as offer interpretations. Table 5.1 summarizes all the identified terrain classes, units, and unit codes in addition to locations of characteristic examples of the units.

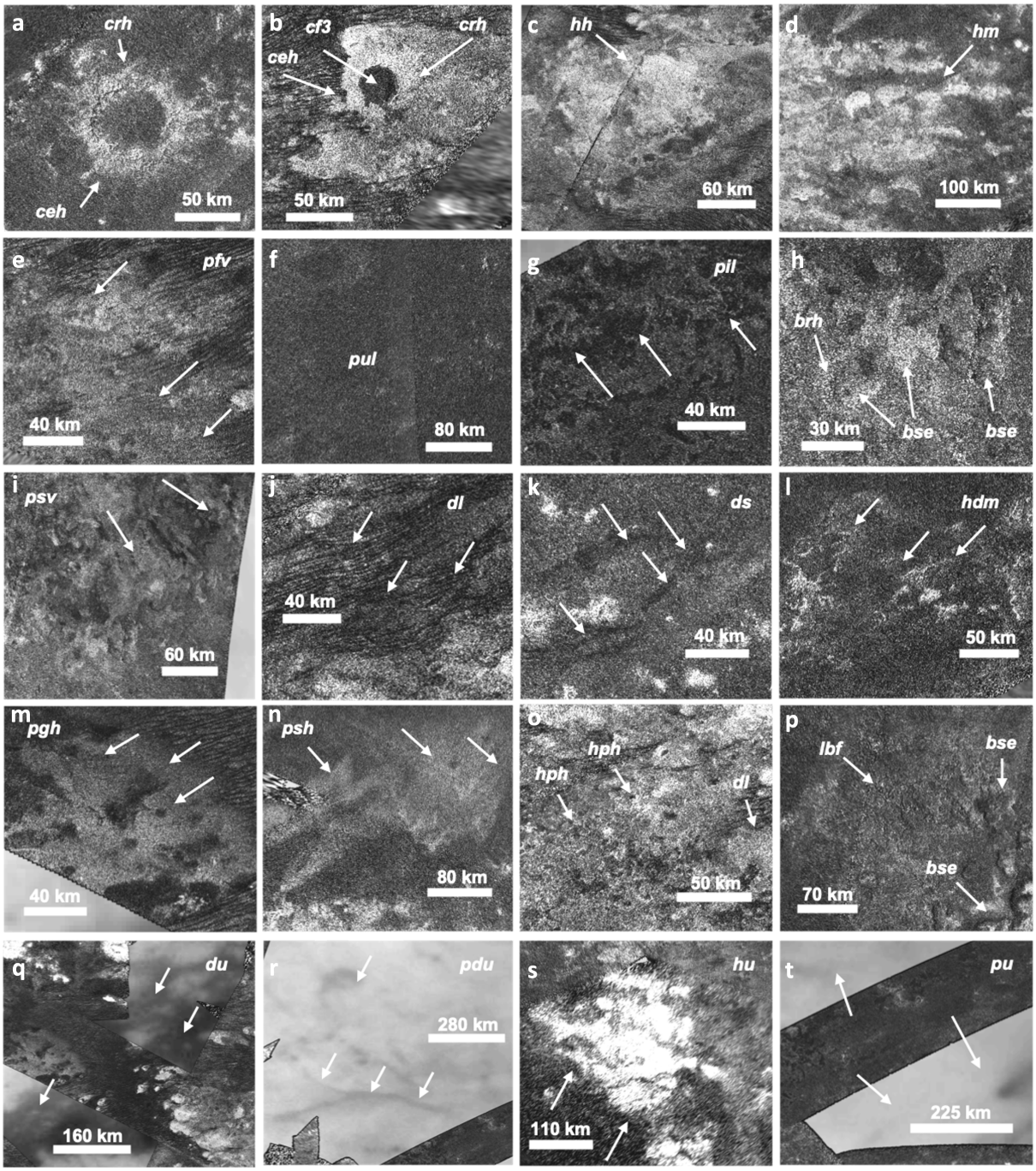

Fig. 5.3 SAR images of type examples of terrain units used within the Soi crater region. White arrows point to the type feature. The code references the terrain code in the text and in Table 5.2. Abbreviation key: (a) (image center: 24.3.5°N, 141°W) *crh* = crater rim, *ceh* = crater ejecta, (b) (11.5°N, 141°W) *cf3* = crater fill 3, (c) (7.9°N, 149.8°W) *hh* = hummocky, (d) (9.8°N, 174.5°W)

hm = mountains, (e) (7.8°N, 163.7°W) *pfv* = variable-featured plains, (f) (34.3°N, 144.3°W) *pul* = undifferentiated plains, (g) (36.8°N, 124.9°W) *pil* = dark irregular plains, (h) (55.3°N, 142.5°W) *bse* = sharp-edged depressions, *brh* = rampart (i) (57.6°N, 142°W) *psv* = scalloped plains, (j) (16.8°N, 137.4°W) *dl* = dark linear dunes, (k) (20.7°N, 142.9°W) *ds* = featureless sand sheets, (l) (27.7°N, 128.4°W) *hdm* = degraded hummocky, (m) (14.7°N, 157.4°W) *pgh* = bright gradational plains, (n) (15.4°N, 174.4°W) *psh* = streak-like plain, (o) (8.9°N, 115.3°W) *hph* = pitted hummocky, (p) (11.5°N, 141°W) *lbf* = finely dissected labyrinth, (q) (15.7°N, 153.3°W) *du* = undivided dunes, (r) (45.6°N, 126.6°W) *pdu* = undivided dark plains, (s) (4°N, 168.1°W) *hu* = undivided hummocky/mountainous, (t) (38.3°N, 120°W) *pu* = undivided plains.

*5.4.1.1 Bright gradational plains (*pgh*)*

The bright gradational plains (*pgh*) (type area*:* 14.5°N, 157.9°W) appear bright in radar, with a fairly uniform interior texture but with diffuse or gradational boundaries (Fig. 5.4a). Channels can be seen within or adjacent to the unit (Fig. 5.4b-e). Microwave emissivity of this unit (Fig. 5.4d) is relatively low (~0.92), appearing lower than the undifferentiated plains (*pul*) (~0.97), but not quite as low as the bright alluvial plains (*pah*), a unit present in the South Belet region (Schoenfeld et al., 2021). Similarly, in VIMS the unit appears blue in RGB (Fig. 5.4c) but not quite to the same degree as the bright alluvial plains (Schoenfeld et al., 2021), which seem to be associated with channels (e.g., Barnes et al., 2007; Langhans et al., 2012). In ISS the unit appears variable (Fig. 5.4b), characterized as varying patches of medium dark and bright. We also compare the bright gradational plains to the bright streak-like plains (*psh*). Fig. 5.4 present examples of both *pgh* and *psh* from the Soi crater region as shown in SAR and their equivalent annotated map (Fig. 5.4e,j), as well as their compared appearance in VIMS, ISS, and SARTopo.

Both units have similar signatures in radar (Fig. 5.4a,f), emissivity (Fig. 5d,i), VIMS (Fig. 5.4c,h), and ISS (Fig. 5.4b,g) , yet have different morphological boundaries. Their similarities suggest a shared origin with divergent endmember processing that accounts for their differences in morphology. We discuss further the similarity of these units in section 5.1.3.2. and offer a more detailed geologic interpretation.

Due to their lower microwave emissivity compared to the other plains units (Fig. 5.4d), such as the *pul* or *pfv*, and due to their association with adjacent channels (blue lines in Fig. 5.4) and highlands, we interpret the bright gradational plains as high backscatter material originating from fluvial processes. Their blue appearance in VIMS RGB colors (Fig. 5.4c), indicates spectral characteristics that may be consistent with that of water-ice (e.g., Barnes et al., 2007; Langhans et al., 2012; Coutelier et al., 2021). Both *pgh* and *psh* terrain units appear similar in VIMS and ISS to the linear (*dl*) and undivided (*du*) dunes terrain unts. Morphologically, the bright gradational plains are broader than the bright alluvial plains and lack their planform triangular morphology. We specifically interpret the *pgh* units as broad plains of SAR bright materials originating from alluvial fans and channels, perhaps accumulating in lowlands, similar to the SAR-bright lowlands described in Radebaugh et al. (2018) (Fig. 5.4k,l), eventually interacting or transitioning into darker plains/dunes. The *pgh* similarly may contain coalescing alluvial fans and channels that are unable to be individually resolved in the SAR. The broad reach of the bright gradational plains may also explain why they do not appear as radar-bright as the bright alluvial plains: further away from the highlands, the abundance of SAR-dark materials increases, consistent with the presence of finer grained materials capable of being transported over larger distances, and/or indicating the intrusion and mixing of organics sands from adjacent dunes or plains. The medium emissivity of the bright gradational plains supports this narrative, suggesting that loose conglomerates of fluvial

materials, which favor volume scattering, have since been mixed or buried by smoother, smaller-grained materials, dampening scattering effects.

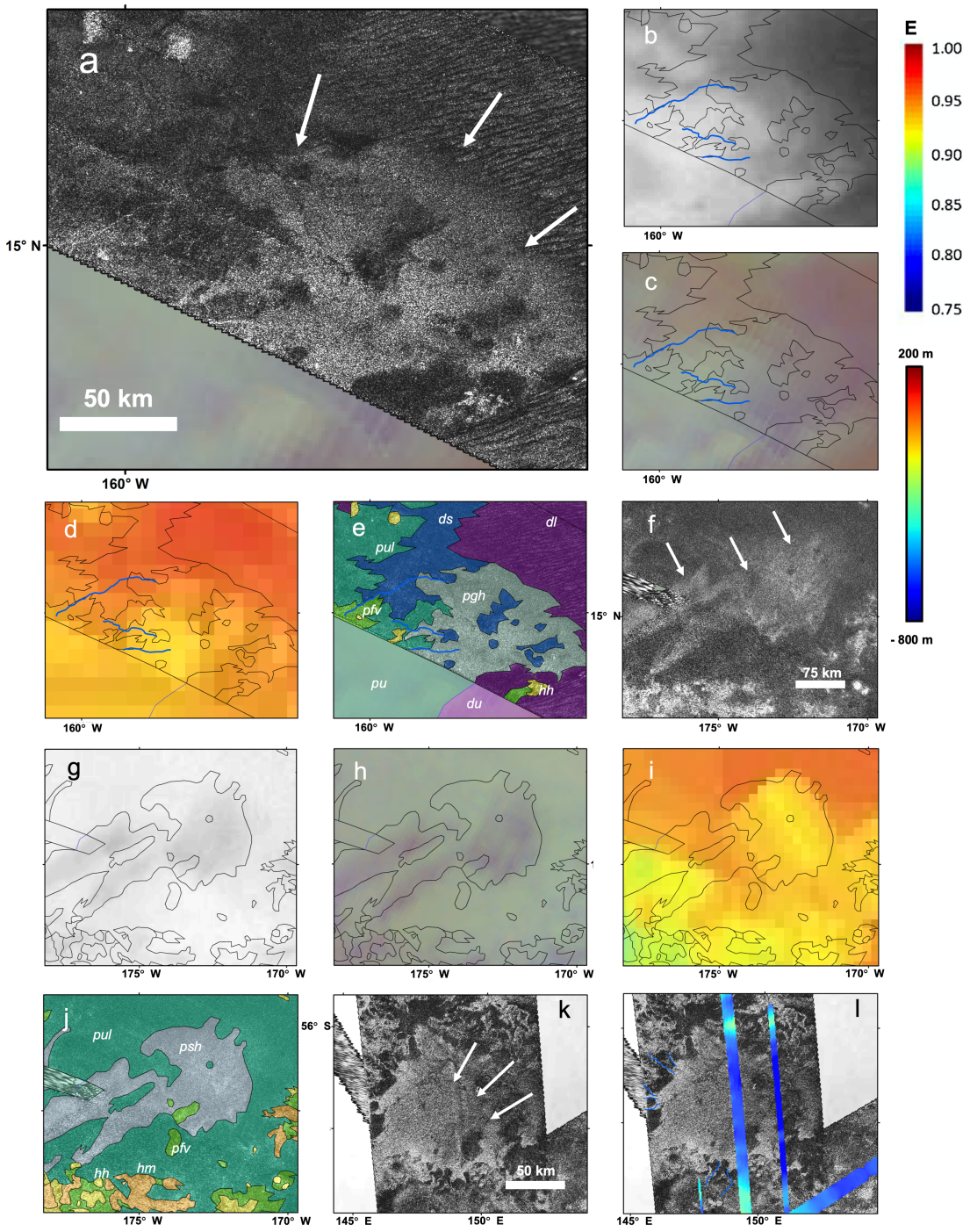

Fig. 5.4 Example of bright gradational plains (*pgh*) (a-e) and streak-like plains (*psh*) (f-j) within the Soi crater region: (a & f) SAR mosaic of the *pgh* and *psh* indicated by white arrows respectively. (b & g) ISS mosaic of the *pgh* and *psh* overlain with terrain unit contacts. Blue lines indicate channels identified in the image. (c & h) VIMS RGB mosaic of the *pgh* and *psh* with contacts (RGB colors controlled by 2, 1.59, and 1.27 μm channels respectively). (d & i) Emissivity map overlain with contacts. (e & j) Annotated terrain unit mapping on the SAR mosaics. Magenta corresponds to linear dunes (*dl*); blue to featureless sand sheets (*ds*), purple to undivided dunes (*du*); yellow to hummocky terrains (*hh*); dark yellow to mountains (hm); turquoise green to undifferentiated plains (*pul*); lime green to variable plains (*pfv*); grey to gradational plains (*pgh*); blue grey to streak-like plains (*psh*); and mint green to undivided plains (*pu*). The blue lines in (b-e) correspond to channels. (k) SAR mosaic of a "SAR-bright basin" as discussed in Radebaugh et al. (2018), located in South Ching Tu. Visible in the image are triangular, SAR-bright fans that grade away into moderately SAR-bright materials consistent with our definition of "bright gradational plains" (indicated by white arrows). (l) The same feature but with topographic information and channels indicated with blue lines. The *pgh* examples in the Soi crater region do not have topo traces overlapping the feature in such a way.

*5.4.1.2 Sharp-edged depressions (*bse*)*

The sharp-edged depressions (SEDs) (type area: 55.4°N, 141.3°W) are quasi-circular depressions that are either fully or partially enclosed by narrow rims (<10 km wide) that are several hundreds of meters higher than the surrounding area (Birch et al., 2019). The depressions have steep sloping walls that descend rapidly to relatively flat floors (e.g. Hayes et al., 2017) that span the entire interior of these depressions, which appear radar medium to radar dark with uniform

internal texture. The depressions are often entirely closed, with no evidence for inflow or outflow morphology (Hayes et al., 2017). Many SEDs have a bright-dark pairing around their boundary that correlates to elevated rim features on the order of hundreds of meters (Hayes et al., 2018; Birch et al., 2019). This pattern is similar to quasi-specular increases in backscatter seen on Titan's dunes and occurs due to slopes oriented perpendicular to the radar (Birch et al., 2019).

We interpret several features in the Soi crater region as SEDs with terrain unit code '*bse*' (Fig. 5.5). The SEDs of the Soi crater region are (Fig. 5.5a) morphologically consistent with the SEDs described in Hayes et al. (2017), and Birch et al. (2017; 2019) (Fig. 5.5i). The morphological similarities between filled and empty SEDs (e.g., Hayes et al., 2008; 2017; Birch et al., 2019), and the non-existence of radar-dark return characteristic of liquids, suggest that the dry SEDs represent previously filled, but now empty, lakes (Fig. 5.5i). Hence, we interpret the *bse* unit as a now empty lake basin, representing an increased latitudinal extent of lacustrine processes previously thought of as restricted to the polar regions. Fig. 5.5g shows a part of the annotated map of the Soi crater region including the *bse*.

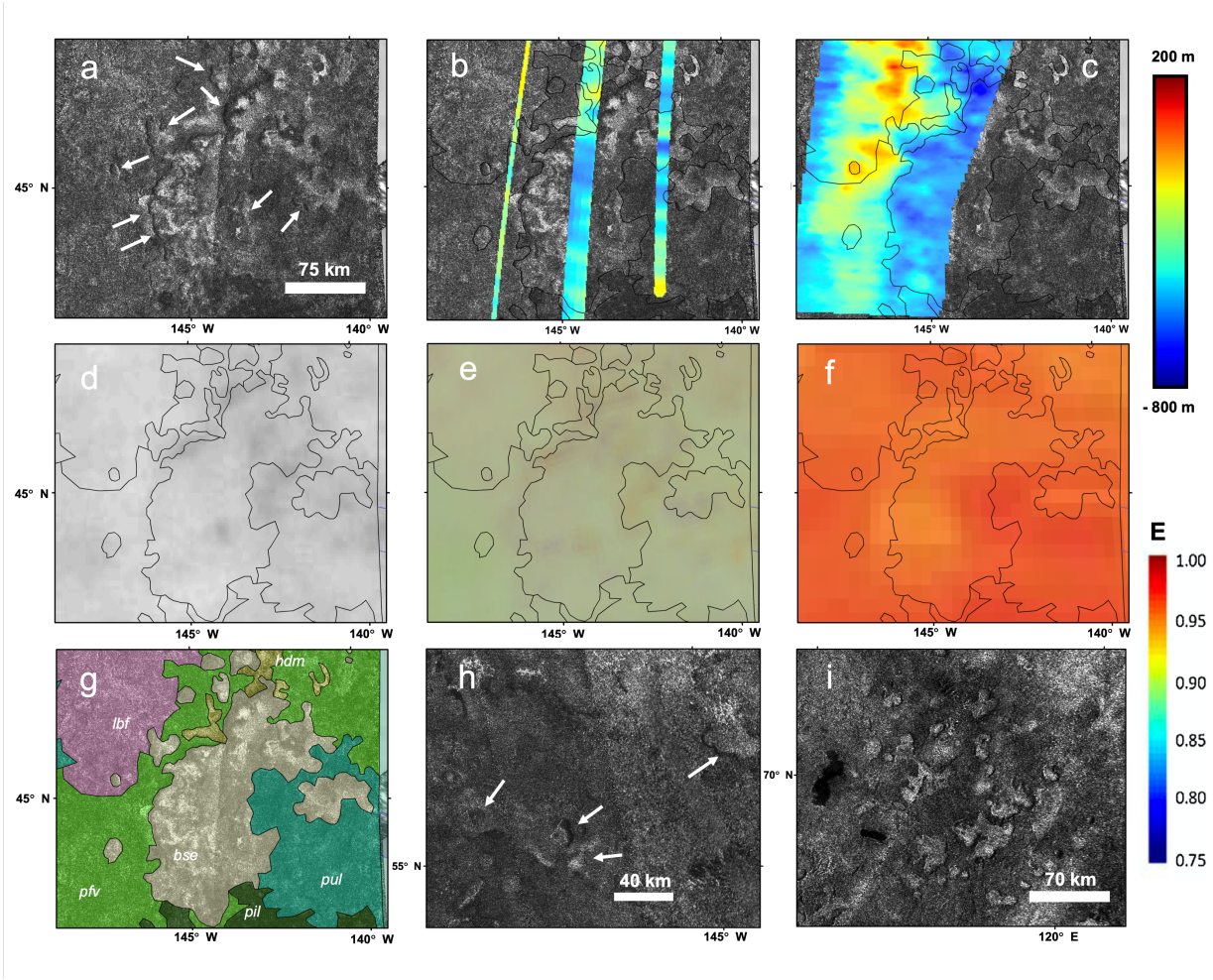

Fig. 5.5 Examples of sharp-edged depressions (*bse*) in the midlatitudes of the Soi crater region: (a) SAR mosaic, several of the empty depressions indicated by white arrows. Look direction is to the right. (b) SARTopo overlain on the SAR mosaic with contacts between mapped terrain units. (c) DTM overlain on the SAR mosaic. (d) ISS mosaic with terrain contacts. (e) VIMS RGB mosaic with terrain contacts (RGB colors controlled by 2, 1.59, and 1.27 μm channels respectively). (f) Emissivity map with terrain contacts. (g) Annotated terrain unit mapping on the SAR mosaic. Yellowish brown: degraded hummocky terrains (*hdm*); beige: sharp-edged depressions (*bse*); dark pink: finely dissected labyrinth (*lbf*); dark green: dark irregular plains (*pil*); lime green: variable featured plains (*pfv*); turquoise green: undifferentiated plains (*pul*). (h) Several instances of SEDs

identified in the Afekan crater region. (i) SAR image of an area in the north pole with empty and filled SEDs.

5.4.1.3 Ramparts (*brh*)

Ramparts (*brh*) (type area: 54.8°N, 144°W) are SAR-bright mound-like annuli that encircle a small population of Titan's lakes (Fig. 5.6a). They extend up to 10's of kilometers away from the shore of certain lakes (Solomonidou et al., 2020b) and appear locally elevated with respect to the surrounding terrain (Fig. 5.6b,c). SAR-bright, raised ramparts were first described in Solomonidou et al. (2020b), having been identified around some of the north polar lakes. The ramparts of the Soi crater region are morphologically consistent with the ramparts described in Solomonious et al. (2020b), and thus we consider them the same feature (Fig. 5.6f). Emissivity analysis of the raised ramparts show them to be radiometrically warm, close in value to that of Titan's labyrinth terrains and to the empty lake floors, pointing to an organic-rich composition (Fig. 5.6d). This compositional similarity is confirmed by VIMS analysis that shows that the infrared spectral response of the raised ramparts is similar to that of many of the empty lake floors, suggesting that both features are covered or made up of comparable materials (Solomonidou et al., 2020b).

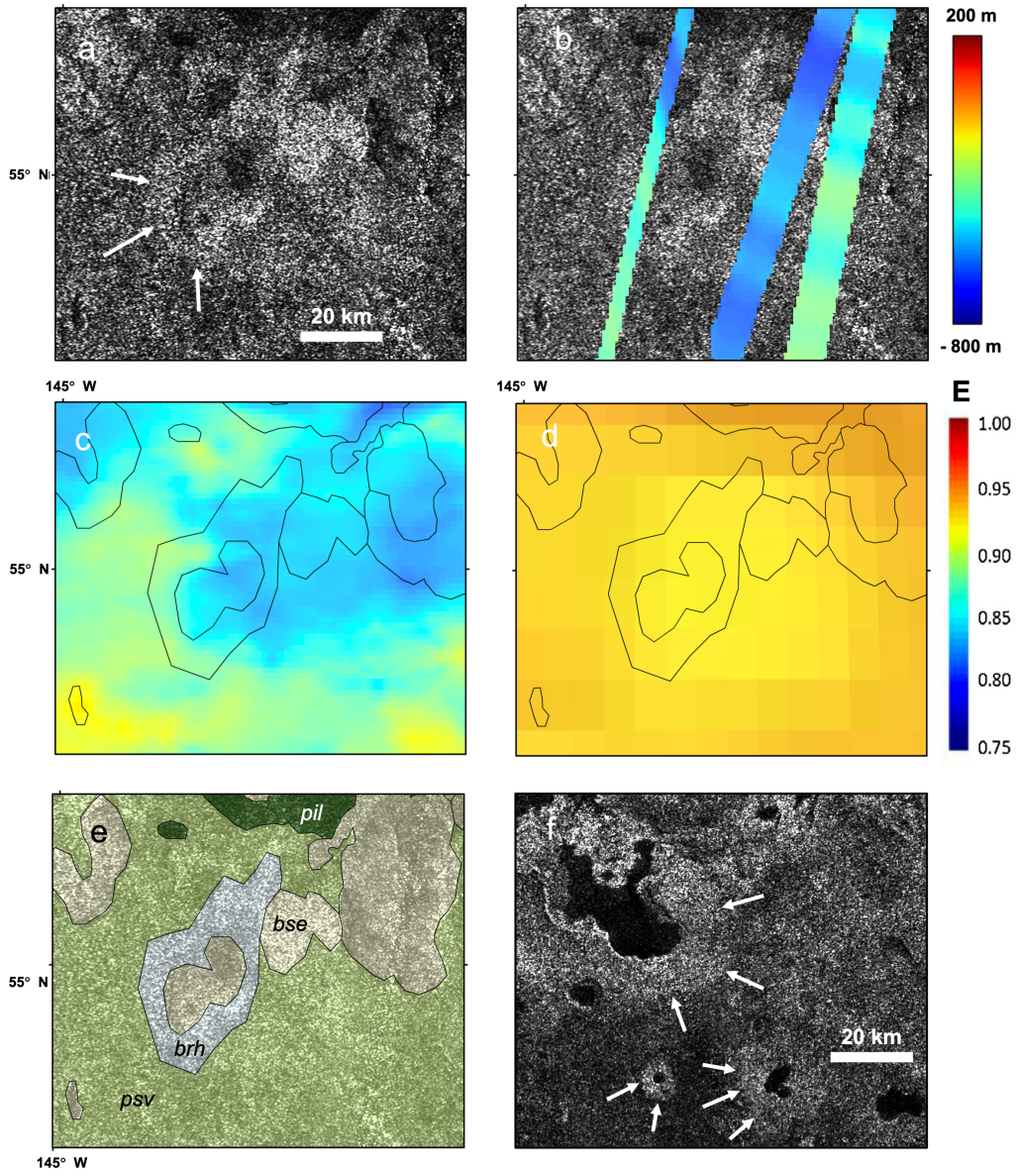

Fig. 5.6 Examples of ramparts (*brh*) in the midlatitudes of the Soi crater region: (a) SAR mosaic, a rampart around one of the empty depressions indicated by white arrows. Look direction is to the right. (b) SARTopo overlain on the SAR mosaic. (c) DTM overlain on the SAR mosaic with contacts between mapped terrain units. (d) Emissivity map with terrain contacts. (e) Annotated terrain unit mapping on the SAR mosaic. Beige: sharp-edged depressions (*bse*); dark green: dark

irregular plains (*pil*); olive green: scalloped plains (*psv*); light blue-grey: ramparts (*brh*). (f) SAR image of an area in the north pole with ramparts that were analyzed in Solomonidou et al. (2020b).

5.4.2 Non-SAR units

We use non-SAR data in an effort to maximize the use of Cassini surface data and to provide the most complete geomorphological map for the Soi crater region. These "non-SAR" mapping units have not been described in our previous mapping studies (e.g., Malaska et al., 2016a; Schoenfeld et al., 2021), but were briefly mentioned in Lopes et al. (2020). We thus elaborate on the descriptions and associated interpretations for the non-SAR mapping units that appear in the Soi crater region, which include undivided dunes (*du*), undivided hummocky/mountainous (*hu*), undivided dark plains (*pdu*), and undivided plains (*pu*).

*5.4.2.1 Undivided dunes (*du*)*

The undivided dunes (*du*) (type area: 7.8°N, 134.2°W) (Fig. 5.3q) are characterized as ISS dark areas that are extensive. Margins of this unit may show elongation in W-E direction with fingers that trend towards higher latitudes away from equator. On the boundaries of the SAR swaths, where mapped units extend beyond the borders and into the non-SAR datasets, regions of non-SAR that match the aforementioned characteristics tend to align well with mapping designated as dunes in the SAR. Radiometry shows high emissivity, similar to the linear dunes (*dl*) and the featureless sand sheets (*ds*). Undivided dunes appear dark brown in RGB VIMS, which is also similar to the appearance of the linear dunes (*dl*) and featureless sand sheets (*ds*) units. Given the low-resolution nature of non-SAR mapping, we permit less than 10% hummocky or plain terrains to be included within the mapped area.

Given their appearance in VIMS, ISS, and emissivity and their respective correlation to the characteristics expected of the dune units in these datasets, we interpret this unit as dune material deposits. Similarly, the strong directionality suggested by W-E elongation matches the material transport of dune materials and wind-swept morphology of aeolian processes (Malaska et al., 2016b). Subcategories of the dune unit that may be contained within the undivided dunes (*du*) include linear dunes (*dl*), reticulated dunes (*dr*), and featureless sand sheets (*ds*).

*5.4.2.2 Undivided hummocky/mountainous (*hu*)*

The undivided hummocky/mountainous (type area: 8.8°N, 149.2°W) (Fig. 5.3s) appear medium-dark in ISS, bright in RGB VIMS, and radar bright in HiSAR. In radiometry, this unit shows low emissivity (~0.91), akin to the emissivity of the hummocky (*hh*) (~0.87) and mountainous (*hm*) (~0.90) SAR units. In some instances, this unit shows E-W linearity, while other times it is more globular or amorphous. Broad areas of the unit may contain up to 50% of other units. Areas extrapolated beyond the borders of the SAR swaths generally align with units falling under the "hummocky/mountainous" major terrain category.

We interpret this unit as encompassing the units that fall into the "hummocky/mountainous" major terrain category, which include mountains, hummocky, and pitted hummocky (*hph*) terrain units. Thus, we also interpret this unit as exposure of ancient crust, with a radiometric and spectral response consistent with fractured water ice mixed with organic material (Malaska et al., 2016b; Solomonidou et al., 2018). Undivided hummocky/mountains units that are lineated in roughly the W-E direction we specifically interpret as mountain chains, although in the non-SAR and low resolution HiSAR we cannot see the bright-dark pairing in radar that is diagnostic of a mountain peak (Liu et al., 2016; Cook-Hallet et al., 2015).

*5.4.2.3 Undivided plains (*pu*)*

The undivided plains (*pu*) (type area: 49.5°N, 167.2°W) (Fig. 5.3t) are broad areas that appear bright in ISS and high in emissivity. This unit dominates the mid-latitudes, but it also appears in the polar and equatorial regions in patches broken up by the sand seas and the undivided dunes. In low resolution HiSAR, they have a medium level of backscatter, comparable to the undifferentiated plains (*pul*). Given their broad area, they may contain up to 20% of other terrain units that cannot be distinguished at the non-SAR mapping scale.

We interpret this unit as a broad plains unit that contains the plains units that appear bright in ISS, such as "undifferentiated plains", "variable feature plains", "scalloped plains", etc. Given the identification of sharp-edged depressions and labyrinths at the mid-latitudes, it is possible that the undivided plains may contain a certain number of either unit that cannot be resolved with the lower-resolution datasets.

*5.4.2.4 Undivided dark plains (*pdu*)*

The undivided dark plains (*pdu*) (type area: 45.6°N, 116.9°W) (Fig. 5.3r) appear ISS dark, and do not cover as broad of an area as the undivided plains. In the low-resolution HiSAR, this unit has medium to variable backscatter. Similarly, this unit has varying levels of microwave emissivity, but mostly medium to high emissivity, never low (>0.95). This unit is mostly found in the mid-latitude regions and may be globular to lineated in planform.

Due to their dark appearance in ISS and their high emissivity, we interpret this unit as primarily consisting of "dark irregular plains". However, due to their elongated form in certain mid-latitude areas this unit may also contain the elongated "streak-like plains" unit. While the

"undivided dunes" also appear dark in ISS and have elongated morphology, the dunes are not expected be found in the mid-latitude regions. It is also possible that this unit may contain a certain amount of "labyrinth" terrain, which sometimes appear dark in ISS and have high emissivity, but they cannot be resolved unambiguously (Malaska et al., 2020).

Table 5.1 summarizes the identified terrain classes, units, and unit codes in addition to locations of characteristic examples of the units.

Table 5.1 Terrain class, terrain units, terrain unit code, and type feature locations. Dataset properties: SAR backscatter (SB), HiSAR backscatter (HSB), VIMS RGB (VR), ISS brightness (IB), Radiometry (R). We use undifferentiated plains as the reference standard for our qualitative descriptions, i.e., dune units are radar "dark" with respect to the undifferentiated plains, which are radar "medium-bright."

Dataset	Terrain class	Terrain unit name / code / description	Location (example)	Dataset properties	Relative topography
SAR	Plains	Undifferentiated plains (*pul*): most extensive unit on Titan, dominate mid-latitudes, bland appearance in radar. Interpreted as wind-blown deposits of organic materials.	33.8°N, 145.7°W	SB: medium-bright R: 0.96-0.97	lower than craters / mountains
		Variable plains (*pfv*): regions containing broad patches of SAR dark and bright	10.2°N, 119.1°W	SB: variable	variable

		materials. Interpreted as deposits of organics mixed with eroded material derived from mountains and hummocks.		R: 0.91-0.96	
		Scalloped plains (*psv*): radar low to radar medium patches mostly at high latitudes, lobate morphology, and patchy internal texture. Interpreted as eroded crustal material partially covered by organics, or potentially remnant evaporitic material.	58.7°N, 141.7°W	SB: medium - dark R: 0.93-0.94	variable
		Dark irregular plains (*pil*): irregular patches of SAR-dark terrains with lobate boundaries. Interpreted as low-lying basins dampened by liquids.	36.7°N, 125.4°W	SB: medium – dark R: 0.97-0.98	locally low
		Streak-like plains (*psh*): radar bright with diffuse-internal texture and longated morphology, generally parallel to local dunes. Interpreted as aeolian deposits of radar bright materials.	30.4°N, 147.3°W	SB: bright R: 0.94-0.96	not discernible
		Bright gradational plains (*pgh*): radar bright with diffuse but fairly uniform internal texture and gradational	14.5°N, 157.9°W	SB: medium – bright	locally low

		boundaries. Interpreted as radar bright material deposited by fluvial action.		R: 0.92-0.93	
		Undivided plains (*pu*): broad plains unit that may contain undifferentiated plains, scalloped plains, lineated plains, and variable featured plains.	49.5°N, 167.2°W	HSB: medium - dark VR, IB: bright R: 0.95-0.98	variable
		Undivided dark plains (*pdu*): broad plains unit that may contain dark irregular plains, streak-like plains, and perhaps a certain amount of labyrinth terrains.	45.6°N, 116.9°W	VR, IB: gray R: 0.94-0.98	variable
SAR	**Dunes**	Featureless sand sheets (*ds*): featureless SAR-dark areas that may be elongated in the W-E direction. Interpreted as organic sand deposits deposited by aeolian action.	16.9°N, 158.5°W	SB: dark R: 0.93-0.96	variable
		Linear dunes (*dl*): parallel to sub-parallel SAR-dark lines on a variable backscatter substrate. Interpreted as organic longitudinal dunes.	4.5°N, 156.3°W	SB: dark R: 0.96-0.98	elevated with rises and falls

Radio/ISS/VIMS		Undivided dunes (*du*): broad dune unit that may contain linear dunes, featureless sand sheets, and reticulated dunes. Only found within the equatorial regions.	7.8°N, 134.2°W	HSB: dark R: 0.93-0.97 IB: dark VR: brown	variable
SAR	**Mountains / Hummocky / Labyrinth**	Mountain (*hm*): elongated to globular features with evident SAR bright/dark pairing. Interpreted as rugged exposures of ancient crust.	10.6°N, 173.7°W	SB: bright R: 0.89-0.90	elevated
		Hummocky (*hh*): radar bright globular regions generally small in areal extent. Interpreted as highland exposures of ancient crust.	8.8°N, 149.2°W	SB: bright R: 0.85-0.90	elevated
		Degraded hummocky (*hdm*): radar high to radar medium exposures of hummocky-like materials. Interpreted as remnant hummocks that have been partially buried by organics or eroded.	24.5°N, 134.3°W	SB: bright R: 0.93-0.94	locally raised
		Pitted hummocky (*hph*): radar-bright hummocks populated by radar-dark, pit-like structures. Interpreted as fine grained, low backscatter materials	8.2°N, 115.2°W	SB: bright R: 0.86-0.90	elevated

		deposited in pre-existing depressions in the exposed icy crust.			
		Finely dissected labyrinth (*lbf*): large regions of relatively featureless, high-standing plateaux. Any internal texture consists of thin, high radar-backscatter patterns. Interpreted as labyrinth with tightly spaced subparallel or orthogonal channels/valleys that are just below the resolution limit (definition from Malaska et al. 2020).	48.6°N, 147.3°W	SB: mid-gray R: 0.94-0.97	elevated
Radio/ISS		Undivided mountain chains/hummocky areas (*hu*): broad hummocky unit that may contain hummocky terrains, mountains, degraded hummocky, and pitted hummocky terrains.	4.0°N, 168.1°W	SB: mid-gray R: 0.84-0.90	Locally high
SAR	**Craters**	Crater rim (*crh*): high backscatter circular exposure. Interpreted as a remnant impact crater rim.	25.9 N, 200.3W	SB: bright R: 0.93-0.94	locally raised
		Crater ejecta (*ceh*): radar bright materials grading radially out from crater rim. Interpreted as impact ejecta.	24.3°N, 141°W	SB: bright R: 0.93-0.94	locally raised

		Crater fill 3 (*cf3*): featureless, radar dark materials completely or partially enclosed by a rim. Interpreted as either material eroded from the rim or organic wind-blown deposits.	24.3°N, 141°W	SB: dark R: 0.93	lower than rim
SAR	**Lakes**	Sharp-edged depression (*bse*): depressions with radar-medium floors and lobate boundaries defined by a sharp, radar-bright boundary. Interpreted as an empty lake basin.	55.4°N, 141.3°W	SB: medium R: 0.92-0.94	low
		Ramparts (*brh*): SAR-bright mound-like annuli extending away from the lake for up to tens of kilometers from the shoreline.	54.7°N, 144°W	SB: bright R: 0.92-0.94	locally raised

5.4.3 The Soi crater region geomorphological map

Through the combined information provided by the detailed analysis of all different types of data, including SAR and non-SAR, in addition to previous knowledge gained through the mapping of the Afekan crater region, the South Belet region, and of the global geomorphological map of Titan, we constructed the detailed geomorphological map of the Soi crater region (Fig. 5.7). As mentioned earlier, all of the main categories of Titan units (e.g., Lopes et al., 2020) are present within the Soi crater region. Fig. 5.7 shows the results of mapping with the use of the high-

resolution SAR and HiSAR data including all available information from all Cassini surface instruments.

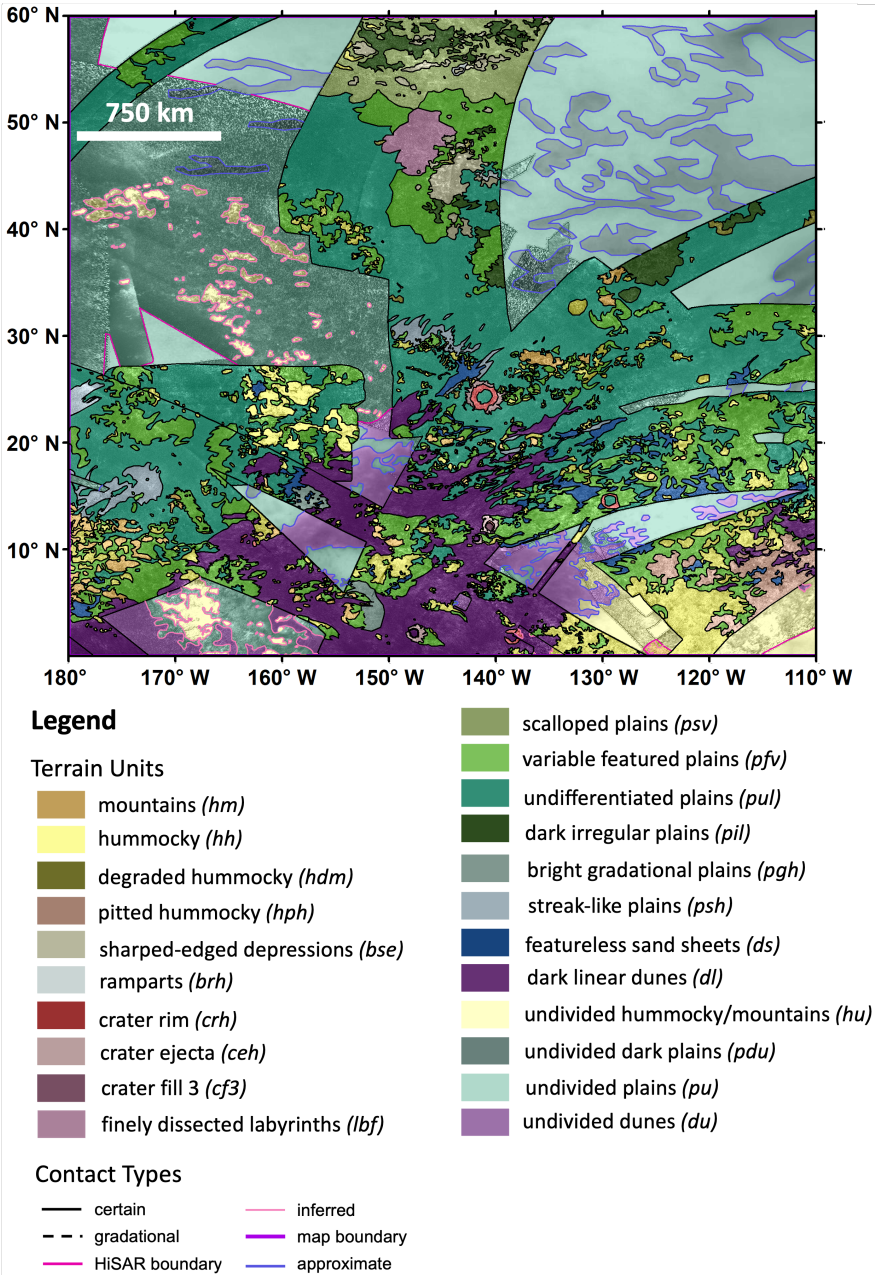

Fig. 5.7 Geomorphological map of the Soi crater region from high-resolution SAR, HiSAR, and non-SAR data (Radiometry, VIMS, ISS, poor HiSAR). Characteristics and interpretations for each terrain unit is described in Table 5.1. Contact types: 'certain' for units defined by SAR and "good" HiSAR; 'gradational' indicates that a clear boundary could not be made at the resolution of the

SAR images; ‘HiSAR boundary’ indicates the boundary between low-resolution HiSAR and other non-SAR datasets; ‘Inferred’ for units defined using the low-resolution HiSAR; ‘map boundary’ to indicate the regional extent of the mapping; and ‘approximate’ for units defined using ISS and VIMS.

5.4.4 Terrain unit areal extent

Table 5.2 shows the areal extent of each terrain unit in the Soi crater region. The plains units dominate the mapped area (~72.6%), consistent with the general trend around Titan’s globe (see Lopes et al., 2020). The dune units are the next dominant (~14.3%), followed by mountainous terrains (~11.6%), labyrinth terrain, empty SEDs, and then craters (each of which represent less than 1% of total area). Breaking down the plains into their subunit makeup, the undivided plains make up ~27% of the mapped area, followed by the undifferentiated plains and variable featured plains, which make up ~22% and ~14% of the mapped area, respectively. Of the dune subunits, linear dunes constitute the major dune material unit (~9%), likely owing to the inclusion of part of the Shangri-La dune sea within the regional extent. Undivided dunes (~4%) and featureless sand sheets (~2%) are minor. Hummocky terrain units are the most numerous unit, but are comparatively small in terms of areal extent, with an average size of ~620 km^2. The undivided, scalloped, and undifferentiated plains, while not as numerous, represent the most extensive units, with an average size of roughly 38,000 km^2, 18,000 km^2, and 13,000 km^2, respectively. Crater units such as rim, ejecta, and fill comprise less than 1% of the mapped surface when combined together. This is consistent with scarcity of craters on Titan’s surface, likely owing to active or recently active erosional and depositional process (Wood et al., 2010; Neish et al., 2015; Crosta et al., 2021).

Table 5.2 Areal extent of terrain units in the Soi crater region.

Terrain Class	Terrain Unit Name	Number of Features	Total Area (km^2)	% of mapped area (SAR and Non-SAR)	% mapped of each terrain class
Craters	Crater ejecta (*ceh*)	5	12,348	0.18%	*0.38%*
	Crater rim (*crh*)	13	13,025	0.19%	
	Crater Peak (*cph*)	1	125	<0.01%	
	Crater fill 3 (*cf3*)	1	948	0.01%	
Labyrinth	Finely dissected (*lbf*)	1	32,559	0.47%	*0.47%*
Mountains/ hummocky	Hummocky (*hh*)	624	382,233	5.46%	*11.61%*
	Mountain (*hm*)	95	79,336	1.13%	
	Degraded hummocky (*hdm*)	51	11,063	0.16%	
	Pitted hummocky (hph)	8	78,571	1.12%	
	Undivided mountains/hummocky (*hu*)	96	260,932	3.73%	
Plains	Undifferentiated plains (*pul*)	129	1,557,600	22.28%	*72.64%*
	Variable featured plains (*pfv*)	304	992,950	14.20%	
	Streak-like plains (*psh*)	20	72,565	1.04%	
	Scalloped plains (*psv*)	6	109,781	1.57%	
	Dark irregular plains (*pil*)	28	79,879	1.14%	
	Bright gradational plains (*pgh*)	2	24,535	0.35%	

	Undivided plains (pu)	59	1,907,952	27.29%	
	Undivided dark plains (*pdu*)	26	333,752	4.77%	
Dunes	Linear dunes (*dl*)	36	630,551	9.02%	*14.25%*
	Featureless sand sheets (*ds*)	122	115,502	1.65%	
	Undivided dunes (*du*)	25	250,582	3.58%	
Basin and Lake	Sharp-edged depressions (*bse*)	60	43,079	0.62%	*0.65%*
	Ramparts (*brh*)	3	2,615	0.04%	

5.5 Geologic Synthesis

5.5.1 Surface Processes in Soi crater region

5.5.1.1 Impact processes

We identified ten impact craters in the Soi crater region with confidence (Table 5.S2), seven of which had previously been identified by Wood et al. (2010), Neish and Lorenz (2012), Neish et al. (2015), and Hedgepeth et al. (2020). Craters identified with confidence are mapped with the crater terrain units while putative craters are mapped with a putative crater feature polyline (Fig. 5.8). In their post-Cassini assessment of Titan's crater population, Hedgepeth et al. (2020) identified five additional crater features that we do not feel confident in identifying as craters and thus do not include as part of our geomorphological terrain map, which only includes "certain" craters. Our assessment is based on the lack of a pseudo circular or circular form of the craters in the RADAR data. Instead, we map two of these five craters as "putative craters" (black solid line) in our surface feature map (Fig. 5.8). We additionally identify three putative craters not included in Hedgepeth et al. (2020) (Table 5.S2). Many of Titan's known and suspected impact craters have

been heavily eroded or modified by deposition, making interpretation subjective (Lopes et al., 2010; Wood et a al., 2010; Neish and Lorenz, 2012; Neish et al., 2015). In our SAR mapping, we see examples of how dunes and dune materials invade crater interiors, breaching the rim, allowing mobile organic sands to intrude. For example, the craters located at 11º N, 141.8º W and 2º N, 147.6 º W, both feature a preserved zone of crater ejecta on the eastward side of their respective rims, with the local topography presumably protecting the eastward ejecta from burial by the encroaching dunes. Both craters similarly feature substantial breaching on the western side of their rims and burial of the western-most ejecta. Furthermore, the crater floor materials are low backscatter yet contain the parallel bright-dark pairings indicative of linear dunes, suggesting that adjacent sand materials were transported from the west to the east and was able to fill the depression left behind by the initial impact.

5.5.1.2 Inferred Material Transport

We used alignments of streak-like plains (*psh*), featureless sand sheets (*ds*), and linear dunes (*dl*) to infer material transport directions using the method described in Malaska et al. (2016a) and Schoenfeld et al. (2021). The inferred directions are shown in Fig. 5.8 and are consistent with inferred global patterns. Broadly, the overall direction of material transport appears to be from the equator to midlatitudes, along a SW to NE direction, up to latitude 35ºN, then becoming roughly eastward at latitude 35°N. For latitudes above 35°N, the inferred direction of transport is from NW to SE down approximately latitude 35ºN, when the inferred direction becomes roughly W to E. The alignments are interpreted to indicate sediment transport primarily by aeolian mechanisms, resulting in material being deposited at midlatitudes (Malaska et al., 2016b). Local deflections of the inferred material transport vectors can be observed due to inferred topographical effects.

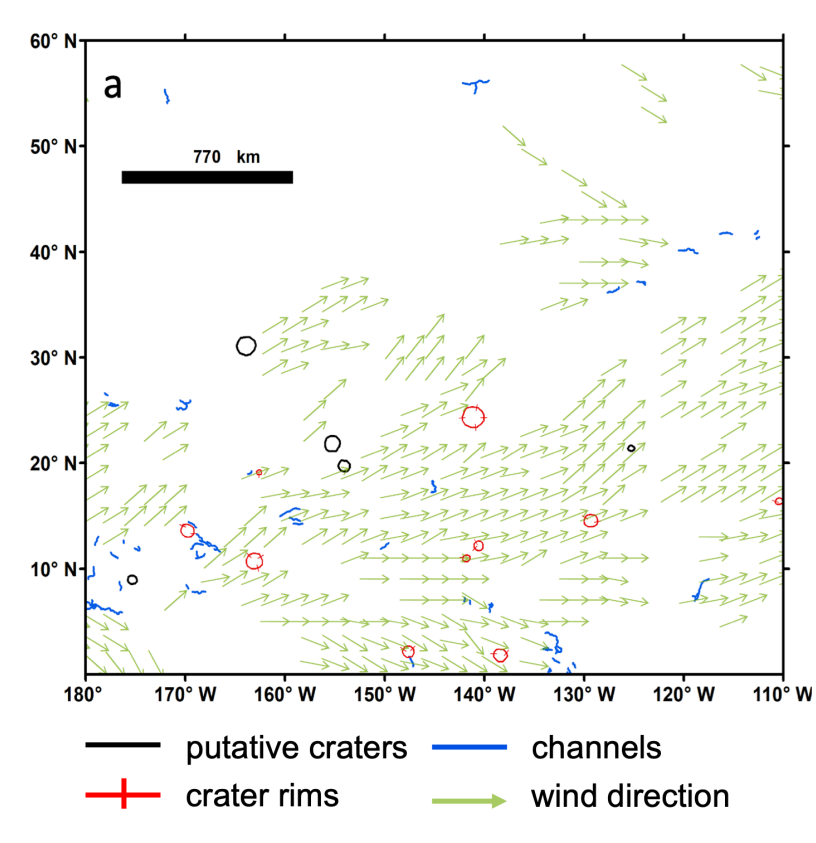

Fig. 5.8 (a) Sketch map of inferred material transport direction (arrows) in the Soi crater region after Malaska et al. (2016b), with valleys and channels (blue lines), craters (red), and putative craters (black).

5.5.1.3 Fluvial and Aeolian Processes

5.5.1.3.1 Valleys and Channels

Valley and channel features are mapped (blue lines in Fig. 5.8) using radar bright–dark pairing, networked morphology, and curvilinear appearance using the techniques and definitions in Burr et al. (2013a) and applied to the Afekan region by Malaska et al. (2016a). Dark floored channels are more common in labyrinth terrains and mountain valleys, while bright floored

channels were more often observed in the rare valleys observed within the undifferentiated plains. Valleys and channel features can only be identified if they are significantly larger than the SAR scale (Miller et al., 2021). Smaller features, such as those imaged by the Huygens probe during descent (e.g., Soderblom et al., 2007) may be present but cannot be identified at the available resolution.

5.5.1.3.2 Gradational vs. Streak-like Plains

We find that the bright gradational plains, a unit we discuss in section 4.1.1., possess signatures very similar to the bright streak-like plains (*psh*) across all the mapping datasets. The streak-like plains are characterized as radar-bright features with diffuse internal texture with elongated morphology (Malaska et al., 2016a). The elongation of this terrain unit has been observed extending in directions parallel to nearby linear dunes, suggesting that the streak-like plains represent material that has been transported and deposited by aeolian means. Both *pgh* and *psh* appear bright in radar, with diffuse internal texture (Fig. 5.4a,f). Their microwave emissivity is comparable, and both appear to have lower microwave emissivity than the undifferentiated plains (*pul*) or variable feature plains (*pfv*) (Fig. 5.4d,i). In VIMS maps by Le Mouélic et al. (2019), both units appear "blue" (Fig. 5.4c,h), and in ISS both units appear generally darker than surrounding bright plains (although the bright gradational plains can be patchy and variable) (Fig. 5.4b,g).

Due to the aforementioned characteristics, we interpret the bright gradational plains as high backscatter materials originating from the icy hummocky materials. Their orientation and directions can then reflect one of two scenarios: (1) they are aeolian sediments; (2) they are fluvial sediments that have been cleared off by winds. Similarly, in Malaska et al. (2016a), the bright streak-like plains have been interpreted as fluvially derived materials subjected to aeolian

transport, generally following inferred downwind directions. However, an alternative to a deposit of streak-like material would be the removal or scouring of material to reveal a deeper icy substrate. Due to their similar signatures across all utilized mapping dataset despite differing planform morphologies, we propose that the bright streak-like plains and the bright gradational are two endmembers of the same fundamental feature, reflecting either dominantly fluvial or aeolian transport. Where the bright gradational plains result in lobate, fan-like structure, we favor a fluvial origin. Meanwhile, the bright streak-like plains are linear and structured, suggesting downwind aeolian deposition or directed scouring. We propose that the initial grain forming process was fluvial erosion of either an organic or icy substrate, but that the final deposition of the fine-grained sediment was either through fluvial or aeolian means. The dominant process determines the endmember morphology, resulting in either a fluvial lobate (*pgh*) unit or an aeolian streak-like (*psh*) unit.

5.5.1.4 Lacustrine Processes and the Midlatitude Plains

In our mapping of the Soi crater region, we identified 60 features consistent in size and morphology to the polar SEDs, which we also refer to as sharp-edged depressions (*bse*) (Fig. 5.5). The spatial extent of these features reaches as far south as 40°N (Fig. 5.9). Additionally, remapping of Afekan's midlatitudes has revealed 31 features that are morphologically consistent with the SEDs (Fig. 5.5h), extending to 48°N. Using available elevation data (SARTopo, DTM for 46 out of 60 SEDs), the majority of the depressions seen in the Soi crater region have flat floors, to within 100 m certainty, consistent with observations of empty depressions in the polar regions (Birch et al., 2017; Hayes et al., 2017). However, the largest of the sharp-edged depressions we identify have more complex floor topography (i.e., terraced), potentially indicating either a higher degree of fluvial/aeolian desiccation, or coalescence of multiple smaller depressions (Hayes et al., 2017).

We interpret the *bse* units in the Soi crater region as now empty lake basin, indicating that processes previously thought as "polar" were once operating in the mid-latitudes, suggesting a once wetter Titan.

Three of the SEDs, or empty lakes, in Soi crater region have an associated rampart, supporting the hypothesis that the ramparts are features that formed as part of the lake emplacement, but are progressively eroded away. Thus only the youngest lakes would still possess their ramparts (Solomonidou et al., 2020b), explaining their scarcity. Nonetheless, the identification of ramparts in the Soi crater region reinforce the idea that the mid-latitude lakes formed and evolved in much that same way as the polar lakes.

The sharp-edged depressions are found adjacent to two other units unique to the midlatitudes of Titan: the scalloped plains (*psv*) and the dark irregular plains (*pil*) (Fig. 5.10). These two units in particular seem to define the morphology of Titan's midlatitude-to-pole transitional zones and have been identified in the northern (Malaska et al., 2016a; Lopes et al., 2020) and southern hemispheres (Schoenfeld et al., 2021). Topographically, the scalloped plains undulate, but typically appear elevated with respect to the dark-irregular plains and the sharp-edged depressions (Fig. 5.10b,c). Additionally, the scalloped plains appear radiometrically distinct, having a lower emissivity (0.93-0.94) from the dark irregular plains (0.97-0.98) (Fig. 5.10d). These observations are consistent with the interpretation of the scalloped plains being either a thick organic layer mixed with higher dielectric constant materials, or as a more textured surface of the organics typical of the undifferentiated plains, with higher backscatter due to more surface roughness. Furthermore, VIMS analyses agrees with the organic nature of the top surfaces of *psv* (Solomonidou et al., 2018).

The topography of the dark irregular plains (*pil*), and their relationship to the sharp-edged depressions (*bse*), appear more complicated. Previous work (e.g., Stofan et al., 2007; Malaska et al., 2016a; Schoenfeld et al., 2021) interpreted the dark irregular plains as consisting of local basins dampened by liquid hydrocarbons pooling in either the surface or the near-subsurface. The Huygens probe, for example, detected a surface damp with hydrocarbon liquids upon touchdown (Lorenz, 2006b). These areas could be transient ponds that have mostly evaporated, leaving behind remnant liquids that continue to wet sediments. Precipitation events, as evidences by surface brightness changes in VIMS/ISS (Barnes et al., 2013)., may be responsible for such transient wetting. Alternatively, the liquid may have infiltrated downward, but left behind locally damp material, if we assume a low evaporation rate. Based on laboratory measurements (e.g. Grundy et al. 2002), it is possible that methane exists on Titan's surface as a liquid mixed with other ices, possibly filling the space between their grains. Remnant liquids are possibly composed of higher order hydrocarbons, including ethane, propane, and perhaps even 1-butene; these hydrocarbons would be more refractory than methane and could therefore create remnant damp sediment even after the more volatile methane has evaporated (Malaska and Hodyss, 2014; Cordier et al., 2016). Another possibility is that low backscatter is from very fine-grained material that has been sorted and redeposited, again, from localized transient ponding (Turtle et al., 2011). In suspension, the material would fine upwards.

While some of the dark irregular plains are indeed the lowest feature along a topographic trace, this is not always the case. Some of the dark irregular plains observed in the Soi crater region are topographic highs (Fig. 5.9b,c), especially with respect to the lakes (*bse*). While, this is inconsistent with our prior interpretation, it is possible we may be seeing two different terrain types that have broadly been classified as dark irregular plains owing to their similarity in radar and

other supplementary datasets. However, topographic data over SAR-dark features is less reliable (Corlies et al., 2017), and so our relative elevations of these features may be particularly skewed. Future analyses may split these terrains out into two separate categories, yet still falling under the major plains terrain class. The topographically higher dark irregular plains adjacent to the sharp-edged depressions may be remnant highs left over from lake aggregation, similar to what is observed at the poles (Birch et al., 2017). Thus, their dark appearance in radar may be owing to low-backatter materials, rather than near-surface wetting. The dark irregular plains that do sit lower than nearby empty lakes, however, may in fact represent wetted lowlands**,** or at least represent the sites of localized ponding. The largest patch of dark irregular plains in the Soi crater region, for example, sits at 37°N, and represents a large topographic low (Fig 5.10e,f). The dark irregular plains that are lower than the empty lakes may be approaching or interfacing with the phreatic surface of the methane table no longer accessible by the now empty lakes, consistent with predictions from global circulation models of Titan's climate (e.g., Faulk et al., 2020). Or, the dark irregular plains may be the result of higher precipitation/humidity with increasing latitude interacting with porous regolith and local topography to create ephemeral surface and near surface wetting.

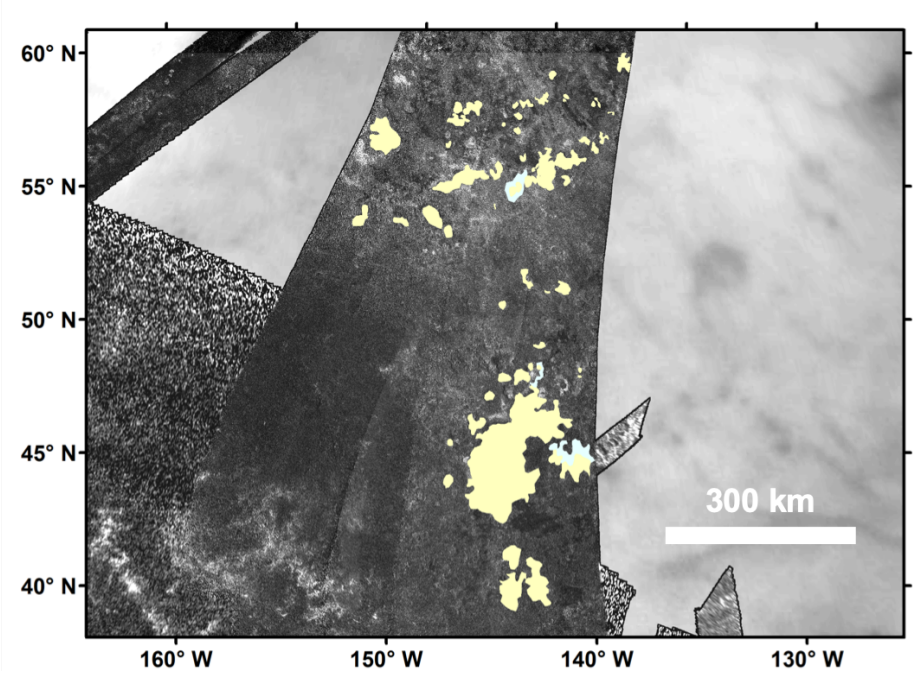

Fig. 5.9 Mapping of all instances of Basin and Lake units in the mid-latitudes of the Soi crater region. Beige: sharp-edged depressions (*bse*); light blue-grey: ramparts (*brh*).

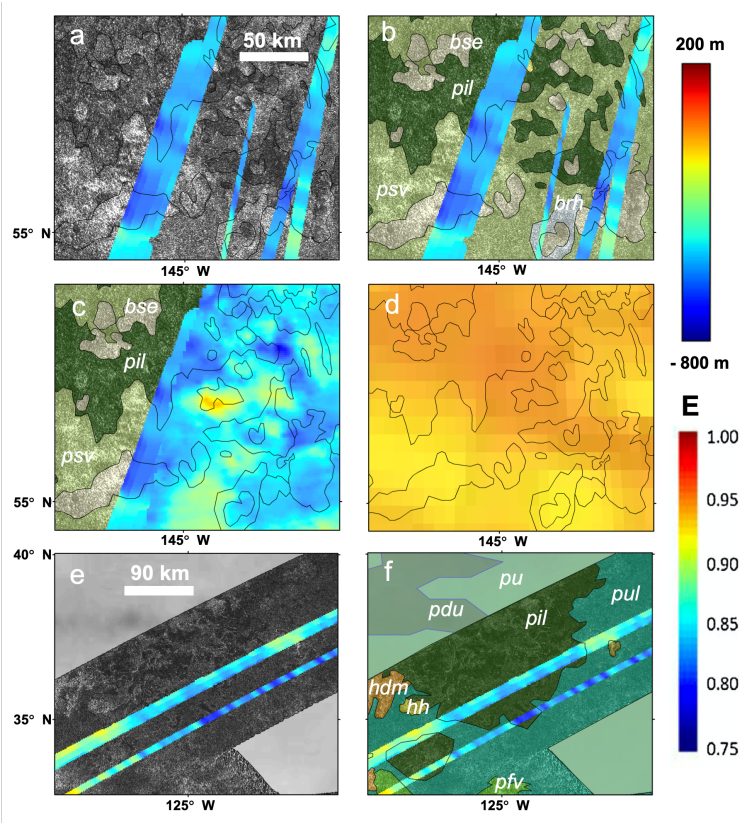

Fig. 5.10 The dark irregular plains (*pil*) and their relationship to the sharp-edged depressions (*bse*). (a) Topography from SARTopo of northern reach of the Soi crater region *pil*; (b) Same as (a) with the annotated terrain unit mapping as background; (c) DTM of northern part of the Soi crater region showing topographic highs among *pil*; (d) Emissivity map covering area shown in a, b, and c; (e) SARTopo with SAR as background and annotated unit map (f) of the largest patch of dark irregular plains in the Soi crater region, showing large topographic lows.

5.5.1.4 Equatorial Pits in the Soi crater region

Within the Soi crater regional map, there are numerous radar dark, circular features with diameters ranging in size from about 1-6 km. In total, 230 of these features were identified (Fig. 5.11). Similar features of this specific morphology, assumed to be depressions or pits, were first identified by Lopes et al. (2007) within Cassini's T8 swath, and were similarly mapped in the South Belet region (Schoenfeld et al., 2021). The size range of the Soi crater region pits is similar to that of South Belet and the T8 pits, with a similar level of random distribution within a given location. We thus interpret the pits of the Soi crater region to have formed in the same manner as the pits found in the T8 SAR swath and in South Belet. As a note, we only use the highest resolution SAR to map the pits (Fig. 5.11b).

The equatorial pits primarily occur within large areas of exposed crust; this association is the qualitative basis behind distinguishing "pitted hummocky" (*hph*) from regular "hummocky" (*hh*). It could be that, being locally elevated to the surrounding terrain, pitted depressions are preserved from complete burial by windward sediments and incidentally become associated with mountains and hummocks. Alternatively, it could be a contrast effect, where backscatter afforded by the radar bright hummocky terrain makes the pits easier to identify. Within the Soi crater region,

collections of pits are particularly dense in areas adjacent to dune fields (Fig. 5.11a). This observation is consistent with our past interpretation (e.g., Schoenfeld et al., 2021) of the pits as wind-blown organic sands deposited and concentrated into pre-existing depressions within exposure of the ancient ice crust. In particular, the highest concentration of pits occurs within the northwestern margin of Xanadu that overlaps into the Soi crater region, which is also down-wind to a large dune field. The ubiquity of pits in equatorial regions may then be owing to the prevalence of both mountainous regions and dune fields at these latitudes, as opposed to a formation mechanism limited to equatorial areas. The ancient crust of Titan, therefore, may be pocked and pitted by processes separate from cratering, as the morphologies and size distributions of these pits are not consistent with those of impact craters (e.g., Lopes et al., 2007; Lunine et al., 2008). Schoenfeld et al. (2021) hypothesizes that the equatorial pits may have formed as a result of either cryovolcanism, the removal of methane (either from outgassing or the retreat of a ground reservoir) in the near surface, or as a result of the dissolution of soluble organics in an otherwise icy matrix. Eventually, the pits were infilled with windward dune material.

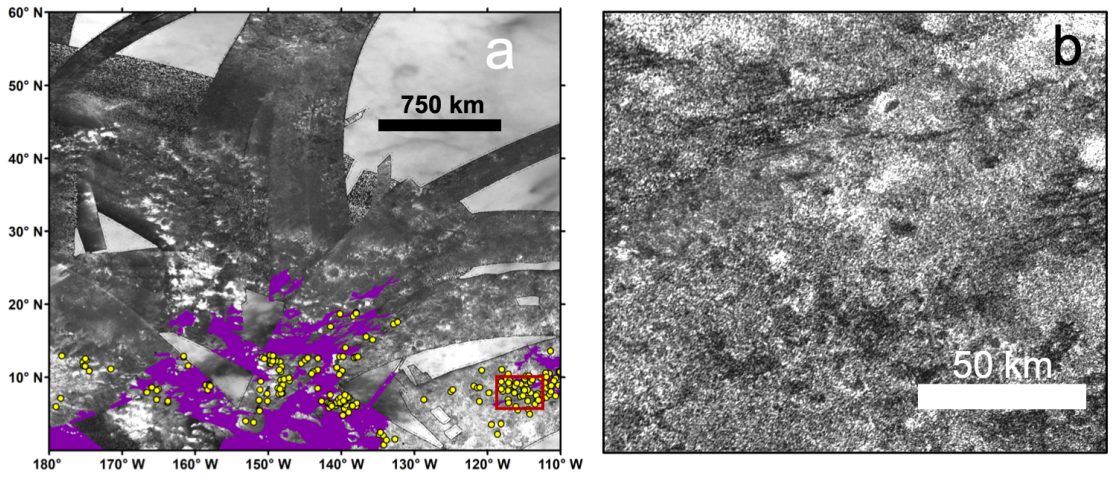

Fig. 5.11 Equatorial pits in the Soi crater region (yellow dots). (a) Pit mapping in the SAR, with the dune fields (in purple) also lit up. (b) Zoom in of area marked by red square in (a), centered on 8.9°N, 115.3°W.

5.6 Geologic History

The goal of this paper is to create a geomorphological terrain map of the Soi crater region, in order to better understand the geologic evolution of the region, as well as offers a complementary dataset for compositional analysis (e.g. Solomonidou et al. 2018). We identified 22 geomorphological units in the Soi crater region, 3 of which not previously described in our mapping. Some newly identified features include 60 SEDs, which reach as far south as 40°N. We also introduce 3 impact craters to the literature. The Soi crater region contains the NE section of Shangri-La dune field, a vast field of equatorial dunes at lower latitudes, part of the Xanadu region, and also large expanses of plains at mid-latitudes.

The Soi crater region is representative of the transition between the equatorial, mid-latitude, and high latitude northern regions of Titan and largely has the same collection and proportion of geomorphological units (plains, dunes, hummocky/mountains) to other mapped regions on Titan (Malaska et al., 2016a; Lopes et al., 2020; Schoenfeld et al., 2021). The results of this study further support the hypothesis that surface processes are, broadly speaking, the same in all around Titan's middle and equatorial latitudes, with the notable exception of the equatorial Xanadu region. Only at higher latitudes do these trends begin to change, as evidenced by morphologies suggestive of lacustrine processes in the Soi crater region.

The mountainous units are interpreted as the oldest unit, the undifferentiated plains are of intermediate age, and the dune are the youngest. We also consider the SEDs and the ramparts unit to be some of the youngest in the Soi crater region, having printed into the plains. That said, active lacustrine processes seem to no longer operate in the mid-latitudes, as is evident by the lack of filled lakes. Solomonidou et al. (2020b) showed that the ramparts and the floors of the empty lakes are of same composition. They furthermore suggest that during or after the formation of the lake basin, residual material is built into the raised rim feature and develops later into the ramparts. Lakes retaining a complete rampart structure around their circumference may be younger compared to other lakes with incomplete or degraded ramparts, which are further along in the process of having their ramparts eroded away.

Topography data acquired from DTMs and SARTopo shows that the mountainous terrains are topographically higher, and the dunes are lower. The Soi crater region presents similar bulk geomorphology as the rest of Titan's surface, which is rich in plains and dunes. The plains cover 3/4 of the region, of which half is the undivided plains and the undifferentiated plains. While the undivided plains unit dominate the midlatitude region of the Soi crater region, there are likely other subunits contained therein, unresolved at the nonSAR scale. There are plenty of exposures of mountainous terrains around the region, but they do not cover a significant amount of the surface, in contrast to the undivided and undifferentiated plains that cover almost half of the Soi crater region. Dune materials cover ~14% of the area, which is less than seen in other mapped regions like the South Belet and Afekan regions (Malaska et al., 2016a; Schoenfeld et al., 2021). The sharp-edged depressions, the ramparts, and the crater units combined comprise around 1% of the mapped surface.

The identification of lakes (SEDs) outside of the polar regions and into the mid-latitudes strengthens the argument that in Titan's past, lacustrine processes typically associated with the polar regions were operating long enough to leave behind surface expressions consistent with lacustrine processes (e.g., Turtle et al., 2009; Barnes et al., 2011; MacKenzie et al., 2014; Birch et al., 2018; Hofgartner et al., 2020). Previous studies have proposed that features in Tui and Hotei Regio, located at equatorial latitudes, are morphologically and topographically consistent with the polar empty lakes (Moore and Howard, 2010). Additionally, global distribution of evaporatic features places a high areal concentration of the associate 5-μm bright signal within these same basins (MacKenzie et al., 2014). We can similarly conclude that the substrate of the midlatitudes support the formation of lacustrine features, much like the polar regions, and perhaps may be the same underlying material. Furthermore, their presence speaks to a wetter climate, where the mid-latitudes were once as humid as the poles (e.g., Moore et al., 2014). Alternatively, we may consider a scenario where the climate is unchanged (over the lifetime of the lakes), but that frequency of rain is less at these latitudes such that abundance of filled lake features is less. It is predicted that total precipitation for Titan are largest over the poles when compared to the mid-latitudes (e.g. Faulk et al., 2017). However, there are several lines of evidence that favor the hypothesis of a desiccating Titan. For one, there is the issue of methane being progressively lost over time (e.g., Larsson and McKay, 2013; Moore et al., 2014), as a result of photodissociation in the upper atmosphere, conversion to solid organics, or incorporation into clathrate. While there may be periods of methane outgassing and atmospheric replenishment, there is nonetheless net loss and humidity recedes to the poles. Within the north pole, evidence of such loss is observed: empty sharp-edged depressions located adjacent to filled lakes sit at slightly higher elevations (Hayes et al., 2017), presumably having been filled during a previous epoch with larger liquid inventories

(Birch et al., 2017). Similarly, the rounded lakes are thought to form on geologic timescales (e.g. Birch et al., 2017), requiring time for them to imprint onto the landscape. Thus, the timescale of interaction with a liquid-methane reservoir was such that lakes consistent in size, complexity, and frequency with that of the poles were once operating in the mid-latitudes. However, if the initial depression was formed by other means, i.e. maar-like explosion (e.g. Mitri et al., 2019), then this argument may not apply. That said, the morphology of the lake boundaries as rounded with sharp shorelines and no associated inflow channels (at least not at Cassini resolution) are consistent with seepage lakes interacting with a local ground-methane system, as opposed to runoff from precipitation (Hayes et al., 2008).

Craters appear to get filled with aeolian material and eventually are buried, which could explain the relatively few number of craters on Titan (e.g. Wood et al., 2010; Neish et al., 2015; Neish et al., 2016; Hedgepeth et al., 2020). The craters located close to the equator (including Santorini) appear organic in composition, as they are rich in the dark organic material and tholin-like material, without the presence of any water ice (Solomonidou et al., 2020a). The Soi crater rim and ejecta appears primarily composed of tholin-like material, followed by water-ice, a mixture that is characteristic of the plains craters located around the 30ºN latitude zone (Solomonidou et al., 2020a). The Soi crater region impact craters offer good examples of dune material 'invading' the interior of the craters.

In terms of surface area, the scalloped plains unit is of minor importance in the Afekan crater region but is extensive in the Soi crater region. This unit, as well as the dark irregular plains, appear to be transitional between the aeolian-dominated mid-latitudes and the fluvially-dominated polar regions, where aeolian deposition is scarce. Hence, the scalloped (*psv*) and dark irregular plains (*pil*), both of which are found adjacent to the SEDs (*bse*) in the Soi crater region, seem to

play a major role in defining the morphology of Titan's mid-latitude-to-pole transitional zones. These three units occupy the middle northern part of the Soi crater region. The scalloped plains are topographically higher than the other two units. We suggest that the northern *pil* close to the SEDs are remnant highs left over lake aggregation similarly to the ramparts; dark irregular plains that sit in topographic lows alternatively may represent near-surface wetting by ground methane.

5.7 Conclusion

We have presented and described a geomorphologic map of the Soi crater region of Titan. We used Cassini SAR as our basemap, supplemented with other datasets such as radiometry, topography, ISS, and VIMS. This entire region makes up ~10% of Titan's areal surface, whereas the parts of the region imaged by SAR make up ~5.6% of Titan's surface. This area represents the main geological processes that have occurred in Titan's equatorial and the northern mid-latitudes. We describe in detail three new mapping units: the "bright gradational plains", sharp-edged depressions (SEDs)", and "ramparts". These units have been identified elsewhere on Titan and have been described in the literature. Here we discuss them in the context of the Soi crater region and incorporate them into our mapping schema, building on the work presented in Malaska et al. (2016a) and Schoenfeld et al. (2021). We also use the correlation between Cassini SAR and secondary datasets to map into areas not imaged by SAR, elaborating on a methodology for a more comprehensive map of Titan's surface (first introduced in Lopes et al., 2020). Additionally, we use lower resolution HiSAR for the low-resolution mapping. In the Soi crater region, these "nonSAR" units included undivided dunes (*du*), undivided hummocky (*hu*), undivided plains (*pu*), and undivided dark plains (*pdu*).

The Soi crater region contains all six of the main terrain units: Dunes, Plains, Mountain/hummocky, Crater, Labyrinths, and the Basin and Lake units. We find that plains dominate the make-up of this region, accounting for 72.6% of the mapped area, followed by dunes (14.2%), mountains/hummocky terrains (11.6%), labyrinth (0.47%), basin and lake (0.65%), and crater terrains (0.38%). The emissivity and spectral properties of the undifferentiated plains and dunes are consistent with organic materials, whereas the emissivity and spectral properties of the mountain/hummocky and crater terrains are more consistent with water ice. We identify ten impact craters in the Soi crater region with confidence, seven of which have been identified in the literature.

Broadly, the geologic history of the Soi crater region presents a story familiar to that of the Afekan crater region and South Belet, but with some notable differences. We observe small instances of fluvial transport in the Soi crater region in the form of channels. Instead, material transport patterns are more consistent with widespread aeolian deposition of dunes and plains units. If fluvial activity was once more present in this region, it has since been buried by aeolian deposits. However, we interpret the bright gradational plains (pgh) as high backscatter material originating from fluvial processes, representing a fluvially derived depositional units. They are similarly found in association with mapped channels in both the Soi crater region and in other regions (Fig. 5.4k). We also find that the bright gradational plains possess signatures very similar to the bright streak-like plains (*psh*) across all the mapping datasets. Accordingly, we propose that the bright streak-like plains and the bright gradational are two endmembers of the same fundamental feature, reflecting either dominantly fluvial or aeolian transport. The dominant process determines the endmember morphology, resulting in either a fluvial lobate (*pgh*) unit or an aeolian streak-like (*psh*) unit.

The identification of lake units in the Soi crater region, the sharp-edged depression (*bse*) and ramparts (*brh*) challenges the idea of lacustrine processes being limited to Titan's polar regions, suggesting a historically wetter Titan (e.g. Aharonson et al., 2009; Neish et al., 2013; MacKenzie et al., 2014; Birch et al, 2018). The amount of methane in the atmosphere and on the surface may have changed over time, resulting in a complex interplay of the hydrocarbon 'aquifer' level. During a base-level lowering, depressions sitting at the highest elevation would be abandoned first, losing their connection to the receding methane aquifer (Hayes et al., 2017). The spatial extent of these features in the Soi crater region reaches as far south as 40°N. Additionally, remapping of Afekan's midlatitudes has revealed 31 features that are morphologically consistent with the SEDs, suggesting that the prevalence of empty lakes at those latitudes is not necessarily unique to the Soi crater region. The morphology and complexity of the Soi SEDs are consistent with observations of empty depressions in the polar regions (Birch et al., 2017; Hayes et al., 2017), suggesting a shared formation history, including instances of smaller depressions coalescing.

The sharp-edged depressions are found adjacent to two other units unique to the midlatitudes of Titan: the scalloped plains (*psv*) and the dark irregular plains (*pil*) (Fig. 5.9). Some of the dark irregular plains observed in the Soi crater region are topographic highs, while are the lowest feature along a topographic trace, including with respect to the lakes (*bse*). While, this is inconsistent with our prior interpretation of the dark irregular plains as consisting of local basins dampened by liquid hydrocarbons pooling in either the surface or the near-subsurface, it is possible we are seeing two different terrain types that have broadly been classified as dark irregular plains. The topographically higher dark irregular plains adjacent to the sharp-edged depressions may be remnant highs left over from lake aggregation, similar to what is observed at the poles (Birch et

al., 2017). Thus, their dark appearance in radar may be owing to a more absorptive material, rather than near-surface wetting. The dark irregular plains that do sit lower than nearby empty lakes, however, may in fact represent wetted lowlands. The dark irregular plains that are lower than the empty lakes may be approaching or interfacing with the phreatic surface of the methane table.

Our geomorphological mapping results for the Soi crater region is consistent with the narrative of Titan's equatorial and mid-latitudes being dominated by organic materials that have been deposited and emplaced by aeolian activity. Additionally, the presence of similar units found in both Afekan, South Belet, and Soi suggests latitudinal symmetry in Titan's surface processes and their evolution across a broad longitudinal spread.

5.8 Supplementary

Here we present the descriptions of the SAR (Table 5.S1), and the non-SAR datasets used in our analysis which include: SARTopo, Radiometry-Emissivity, ISS, and VIMS (Section 5.9.1). The global context of Soi can be seen in Fig. 5.S1. The SAR and non-SAR coverage of the Soi crater region can be seen in Fig. 5.2b. The craters confirmed to exist in the Soi crater region along with new ones identified in our analysis are described in Table 5.S2.

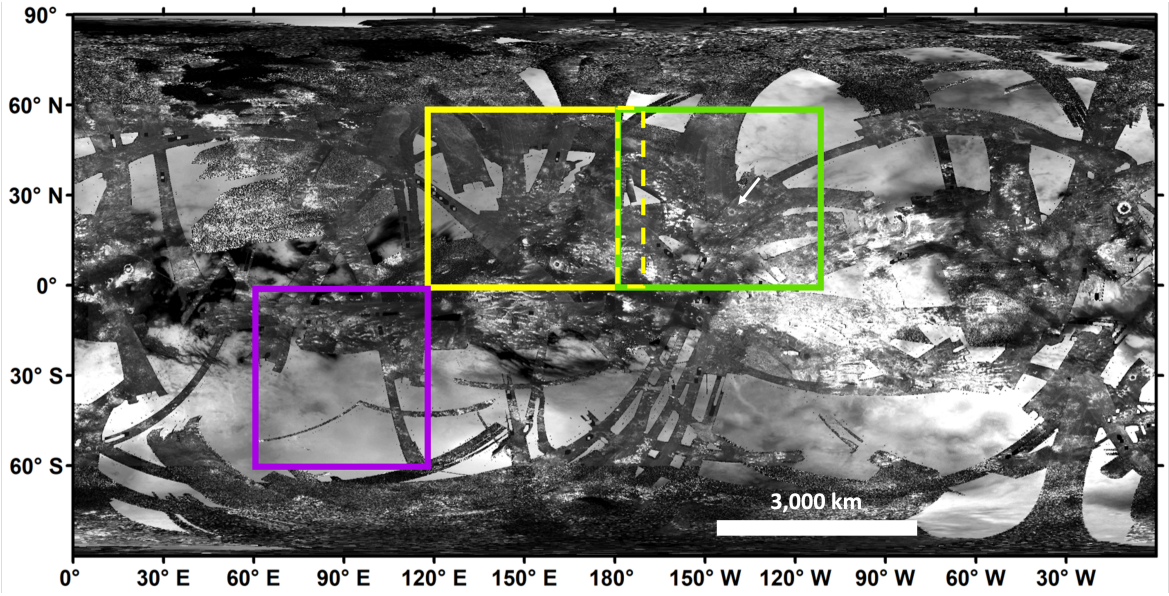

Fig. 5.S1 Global context of the Soi crater region (green outline), the Afekan region (yellow outline) (Malaska et al., 2016a), and the South Belet region (magenta outline) (Schoenfeld et al., 2021). The dashed yellow lines indicate the overlap between the Afekan and Soi crater regions previously published in Malaska et al. (2016a). The arrow points to the Soi crater. SAR swaths covering the region are superposed on a global mosaic of Titan created from Imaging Science Subsystem (ISS) data (USGS Astrogeology Science Center). The total area of the region in the green box is 8×10^6 km^2. Scale bar applies to equatorial latitudes. North is at the top.

5.8.1 SAR & Non-SAR datasets (Topography, Emissivity, ISS, VIMS)

The SAR dataset was used as a basemap for our geomorphological mapping. In total, we have used information from swaths acquired from 15 different flybys (Table 5.S1), in both SAR and HiSAR (Fig. 5.2b). At Titan, the SAR mode is primarily used at altitudes under ~4,000 km, resulting in resolution cell sizes ranging from ~300 m to >1 km. At each Titan encounter used by the RADAR, a swath 120–450 km in width and 1000–5000 km in length is created from 5 antenna

beams, with coverage largely determined by spacecraft range and orbital geometry. SAR data cover about 46% of Titan's surface at less than 1 km resolution, while the higher-altitude SAR data cover an additional 24% at less than 5 km resolution (Lopes et al., 2020). The coverage of the Soi region by SAR swaths is shown in Fig. 5.2a. Radar data is incidence angle corrected to be the same globally and for all terrains (Stiles et al., 2006); relative backscatter is then used to evaluate terrain brightness. Some terrain types are more sensitive to incidence angle than others (e.g. Malaska et al., 2016), so a uniformly applied incidence angle correction introduces some uncertainty in backscatter response. In general, high-backscatter materials appear in lighter tones, while lower-backscatter materials are darker toned.

Other modes from the RADAR instrument, what we call the 'non-SAR datasets', provide additional information on surface physical properties, such as radiometry (e.g., Wye et al., 2007; Janssen et al., 2009; 2011; 2016) (Fig. 5.2d) and topography (e.g., Kirk et al., 2005; Stiles et al., 2009) (Fig. 5.2c) that were used to complement SAR in the geomorphologic mapping. We have also used observations from ISS (Fig. 5.2f) and VIMS (Fig. 5.2e) to help characterize the terrain units.

5.8.1.1 Topography

The RADAR instrument can obtain topographic data in one of several ways. The instrument has an altimetry mode that can provide absolute elevation. However, altimetry cannot be obtained simultaneously with SAR and covers relatively small segments of the surface as a result. SARTopo (Stiles et al., 2009) can derive relative topographic information from the overlap of neighboring radar beams. SARTopo is useful for mapping as it provides the most topographic coverage, yielding 1–3 profile strips roughly 10's of km wide and 1000's of km along each SAR swath.

Relative vertical errors in SARTopo are < 75 m within a swath. While limited, there was also some stereophotogrammetry topographic data also available to use, covering an additional ~2.1% of Titan's surface, with a typical error of ~100 m (Kirk et al., 2012; Corlies et al., 2017). Stereophotogrammetry uses the spacecraft position and viewing geometry to triangulate features observed in multiple SAR images to determine their location on Titan's surface (Kirk et al., 2012). A SAR mosaic of the Soi crater region overlain with SARTopo data from Corlies et al. (2017) is shown in Fig. 5.2b. When using SARTopo to ascertain relative elevation information, we only make comparisons along the same SARtopo strip, rather than comparing two different strips taken either from the same or different SAR observations, which would yield considerable error.

5.8.1.2 Radiometry - Emissivity

The RADAR instrument has a passive radiometry mode that measures the brightness temperature of Titan's surface (Janssen et al., 2009; 2016). The brightness temperature can be converted to the emissivity (E) using knowledge of Titan's surface temperature (~95 K at the equator) acquired from the Cassini Composite Infrared Spectrometer (CIRS) (Jennings et al., 2009) and Huygens probe measurements (Fulchignoni et al., 2005). The resolution of the radiometry measurements ranges from 5 to 500 km, with the higher resolutions obtained inside the SAR swaths. In general, materials such as fractured water ice blocks have a low emissivity, while low-dielectric organic materials have a high emissivity (Janssen et al., 2016). This is shown in the emissivity of the Soi crater region in Fig. 5.2d. The Xanadu region has low emissivity, indicating icy materials, while the dunes and undifferentiated plains show higher emissivity indicating organic nature.

5.8.1.3 ISS

Cassini's ISS instrument (Porco et al., 2004) consists of Wide and Narrow Angle Cameras that include 0.938 μm narrow bandpass filters and infrared polarizing filters that can see Titan's surface through one of the atmospheric transmission windows. Scattering by Titan's atmosphere limits the usefulness of ISS images. The spatial resolution is at best several hundred meters and topographic shading is not observed. To help our analysis, we used a controlled and corrected ISS mosaic that covers the surface at ~1km spatial resolution (Karkoschka et al. (2017, LPSC). The ISS data of the Soi crater region is shown in Fig. 5.2e.

5.8.1.4 VIMS

Cassini's VIMS (Brown et al., 2004) was a hyperspectral mapping spectrometer that operates in the range from 0.35 to 5.12 μm. VIMS could observe Titan's surface though atmospheric transmission windows at 0.94, 1.08, 1.28, 1.59, 2.03, 2.69-2.79, and 5.0 μm (Barnes et al., 2007a). The VIMS data provide constraints on the chemical composition of the surface by using the spectral responses and surface albedo values (Soderblom et al., 2007; Barnes et al., 2009; Solomonidou et al., 2014). VIMS resolution varies from a few km to a hundred km. For some targeted areas, the resolution can be as high as 250 m/pixel (Jaumann et al., 2009). For our mapping and analysis, we used the global VIMS mosaic described in Le Mouélic et al. (2012), the Soi crater region is shown in Fig. 5.2f, while Fig. 5.3 shows the extended coverage VIMS provides over the SAR swath base mosaic.

Table 5.S1 Information on the RADAR swaths used in this analysis: flyby, date of observation, and type of coverage. Radar data is incidence angle corrected to be the same globally; relative backscatter is then used to evaluate terrain brightness.

Flyby	Date	SAR or HiSAR or both
T1	12/2004	SAR
T3	02/2005	SAR
T16	07/2006	SAR
T19	10/2006	SAR
T20	10/2006	HiSAR
T43	05/2008	SAR
T44	05/2008	SAR
T55	05/2009	Both
T56	06/2009	Both
T58	07/2009	SAR
T61	08/2009	SAR
T83	05/2012	HiSAR
T95	10/2013	SAR
T98	02/2014	HiSAR
T121	07/2016	Both

Table 5.S2 Craters within the Soi crater region. Certainty as described in Hedgepeth et al. (2020): 1 = certain, 2 = nearly certain, 3 = probable, 4 = possible.

Crater name (if available)	Latitude, longitude Diameter (km)	Previously identified	Hedgepeth et al. classification of certainty (1-4)	Included in Soi mapping
Soi	24.3ºN, 140.9ºW 85±15	Yes -T16, T55, T56, T120 (Wood et al., 2010)	1	Yes
Near Santorini Facula	2.1ºN, 147.6ºW 40±5	Yes -T44, T56 (Neish and Lorenz, 2012)	1	Yes
-	16.4ºN, 110.4ºW	No	N/A	Yes
-	10.7ºN, 163.3ºW	No	N/A	Yes
-	13.6ºN, 169.8ºW	No	N/A	Yes
-	1.8ºN, 138.4ºW 55±5.5	Yes -T91 (Hedgepeth et al., 2020)	2	Yes
-	12.1ºN, 140.5ºW 32±1	Yes -T56 (Neish and Lorenz, 2012)	2	Yes

-	11ºN, 141.8ºW 23±0.5	Yes -T20, T56 (Neish and Lorenz, 2012)	2	Yes
-	31.3ºN, 164.4ºW 63±1.5	Yes -T120 (Hedgepeth et al., 2020)	3	Putative
-	14.5ºN, 129.2ºW 59±1	Yes -T120 (Hedgepeth et al., 2020)	3	Yes
-	19.2ºN, 162.7ºW 18±0.5	Yes -T57, T56 (Neish and Lorenz, 2012)	3	Yes
-	19.8ºN, 154ºW 34±1	Yes -T49 (Hedgepeth et al., 2020)	3	Putative
-	33.4ºN, 129.7ºW 16±1	Yes -Ta (Wood et al., 2010)	3	No
-	22.7ºN, 173.4ºW 10±0.5	Yes -T21, T29, T83 (Wood et al., 2010)	3	No
-	21.8ºN, 170.7ºW	Yes -T56, T98 (Hedgepeth et al., 2020)	4	No

	16±0.5			
-	22.0ºN, 155.4ºW	No	N/A	Putative
-	9.0ºN, 175.3ºW	No	N/A	Putative
-	21.4ºN, 125.3ºW	No	N/A	Putative

5.9 References

Aharonson, O., Hayes, A.G., Lunine, J.I., Lorenz, R.D., Allison, M.D. and Elachi, C., 2009. An asymmetric distribution of lakes on Titan as a possible consequence of orbital forcing. *Nature Geoscience*, *2*(12), pp.851-854.

Alberti, G., 2017. CASSINI ORBITER RADAR ALTIMETER BURST DATA RECORD SUMMARY. https://doi.org/10.17189/1520209.

Barnes, J.W., Radebaugh, J., Brown, R.H., Wall, S., Soderblom, L., Lunine, J., Burr, D., Sotin, C., Le Mouélic, S., Rodriguez, S., Buratti, B.J., Clark, R., Baines, K.H., Jaumann, R., Nicholson, P.D., Kirk, R.L., Lopes, R., Lorenz, R.D., Mitchell, K., Wood, C.A., 2007. Near-infrared spectral mapping of Titan's mountains and channels. Journal of Geophysical Research 112, E11006. doi: 10.1029/2007JE002932.

Barnes, J.W., Brown, R.H., Soderblom, L., Sotin, C., Le Mouèlic, S., Rodriguez, S., Jaumann, R., Beyer, R.A., Buratti, B.J., Pitman, K. and Baines, K.H., 2008. Spectroscopy, morphometry, and photoclinometry of Titan's dunefields from Cassini/VIMS. *Icarus*, *195*(1), pp.400-414.

Barnes, J.W., Bow, J., Schwartz, J., Brown, R.H., Soderblom, J.M., Hayes, A.G., Vixie, G., Le Mouélic, S., Rodriguez, S., Sotin, C. and Jaumann, R., 2011. Organic sedimentary deposits in Titan's dry lakebeds: Probable evaporite. Icarus, 216, 136-140.

Barnes, J.W., Buratti, B.J., Turtle, E.P., Bow, J., Dalba, P.A., Perry, J., Brown, R.H., Rodriguez, S., Mouélic, S.L., Baines, K.H. and Sotin, C., 2013. Precipitation-induced surface brightenings seen on Titan by Cassini VIMS and ISS. *Planetary Science*, *2*(1), pp.1-22.

Birch, S.P.D., Hayes, A.G., Howard, A.D., Moore, J.M., Radebaugh, J., 2016. Alluvial Fan Morphology, distribution and formation on Titan. Icarus 270, 238-247. 10.1016/j.icarus.2016.02.013.

Birch, S.P.D., Hayes, A.G., Dietrich, W.E., Howard, A.D., Bristow, C.S., Malaska, M.J., Moore, J.M., Mastrogiuseppe, M., Hofgartner, J.D., Williams, D.A. and White, O.L., 2017. Geomorphologic mapping of titan's polar terrains: Constraining surface processes and landscape evolution. Icarus, 282, pp.214-236.

Birch, S.P.D., Hayes, A.G., Corlies, P., Stofan, E.R., Hofgartner, J.D., Lopes, R.M.C., Lorenz, R.D., Lunine, J.I., MacKenzie, S.M., Malaska, M.J. and Wood, C.A., 2018. Morphological evidence that Titan's southern hemisphere basins are paleoseas. *Icarus*, *310*, pp.140-148.

Birch, S.P.D., Hayes, A.G., Poggiali, V., Hofgartner, J.D., Lunine, J.I., Malaska, M.J., Wall, S., Lopes, R.M.C. and White, O., 2019. Raised rims around Titan's sharp-edged depressions. Geophysical Research Letters, 46(11), pp.5846-5854.

Bratsolis, E., Bampasidis, G., Solomonidou, A., Coustenis, A., 2012. A despeckle filter for the Cassini synthetic aperture radar images of Titan's surface. Planetary and Space Science, 61, 108–113.

Brossier, J.F., Rodriguez, S., Cornet, T., Lucas, A., Radebaugh, J., Maltagliati, L., Le Mouélic, S., Solomonidou, A., Coustenis, A., Hirtzig, M., Jaumann, R., Stephan, K., Sotin, C., 2018. Geological evolution of titan's equatorial regions: possible nature and origin of the dune material. JGR, 123, 1089–1112.

Burr, D.M., Jacobsen, R.E., Roth, D.L., Phillips, C.B., Mitchell, K.L., Viola, D., 2009. Fluvial

network analysis on Titan: Evidence for subsurface structures and west to east wind flow, southwestern Xanadu. Geophysical Research Letters 36, L22203. doi: 10.1029/2009GL040909.

Burr, D.M., Perron, J.T., Lamb, M.P., Iriwin, R.P. III, Collins, G.C., Howard, A.D., Sklar, L.S., Moore, J.M., Ádámkovics, M., Baker, V.R., Drummond, S.A., Black, B.A., 2013a. Fluvial features on Titan: Insights from morphology and modeling. Geological Society of America Bulletin 125, 299-321. doi: 10.1130/B30612.1

Burr, D.M., Drummond, S.A., Cartwright, R., Black, B.A. and Perron, J.T., 2013b. Morphology of fluvial networks on Titan: Evidence for structural control. *Icarus*, *226*(1), pp.742-759.

Clark, R.N., Curchin, J.M., Barnes, J.W., Jaumann, R., Soderblom, L., Cruikshank, D.P., Brown, R.H., Rodriguez, S., Lunine, J., Stephan, K., Hoefen, T.M., Le Mouelic, S., Sotin, C., Baines, K.H., Buratti, B.J., Nicholson, P.D., 2010. Detection and mapping of hydrocarbon deposits on Titan. Journal of Geophysical Research 115, E10005. doi: 10.1029/2009JE003369.

Cook-Hallett, C., Barnes, J.W., Kattenhorn, S.A., Hurford, T., Radebaugh,J., Stiles, B.,Beuthe, M., 2015. Global contraction/expansion and polar lithospheric thinning on Titan from patterns of tectonism, Journal of Geophysical Research: Planets, 120, 1220–1236. doi:10.1002/2014JE004645.

Cordier, D., Cornet, T., Barnes, J.W., MacKenzie, S.M., Le Bahers, T., Nna-Mvondo, D., Rannou, P. and Ferreira, A.G., 2016. Structure of Titan's evaporites. *Icarus*, *270*, pp.41-56.

Corlies, P., Hayes, A.G., Birch, S.P.D., Lorenz, R., Stiles, B.W., Kirk, R., Poggiali, V., Zebker, H., Iess, L., 2017. Titan's topography and shape at the end of the Cassini mission. Geophys. Res. Lett. 44, 11754–11761. https://doi.org/10.1002/ 2017GL075518.

Coutelier, M., Cordier, D., Seignovert, B., Rannou, P., Le Gall, A., Cours, T., Maltagliati, L. and Rodriguez, S., 2021. Distribution and intensity of water ice signature in South Xanadu and Tui Regio. *Icarus*, *364*, p.114464.

Crosta, A., Silber, E., Lopes, R., Johnson, B., Bjonnes, E., Malaska, M., Vance, S., Sotin, C., Solomonidou, A., Soderblom, J., 2021. Modeling the formation of Menrva impact crater on Titan: Implications for habitability. Icarus 370, 114679.

Elachi, C., Wall, S., Allison, M., Anderson, Y., Boehmer, R., Callahan, P., Encrenaz, P., Flamini, E., Franceschetti, G., Gim, Y., Hamilton, G., Hensley, S., Janssen, M., Johnson, W., Kelleher, K., Kirk, R., Lopes, R., Lorenz, R., Lunine, J., Muhleman, D., Ostro, S., Paganelli, F., Picardi, G., Posa, F., Roth, L., Seu, R., Shaffer, S., Soderblom, L., Stiles, B., Stofan, E., Vetrella, S., West, R., Wood, C., Wye, L., Zebker, H., 2005. Cassini Radar views the surface of Titan. Science 308, 970–974.

Elachi, C., Wall, S., Janssen, M., Stofan, E., Lopes, R., Kirk, R., Lorenz, R., Lunine, J., Paganelli, F., Soderblom, L., Wood, C., Wye, L., Zebker, H., Anderson, Y., Ostro, S., Allison, M., Boehmer, R., Callahan, P., Encrenaz, P., Flamini, E., Francescetti, G., Gim, Y., Hamilton, G., Hensley, S., Johnson, W., Kelleher, K., Muhleman, D., Picardi, G., Posa, F., Roth, L., Seu, R., Shaffer, S., Stiles, B., Vetrella, S., West, R., 2006. Titan Radar Mapper observations from Cassini's T3 fly-by. Nature 441, 709–713.

Faulk, S., Mitchell, J., Moon, S., Lora, J., 2017. Regional patterns of extreme precipitation on Titan consistent with observed alluvial fan distribution. Nature Geoscience, 10, 827-832.

Faulk, S., Lora, J., Mitchell, J., Milly, P., 2020. Titan's climate patterns and surface methane distribution due to the coupling of land hydrology and atmosphere. Nature Astronomy, 4, 390-398.

Greeley R. and Batson, R.M., 1990. Planetary Mapping. New York: Cambridge University Press.

Grundy, W.M., Schmitt, B. and Quirico, E., 2002. The temperature-dependent spectrum of methane ice I between 0.7 and 5 μm and opportunities for near-infrared remote thermometry. Icarus, 155(2), pp.486-496.

Hayes, A., Aharonson, O., Callahan, P., Elachi, C., Gim, Y., Kirk, R., Lewis, K., Lopes, R., Lorenz, R., Lunine, J., Mitchell, K., Mitri, G., Stofan, E., Wall, S., 2008. Hydrocarbon lakes on Titan: Distribution and interaction with a porous regolith. Geophysical Research Letters 35, L09204. doi: 10.1029/2008GL033409.

Hayes, A.G., Birch, S.P.D., Dietrich, W.E., Howard, A.D., Kirk, R.L., Poggiali, V., Mastrogiuseppe, M., Michaelides, R.J., Corlies, P.M., Moore, J.M. and Malaska, M.J., 2017. Topographic constraints on the evolution and connectivity of Titan's lacustrine basins. Geophysical Research Letters, 44(23), pp.11-745.

Hayes, A. G., Lorenz, R. D., & Lunine, J. I., 2018. A post-Cassini view of Titan's methane-based hydrologic cycle. Nature Geoscience, 11, 306 – 313.

Hedgepeth, J.E., Neish, C.D., Turtle, E.P., Stiles, B., Kirk, R., Lorenz, R.D., 2020. Titan's impact crater population after Cassini. Icarus, 344, 113664. doi.org/10.1016/j.icarus.2020.113664.

Hofgartner, J. D., et al. (2020), The root of anomalously specular reflections from solid surfaces on Saturn's moon Titan, Nat. Comm. 11, 2829.

Janssen, M.A., Le Gall, A., Lopes, R.M., Lorenz, R.D., Malaska, M.J., Hayes, A.G., Neish, C.D.,

Solomonidou, A., Mitchell, K.L., Radebaugh, J. and Keihm, S.J., 2016. Titan's surface at 2.18-cm wavelength imaged by the Cassini RADAR radiometer: Results and interpretations through the first ten years of observation. Icarus, 270, pp.443-459.

Jaumann, R., Brown, R.H., Stephan, K., Barnes, J.W., Soderblom, L.A., Sotin, C., Le Mouélic, S., Clark, R.N., Soderblom, J., Buratti, B.J., Wagner, R., McCord, T.B., Rodriguez, S., Baines, K.H., Cruikshank, D.P., Nicholson, P.D., Griffith, C.A., Langhans, M., Lorenz, R.D., 2008. Fluvial erosion and post-erosional processes on Titan. Icarus 197, 526-538. doi: 10.1016/j.icarus.2008.06.002.

Jaumann, R., Kirk, R. L. Lorenz, R. D., Lopes, R. M.C., Stofan, E. Turtle, E. P. Keller, H. U. Wood, C. A., Sotin, C. Soderblom, L. A., Tomasko, M. G., 2009. Geology and Surface Processes on Titan. In: Brown, R. H., Leberton, J.-P., Waite, J. H. (Eds.), Titan from Cassini-Huygens. Springer, New York, pp 75–140.

Karkoschka E., McEwen A., Perry J., 2017. Producing the Best Global Mosaic of Titan's Surface Albedo Using Cassini Images. LPSC 48, #2518.

Kirk, R., Howington-Kraus, E., Redding, B., Callahan, P., Hayes, A., Le Gall, A., Lopes, R., Lorenz, R., Lucas, A., Mitchell, K., Neish, C., Aharonson, O., Radebaugh, J., Stiles, B., Stofan, E., Wall, S., Wood, C., Cassini RADAR Team, 2012. Topographic Mapping of Titan: Latest Results. 43rd Lunar and Planetary Science Conference, LPI 1659, 2759.

Krasnopolsky, V.A., 2009. A photochemical model of Titan's atmosphere and ionosphere. Icarus 201, 226-256. doi: 10.1016/j.icarus.2008.12.038.

Langhans, M.H., Jaumann, R., Stephan, K., Brown, R.., Buratti, B.J., Clark, R.N., Baines, K.H., Nicholson, P.D., Lorenz, R.D., Soderblom, L.A., Soderblom, J.M., Sotin, C., Barnes, J.W.,

Nelson, R., 2012. Titan's fluvial valleys: Morphology, distribution, and spectral properties. Planetary and Space Science 60, 34-51. doi: 10.1016/j.pss.2011.01.020.

Larsson, R. and McKay, C. P., 2013. Timescale for oceans in the past of Titan, P&SS, 78, 22–24, doi: 10.1016/j.pss.2012.12.001.

Lavvas, P.P., Coustenis, A., Vardavas, I.M., 2008. Coupling photochemistry with haze formation in Titan's atmosphere, Part II: Results and validation with Cassini/Huygens data. Planetary and Space Science 56, 67-99. doi: 10.1016/j.psss.2007.05.027.

Le Mouélic, S., Cornet, T., Rodriguez, S., Sotin, C., Seignovert, B., Barnes, J.W., Barnes, J., Brown, R.H., Baines, K.H., Buratti, B.J., Clark, R.N., Nichilson, P.D., Lasue, J., Pasek, V., Soderblom, J.M., 2019. The Cassini VIMS archive of Titan: From browse products to global infrared color maps. Icarus, 319, 121-132.

Liu, Z.Y.C., Radebaugh, J., Harris, R.A., Christiansen, E.H., Neish, C.D., Kirk, R.L., Lorenz, R.D. and Cassini RADAR Team, 2016. The tectonics of Titan: Global structural mapping from Cassini RADAR. Icarus, 270, pp.14-29.

Lopes, R.M., Mitchell, K.L., Stofan, E.R., Lunine, J.I., Lorenz, R., Paganelli, F., Kirk, R.L., Wood, C.A., Wall, S.D., Robshaw, L.E. and Fortes, A.D., 2007. Cryovolcanic features on Titan's surface as revealed by the Cassini Titan Radar Mapper. Icarus, 186, 395-412.

Lopes, R.M.C., Stofan, E.R., Pecyno, R., Radebaugh, J., Mitchell, K.L., Mitri, G., Wood, C.A., Kirk, R.L., Wall, S.D., Lunine, J.L., Hayes, A., Lorenz, R., Farr, T., Wye, L., Craig, J., Ollerenshaw, R., Janssen, M., LeGall, A., Paganelli, F., West, R., Stiles, B., Callahan, P., Anderson, Y., Valora, P., Soderblom, L., and the Cassini RADAR Team, 2010. Distribution and interplay of geologic processes on Titan from Cassini radar data. Icarus 205, 540–558. doi: 10.1016/j.icarus.2009.08.010.

Lopes, R.M.C., Kirk, R.L.; Mitchell, K.L., Le Gall, A., Barnes, J.W., hayes, A., Kargel, J., Wye, L., Radebaugh, J., Stofan, E.R., Janssen, M., Neish, C., Wall, S., Wood, C.A., Lunine, J.I., Malaska, M.J., 2013. Cryovolcanism on Titan: New results from Cassini RADAR and VIMS. Journal of Geophysical Research: Planets 118, 1-20. doi: 10.1002/jgre.20062.

Lopes, R.M.C., Malaska, M.J., Solomonidou, A., LeGall, A., Janssen, M.A., Neish, C., Turtle, E.P., Birch, S.P.D., Hayes, A.G., Radebaugh, J., Coustenis, A., Schoenfeld, A., Stiles, B.W., Kirk, R.L., Mitchell, K.L., Stofan, E.R., Lawrence, K.J., and the Cassini RADAR Team, 2016. Nature, Distribution, and Origin of Titan's Undifferentiated Plains ("Blandlands"). Icarus, 270, 162-182.

Lopes, R.M.C., Wall, S.D., Elachi, C., Birch, S.P., Corlies, P., Coustenis, A., Hayes, A.G., Hofgartner, J.D., Janssen, M.A., Kirk, R.L. and LeGall, A., 2019. Titan as revealed by the Cassini radar. Space Science Reviews, 215(4), pp.1-50.

Lopes, R.M., Malaska, M.J., Schoenfeld, A.M., Solomonidou, A., Birch, S.P.D., Florence, M., Hayes, A.G., Williams, D.A., Radebaugh, J., Verlander, T. and Turtle, E.P., 2020. A global geomorphologic map of Saturn's moon Titan. Nature astronomy, 4(3), pp.228-233.

Lorenz, R.D., Wall, S., Radebaugh, J., Boubin, G., Reffet, E., Janssen, M., Stofan, E., Lopes, R., Kirk, R., Elachi, C., Lunine, J., Mitchell, K., Paganelli, F., Soderblom, L., Wood, C., Wye, L., Zebker, H., Anderson, Y., Ostro, S., Allison, M., Boehmer, R., Callahan, P., Encrenaz, P., Ori, G.G., Francescitti, G., Gim, Y., Hamilton, G., Hensley, S., Johnson, W., Kelleher, K., Muhleman, D., Picardi, G., Posa, F., Roth, L., Seu, R., Shaffer, S., Stiles, B., Vetrella, S., Flamini, E., West, R., 2006a. The Sand Seas of Titan: Cassini RADAR Observations of Longitudinal Dunes. Science 312, 724-727. doi: 10.1126/science.1123257.

Lorenz, R.D., Niemann, H.B., Harpold, D.N., Way, S.H. and Zarnecki, J.C., 2006b. Titan's damp

ground: Constraints on Titan surface thermal properties from the temperature evolution of the Huygens GCMS inlet. *Meteoritics & Planetary Science*, *41*(11), pp.1705-1714.

Lorenz, R.D., MacKenzie, S.M., Neish, C.D., Le Gall, A., Turtle, E.P., Barnes, J.W., Trainer, M.G., Werynski, A., Hedgepeth, J. and Karkoschka, E., 2021. Selection and characteristics of the Dragonfly landing site near Selk crater, Titan. The Planetary Science Journal, 2(1), p.24.

Lunine, J.I., Elachi, C., Wall, S.D., Janssen, M., Allison, M.D., Anderson, Y., Boehmer, R., Callahan, P., Encrenaz, P., Flamini, E., Franceschetti, G., Gim, Y., Hamilton, G., Hensley, S., Johnson, W.T.K., Kelleher, K., Kirk, R.L., Lopes, R.M., Lorenz, R., Muhlemen, D.O., Orosei, R., Ostro, S.J., Paganelli, F., Paillou, P., Picardi, G., Posa, F., Radebaugh, J., Roth, L.E., Seu, R., Shaffer, S., Soderblom, L.A., Stiles, B., Stofan, E.R., Vetrella, S., West, R., Wood, C.A., Wye, L., Zebker, H., Alberti, G., Karkoschka, E., Rizk, B., McFarlane, E., See, C., Kazeminejad, B., 2008. Titan's diverse lanscapes as evidenced by Cassini RADAR's third and fourth looks at Titan. Icarus 195, 415-433. doi: 10.1016/j.icarus.2007.12.022.

MacKenzie, S.M., Barnes, J.W., Sotin, C., Soderblom, J.M., Le Mouélic, S., Rodriguez, S., Baines, K.H., Buratti, B.J., Clark, R.N., Nicholson, P.D. and McCord, T.B., 2014. Evidence of Titan's climate history from evaporite distribution. Icarus, 243, 191-207.

Malaska, M.J. and Hodyss, R., 2014. Dissolution of benzene, naphthalene, and biphenyl in a simulated Titan lake. *Icarus*, *242*, pp.74-81.

Malaska, M. J., Lopes, R. M. C., Williams, D. A., Neish, C. D., Solomonidou, A., Soderblom, J. M., et al., 2016a. Geomorphological map of the Afekan Crater region, Titan: Terrain relationships in the equatorial and midlatitude regions. Icarus, 270, 130–161.

Malaska, M.J., Lopes, R.M., Hayes, A.G., Radebaugh, J., Lorenz, R., Turtle, E., 2016b. Material transport map of Titan: the fate of dunes. Icarus, 270, 183-196.

Malaska, M. J., Radebaugh, J., Lopes, R. M. C., Mitchell, K., Verlander, T., Schoenfeld, A., Florence, M., Le Gall, A., Solomonidou, A., Hayes, A., Birch, S., Janssen, M., Schurmeier, L., Cornet, T., Ahrens, C., and the Cassini RADAR team, 2020. Labyrinth Terrain on Titan. Icarus, 344, 113764.

Michaelides, R.J., Hayes, A.G., Mastrogiuseppe, M., Zebker, H.A., Farr, T.G., Malaska, M.J., Poggiali, V. and Mullen, J.P., 2016. Constraining the physical properties of Titan's empty lake basins using nadir and off-nadir Cassini RADAR backscatter. *Icarus*, *270*, pp.57-66.

Miller, J.W., Birch, S.P.D., Hayes, A.G., Malaska, M.J., Lopes, R.M.C., Schoenfeld, A.M., Corlies, P.M., Burr, D.M., Farr, T.G. and Perron, J.T., 2021. Fluvial Features on Titan and Earth: Lessons from Planform Images in Low-resolution SAR. The Planetary Science Journal, 2(4), p.142.

Mitri, G., A.P. Showman, J.I. Lunine, and R.D. Lorenz, 2007. Hydrocarbon lakes on Titan. Icarus 186, 385-394.

Mitri, G., Showman, A.P., Lunine, J.I. and Lopes, R.M., 2008. Resurfacing of Titan by ammonia-water cryomagma. Icarus, 196, 216-224.

Mitri, G., Bland, M.T., Showman, A.P., Radebaugh, J., Stiles, B., Lopes, R.M.C., Lunine, J.I., pappalardo, R.T., 2010. Mountains on Titan: Modeling and observations. Journal of Geophysical Research: Planets 115, E10002.

Mitri, G., Lunine, J.I., Mastrogiuseppe, M. and Poggiali, V., 2019. Possible explosion crater origin of small lake basins with raised rims on Titan. Nature Geoscience, 12, 791-796.

Moore, J.M. and Howard, A.D., 2010. Are the basins of Titan's Hotei Regio and Tui Regio sites

of former low latitude seas?. Geophysical Research Letters, 37(22).

Moore, J.M., Howard, A.D., Morgan, A.M., 2014. The landscape of titan as witness to is climate evolution. Journal of Geophysical Research: Planets 119, 2060-2077. doi: 10.1002/2014JE004608.

Nelson, R.M., Kamp. L.W., Lopes, R.M.C., Matson, D.L., Kirk, R.L., Hapke, B.W., Wall, S.D., Boryta, M.D., Leader, F.E., Smythe, W.D., Mitchell, K.L., Baines, K.H., Jaumann, R., Sotin, C., Clark, R.N., Cruikshank, D.P., Drossart, P., Lunine, J.I., Combes, M., Bellucci, G., Bibring, J-P., Capaccioni, F., Cerroni, P., Coradini, A., Formisano, V., Filacchione, G., Langevin, Y., McCord, T.B., Mennella, V., Nicholson, P.D., Sicardy, B., Irwin, P.G.J., 2009. Photometric Changes on Saturn's Moon Titan: Evidence for Cryovolcanism. Geophys. Res. Lett., 36, L04202, doi:10.1029/2008GL036206.

Neish, C.D. and Lorenz, R.D., 2012. Titan's global crater population: a new assessment. Planet. Space Sci. 60, 26–33.

Neish, C. D., Kirk, R. L., Lorenz, R. D., Bray, V. J., Schenk, P., Stiles, B. W., Turtle, E, Mitchell, K., Hayes, A., and the Cassini RADAR team, 2013. Crater topography on Titan: Implications for landscape evolution. Icarus, 223, 82-90.

Neish, C.D., Barnes, J.W., Sotin, C., MacKenzie, S., Soderblom, J.M., Le Mouélic, S., Kirk, R.L., Stiles, B.W., Malaska, M.J., Le Gall, A., Brown, R.H., Baines, K.H., Buratti, B., Clark, R.N., Nicholson, P.D., 2015. Spectral properties of Titan's impact craters imply chemical weathering of its surface. Geophys. Res. Lett. 42, 3746–3754.

Neish, C.D., Molaro, J.L., Lora, J.M., Howard, A.D., Kirk, R.L., Schenk, P., Bray, V.J. and Lorenz, R.D., 2016. Fluvial erosion as a mechanism for crater modification on Titan. *Icarus*, *270*, pp.114-129.

Poggiali, V., Mastrogiuseppe, M., Hayes, A., Seu, R., Birch, S., Lorenz, R., Grima, C., Hofgartner, J., 2016. Liquid-filled canyons on Titan. Geophysical Research Letter, 43, 7887-7894.

Radebaugh, J., Lorenz, R.D., Kirk, R.L., Lunine, J.I., Stofan, E.R., Lopes, R.M.C., Wall, S.D., 2007. Mountains on Titan as observed by Cassini Radar. Icarus 192, 77-91. doi: 10.1016/j.icarus.2007.026.020.

Radebaugh, J., Lorenz, R.D., Lunine, J.I., Wall, S.D., Boubin, G., Reffet, E., Kirk, R.L., Lopes, R.M., Stofan, E.R., Soderblom, L., Allison, M., Janssen, M., Paillouo, P., Callahan, P., Spencer, C., Cassini RADAR Team, 2008. Dunes on Titan observed by Cassini Radar. Icarus 194, 690-703. doi: 10.1016/j.icarus.2007.10.015.

Radebaugh, J., R. D. Lorenz, S. D. Wall, R. L. Kirk, C. A. Wood, J. I. Lunine, E. R. Stofan, R. M. C. Lopes, P. Valora, T. G. Farr, A. Hayes, B. Stiles, G. Mitri, H. Zebker, M. Janssen, L. Wye, A. LeGall, K. L. Mitchell,F. Paganelli, R.D. West, E.L. Schaller, and the Cassini Radar Team, 2011. Regional geomorphology and history of Titan's Xanadu province. Icarus 211, 672-685. doi: 10.1016/j.icarus.2010.07.022.

Radebaugh, J., Ventra, D., Lorenz, R.D., Farr, T.G., Kirk, R.L., Hayes, A., Malaska, M.J., Birch, S., Liu, Z.Y.C., Lunine, J.I., Barnes, J., Le Gall, A., Lopes, R., Stofan, E., Wall, S., Pailloy, P., 2018. Alluvial and fluvial fans on Saturn's moon Titan reveal processes, materials and regional geology. Ventra, D. & Clarke, L. E. (eds) Geology and Geomorphology of Alluvial and Fluvial Fans: Terrestrial and Planetary Perspectives. Geological Society, London, Special Publications, 440.

Rodriguez, S., Garcia, A., Lucas, A., Appéré, T., Le Gall, A., Reffet, E., Le Corre, L., Le

Mouélic, S., Cornet, T., Du Pont, S.C. and Narteau, C., 2014. Global mapping and characterization of Titan's dune fields with Cassini: Correlation between RADAR and VIMS observations. *Icarus*, *230*, pp.168-179.

Rodriguez, S., Vinatier, S., Cordier, D., Tobie, G., Achterberg, R.K., Anderson, C.M., Badman, S.V., Barnes, J.W., Barth, E.L., Bézard, B. and Carrasco, N., 2022. Science goals and new mission concepts for future exploration of Titan's atmosphere, geology and habitability: titan POlar scout/orbitEr and in situ lake lander and DrONe explorer (POSEIDON). Experimental Astronomy, pp.1-63.

Schoenfeld, A., Lopes, R., Malaska, M., Solomonidou, A., Williams, D., Birch, S., Hayes, A., Corlies, P., Le Gall, A., Janssen, M., Le Mouelic, S., Turtle, E., Florence, M., Verlander, T., 2021. Geomorphological map of the South Belet Region of Titan. Icarus, 366, 114516.

Schoenfeld, A., 2022. Soi crater region mapping shapefiles, Mendeley Data, V1, doi: 10.17632/z4jkvsr25b.1

Seignovert, B., Le Mouelic, S., Brown, R.H., Joseph, E., Karkoschka, E., Pasek, V., Sotin, C., Turtle, E.P., 2019. Titan's Global Map Combining VIMS and ISS Mosaics. EPSC, 2019, EPSC-DPS2019.

Soderblom, L.A., Kirk, R.L., Lunine, J.I., Anderson, J.A., Baines, K.H., Barnes, J.W., Barrett, J.M., Brown, R.H., Buratti, B.J., Clark, R.N., Cruikshank, D.P., Elachi, C., Janssen, M.A., Jaumann, R., Karkoschka, E., Le Mouélic, S., Lopes, R.M., Lorenz, R.D., McCord, T.B., Nicholson, P.D., Radebaugh, J., Rizk, B., Sotin, C., Stofan, E.R., Sucharski, T.L., Tomasko, M.G., Wall, S.D., 2007. Correlations between Cassini VIMS spectra and RADAR SAR images: Implications for Titan's surface composition and the character of the Huygens Probe Landing Site. Planetary and Space Science 55, 2025-2036. doi: 10.1016/j.pss.2007.04.014.

Sohl, F., Solomonidou, A., Wagner, F.W., Coustenis, A., Hussmann, H. and Schulze-Makuch, D., 2014. Tidal stresses on Titan and implications for its geology and habitability. Journal of Geophysical Research: Planets, 119, pp.1013-1036.

Solomonidou, A., Bampasidis, G., Hirtzig, M., Coustenis, A., Kyriakopoulos, K., Seymour, K.S., Bratsolis, E. and Moussas, X., 2013. Morphotectonic features on Titan and their possible origin. Planetary and Space Science, 77, pp.104-117.

Solomonidou, A., Coustenis, A., Hirtzig, M., Rodriguez, S., Stephan, K., Lopes, R.M.C., Drossart, P., Sotin, C., Le Mouélic, S., Lawrence, K. and Bratsolis, E., 2016. Temporal variations of Titan's surface with Cassini/VIMS. Icarus, 270, pp.85-99.

Solomonidou, A., Coustenis, A., Lopes, R.M., Malaska, M.J., Rodriguez, S., Drossart, P., Elachi, C., Schmitt, B., Philippe, S., Janssen, M. and Hirtzig, M., 2018. The spectral nature of Titan's major geomorphological units: constraints on surface composition. Journal of Geophysical Research: Planets, 123(2), pp.489-507.

Solomonidou, A., Neish, C., Coustenis, A., Malaska, M., Le Gall, A., Lopes, R., Werynski, A., Markonis, Y., Lawrence, K., Altobelli, N., Witasse, O., Schoenfeld, A., Matsoukas, C., Baziotis, I., Drossart, P., 2020a. The chemical composition of impact craters on Titan I. Implications for exogenic processing. Astronomy & Astrophysics, 641, A16.

Solomonidou, A., Le Gall, A., Malaska, M.J., Birch, S.P.D., Lopes, R.M.C., Coustenis, A., Rodriguez, S., Wall, S.D., Michaelides, R.J., Nasr, M.R. and Elachi, C., 2020b. Spectral and emissivity analysis of the raised ramparts around Titan's northern lakes. Icarus, 344, p.113338.

Stiles, B.W., Gim, Y., Hamilton, G., Hensley, S., Johnson, W.T., Shimada, J., West, R.D. and

Callahan, P., 2006, April. Ground processing of Cassini RADAR imagery of Titan. In *2006 IEEE Conference on Radar* (pp. 8-pp). IEEE.

Stiles, B.W., Hensley, S., Gim, Y., Bates, D.M., Kirk, R.L., Hayes, A., Radebaugh, J., Lorenz, R.D., Mitchell, K.L., Callahan, P.S., Zebker, H., Johnson, W.T.K., Wall, S.D., Wood, C.A., Janssen, M., Pelletier, F., West, R.D., Veramacheneni, C., Cassini RADAR Team, 2009. Determining Titan Surface Topography from Cassini SAR data. Icarus 202, 584-598. doi: 10.1016/j.icarus.2009.03.032.

Stiles, B.W., 2017a. CASSINI ORBITER SSA RADAR 5 BIDR V1.0. https://doi.org/10.17189/1520231

Stiles, B.W., 2017b. CASSINI ORBITER SSA RADAR 5 STDR V1.0. https://doi.org/10.17189/1520238

Stofan, E.R., Lunine, J.I., Lopes, R., Paganelli, F., Lorenz, R.D., Wood, C.A., Kirk, R., Wall, S., Elachi, C., Soderblom, L.A., Ostro, S., Janssen, M., Radebaugh, J., Wye, L., Zebker, H., Anderson, Y., Allison, M., Boehmer, R., Callahan, P., Encrenaz, P., Flamini, E., Francescetti, G., Gim, Y., Hamilton, G., Hensley, S., Johnson, W.T.K., Kelleher, K., Muhleman, D., Picardi, G., Posa, F., Roth, L., Seu, R., Shaffer, S., Stiles, B., Vetrella, S., West, R., 2006. Mapping of Titan: Results from the First Two Titan Radar Passes. Icarus 185, 443-456. doi: 101016/j.icarus.2006.07.015.

Stofan, E.R., Elachi, C., Lunine, J.I., Lorenz, R.D., Stiles, B., Mitchell, K.L., Ostro, S., Soderblom, L., Wood, C., Zebker, H., Wall, S., Janssen, M., Kirk, R., Lopes, R., Paganelli, F., Radebaugh, J., Wye, L., Anderson, Y., Allison, M., Boehmer, R., Callahan, P., Encrenaz, P., Flamini, E., Francescetti, G., Gim, Y., Hamilton, G., Hensley, S., Johnson, W.T.K., Kelleher, K., Muhlman,

D., Paillou, P., Picardi, G., Posa, F., Roth, Seu, R., Shaffer, S., Vetrella, S., West, R., 2007. The lakes of Titan. Nature 445, 61-64. doi: 10.1038/nature05438.

Sulaiman, A.H., Achilleos, N., Bertucci, C., Coates, A., Dougherty, M., Hadid, L., Holmberg, M., Hsu, H.W., Kimura, T., Kurth, W. and Gall, A.L., 2021. Enceladus and Titan: emerging worlds of the Solar System. Experimental Astronomy, pp.1-28.

Tobie, G., Teanby, N.A., Coustenis, A., Jaumann, R., Raulin, F., Schmidt, J., Carrasco, N., Coates, A.J., Cordier, D., De Kok, R. and Geppert, W.D., 2014. Science goals and mission concept for the future exploration of Titan and Enceladus. Planetary and Space Science, 104, pp.59-77.

Turtle, E.P., Perry, J.E., McEwen, A.S., Del Genio, A.D., Barbara, J., West, R.A., Dawson, D.D., Porco, C.C., 2009. Cassini imaging of Titan's high-latitude lakes, clouds, and south-polar surface changes. Geophys. Res. Lett. 36, L02204.

Turtle, E.P., Del Genio, A.D., Barbara, J.M., Perry, J.E., Schaller, E.L., McEwen, A.S., West, R.A. and Ray, T.L., 2011. Seasonal changes in Titan's meteorology. Geophysical Research Letters, 38(3).

Wall, S.D., Lopes, R.M., Stofan, E.R., Wood, C.A., Radebaugh, J.L., Hörst, S.M., Stiles, B.W., Nelson, R.M., Kamp, L.W., Janssen, M.A. and Lorenz, R.D., 2009. Cassini RADAR images at Hotei Arcus and western Xanadu, Titan: Evidence for geologically recent cryovolcanic activity. Geophysical Research Letters, 36.

Werynski, A., Neish, C.D., Le Gall, A., Janssen, M.A., The Cassini RADAR Team, 2019. Compositional variations of Titan's impact craters indicates active surface erosion. Icarus, 321, 508-521.

Williams, D.A., Radebaugh, J., Lopes, R.M.C., Stofan, E., 2011. Geomorphologic mapping of the Menrva region of Titan using *Cassini* RADAR data. Icarus 212, 744-750. doi: 10.1016/j.icarus.2011.01.014.

Wilson, E.H., Atreya, S.K., 2004. Current state of modeling the photochemistry of Titan's mutually dependent atmosphere and ionosphere. Journal of Geophysical Research 109, E06002. doi: 10.1029/2003JE002181.

Wood, C.A., Lorenz, R., Kirk, R., Lopes, R., Mitchell, K., Stofan, E., and the Cassini RADAR Team, 2010. Impact craters on Titan. Icarus, 206 (2010) 334-344.

- Chapter 6 -

6 A Global Geomorphological Map of Saturn's Moon Titan

6.1 Introduction

Titan has a complex geologic landscape shaped by its active methane-based hydrologic cycle, making its surface one of most geologically diverse in the Solar System. Despite the differences in materials, temperatures, and the gravity fields between Earth and Titan, many of Titan's surface features are remarkably similar and can be interpreted as results of the same fundamental geologic processes, including impact cratering (Wood et al., 2010; Neish et al., 2015), fluvial/aeolian erosion and deposition (Burr et al., 2006; Lorenz et al., 2006, 2008; Radebaugh et al., 2016; Lopes et al., 2016), precipitation (Turtle et al., 2011), dissolution (Cornet et al., 2015), tectonism (Mitri et al., 2010), and even possible cryovolcanism (Lopes et al., 2013). The Cassini spacecraft has also revealed Titan to be a world rich in organic materials (Lorenz et al., 2006; Clark et al., 2010) that mantle the surface to a depth of at least several tens of centimeters in most places (Janssen et al., 2016). Titan's thick atmosphere enables these materials to be eroded, transported and deposited across the landscape (Lorenz et al., 2006; Malaska et al., 2016). However, Titan's thick and hazy atmosphere has also hindered the identification of its geologic features at visible wavelengths and the study of its surface composition. Here we identify and globally map the major geological units on Titan's surface using radar and infrared data from the Cassini orbiter spacecraft, place Titan's terrain types in stratigraphic order (Lopes et al., 2010; Malaska et al., 2016; Birch et al., 2017), and constrain the relative importance and global distribution of various endogenic and exogenic processes (Lopes et al., 2010). Correlations between datasets enabled us to produce a global map even where the SAR datasets were incomplete. We defined the six major geological units (based primarily on backscatter and overall morphology, as done for prior mapping) as: plains, dunes, hummocky

terrain, lakes, labyrinth terrain and craters (Fig. 6.1). We find that the equatorial dunes and polar lakes are relatively young, whereas the hummocky or mountainous terrains are the oldest on Titan. Our results also show that Titan's surface is dominated by sedimentary or depositional processes with a clear latitudinal variation, with dunes at the equator, plains at mid-latitudes and labyrinth terrains and lakes at the poles.

6.2 Methods

6.2.1 Mapping Technique

Titan's hazy atmosphere scatters light at visual to near-infrared wavelengths, limiting the detailed visual and infrared spectroscopy data that can constrain surface composition. Longer-wavelength microwave radiation, however, penetrates the atmosphere and interacts with the surface with no significant atmospheric interference. We primarily used data from the Cassini RADAR instrument in its Synthetic Aperture Radar (SAR) mode to map Titan's geology, following mapping methodologies outlined in previous work (Lopes et al., 2010; Malaska et al., 2016; Schoenfeld et al., 2021). SAR data responds to near-surface roughness at the wavelength scale (2.17 cm), to surface slopes at the pixel scale, and to the dielectric properties of near-surface materials. SAR can penetrate many wavelengths into some materials as well (Janssen et al., 2016). Global imaging by ISS (Porco et al., 2004; Karkoschka et al., 2018) (at 0.938 μm) and VIMS (1–5 μm; Brown et al., 2004; Le Mouélic et al., 2012, 2019) (1–5 μm) are helpful in unit characterization and global distribution; they provide a complementary dataset that is sensitive to the top surface layering on the order of tens of micrometers, while microwave emissivity penetrates tens of centimeters into the surface (Janssen et al., 2016). Furthermore, analysis and interpretation of VIMS data provide information on the spectral nature and chemical composition

of the surface (Solomonidou et al., 2018). Terrain units have therefore been characterized in terms of radar backscatter, morphology, contact relations, internal texture, topographic relationships and other observed characteristics (ISS, VIMS, and radiometry), following the methodology outlined in previous mapping work.

The Cassini RADAR instrument (Elachi et al., 2004) operates in four modes: SAR, altimetry, scatterometry and radiometry. The SAR mode was mostly used at spacecraft altitudes under approximately 5,000 km, imaging Titan's surface at incidence angles of 15–35°. The SAR data yielded images with spatial resolution from around 350 m to 1.5 km, sufficient to identify major terrains for geological maps (Williams et al., 2011). During each Titan encounter with SAR imaging, a swath 120–450 km in width and 1,000–5,000 km in length was created from five antenna beams, with coverage largely determined by spacecraft range and orbital geometry. SAR data (in nominal mode) covers about 46% of Titan's surface at less than 1 km resolution, while the higher-altitude SAR data covers an additional 24% at less than 5 km resolution.

The SAR dataset was used as the basemap for our geomorphological mapping. We used SAR data to define the boundaries of the terrain contacts and the main units, but data from other radar modes and other instruments were utilized as supplementary datasets, particularly in areas where SAR was not available. Topography was obtained from the SAR swaths by the SARTopo technique (Stiles et al., 2009) and in some other locations by using the RADAR in altimetry mode. The RADAR radiometry mode provided a global map of microwave emissivity. With the use of specific tools, the analysis and interpretation of VIMS data can provide useful information on the spectral nature and chemical composition of the surface (Solomonidou et al., 2018). The terrain units were therefore characterized in terms of SAR backscatter, morphology, contact relations, internal texture, topographic relationship and observed characteristics in ISS, VIMS

and radiometry, following the method previously outlined (Malaska et al., 2016; Schoenfeld et al., 2021; 2023).

Global coverage of the surface was acquired by ISS, VIMS and RADAR radiometry, with variable spatial resolution. The characteristics of each unit in the different datasets provide other information and can be used to infer the main type of unit in areas not imaged by SAR. We removed areas too small to be observed at the 1:20,000,000 scale (approximately areas less than 30 km^2 in spatial extent). For example, the crater subunits in the 1:800,000 scale regional maps (crater rim, crater ejecta, central peak, crater fill shown in Fig. 6.2) were simply mapped as the crater unit in the 1:20,000,000 scale global map. Likewise, areas showing linear dunes and dark areas interpreted as featureless sand sheets were mapped as the dune unit; filled and empty lakes and seas were mapped as the lake unit; hummocky, mountainous and degraded mountain subunits were mapped as hummocky; and plains subunits (undifferentiated, streak-like, variable featured, dark irregular, scalloped and bright gradational) were mapped as plains. Detailed discussions of these different terrains are given in a previous work (Malaska et al., 2016; Schoenfeld et al., 2021; 2023).

The mapping was done using ArcGIS (ESRI) software. Starting with the SAR-imaged areas, we drew contacts between regions based on radar backscatter and gross geomorphology (Lopes et al., 2010; Malaska et al., 2016; Schoenfeld et al., 2021; 2023). The contacts were then used to build polygons using ArcGIS functionalities, and then assigned a terrain attribute based on surface characteristics in the SAR. Geometry of the contacts, sharpness of contact, internal texture, degree of dissection, preferred orientation of diagnostic features or contacts, and overall morphology were all considered when assigning a terrain unit. Data from the other radar modes

and other instruments were used to further characterize each unit (Malaska et al., 2016a; Schoenfeld et al., 2021; 2023).

Crosscutting and superposition relations and available topography were used to determine the relative stratigraphic sequence between terrain units. The plains units are extensive and appear continuous in many areas. More importantly, the plains unit shows a direct contact with all other terrain units mapped. Therefore, the plains unit was used to determine embayment and superposition relations for all other units, from which relative ages could be inferred, with the caveat that exposures of the plains units may not have been formed at the same time and in the same location. Although all units were found to be in contact with the plains, some units were not in contact with each other, so a definitive stratigraphic sequence could not be determined for them. For example, direct contacts were not observed between hummocky and labyrinth units, but both were observed to have been superposed by plains and must therefore be older.

6.2.2 Description of Units

We used correlations established from the primary SAR mapping with the other datasets to extend the mapping to areas not imaged by SAR. For these areas, we used global datasets from ISS, VIMS, radiometry and, where available, high-altitude SAR (HiSAR) and topography from altimetry and SARTopo (Stiles et al., 2009; Corlies et al., 2017). For example, undifferentiated plains appear bland and dark in SAR and HiSAR but bright in ISS and have high emissivity in radiometry (Lopes et al., 2016). Correlations across several datasets have been discussed in detail in previously published papers (Malaska et al., 2016; Solomonidou et al., 2018; Lopes et al., 2016; Schoenfeld et al., 2021). An example of "NonSAR" mapping is shown in Fig. 6.2. Because the NonSAR areas were mapped at a much lower resolution than the SAR

area, they are already at a scale appropriate to be included in the 1:20,000,000 scale global map. Below we describe the subunits contained within each of our major geologic units.

6.2.2.1 Plains

Plains were classified into several subunits (Malaska et al., 2016; Schoenfeld et al., 2021; 2023), but undifferentiated plains (Lopes et al., 2016) are by far the most extensive on Titan. They are low-backscatter regions that appear largely uniform in SAR data, having only a few (<5% by surficial area) observable features at the mapping scale of 1:800,000. Topographically, there is some variation in relief across the undifferentiated plains, but they are lower in local elevation than the hummocky unit. These terrains appear bright in ISS data. The same is true for VIMS data for the undifferentiated plains located in the high latitudes. Much smaller patches of other types of plain have been identified in our 1:800,000 scale regional mapping, generally at mid-to-high latitudes. They are divided into bright lineated plains, bright gradational plains, bright alluvial plains, bright streak-like plains, variable featured plains, dark irregular plains and scalloped plains (Malaska et al., 2016; Schoenfeld et al., 2021; 2023). The bright lineated plains and the bright streak-like plains are interpreted as aeolian-dominated landscapes consisting of high-backscatter materials, whereas the bright gradational plains and the bright alluvial plains are interpreted as being derived by fluvial means. Variable featured plains are interpreted to result from erosion of hummocky terrains, possibly involving fluvial erosion and deposition. Dark irregular plains are topographically lower than surrounding terrains, interpreted as areas dampened by liquid hydrocarbons, or lowland muds (within the top tens of centimeters of the surface). Scalloped plains are interpreted as eroded hummocky terrains with a cover of organic

materials not thick enough to mask their nature. Scalloped plains may be a transitional unit between hummocky terrains and undifferentiated plains.

All the plains are mapped as a single unit in the 1:20,000,000 scale global map. They have a variety of radar appearances, however, with some appearing radar-bright relative to their surroundings, while others do not. In all cases, empty lakes are morphologically distinct features that are recognizable at the 1:800,000 scale. At both poles, lakes (either empty or filled) always appear in clusters, while the seas occupy topographic lows. The total number of filled or empty lakes is similar at both poles (Birch et al., 2017), but 97% of Titan's liquids (by area) reside in the north polar region, with only nine filled lakes observed in the south.

6.2.2.2 Labyrinth

All the labyrinth terrains are mapped as one unit in the global map, although variations exist in terms of width of valleys and intervening ridge spacing that have led them to be divided into subtypes (Malaska et al., 2020). The labyrinths appear to be highly dissected, with a clear up-to-downrange bright-dark pairing (Malaska et al., 2016) in the SAR images, indicative of plateaus with valleys containing radar-dark fill material. The labyrinth unit shows overall medium radar backscatter and individual exposures are generally more than 5,000 km^2 in extent. Topographic data show that labyrinths are locally elevated. Valley and ridge widths are variable; in areas where the valleys are wide (>2 km) and the exposures of elevated terrain are narrow (<2 km), the area appears as a series of remnant ridges. In contrast, where the valleys are narrow (<2 km) and the intervening elevated terrains are wide (>2 km), the area can appear as a highly dissected plateau. ISS and VIMS data show the labyrinth unit to be slightly darker in the near-infrared than the surrounding plains (Malaska et al., 2016, 2020). The labyrinth unit is thus

interpreted as dissected plateaus and remnant ridges of organic materials that have since been eroded and transported into adjacent plains and into downstream basins (Malaska et al., 2016). Undifferentiated plains are often found in the valleys as fill and at the distal edges of the valleys, suggesting that the labyrinth terrains may be plateaus composed of undifferentiated plains materials.

6.2.2.3 Crater

The overall morphologic expression of a Titan crater is a partial or complete circle of high SAR backscatter materials. Craters can be easily identified if they are larger than several tens of kilometers in diameter. Impact craters and ejecta can often be identified in VIMS and ISS images (Neish et al., 2015). The challenge of identifying partial circular features as craters has been previously described (Wood et al., 2010; Neish et al., 2012). We cross-checked our crater identifications with previous mapping (Wood et al., 2010; Neish et al., 2012; Hedgepeth et al., 2020) and found agreement in all but a few cases where identification was largely subjective, generally because of rim erosion and no discernible ejecta, or because of poor resolution data. Craters may be surrounded by an extended region of crater ejecta, plains, or other near-infrared-bright units; these terrains often extend in the inferred downwind direction (eastward; Malaska et al., 2020). In a few craters, a central peak is observed at the center (or inferred center) of the circular rim. The margins of the crater rim may have become dissected by fluvial erosion or mass-wasting processes (Soderblum et al., 2010; Neish et al., 2015). Ejecta may be covered over by plains materials or in some instances by dunes, which are also seen inside several of the craters, interpreted as wind-blown deposits (Lopes et al., 2016).

6.2.2.4 Dunes

These areas were mapped at the regional 1:800,000 scale as three subunits: linear dunes, reticulated dunes and featureless dune sands (Malaska et al., 2016). The linear dunes subtype shows characteristic dune lineations in the SAR image across most of the areal extent of the terrain unit, whereas the featureless sand sheets contain only a few extended broad lanes that can be discerned in select areas. Both types of terrains are interpreted as deposits of sand-sized grains (Lorenz et al., 2006) that form linear dunes that are generally located at equatorial latitudes. Reticulated dunes are small patches of linear dunes showing a pattern perpendicular to the orientation of linear dunes nearby. These areas are interpreted as regions where the wind field is varying, and the deposition therefore occurs in a more complex pattern than those that generate linear dunes. Dunes appear dark in both ISS and SAR, have high emissivity in microwave radiometry measurements suggestive of organic materials, and correspond to the VIMS 'dark brown unit' in 3-band VIMS global maps (Barnes et al., 2007; Rodriguez et al., 2014). Radiative transfer analysis of VIMS data for various dune fields showed (generally including both dune and interdune features since resolution limits prevent VIMS from distinguishing between the two) that the dunes are spectrally flat and very dark in the VIMS range (Solomonidou et al., 2018). In the 1:20,000,000 scale map, all the dune subunits were mapped as dunes.

6.2.2.5 Hummocky

This unit consists of four subunits previously described (Malaska et al., 2016; Schoenfeld et al., 2021; 2023) as hummocky, mountains, degraded hummocky, pitted hummocky, and cross-cut hummocky. All are areas of high SAR backscatter and show locally positive topographic expression. The main difference between mountains and hummocky subunits is that the

mountains appear elongated in shape and show RADAR up-to-downrange bright-dark pairing, whereas the hummocky unit shows uniform to grainy internal textures. Degraded hummocky are small (<5 km across) and generally found in plains. Cross-cut hummocky terrains are larger (>100 km in diameter) and cut by linear features, possibly graben, and pitted hummocky are radar-bright hummocks populated by radar-dark, pit-like structures. All subunits of hummocky terrains appear bright in ISS images. The microwave radiometric response for all these subunits indicates that they are composed of fractured water ice or mixtures of fractured water ice and organic materials (Janssen et al., 2016), and these areas are interpreted as exposures of ancient crust or bedrock, consistent with the interpretation of the hummocky or mountainous unit previously proposed (Lopes et al., 2010).

6.2.2.6 Lakes

We mapped both filled and empty lakes following criteria discussed in previous work (Birch et al., 2017). Filled lakes are generally radar dark, although their darkness varies as a function of their fill state. Owing to the transparency of liquid methane to Cassini's RADAR (Mastrogiuseppe et al., 2014), all the filled liquid bodies mapped by SAR are at least a few meters deep. The filled lakes and seas are also clearly seen in ISS and VIMS images, allowing for an accurate assessment of lake/sea surface areas in areas not imaged by SAR. Empty lakes appear similar in planform to the filled lakes, because they form closed topographic lows (Hayes et al., 2008; Birch et al., 2017). Their perimeters form steep-sided walls, with a distinct curvature that indicates expansion by uniform scarp retreat (Hayes et al., 2017).

6.3 The Global Map

We use the correlations between SAR and other datasets—obtained using low-resolution, high-altitude SAR, radiometry, the Imaging Science Subsystem (ISS) and the Visible and Infrared Mapping Spectrometer (VIMS)—to produce a global 1:20,000,000 scale map of the major geological units (Fig. 6.3). With that map, we find that the majority of Titan's surface is comprised of plains, which make up 61% of the SAR-imaged areas and 65% of the global area (Table 6.1). Several types of plain were mapped at a regional scale (see Methods), the most extensive of which are the undifferentiated plains, which appear near-uniform and radar-dark in SAR images, lacking major topographical relief (Lopes et al., 2016). The lack of fluvial features in this terrain unit at Cassini SAR scale suggests that it is porous, is not able to support large, integrated channels or that it has buried and reworked older, extinct channel networks (Radebaugh et al., 2016). Plains dominate Titan's mid-latitudes and show high emissivity to radar, consistent with organic materials (Janssen et al., 2017). Previous work (Lopes et al., 2011) argued that undifferentiated plains are depositional or sedimentary in nature, perhaps with aeolian deposition being the major process contributing to their formation. However, latitudinal variations exist. Analyses of VIMS data show that plains closer to the equator, and therefore closest to the largest dune fields, have spectral similarities to dune materials (Lopes et al., 2016; Solomonidou et al., 2018), suggesting that some contamination by dune material was probably transported into the plains by wind. The high-latitude VIMS spectra are consistent with an unknown material that is also observed in the labyrinth unit (Solomonidou et al., 2018).

Dunes (comprising both dunes and interdunes) dominate the equatorial regions (±30° latitude) and make up the second-most extensive unit on Titan by areal coverage, 19% of the SAR-imaged area and 17% of the global area. Dunes appear as long, narrow, SAR-dark features, indicating that dune materials are smooth or absorbing at 2.17 cm. Previous measurements show

that dunes are mostly 1−2 km wide, spaced by 1–4 km and can be hundreds of kilometers long (Lorenz et al., 2006). Limited measurements of heights suggest that the dunes are 80–130m tall (Neish et al., 2010). The general direction of transport of sand (west to east) has been inferred from the way dunes interact with topo- graphic obstacles, such as hummocky and mountainous terrain (Malaska et al., 2016b; Radebaugh et al., 2010). Their large-scale morphology and sizes are similar to those of linear sand dunes on Earth (Radebaugh et al., 2010). Dunes show high emissivity to radar, consistent with organic materials (Janssen et al., 2016).

The hummocky unit consists of mountain chains and isolated terrains that are topographically higher than the surrounding areas (Malaska et al., 2016b). This unit covers 15% of the SAR-imaged surface and 14% of the global area. Hummocky terrains appear bright in SAR images because of the roughness and fractured nature of the materials (Janssen et al., 2016), as well as the terrain topography with respect to the SAR look direction and incidence angle (typically tens of degrees). They are characterized by high scattering and low emissivity in the radiometry mode (Janssen et al., 2017), indicating water-ice materials that increase the likelihood of volume scattering. The largest areal exposure of the hummocky unit is in the equatorial region known as Xanadu (Barnes et al., 2007; Radebaugh et al., 2011). Elsewhere, hummocky materials are exposed as locally isolated peaks or ranges (generally under 30 km^2). Mountains are mostly exposed as gently undulating regions from mid- to high latitudes, generally aligned east-to-west, and may have formed by contractional tectonism (Mitri et al., 2010) early in Titan's history. They are a few to tens of kilometers in length and up to a couple of kilometers high above the reference geoid. Analyses of VIMS data for the hummocky unit indicate a relatively high water-ice component (Barnes et al., 2007). Derived surface albedos of some small exposures of hummocky terrains (not within Xanadu) suggest that the hummocky unit is relatively dark,

containing a spectrally dark constituent (Birch et al., 2017) in addition to water ice in the mixture; other VIMS results (Barnes et al., 2007) suggest differences between Xanadu and other hummocky terrains. These results are consistent with the hummocky unit rep- resenting exposed remnants of Titan's icy shell (Lopes et al., 2010), in parts covered in a sedimentary veil of organics originating in Titan's atmosphere.

The lakes unit comprises lakes and seas, which can either be dry or liquid filled. Titan's polar regions contain over 650 lakes (Birch et al., 2017), either dry or filled with liquid hydrocarbons. The majority of filled lakes and seas (mare) are located in the north polar region, mostly (approximately 80%) in the Kraken, Ligeia and Punga mare. These larger northern mares have varied shorelines indicating flooding and draining of pre-existing topography, whereas the majority of the smaller lakes form steep-sided depressions with no true terrestrial analogue (Hayes et al., 2017). In the south, Ontario Lacus appears as a residual lake inset in a larger palaeobasin. The morphologies of both dry and filled lakes and seas on Titan may provide a record of past and current climatic conditions and surface evolution processes (Birch et al., 2018; Turtle et al., 2018). The lakes unit makes up only 2.2% of the SAR-imaged areas and 1.5% of Titan's total surface area.

The labyrinth unit consists of terrains with medium SAR back- scatter and the appearance of being highly incised and dissected plateaus. These terrains cover 2.1% of the SAR-imaged area and 1.5% of the global area and are primarily located at high latitudes. Topographic data indicate that this unit is locally elevated. VIMS data of the top surface are consistent with a material compatible with hydroxide-bearing constituent (this spectral response has been ascribed to water ice; Solomonidous et al., 2018). Fluvial valley networks (rectangular to dendritic) inside the labyrinth units suggest some structural and topographic control. Radiometry data show that,

like dune materials, this unit has high emissivity, consistent with materials that are organic in composition and thus have a low bulk dielectric constant. Labyrinths have morphologies similar to karstic terrain and may have formed through a combination of dissolution, possibly karstic (Malaska et al., 2020), coupled with mechanical erosion, or other processes or phase changes that could allow the formation of closed valleys (at least at the SAR resolution) and transport of materials to the surrounding plains.

Craters occupy only 0.7% of Titan's SAR-imaged area and 0.4% of the global area. Only 23 craters more than 20km in diameter were identified with a high degree of certainty (plus about ten others as probable) from all datasets, plus a few smaller crater candidates (Neish et al., 2016). This suggests that Titan has a crater retention age of several hundred million years (Wood et al., 2010). The distribution of craters also shows some latitudinal variation, consistent with the oldest exposed surfaces being located near the equator and the youngest surfaces located near the poles (Neish et al., 2016), where there is an almost complete absence of craters. Most craters show evidence of erosion by aeolian and fluvial or pluvial processes. The absence of craters in the polar regions could be due to infilling of the polar basins by sediments (Birch et al., 2017), increased erosion by fluvial processes (Neish et al., 2016) or impacts into former marine environments (Neish et al., 2014). The microwave emissivity of the less-degraded crater rims and ejecta is among the lowest on Titan (Janssen et al., 2016), consistent with icy materials excavated by the impact. The inferred composition from radar and VIMS data is crustal water ice or a mixture of crustal water ice and organic material (Neish et al., 2015).

The scarcity of craters on Titan limits the viability of crater counting statistics for distinguishing the ages of different terrains. However, contacts between units and superposition relations can be used to infer their relative ages. Contacts mapped from the complete SAR

dataset confirm early suggestions (Lopes et al., 2010) that the oldest units on Titan are the hummocky terrains (including mountains). The plains are younger than both the hummocky and labyrinth units. Dunes and lakes (including seas) are the youngest units on Titan (Lopes et al., 2010; Radebaugh et al., 2010; Malaska et al., 2016a). Because there is no contact between lakes and dunes, it is not possible to distinguish the relative ages of these units and, given active seasonal weather patterns including rainfall (Turtle et al., 2011) and wind (Rodriguez et al., 2018), it is likely that both lakes and dunes are still forming and changing on Titan. Craters are an intermediate unit in relative age, with some seen in hummocky terrain, particularly in the Xanadu area, and several infilled by dune and plains materials.

The resulting global-scale geologic map shows a clear latitudinal dependence of the major units. Equatorial regions are dominated by vast dune fields and the mid-latitudes are dominated by plains, while the lakes and labyrinth units are found primarily in the polar regions. This may be related to more humid conditions in the polar regions. Superimposed on top of the global latitudinal unit distribution is a dichotomy in liquid inventories between north and south. The vast majority of filled lakes is currently situated in the northern hemisphere, while the south is nearly dry, possibly the result of global climate cycle (Birch et al., 2017, 2018). The hummocky unit, interpreted as exposed crustal materials, is seen at all latitudes, but primarily in the equatorial Xanadu region, for reasons yet unknown (Radebaugh et al., 2011). In terms of composition, the emissivity data are consistent with organic materials forming the plains, dunes, lakes and labyrinth units, while the emissivity of the crater and hummocky units indicates a higher abundance of water-ice materials. This suggestion that the latter terrains expose icy crustal material is consistent with previous work that predicted and later showed (Clark et al., 2010) that organic materials produced by high-altitude photochemistry of methane and nitrogen

in Titan's atmosphere form a surficial unit that covers much of Titan's surface. Relative ages and distribution of the major units imply that Titan's old, icy crust (hummocky materials) has been covered by sedimentary materials like the dunes and plains, particularly at lower latitudes, with the exception of Xanadu. In the polar regions, where cumulative rainfall outpaces infiltration or evaporation of liquids, lakes are abundant. Labyrinth terrains, which are older than plains and mostly located at higher latitudes, may have begun as uplifted or otherwise elevated terrains, predominantly of organic deposits, that later became heavily incised and dissolved by rainfall, like karstic formations on Earth.

Titan is covered by organic sediments that are reworked, to varying degrees, by aeolian, pluvial and fluvial processes. Though rainfall occurs at all latitudes, Titan's equatorial climate is arid over long enough timescales that aeolian deposition and dune formation dominate. Towards the poles, relative humidity increases, and liquid hydrocarbon lakes and seas dominate the polar landscape. Between these two extremes is a vast area of mid-latitude, featureless, organic plains. The clear distinction between these units and where they are found on Titan indicates that a variety of processes must be acting on the surface of this moon, controlled by climatic, seasonal and elevational conditions.

6.4 Regional Maps in the Global Context

Following our previous mapping efforts, we now compare the areal extent of different terrain units from the detailed regional mapping conducted for the Afekan crater region (Malaska et al., 2016a), the South Belet region (Schoenfeld et al., 2021), the Soi crater region (Schoenfeld et al., 2023), and the global geomorphological map of Titan (Lopes et al., 2020).

In Table 6.1, we compare Soi mapping statistics with Afekan, South Belet, and the Global map of Titan. The Afekan and South Belet did not include non-SAR mapping at the time of their publication in Malaska et al. (2016a) and Schoenfeld et al. (2021) respectively. Here, in Table 6.1, we present new calculations made for Afekan and South Belet that include non-SAR mapping. Starting from the most extended major unit for all three regions, the plains, it seems that the Soi crater region is the richest in plains (~70%) and South Belet the least abundant among the three (~42%), while the undifferentiated are the predominant plains for all regions. The dunes are the second most abundant unit with the linear dunes dominating the other types of dunes for all three regions and most significantly for South Belet, where they cover 37% of the mapping area. The hummocky-mountainous terrains cover very similar areal extent at all three regions, with the hummocky terrains being the predominant type (~5-9%). The crater units and their subunits cover only a small fraction of the high-resolution SAR mapped area with three particular subunits being present only in the Afekan crater region, the crater fills 1 and 2, and the central peak.

In total, it seems that all three regions present many similarities in the high-resolution SAR mapped areal extent of the major geomorphological units, with major difference being the appearance of SEDs in the midlatitude Soi crater region.

Table 6.1. Comparison of areal extent percentage between the global geomorphological map of Titan (Lopes et al., 2020) and three major Titan regions: the Soi crater region (Schoenfeld et al., 2023), the Afekan crater region (Malaska et al., 2016a), and the South Belet crater region (Schoenfeld et al., 2021). The statistics make use of both the high-resolution SAR, HiSAR, and non-SAR mapping.

Terrain Unit	Soi	Afekan	South Belet	Global Map
Crater	**0.4**	**0.6**	**<0.1**	**0.4**
Crater rim (*crh*)	0.19	0.18	<0.1	
Crater ejecta (*ceh*)	0.18	0.33	<0.1	
Crater peak (*cph*)	<0.1	<0.1	-	
Crater fill 3 (*cf3*)	<0.1	-	-	
Crater fill 2 (*cf2*)	-	<0.1	-	
Crater fill 1 (*cf1*)	-	<0.1	-	
Central peak (*cph*)	-	<0.1	-	
Hummocky	**12**	**8.4**	**21**	**14**
Mountain (*hm*)	1.13	2.43	0.62	
Hummocky (*hh*)	5.46	3.36	9.69	
Degraded hummocky (*hdm*)	0.16	0.73	2.18	
Pitted hummocky (*hph*)	1.12	-	6.29	
Undivided hummocky (*hu*)	3.73	0.69	2.56	
Labyrinth	**0.5**	**2.2**	**-**	**1.5**
Valley labyrinth (*lbv*)	-	0.47	-	
Polygonal labyrinth (*lbp*)	-	0.28	-	
Finely dissected (*lbf*)	0.5	-	-	
Undivided labyrinth (*lu*)	-	0.11	-	
Plains	**72.6**	**66.7**	**42**	**65**

Bright alluvial deposit (*pah*)	-	-	0.32	
Bright gradational plains (*pgh*)	0.35	-	-	
Undifferentiated plains (*pul*)	22.28	33.4	18.39	
Variable featured plains (*pfv*)	14.20	13.05	5.03	
Dark irregular plains (*pil*)	1.14	0.68	0.28	
Scalloped plains (*psv*)	1.57	3.4	0.18	
Lineated Plains (*plh*)	-	0.44	-	
Streak-like plains (*psh*)	1.04	2.71	-	
Undivided Bright Plains (*pu*)	27.29	15.67	14.63	
Undivided Dark Plains (*pdu*)	4.77	0.51	2.99	
Dunes	**14.3**	**21.6**	**36.8**	**17**
Featureless sand sheets (*ds*)	1.65	1.31	3.05	
Linear dunes (*dl*)	9.02	11.25	32.75	
Reticulated dunes (*dr*)	-	0.21	-	
Undivided Dunes (*du*)	3.58	8.85	1.03	
Basin and Lakes	**0.7**	**0.3**	**-**	**1.5**
Sharp-edged depressions (*bse*)	0.62	0.28	-	
Ramparts (*brh*)	0.04	-	-	

6.5 Summary

The dataset best suited for interpreting Titan's surface geology from orbit was obtained using synthetic aperture radar (SAR) from Cassini, as Titan's hazy atmosphere limits the signal-to-noise ratio of visible and near-infrared observations but is transparent to the radar's operating

wavelength of 2.17cm (K_u band). On the SAR images, we defined six major geological units (based primarily on backscatter and overall morphology, as done for prior mapping (Malaska et al., 2016; Schoenfeld et al., 2021; 2023) as follows: plains, dunes, hummocky terrain, lakes, labyrinth terrain and craters (Fig. 6.1). Mapping the distribution of these units enables us to discern their latitudinal distribution, superposition relations, composition and areal coverage, and the implications for Titan's geological history. We first mapped the areas covered by SAR (about 46% of Titan's surface at less than 1 km resolution). We then used correlations between SAR and other datasets—obtained using low-resolution, high-altitude SAR, radiometry, the Imaging Science Subsystem (ISS) and the Visible and Infrared Mapping Spectrometer (VIMS)—to extend the mapping to regions not covered by SAR (see Methods), finally producing a global 1:20,000,000 scale map of the major geological units (Fig. 6.3). This scale is appropriate for defining the six major units we present in this paper, although it is coarser than the 1:800,000 scale maps done for individual regions such as that of the Afekan crater (Malaska et al., 2016). The main difference between the 1:800,000 scale map and the 1:20,000,000 scale maps is that the sub-units in the finer-scale map do not appear in the 1:20,000,000 map (Fig. 6.2). Correlations between these datasets enabled us to map the global geology even where datasets were incomplete and to place geomorphological units in relative stratigraphic and areal context to provide a sequence of events for the surface evolution of Titan.

6.6 Figures and Figure Captions

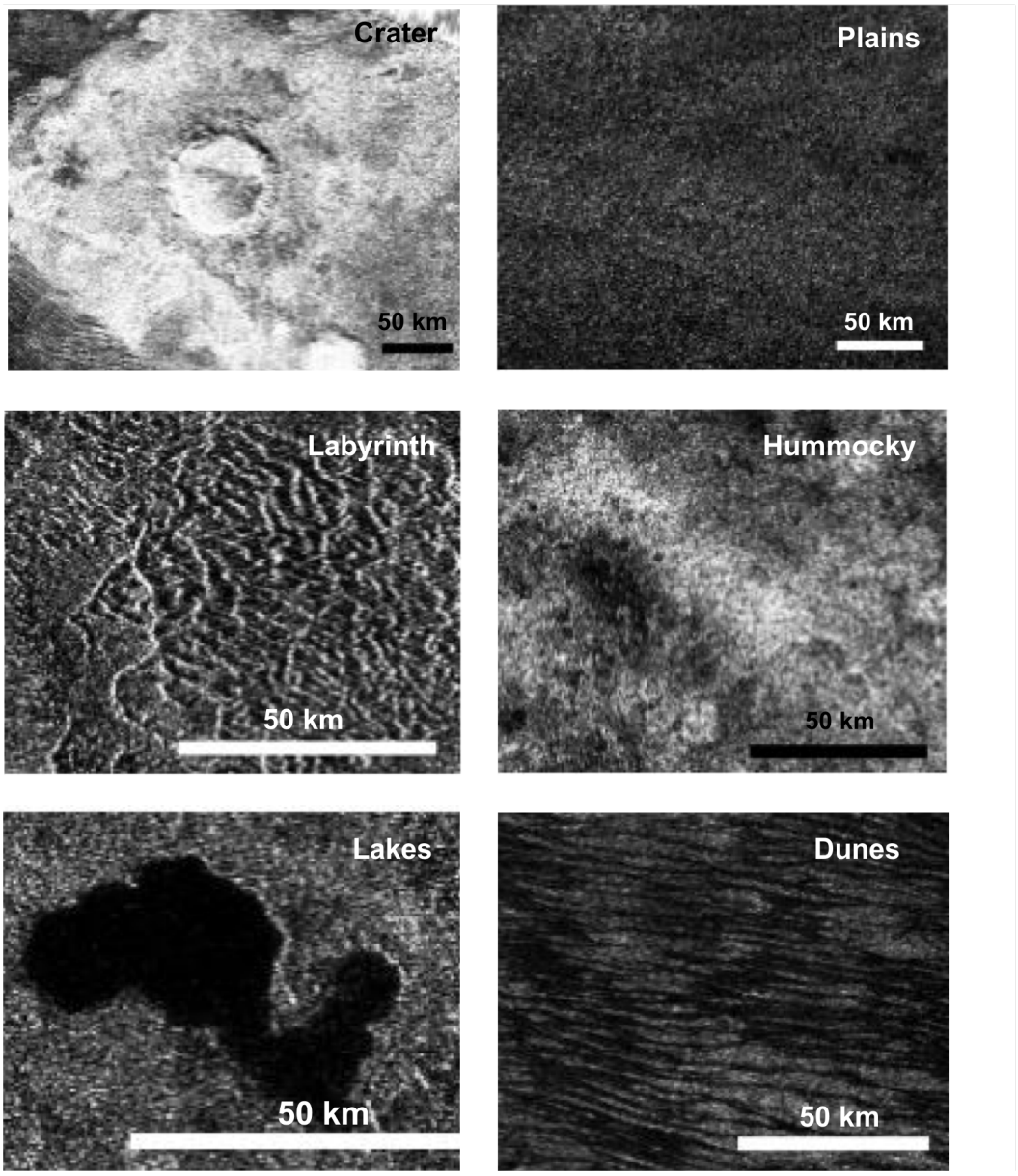

Fig. 6.1 SAR images showing examples of the main classes of geomorphological units on Titan.

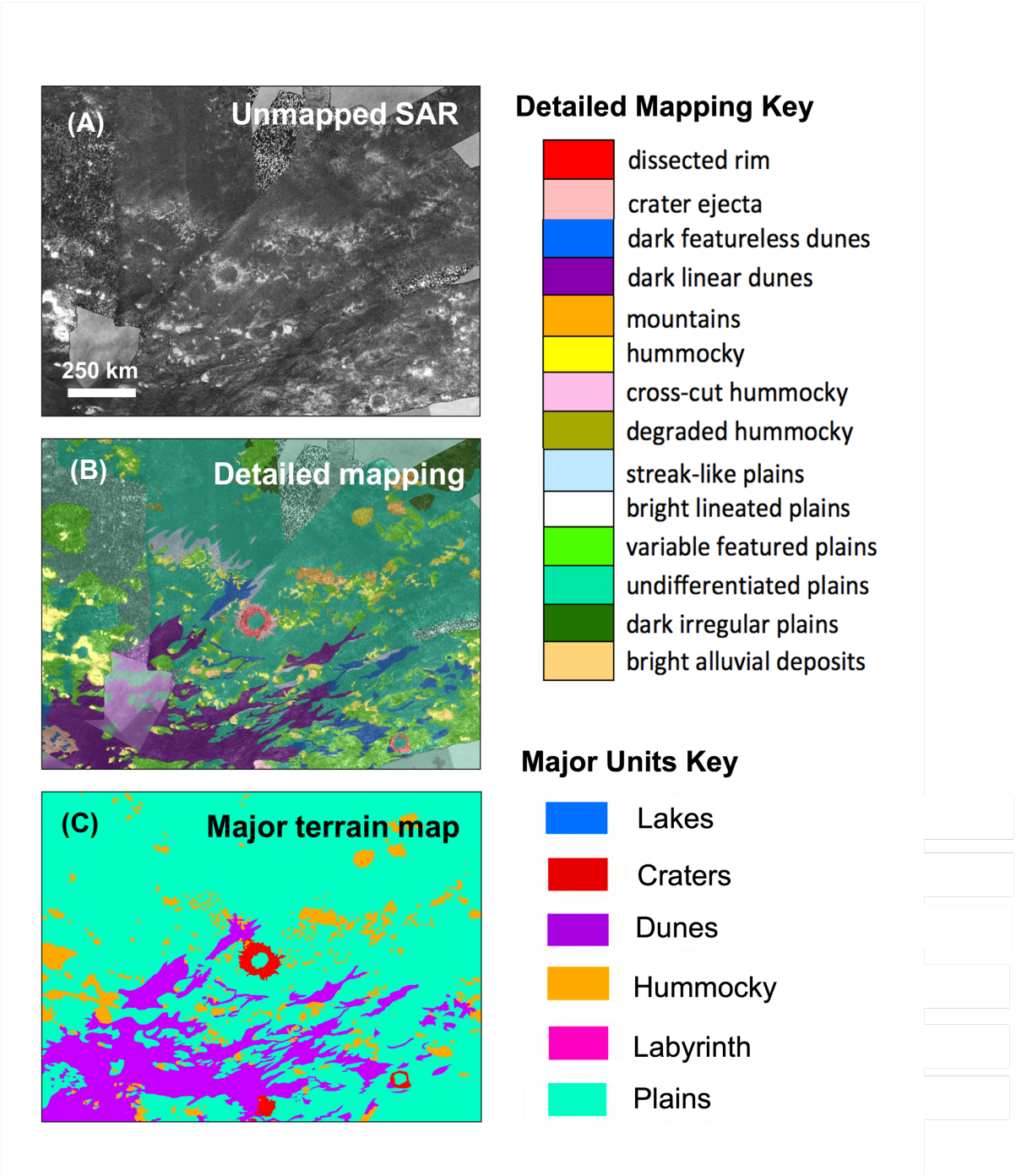

Fig 6.2 Example of the mapping method from regional to global. (A) Unmapped SAR data over ISS data. (B) Detailed mapping over SAR (at 1:800,00 scale) and mapping of areas covered by ISS and other datasets but not SAR (pale colors). (C) Major terrains. The colors correspond to the detailed mapping of terrains and the major units for the 1:20,000,000 scale map.

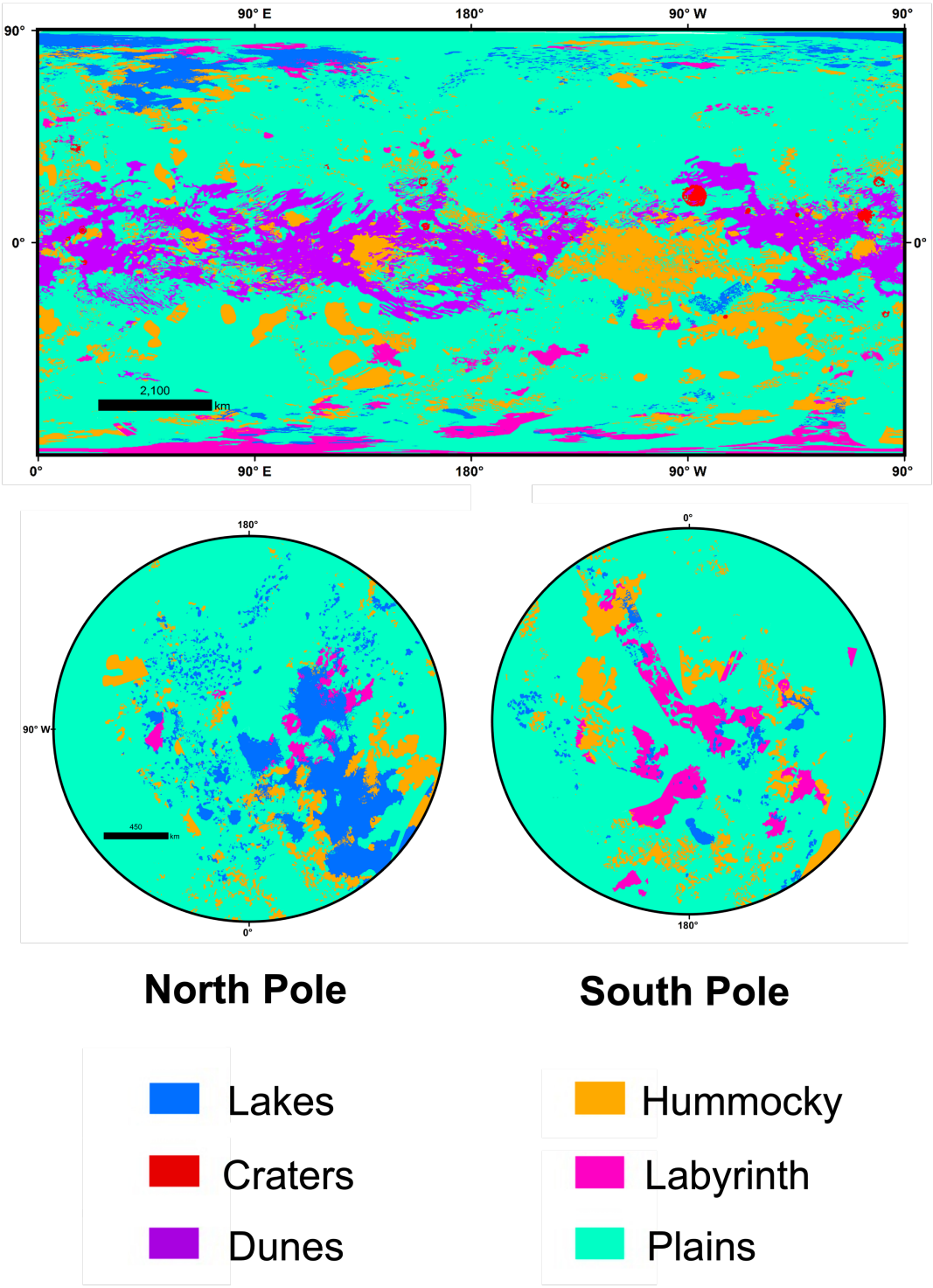

Fig 6.3 Global map of Titan's major geomorphological units. The map projections are Mercator (top) and polar stereographic (bottom, for > 55°N and °S).

6.7 References

1. Hayes, A. G., Lunine, J. I. & Lorenz, R. D. Titan's hydrologic cycle: a post-Cassini view. *Nat. Geosci.* **11**, 306–313 (2018).
2. Lopes, R. M. C. et al. Distribution and interplay of geologic processes on Titan from Cassini RADAR data. *Icarus* **205**, 540–588 (2010).
3. Malaska, M. J. et al. Geomorphological map of the Afekan Crater region, Titan: terrain relationships in the equatorial and mid-latitude regions. *Icarus* **270**, 130–161 (2016).
4. Solomonidou, A. et al. The spectral nature of Titan's major geomorphological units: constraints on surface composition. *J. Geophys. Res. Planet* **123**, 489–507 (2018).
5. Wood, C. A. et al. Impact craters on Titan. *Icarus* **206**, 334–344 (2010). 6. Neish, C. D. et al. Spectral properties of Titan's impact craters imply chemical weathering of its surface. *Geophys. Res. Lett.* **42**, 3746–3754 (2015).
6. Burr, D. M., Emery, J. P., Lorenz, R. D., Collins, G. C. & Carling, P. A. Sediment transport by liquid surficial flow: application to Titan. *Icarus* **181**, 235–242 (2006).
7. Lorenz, R. D. et al. Fluvial channels on Titan: initial Cassini RADAR observations. *Planet. Space Sci.* **56**, 1132–1144 (2008).
8. Lorenz, R. D. et al. The sand seas of Titan: Cassini RADAR observations of ongitudinal dunes. *Science* **312**, 724–727 (2006).
9. Radebaugh, J. et al. Alluvial and fluvial fans on Saturn's moon Titan reveal processes, materials, and regional geology. In *Geology and Geomorphology of Alluvial and Fluvial Fans: Terrestrial and Planetary Perspectives* (eds Ventra, D. & Clarke, L. E.) (Geol. Soc. Lond. Spec. Publ. 440, 2016).

10. Lopes, R. M. C. et al. Nature, distribution, and origin of Titan's undifferentiated plains ("blandlands"). *Icarus* **270**, 162–182 (2016).
11. Turtle, E. P. et al. Rapid and extensive surface changes near Titan's equator: evidence of April showers. *Science* **331**, 1414–1417 (2011).
12. Cornet, T. et al. Dissolution on Titan and on Earth: toward the age of Titan's karstic landscapes. *J. Geophys. Res. Planets* **120**, 1044–1074 (2015).
13. Mitri, G. et al. Mountains on Titan: modeling and observations. *J. Geophys. Res.* **115**, E10 (2010).
14. Lopes, R. M. C. et al. Cryovolcanism on Titan: new results from Cassini RADAR and VIMS. *J. Geophys. Res. Planets* **118**, 1–20 (2013).
15. Clark, R. N. et al. Detection and mapping of hydrocarbon deposits on Titan. *J. Geophys. Res. Planets* **115**, (2010).
16. Janssen, M. A. et al. Titan's surface at 2.18-cm wavelength imaged by the Cassini RADAR radiometer: results and interpretations through the first ten years of observation. *Icarus* **270**, 443–459 (2016).
17. Malaska, M. J. et al. Material transport map of Titan: the fate of dunes. *Icarus* **270**, 183–196 (2016).
18. Birch, S. P. D. et al. Geomorphologic mapping of Titan's polar terrains: constraining surface processes and landscape evolution. *Icarus* **282**, 1–23 (2017).
19. Neish, C. D. et al. Radarclinometry of the sand seas of Africa's Namibia and Saturn's moon Titan. *Icarus* **208**, 385–394 (2010).
20. Radebaugh, J. et al. Linear dunes on Titan and Earth: initial remote sensing comparisons. *Geomorphology* **121**, 122–132 (2010).

21. Barnes, J. W. et al. Near-infrared spectral mapping of Titan's mountains and channels. *J. Geophys. Res. Planets* **112**, E11006 (2007).

22. Radebaugh, J. et al. Regional geomorphology and history of Titan's Xanadu province. *Icarus* **211**, 672–685 (2011).

23. Hayes, A. G. et al. Topographic constraints on the evolution and connectivity of Titan's lacustrine basins. *Geophys. Res. Lett.* **44**, 11745–11753 (2017).

24. Birch, S. P. D. et al. Morphological evidence that Titan's southern hemisphere basins are paleoseas. *Icarus* **310**, 140–148 (2018).

25. Turtle, E. P. et al. Titan's meteorology: evidence for extensive subsurface methane reservoirs. *Geophys. Res. Lett.* **45**, 5320–5328 (2018).

26. Neish, C. D. et al. Fluvial erosion as a mechanism for crater modification on Titan. *Icarus* **270**, 114–129 (2016).

27. Neish, C. D. & Lorenz, R. D. Elevation distribution of Titan's craters suggests extensive wetlands. *Icarus* **228**, 27–34 (2014).

28. Rodriguez, S. et al. Observational evidence for active dust storms on Titan at equinox. *Nat. Geosci.* **11**, 727–732 (2018).

29. Griffith, C. A. et al. A corridor of exposed ice-rich bedrock across Titan's tropical region. *Nat. Astron.* **3**, 642–648 (2019).

30. Williams, D. et al. Geologic mapping of the Menrva region of Titan using Cassini RADAR data. *Icarus* **212**, 744–750 (2011).

31. Porco, C. C. et al. Cassini imaging science: instrument characteristics and anticipated scientific investigations at Saturn. *Space Sci. Rev.* **115**, 363–497 (2004).

32. Karkoschka, E. et al. A global mosaic of Titan's surface albedo using Cassini images. In *Division for Planetary Sciences 50th Meeting* 216.02 (American Astronomical Society, 2018).

33. Brown, R. H. et al. The Cassini Visual and Infrared Mapping Spectrometer (VIMS) investigation. *Space Sci. Rev.* **115**, 111–168 (2004).

34. Le Mouelic, S. et al. The Cassini VIMS archive of Titan: from browse products to global infrared color maps. *Icarus* **319**, 121–132 (2019).

35. Le Mouélic, S. et al. Global mapping of Titan's surface using an empirical processing method for the atmospheric and photometric correction of Cassini/VIMS images. *Planet. Space Sci.* **73**, 178–190 (2012).

36. Elachi, C. et al. Radar: the Cassini Titan radar mapper. *Space Sci. Rev.* **115**, 71–110 (2004).

37. Stiles, B. W. et al. Determining Titan surface topography from Cassini SAR data. *Icarus* **102**, 584–598 (2009).

38. Barnes, J. W. et al. Global-scale surface spectral variations on Titan seen from Cassini/VIMS. *Icarus* **186**, 242–258 (2007).

39. Rodriguez, S. et al. Global mapping and characterization of Titan's dune fields with Cassini: correlation between RADAR and VIMS observations. *Icarus* **230**, 168–179 (2014).

40. Mastrogiuseppe, M. et al. The bathymetry of a Titan sea. *Geophys. Res. Lett.* **41**, 1432–1437 (2014).

41. Hayes, A. G. et al. Hydrocarbon lakes on Titan: distribution and interaction with a porous regolith. *Geophys. Res. Lett.* **35**, 9204 (2008).

42. Malaska, M. J. et al. Identification of karst-like terrain on Titan from valley analysis. *Lunar Planet. Sci. Conf*. **41**, abstr. 1544 (2010).

43. Neish, C. D. & Lorenz, R. D. Titan's global crater population: a new assessment. *Planet. Space Sci.* **60**, 26–33 (2012).

44. Soderblom, J. M. et al. Geology of the Selk crater region on Titan from Cassini VIMS observations. *Icarus* **208**, 905–912 (2010).

- Chapter 7 -

7.1 Summary and Conclusions

In Chapter 2, I posited that thermal convection in Enceladus' oceans may cause the upward transport of hydrothermal products, explaining the observation of silica particles in Enceladus' plumes (Sekine et al., 2015; Hsu et al., 2015). To test this, I applied a particle entrainment model (Solomatov et al., 1993; Lavorel and Le Bars, 2009) and used known fluid scaling relations (e.g., Soderlund et al., 2014, 2019) to quantify the proposed ocean convection. I found that both the core-ocean heat fluxes and the transport timescale necessary to drive oceanic convection and entrain particles of the observed sizes are consistent with observations and predictions from existing thermal models. I then conclude that convection in the ocean of Enceladus can explain the entrainment, transport, and ultimate delivery of silica particles from Enceladus' core/ocean interface to the ice shell.

In Chapter 3, I presented detailed structural mapping along two segments of the tiger stripe fractures. I identified evidence suggestive of left-slip deformation along the tiger stripes, including structures consistent with en echelon folds/fractures and pull-apart basins. Based on the observed left-slip kinematics, I derived a tensile-shear failure criterion that enabled me to decompose the total stress field at Enceladus' south pole into a tidal and tectonic component. I was then able to infer that the tectonic stress field is comparable in magnitude to the diurnal tide, suggesting that both components are relevant in determining timing and style of plume eruption. The magnitude of stress generated by topography surrounding the South Polar Terrain and associated ice shell variations is on order of the tectonic stresses I infer with my model.

In Chapter 4, I presented detailed mapping of Titan's South Belet region. This area spans from longitude 60°E to 120°E and from latitude 60°S to 0°, encompassing both equatorial and southern mid-latitude regions. I used Cassini RADAR in its Synthetic Aperture Radar (SAR)

mode data as our basemap, which covers 31.8% of the region, supplemented with data from the RADAR's radiometry mode, the Imagining Science Subsystem (ISS), the Visual and Infrared Mapping Spectrometer (VIMS), and topographic data. I followed the mapping procedure described in Malaska et al. (2016a) for the Afekan Crater region and identified four major terrain classes in South Belet: craters, hummocky/mountainous, plains, and dunes. There are two terrain units that were not included in previous studies but were identified in our mapping of South Belet: "bright alluvial plains" and "pitted hummocky". Similar to the Afekan Crater region, we find that plains dominate the surface make-up of South Belet, comprising ~ 47% of the mapped area. Unlike Afekan, the areal extent of the dunes closely rivals the dominance of plains, making up 43% of the mapped area. The next most widespread unit by area in the region following the dunes are the mountains/hummocky terrains (10%), and finally, crater terrains (0.01%). The introduction of two new units, "bright alluvial plains" and "pitted hummocky", are necessary to capture the full range of morphologies seen in South Belet and expands our understanding of processes typical of Titan's equatorial and mid-latitude regions. For example, the presence of alluvial fans indicates a period in Titan's past where discharges and slopes were such that sediment could be mobilized and deposited. Similarly, the pits associated with the "pitted hummocky" may represent an important erosional feature, with implications for the removal of volatiles from Titan's crust. However, analysis of our geomorphological mapping results suggests the geology of South Belet is consistent with the narrative of organics dominating the equatorial and mid-latitudes. Lastly, the applicability of the terrain units from our mapping of the Afekan region, which bears a similar latitude but in the northern hemisphere, to our mapping of South Belet suggests latitudinal symmetry in Titan's surface processes and their evolution.

In Chapter 5, I presented Titan's Soi crater region mapped at 1:800,000 scale using methodology by Malaska et al. (2016) and Schoenfeld et al. (2021). This region spans longitude 110°W to 180°W and latitude 0° to 60°N and is representative of the transition between the equatorial, mid-latitude, and high-latitude northern regions of Titan. I use Cassini Synthetic Aperture Radar (SAR) as the primary mapping dataset. For areas where SAR was not available, I used lower resolution data from the Imaging Science Subsystem (ISS), the Visible and Infrared Mapping Spectrometer (VIMS), radiometry, and high-altitude SAR (HiSAR) for complete mapping coverage of the region. I identify 22 geomorphological units, 3 of which have been discussed in existing literature but have not yet been incorporated into the detailed mapping investigations (e.g., Schoenfeld et al., 2021; Malaska et al., 2016). These units are the sharp-edged depressions (*bse*), ramparts (*brh*), and bright gradational plains (*pgh*). All six major terrain classes are represented in this region: Craters, Labyrinth, Hummocky/mountainous, Plains, Dunes, and Basin and Lakes. I find that plains dominate the surface of the Soi crater region, comprising ~73% of the mapped area, followed by dunes (~14%), mountains/hummocky terrains (~12%), basin and lakes (~0.7%), labyrinth terrains (~0.5%), and crater terrains (~0.4%). I also observe empty lakes as far south as 40°N. The Soi crater region largely has the same collection and proportion of geomorphological units to other mapped regions on Titan. These results further support the hypothesis that surface processes are, broadly speaking, the same across Titan's middle and equatorial latitudes, with the exception of Xanadu.

In Chapter 6, I identified and map the major geological units on Titan's surface using radar and infrared data from the Cassini orbiter spacecraft. Correlations between datasets enabled us to produce a global map even where SAR is incomplete. Because of the lower resolution of

the non-SAR datasets, this map was conducted at the 1:20,000,000 scale and units were broadly classified as either Plains, Dunes, Hummocky, Basin and Lakes, Labyrinth, or Craters. The spatial and superposition relations between major geological units reveals the likely temporal evolution of the landscape and provides insight into the interacting processes driving its evolution. Based on their spatial superposition, I infer that dunes and lakes are relatively young, whereas the hummocky or mountainous terrains are the oldest on Titan. These results also show that Titan's surface is dominated by sedimentary or depositional processes with a clear latitudinal variation, with dunes at the equator, plains at mid-latitudes and labyrinth terrains and lakes at the poles.

7.2 References

Sekine, Y., Shibuya, T., Postberg, F., Hsu, H.W., Suzuki, K., Masaki, Y., Kuwatani, T., Mori, M., Hong, P.K., Yoshizaki, M. and Tachibana, S., 2015. High-temperature water–rock interactions and hydrothermal environments in the chondrite-like core of Enceladus. Nature Communications 6, 8604.

Hsu, H.W., Postberg, F., Sekine, Y., Shibuya, T., Kempf, S., Horányi, M., Juhász, A., Altobelli, N., Suzuki, K., Masaki, Y. and Kuwatani, T., 2015. Ongoing hydrothermal activities within Enceladus. Nature 519, 207-210.

Malaska, M. J., Lopes, R. M. C., Williams, D. A., Neish, C. D., Solomonidou, A., Soderblom, J. M., et al., 2016a. Geomorphological map of the Afekan Crater region, Titan: Terrain relationships in the equatorial and midlatitude regions. Icarus 270, 130–161.

Schoenfeld, A., Lopes, R., Malaska, M., Solomonidou, A., Williams, D., Birch, S., Hayes, A.,

Corlies, P., Le Gall, A., Janssen, M., Le Mouelic, S., Turtle, E., Florence, M., Verlander, T., 2021. Geomorphological map of the South Belet Region of Titan. Icarus 366, 114516.

Solomatov, V.S. and Stevenson, D.J., 1993. Suspension in convective layers and style of differentiation of a terrestrial magma ocean. Journal of Geophysical Research: Planets 98, 5375-5390.

Lavorel, G. and Le Bars, M., 2009. Sedimentation of particles in a vigorously convecting fluid. Physical Review E 80, 046324.

Soderlund, K.M., Schmidt, B.E., Wicht, J. and Blankenship, D.D., 2014. Ocean-driven heating of Europa's icy shell at low latitudes. Nature Geoscience 7, 16-19.

Soderlund, K.M., 2019. Ocean dynamics of outer solar system satellites. Geophysical Research Letters 46, 8700-8710.